

**Nonlinear optical behavior of
lanthanide phthalocyanines and their
conjugates with a selection of
nanomaterials**

A thesis submitted in fulfilment of the requirements

for the degree of

DOCTOR OF PHILOSOPHY

Of

RHODES UNIVERSITY

By

KUTLOANO EDWARD SEKHOSANA

February 2016

Dedication

To

My Mother

MASEBOKA ANNA SEKHOSANA

May God give you strength to continue loving, guiding and supporting us.

My Sisters

**MALEHLOHONOLO, RORISANG, REFILOE, FUSI
AND RELEBOHILE**

My Brothers

TANKISO AND THAROLLO

My Cousin

ELELLOANG MOHLAKOANA

Acknowledgements

I am thankful to God for all the strength He gave me during my PhD programme.

My truthful thankfulness is extended to my supervisor **Prof. Tebello Nyokong**. Her excellent guidance and frequent interaction with me throughout my PhD programme was a pillar of success. I like express my cordial gratitude to Dr Christian Litwinski (my former supervisor) for his assistance in the equipment. My sincere gratitude goes to Dr Edith Antunes for thoroughly training me on electron spin resonance. I am thankful to Dr John Mack, Dr Samson Khene, Dr Khavwajira Edith Amuhaya and Dr Jonathan Britton for their kind assistance in different ways. I am very thankful to Ms Gail Cobus for her tireless assistance in all administration issues.

I am grateful to my sponsors, Council for Scientific and Industrial Research in South Africa and the Armaments Corporation of South Africa SOC Ltd (ARMSCOR), for their support throughout my PhD programme.

Thanks also to my current and former S22 research group colleagues and colleagues from the other laboratories such as F22 for all the help I got from them. My special thanks go to my family and friends for their support.

I also like to sincerely thank the Chemistry Department technical team for their assistance.

Abstract

This thesis presents novel asymmetrical and symmetrical lanthanide phthalocyanines (Pcs) characterized using a number techniques including proton nuclear magnetic resonance, electron spin resonance, time correlated single photon counting, FTIR spectrometry, MALDI-TOF mass spectrometry, UV-Vis spectrometry, Raman spectroscopy and CHNS elemental analysis. The design of these lanthanide Pcs takes the form of mononuclear, binuclear, trinuclear, bis- and tris(phthalocyanines). Nanomaterials such as zinc oxide nanoparticles (ZnO NPs), multi-walled carbon nanotubes (MWCNTs) and graphene oxide nanosheets (GONS) (oxidized and reduced) were employed for covalent linkage to mono- and binuclear phthalocyanines as conjugates.

Transmission electron microscopy was used to characterize ZnO NPs, MWCNTs and GONS alone and when linked to lanthanide Pcs. Lanthanide Pcs alone and when linked to ZnO NPs, MWCNTs and GONS were embedded in polymers such as poly (methyl methacrylate) (PMMA), poly (bisphenol A carbonate) (PBC) and poly (acrylic acid) (PAA) for thin film preparation. The thickness of the thin films was determined by utilization of the knife edge attachment of the A Bruker D8 Discover X-ray diffraction (XRD).

Optical limiting properties of lanthanide Pcs alone and as conjugates in solution and when incorporated into polymers were determined by employing a Z-scan technique. It emerged that low symmetry lanthanide Pcs (**19**, **20** and **21**), the blue forms of bis(phthalocyanines) (only in solution; **24** and **28**) as well as tris(phthalocyanines) (**30** and **31**) exhibit low limiting threshold (I_{lim}) values in solution and thin films (particularly PBC and PAA). The low limiting threshold values make these lanthanide Pcs reliable optical limiters.

Table of contents

Dedication	ii
Acknowledgements	iii
Abstract	iv
List of Symbols	xi
List of Abbreviations	xiii
List of Figures	xvii
List of Schemes	xxi
List of Tables	xxiii
Chapter 1	1
Introduction	1
1. Introduction	2
1.1 Phthalocyanines	2
1.1.1 <i>History, applications and structure of phthalocyanines</i>	2
1.1.2 <i>Synthesis</i>	4
1.1.2.1 <i>General synthesis of mono-nuclear phthalocyanines</i>	4
1.1.2.2 <i>Clam shell and trimeric phthalocyanines</i>	5
1.1.2.3 <i>Multi-decker phthalocyanines</i>	19
1.1.2.3.1 <i>Double-decker phthalocyanines</i>	19
1.1.2.3.2 <i>Triple-decker phthalocyanines</i>	21
1.1.3 <i>Electronic absorption spectra of phthalocyanines</i>	24
1.1.3.1 <i>Monomeric phthalocyanines</i>	24
1.1.3.2 <i>Multi-decker phthalocyanines</i>	26
1.2 Nonlinear optical limiting	30
1.2.1 <i>Definition of optical limiting</i>	30
1.2.2 <i>Nonlinear optical mechanisms</i>	31
1.2.3 <i>Calculations of nonlinear optical parameters</i>	36

1.2.4 Nonlinear optical behavior of phthalocyanines.....	38
1.2.5 Nonlinear optical limiting of phthalocyanines in the presence of carbon nanotubes	41
1.2.6 Nonlinear optical limiting of phthalocyanines in the presence of graphene oxide nanosheets	43
1.2.7 Nonlinear optical limiting of phthalocyanines in the presence of zinc oxide nanoparticles	45
1.3 Photophysico-chemical parameters	46
1.3.1 Fluorescence quantum yields and lifetimes	46
1.3.2 Triplet quantum yields and lifetimes.....	47
1.3.3 Singlet oxygen quantum yield.....	48
Summary of the aims of this thesis.....	52
Chapter 2.....	53
Experimental	53
2.1 Materials	54
2.1.1 Solvents.....	54
2.1.2 Synthesis reagents	54
2.1.3 Previously synthesized phthalonitriles, phthalocyanines and nanoparticles	55
2.1.3.1 Phthalonitriles.....	55
2.1.3.2 Phthalocyanines	55
2.1.3.3 Nanoparticles	55
2.2 Instrumentation.....	55
2.3 Synthesis.....	63
2.3.1 Synthesis of phthalonitriles.....	63
2.3.1.1 Synthesis of 3,4-Bis-(3,4-dicyano-phenoxy)-benzoic acid (48) (Scheme 3.1).....	63
2.3.1.2 Synthesis of 2,4,6-tris(3-thiophthalonitrile)-s-triazine (49) (Scheme 3.2).....	64
2.3.2 Synthesis of phthalocyanines	65
2.3.2.1 Synthesis of 2(3), 9(10), 16(17), 23(24)-(tetrapyrroline-3-ylphthalocyaninato) neodymium (III) acetate (18) (Scheme 3.3)	65
2.3.2.2 Synthesis of bis{23-(3,4-di-ylphthalocyaninato)} dineodymium (III) acetate (19) (Scheme 3.4)	66

2.3.2.3 Synthesis of 2,4,6-tris[3-thio-9,10,16,17,23,24-hexa(4-tertbutylphenoxy) phthalocyaninato ytterbium (III) chloride]-s-triazin (20) (Scheme 3.2)	67
2.3.2.4 Synthesis of 2,4,6-tris[3-thio-9,10,16,17,23,24-hexa(4-tertbutylphenoxy) phthalocyaninato lutetium (III) chloride]-s-triazin (21) (Scheme 3.2)	68
2.3.2.5 Synthesis of bis-{1(4), 8(11), 15(18), 22(25)-(tetrapyridin-2-yloxy phthalocyaninato)} ytterbium (III) (22) (Scheme 3.5)	68
2.3.2.6 Synthesis of bis-{1(4), 8(11), 15(18), 22(25)-(tetrapyridin-4-yloxy phthalocyaninato)} ytterbium (III) (23) (Scheme 3.6)	69
2.3.2.7 Synthesis of bis-{1(4), 8(11), 15(18), 22(25)-tetra(4-tert-butylphenoxy) phthalocyaninato} ytterbium (III) (24) (Scheme 3.7)	70
2.3.2.8 Synthesis of bis-{2(3), 9(10), 16(17), 23(24)-(tetrapyridin-4-yloxy phthalocyaninato)} ytterbium (III) (25) (Scheme 3.8)	71
2.3.2.9 Synthesis of bis-{2(3), 9(10), 16(17), 23(24)-(tetrapyridin-4-yloxy phthalocyaninato)} lanthanum (III) (26) (Scheme 3.8).....	72
2.3.1.10 Synthesis of bis-{2,3,9,10,16,10,16,17,23,24-octa(4-tertbutylphenoxy) phthalocyaninato} cerium(III) (27) (Scheme 3.9)	72
2.3.2.11 Synthesis of bis-{2,3,9,10,16,10,16,17,23,24-octa(4 tert-butylphenoxy) phthalocyaninato} lutetium (III) (28) (Scheme 3.9)	73
2.3.2.12 Synthesis of bis-{2,3,9,10,16,10,16,17,23,24-octa(4-tertbutylphenoxy) phthalocyaninato} gadolinium (III) (29) (Scheme 3.10).....	74
2.3.2.13 Synthesis of tris-{1(4), 8(11), 15(18), 22(25)-tetra(4-tert-butylphenoxy) phthalocyaninato} dineodymium (III) (30) (Scheme 3.11)	74
2.3.2.14 Synthesis of tris-{2,3,9,10,16,10,16,17,23,24-octa(4-tertbutylphenoxy) phthalocyaninato} cerium(III) (31) (Scheme 3.12)	75
2.4 Functionalization of nanomaterials.....	76
2.4.1 Functionalization of MWCNTs with diaminomaleonitrile to form NH-MWCNTs (Scheme 3.13).....	76
2.4.2 Graphene oxide nanosheets	77
2.4.2.1 Reduction of GONS to form rGONS (Scheme 3.14) and their functionalization with diaminomaleonitrile to form NH-rGONS (Scheme 3.15).....	77
2.4.2.2 Functionalization of GONS with diaminomaleonitrile to give NH-GONS (Scheme 3.15)	77
2.5 Preparation of conjugates.....	78

2.5.1 Coordination of phthalocyanines with b	78
2.5.1.1 Covalent linking of complex 18 to ZnO NPs (Scheme 3.16)	78
2.5.1.2 Covalent linking of complex 19 to ZnO NPs (Schemes 3.17 and 3.18)	78
2.5.2 Coordination of complex 19 to NH-GONS or NH-rGONS (Schemes 3.19)	79
2.5.3 Coordination of complex 19 to NH-MWCNTs to form 19-NH-MWCNTs (Scheme 3.20)	80
2.6 Preparation of thin films (TFs)	80
2.6.1 Using poly(bisphenol A carbonate) (PBC) – complexes 20 and 21	80
2.6.2 Using poly (methyl methacrylate) (PMMA) – complexes 23, 25 and 26	80
2.6.3 Using poly (acrylic acid) (PAA) - 18, 19, 18-ZnO NPs, 19-ZnO NPs_A, 19-ZnO NPs_B, 19-NH-MWCNTs, 24, 27, 29 and 31	81
2.7 Photophysical and photochemical conditions	82
2.7.1 Fluorescence quantum yields (Φ_F)	82
2.7.2 Triplet quantum yields (Φ_T) and lifetimes (τ_T)	83
2.7.3 Singlet oxygen quantum yields (Φ_Δ)	83
Chapter 3	85
Synthesis and Characterization	85
3.1 Phthalocyanines	88
3.1.1 Phthalonitriles (48 and 49; Schemes 3.1 and 3.2)	88
3.1.2 Mononuclear and clamshell phthalocyanines (18 and 19; Schemes 3.3 and 3.4)	91
3.1.3 Trinuclear phthalocyanines (20 and 21; Scheme 3.2)	94
3.1.4 Lanthanide bis(phthalocyanines)	96
3.1.5 Dilanthanide tris(phthalocyanines)	106
3.1.6 Ultra violet-visible spectral data	110
3.1.6.1 Effects of π -electron system and symmetry	110
3.1.6.2 Effects of central metals	115
3.1.6.3 Effects of natures of substituents	121
3.1.6.4 Ultra violet-visible spectral data of dilanthanide tris(phthalocyanines)	124
3.2 Characterization of nanomaterials and conjugates	126

3.2.1 Functionalization of multi-walled carbon nanotubes and graphene oxide nanosheets	126
3.2.2 Linking of phthalocyanines to nanomaterials	130
3.2.3 Transmission electron microscopy.....	137
3.2.4 FTIR spectral data	140
3.2.5 Electron spin resonance	146
3.2.6 Ultra violet-visible spectral data of nanomaterials and conjugates.....	146
Chapter 4.....	150
Photophysical and Photochemical Studies	150
4.1 Emission spectral data.....	151
4.1.1 Trinuclear phthalocyanines	151
4.1.2 Lanthanide bis(phthalocyanines).....	152
4.2 Photophysical data.....	155
4.2.1 Fluorescence quantum yields (Φ_F) and lifetimes (τ_F)	155
4.2.2 Triplet quantum yields (Φ_T) and lifetimes (τ_T)	157
4.2.3 Singlet oxygen quantum yields (Φ_Δ).....	160
Chapter 5.....	161
Optical limiting properties	161
5.1 Phthalocyanines alone	162
5.1.1 Effects of π -electron system and symmetry.....	162
5.1.1.1 Complexes 18 and 19	162
5.1.1.2 Complexes 27 and 31	168
5.1.2 Effects of central metals	171
5.1.2.1 Complexes 20 and 21	171
5.1.2.2 Complexes 25 and 26	173
5.1.4 Nonlinear optical behavior of complexes 30.....	186
5.2 Phthalocyanines with nanomaterials as conjugates.....	187
5.2.1 Complexes 18 and 19 with ZnO NPs	187
5.2.2 Complexes 18 and 19 with MWCNTs.....	192
5.2.3 Complexes 19 with NH-GONS and NH-rGONS.....	194

Chapter 6..... 197
Conclusions and future prospects 197
Conclusions..... 198

List of Symbols

τ_F	=	fluorescence lifetime
$\tau_{F(av)}$	=	Average fluorescence lifetime
α	=	Non-peripheral position
β	=	Peripheral position
Φ_F	=	Fluorescence quantum yield
Φ_T	=	Triplet quantum yield
τ_T	=	Triplet lifetime
Φ_Δ	=	Singlet oxygen quantum yield
$\text{Im}[\chi^{(3)}]$	=	Imaginary component of the third order susceptibility
γ	=	Second order hyperpolarizability
β_{eff}	=	Effective nonlinear absorption coefficient
I_{lim}	=	Limiting intensity threshold
I_{lim}	=	Limiting intensity Threshold
σ_{2PA}	=	Two photon cross section
I_{in}	=	Input intensity

I_{out}	=	Output intensity
f	=	Lorentz local field factor
T_{Norm}	=	Normalized transmittance
N	=	Number density
I_0	=	On-focus intensity
ε_0	=	Permeability of free space
ε_T	=	Triplet state molar extinction coefficient
λ	=	wavelength
n	=	Refractive index
z	=	Sample position
z_0	=	Rayleigh length
δ	=	Chemical shift

List of Abbreviations

APTES	=	3-aminopropyltriethoxysilane
DCC	=	Dicyclohexylcarbodiimide
DCM	=	Dichloromethane
DMF	=	Dimethyl formamide
DMSO	=	Dimethyl sulfoxide
DMSO-d ₆	=	Deuterated dimethyl sulfoxide
CDCl ₃	=	Deuterated chloroform
ESA	=	Excited state absorption
H ₂ Pc	=	Metal free phthalocyanine complexes
HOMO	=	Highest molecular orbital
LUMO	=	Lowest unoccupied molecular orbital
ISC	=	Intersystem crossing
MPcs	=	Metallophthalocyanines
ZnO NPs	=	Zinc oxide nanoparticles

NLA	=	Nonlinear Absorption
NLS	=	Nonlinear scattering
NLO	=	Nonlinear Optical
Pcs	=	Phthalocyanine complexes
RSA	=	Reverse saturable absorption
SA	=	Saturable Absorption
LnPc ₂	=	Lanthanide bis(phthalocyanines)
LuPc ₂	=	Lutetium bis(phthalocyanines)
CePc ₂	=	Cerium bis(phthalocyanines)
YbPc ₂	=	Ytterbium bis(phthalocyanines)
GdPc ₂	=	Gadolinium bis(phthalocyanines)
Ln ₂ Pc ₃	=	Dilanthanide tris(phthalocyanines)
Nd ₂ Pc ₃	=	Dineodymium tris(phthalocyanines)
Ce ₂ Pc ₃	=	Dicerium tris(phthalocyanines)
Ln ₃ Pc ₃	=	Trinuclear lanthanide phthalocyanines
Yb ₃ Pc ₃	=	Triytterbium tris(phthalocyanines)

Lu ₃ Pc ₃	=	Trilutetium tris(phthalocyanines)
MWCNTs	=	Multi-walled carbon nanotubes
GONS	=	Graphene oxide nanosheets
NH-GONS	=	Amino-functionalized graphene oxide nanosheets
NH-rGONS	=	Amino-functionalized reduced graphene oxide nanosheets
TCSPC	=	Time correlated single photon counting
TEM	=	Transmission electron microscope
TEOS	=	Tetraethyl orthosilicate
UV-vis	=	Ultraviolet-visible
Zn	=	Zinc
ZnPc	=	Zinc phthalocyanine
PAA	=	Poly (methyl meth acrylate)
PBC	=	Poly (bisphenol A carbonate)
¹ H NMR	=	Proton nuclear magnetic resonance
¹³ C NMR	=	Carbon nuclear magnetic resonance
ESR	=	Electron spin resonance

EPR	=	Electron paramagnetic resonance
2PA	=	Two photon absorption
3PA	=	Three photon absorption
MPA	=	Multiphoton absorption
HRTEM	=	High resolution electron spin resonance
TEM	=	Transmission electron microscopy
Nd-YAG	=	Neodymium-doped aluminium garnet
NIR	=	Near infrared
MALDI	=	Matrix-assisted laser desorption ionization
TOF	=	Time-of-flight
CNTs	=	Carbon nanotubes

List of Figures

Fig. 1.1: General structure and nomenclature of an H ₂ Pc based on positional numbering in accordance with IUPAC.	3
Fig. 1.2: Electronic transitions in phthalocyanines.....	25
Fig. 1.3: Ground state absorption spectra of metallated and unmetallated Pc	26
Fig. 1.4: Electronic excitation transitions observed in LnPc ₂ complexes in accordance with VCH calculations.	28
Fig. 1.5: The absorption spectra of YbPc ₂ complexes in green form and blue form.....	29
Fig. 1.6: Illustration of RSA and SA occurring when high input energies of light are pumped in the NLO material.....	31
Fig. 1.7: A model used to describe the interaction of light with a molecular compound in terms of electronic transitions in the NLO materials.....	33
Fig. 1.8: The behavior of (A) transmission against input intensity (I_{in}) and (B) (the output intensity (I_{out}) transmitted by an optical limiter vs I_{in} from the light source.	35
Fig. 1.9: HRTEM image of a multi-walled carbon nanotube.....	42
Fig. 1.10: Structure of graphene oxide nanosheets.....	44
Fig. 2.1: Schematic diagram of time-correlated single photon counting setup.....	57
Fig. 2.2: Schematic representation of the open-aperture Z-scan setup.	59
Fig. 2.3: Schematic diagram for a laser flash photolysis setup.....	60
Fig. 2.4: Schematic diagram for the singlet oxygen detection setup using its phosphorescence.	61
Fig. 2.5: Schematic diagram of photolysis setup.	62
Fig. 3.1: IR spectra of complexes 48 , 18 and 19 in solid state.....	93
Fig. 3.2: ESR spectral signals of complexes 19 , 18 and 19-ZnO NPs_A in solid state.....	94

Fig. 3.3: Absorption spectra of complexes 18 and 19 in DMSO.	111
Fig. 3.4: Absorption spectra of complexes 27 , 29 and 31 in CHCl ₃	112
Fig. 3.5: Absorption spectra of neutral 28 in CHCl ₃ and reduced 28 in CHCl ₃ in the presence of hydrazine.	113
Fig. 3.6: (A) Normalized absorption spectra of complexes 20 and 21 in DMSO. (B) Absorption spectra of complex 21 in DMSO at different concentrations. (C) Absorption spectra of thin films in 20-TF and 21-TF	118
Fig. 3.7: Ground state electronic absorption spectra for complexes 25 and 26	120
Fig. 3.8: Absorption spectral changes of complexes 25 and 26	121
Fig. 3.9: Absorption spectra of complexes 22 and complex 23 in DMSO at $\sim 4.0 \times 10^{-6}$ M and 8.23×10^{-6} M. Inserts = NIR spectra. (C) Changes in absorbance spectra of 23 on change in concentration. Starting concentration $\sim 1 \times 10^{-5}$ M.	123
Fig. 3.10: Absorption spectra of complex 30 in DMF and DMSO.	125
Fig. 3.11: TEM images of ZnO NPs, 19-ZnO NPs_A , 19-ZnO NPs_B and 18-ZnO NPs	138
Fig. 3.12: TEM images of NH-MWCNTs alone and 19-NH-MWCNTs	139
Fig. 3.13: TEM images of NH-GONS and NH-rGONS.	140
Fig. 3.14: IR spectra of complexes 19 , 18 , ZnO NPs, 19-ZnO NPs_A , 19-ZnO NPs_B and 18-ZnO NPs in solid state.	142
Fig. 3.15: FT-IR spectra for 19 , NH-MWCNTs and 19-NH-MWCNTs	143
Fig. 3.16: IR Spectra for complex 19 , NH-GONS, NH-rGONS, 19-NH-GONS and 19-NH-rGONS	145
Fig. 3.17: absorption spectra of complexes 18 , 19 , 19-ZnO NPs_A , 19-ZnO NPs_B and 18-ZnO NPs in DMSO.	147
Fig. 3.18: UV-Vis spectra for 19 and 19-NH-MWCNTs in DMSO.	148
Fig. 3.19: Absorption spectra for complex 19 , NH-GONS, NH-rGONS, 19-NH-GONS and 19-NH-rGONS in DMSO.	149

Fig. 4.1: Absorption and fluorescence spectra of complex 20 in DMSO.....	152
Fig. 4.2: Absorption, excitation and emission spectra of complex 22 in DMSO.	153
Fig. 4.3: Fluorescence lifetime decay curves of complex 20 and complex 21	156
Fig. 4.4: Triplet decay curves of complexes 18 and 18-ZnO NPs in DMSO.....	159
Fig. 4.5: Singlet oxygen absorption decay for 18-ZnO NPs	160
Fig. 5.1: Open aperture Z-scan curves for complexes 18 and 19	163
Fig. 5.2: Open aperture Z-scan curves for complexes 19 and 19-TF	164
Fig. 5.3: Input against output intensity plot for complexes 18 , 19 (in DMSO), 18-TF and 19-TF obtained at 532 nm.	166
Fig. 5.4: Open aperture Z-scan signatures of (A) complex 31 obtained at $I_0 = 0.19 \text{ GW.cm}^{-2}$ in dichloromethane and (B) 31-TF at $I_0 = 2.41 \text{ GW.cm}^{-2}$	169
Fig. 5.5: Input against output intensity plots of complexes 27 and 31 in dichloromethane and 27-TF and 31-TF	170
Fig. 5.6: β_{eff} against I_0 plots of complexes 27 , 29 and 31 at various energies.	171
Fig. 5.7: Open-aperture Z-scan curve of complex 20 (in DMF) and 20-TF	172
Fig. 5.8: Open aperture Z-scan signal for complex 25 (A) and 26 (B) in DMSO.	174
Fig. 5.9: Open aperture Z-scan curve for 26-TF	175
Fig. 5.10: A plot of the effective nonlinear absorption coefficient (β_{eff}) against the on-focus beam intensity (I_0) for complex 25 in DMSO.	176
Fig. 5.11: Nonlinear absorption coefficient (β_{eff}) against concentration showing β_{eff} concentration dependence for complex 25	177
Fig. 5.12: Open aperture Z-scan curves for neutral 24 (in DMF), reduced 24 (in DMF in the presence of hydrazine) and 24-TF	181
Fig. 5.13: Input intensity (I_{in}) against output intensity (I_{out}) for neutral 24 (in DMF), reduced 24 (in DMF in the presence of hydrazine) and 24-TF	182

Fig. 5.14: Normalized transmittance (T_{Norm}) against I_{in} for neutral 24 (in DMF), reduced 24 (in DMF in the presence of hydrazine) and 24-TF	183
Fig. 5.15: Natural logarithm of $I_{\text{in}}/I_{\text{out}}$ fraction against a change between I_{in} and I_{out} for neutral 24 (in DMF), reduced 24 (in DMF in the presence of hydrazine) and 24-TF at 532 nm for investigation of RSA existence.	185
Fig. 5.16: Open aperture Z-scan curves obtained on simulation using two photon absorption mechanism for complex 30 in DMF.....	187
Fig. 5.17: Open aperture Z-scan curves for complexes 19 , 19-ZnO NPs_A (in DMSO), 19-TF and 19-ZnO NPs_A-TF	188
Fig. 5.18: Input against output intensity plot for complexes 19 , 19-ZnO NPs_A (in DMSO), 19-TF and 19-ZnO NPs_A-TF	190
Fig. 5.19: Open-aperture Z-scan curves for 19-NH-MWCNTs at (A) 0.19 GW.cm^{-2} and (B) 0.48 GW.cm^{-2}	193
Fig. 5.20: Input intensity against output intensity for 19-NH-MWCNTs	194
Fig. 5.21: Open-aperture Z-scan curves for (A) 19-NH-rGONS at 0.23 GW.cm^{-2} in DMSO and (B) 19-NH-rGONS-TF at 1.11 GW.cm^{-2}	195

List of Schemes

Scheme 1.1: Synthetic route of MPc using substituted phthalic anhydride derivatives...	5
Scheme 1.2: Synthesis of a planar clamshell.....	7
Scheme 1.3: Synthesis of a cofacial clamshell.....	8
Scheme 1.4: Synthesis of an s-triazine trimeric Pc.....	9
Scheme 1.5: Synthesis of LnPc ₂ complex via two routes.....	20
Scheme 1.6: Synthesis of an Ln ₂ Pc ₃ complex.....	22
Scheme 1.7: Synthesis of an Ln ₂ Pc ₃ complex from LnPc ₂ and LnPc complexes.....	23
Scheme 3.1: Synthetic route for the preparation of compound 48.....	88
Scheme 3.2: Synthesis of complexes 49, 20 and 21.....	90
Scheme 3.3: Preparation of complex 18.....	92
Scheme 3.4: Preparation of complex 19.....	92
Scheme 3.5: Synthesis of bis-{1(4), 8(11), 15(18), 22(25)-(tetrapyrroline-2-yl)oxy phthalocyaninato} ytterbium (III).....	97
Scheme 3.6: Synthesis of bis-{1(4), 8(11), 15(18), 22(25)-(tetrapyrroline-4-yl)oxy phthalocyaninato} ytterbium (III).....	98
Scheme 3.7: Synthesis of complex 24.....	99
Scheme 3.8: Synthesis of bis-{2(3), 9(10), 16(17), 23(24)-(tetrapyrroline-4-yl)oxy phthalocyaninato} ytterbium (III) (25) and bis-{2(3), 9(10), 16(17), 23(24)-(tetrapyrroline-4-yl)oxy phthalocyaninato} lanthanum (III).....	101
Scheme 3.9: Synthesis of bis-{2,3,9,10,16,10,16,17,23,24-octa(4-tertbutylphenoxy) phthalocyaninato} cerium (III) and bis-{2,3,9,10,16,10,16,17,23,24-octa(4-tertbutylphenoxy) phthalocyaninato} lutetium (III).....	104
Scheme 3.10: Synthesis of bis-{2,3,9,10,16,10,16,17,23,24-octa(4-tertbutylphenoxy) phthalocyaninato} gadolinium (III).....	105

Scheme 3.11: Synthesis of tris-{1(4), 8(11), 15(18), 22(25)-tetra(4-tertbutylphenoxy) phthalocyaninato} dineodymium (III)..... 108

Scheme 3.12: synthesis of tris-{2,3,9,10,16,10,16,17,23,24-octa(4-tertbutylphenoxy) phthalocyaninato} cerium(III). 109

Scheme 3.13: Synthesis of diaminomaleonitrile-functionalized MWCNTs (NH-MWCNTs)..... 127

Scheme 3.14: Reduction of GONS to form rGONS..... 128

Scheme 3.15: Surface modification of GONS with diaminomaleonitrile to form NH-GONS. 129

Scheme 3.16: Schematic representation of complex **18** linked to ZnO NPs to form **18-ZnO NPs**..... 131

Scheme 3.17: Schematic representation of complex **19** linked to ZnO NPs to form **19-ZnO NPs_A** 132

Scheme 3.18: Schematic representation of complex **19** linked to ZnO NPs via axial ligand to form **19-ZnO NPs_B** 133

Scheme 3.19: Covalent linking of complex **19** to NH-rGONS via amide bond to form **19-NH-rGONS**..... 135

Scheme 3.20: Covalent linking of complex **19** to NH-MWCNTs via amide bond to form **19-NH-MWCNTs**..... 136

List of Tables

Table 1.1: Structures of lanthanide Pc complexes synthesized in this thesis, with their names given below this table.	11
Table 1.2: Nonlinear absorption properties of LnPc ₂ complexes.	39
Table 1.3: Photophysico-chemical parameters of lanthanide complexes.....	51
Table 3.1: Photophysical parameters of phthalocyanines alone and conjugates.	114
Table 4.1: Photophysico-chemical parameters of phthalocyanines alone and conjugates presented in this thesis.....	154
Table 5.1: Nonlinear optical parameters of lanthanide phthalocyanines alone and when embedded in PMMA, PBC and PAA.....	167
Table 5.2: Nonlinear optical parameters of complexes mono and binuclear phthalocyanines with ZnO NPs, NH-MWCNTs, NH-GONS and NH-rGONS as conjugates in DMSO and when embedded in poly (acrylic acid).	191

Chapter 1

Introduction

1. Introduction

This thesis presents the examination of new lanthanide phthalocyanines (Pcs) for optical limiting (OL) when alone or in the presence of zinc oxide nanoparticles, multi-walled carbon nanotubes or graphene oxide nanosheets.

1.1 Phthalocyanines

1.1.1 History, applications and structure of phthalocyanines

The discovery of metal-free phthalocyanine (H_2Pc) shown in **Fig. 1.1** was accidental and stretches back to 1907 when a by-product was obtained during the preparation of 2-cyanobenzamide [1]. The synthesis of copper phthalocyanine (Pc) from 1,2-dibromobenzene followed almost twenty years later. Iron Pc also came about accidentally in 1928 as a blue product found in a reaction flask where only white product was expected at the Scottish Dyes Ltd [2-4]. Several metallophthalocyanines (MPcs) were prepared by Linstead and his coworkers, who developed synthetic methods and used the name “phthalocyanine” for the first time [5-10]. The X-ray structural characterization of Pcs was carried out by Robertson and coworkers [11-15].

The applications of Pcs include their use as catalysts [16-21], photosensitizers for photodynamic cancer therapy [22-29], markers for bioimaging [30,31], antibacterial composites [32-35], components in ink-jet printing [36], chemical sensors [37-40], semiconductors [41,42], functional polymers and liquid crystals [43-46], light-harvesting modules for dye-sensitized solar cells and organic photovoltaics [47-54], in

nanotechnology [55-59] and nonlinear optics [60-67]. Pcs are planar aromatic blue or green macrocyclic molecules with 18 π -electrons. Nomenclature of Pcs is position-dependent. One way of naming Pcs is in accordance with the International Union of Pure and Applied Chemistry (IUPAC) [2], which takes into consideration the positions of tetrapyrroles as shown in Fig. 1.1 [68,69]. Another way of naming Pcs takes the form of referring to the positions as β - or α - (peripheral or nonperipheral, respectively).

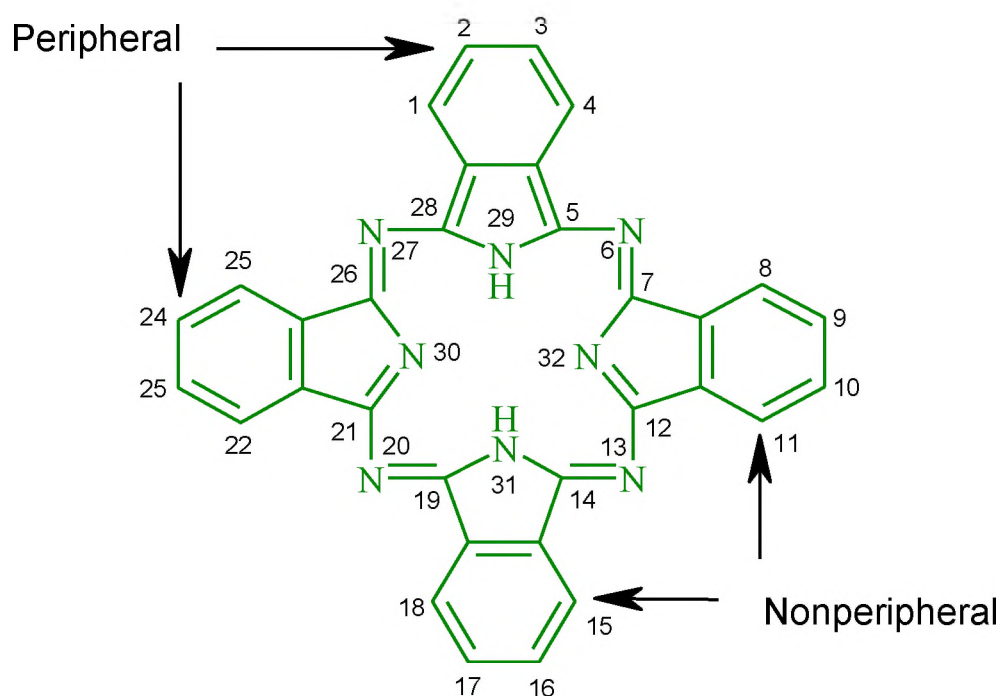


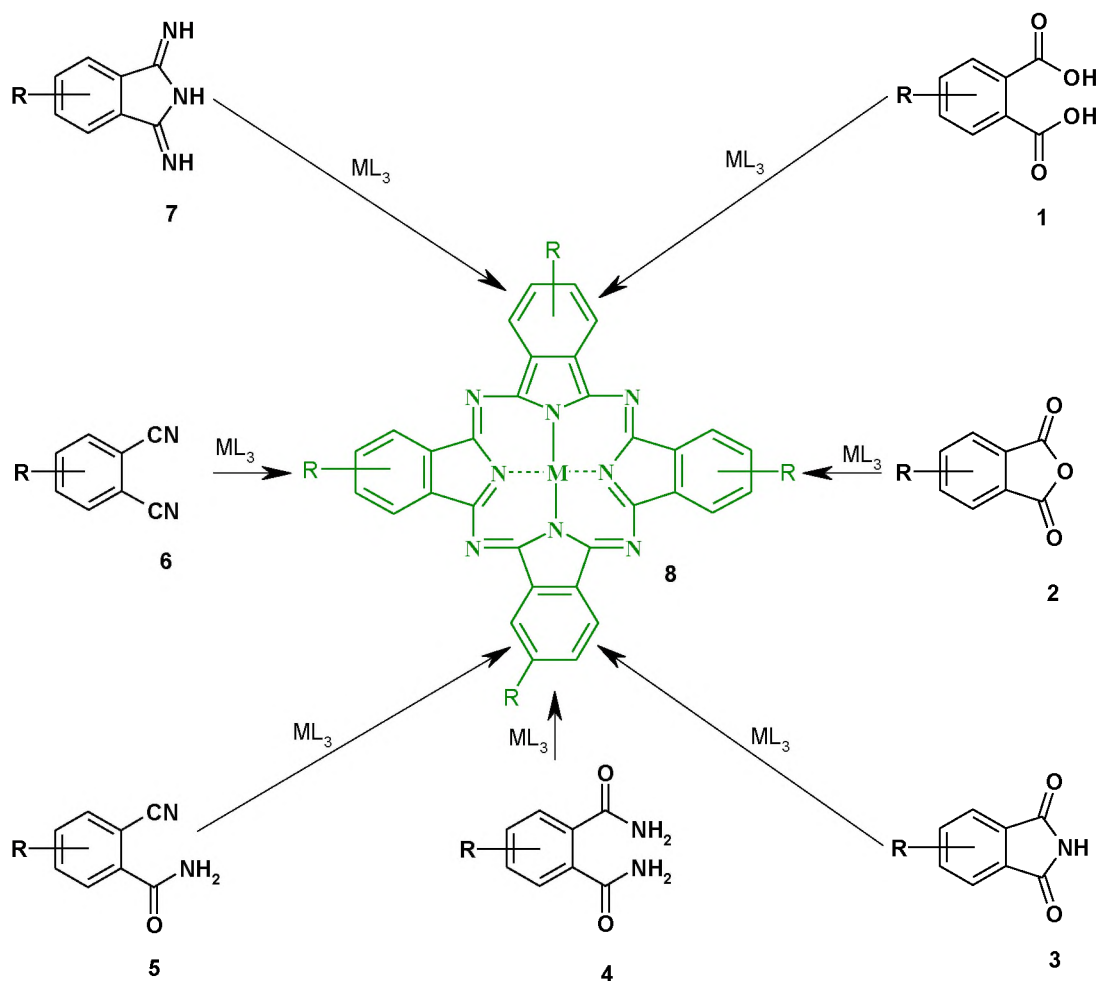
Fig. 1.1: General structure and nomenclature of an H₂Pc based on positional numbering in accordance with IUPAC.

1.1.2 Synthesis

1.1.2.1 General synthesis of mono-nuclear phthalocyanines

The general synthetic route of MPcs is shown in **Scheme 1.1**. The most commonly employed methods in the laboratory involve refluxing a substituted phthalonitrile in an appropriate organic solvent in the absence or presence of a metal salt and a catalyst. These methods include the employment of substituted phthalic acid (**1**), isobenzofuran-1,3-dione (**2**), phthalimide (**3**), phthalamide (**4**), 2-cyano-benzamide (**5**), phthalonitrile (**6**) or isoindole-1,3-diylidenediamine (**7**) to form a substituted MPc (**8**) in the presence of a metal salt [70].

Lanthanide phthalocyanines (LnPcs) [71-76] follow the same synthetic approach with a substituted phthalonitrile refluxed in the presence of a lanthanide salt and a catalyst such as 1,8-diazabicycloundec-7-ene (DBU) at the boiling point of the solvent.

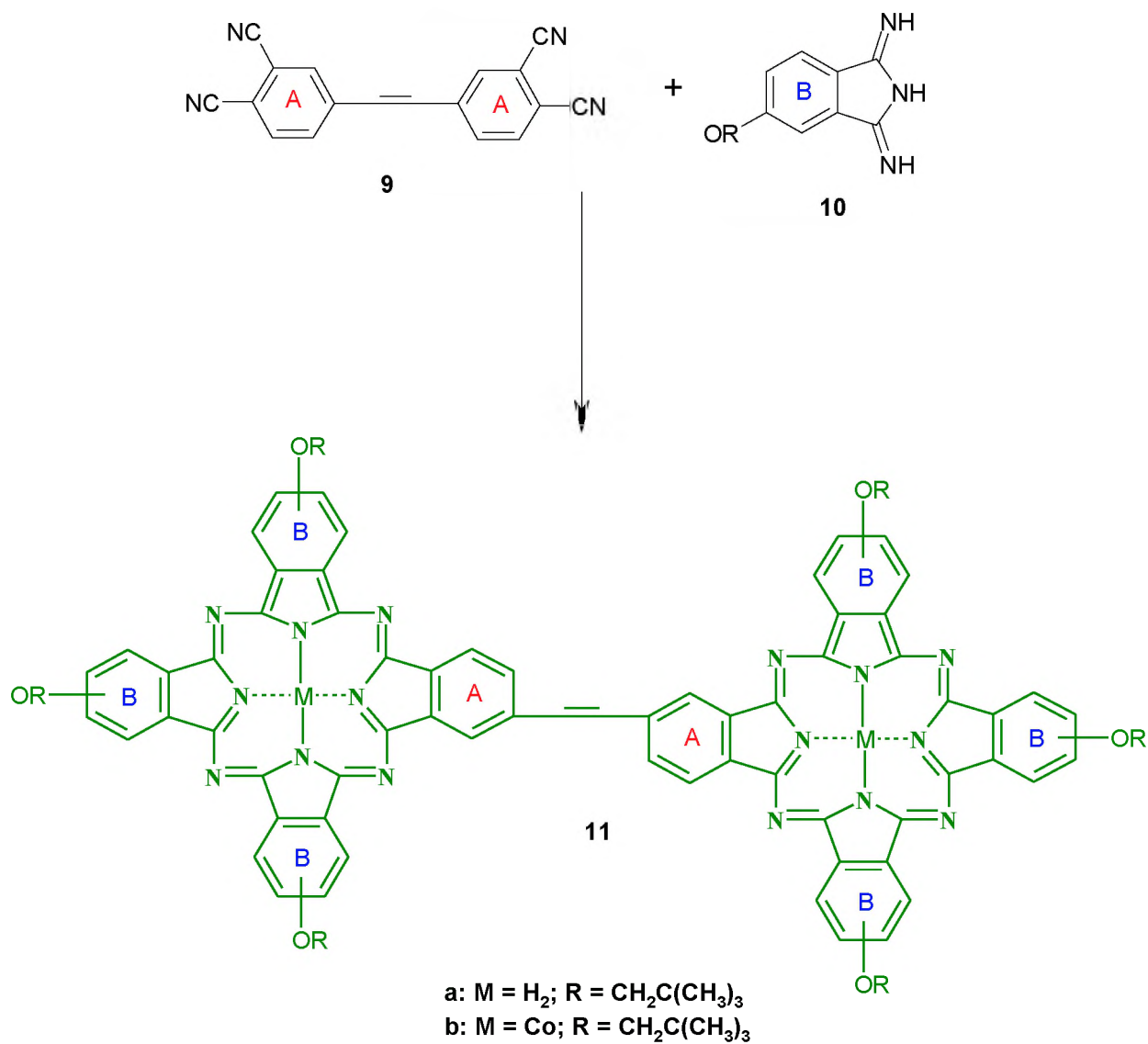


Scheme 1.1: Synthetic route of MPc using substituted phthalic anhydride derivatives [70]. R denotes hydrogen or range of substituents in the peripheral position of MPc and L represents the ligand in the metal salt.

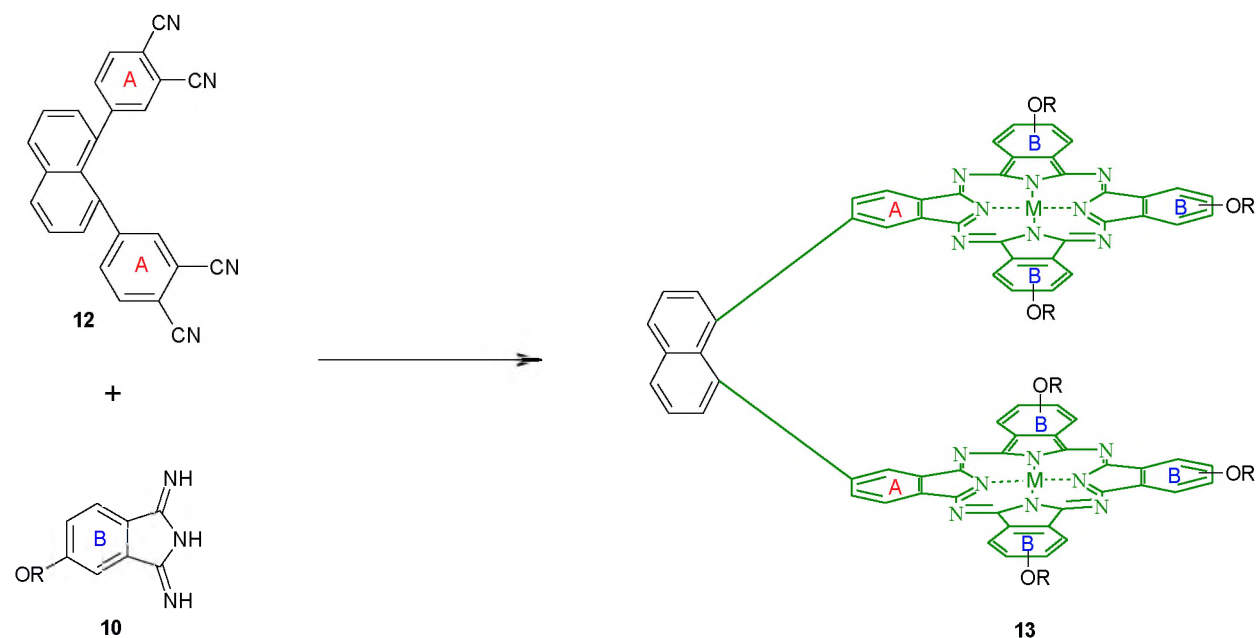
1.1.2.2 Clam shell and trimeric phthalocyanines

Clam shell Pcs are normally prepared by self- and cross-condensation strategy involving bis(phthalonitriles) or tetracyano-benzene with substituted phthalonitriles [77-100]. A bridged phthalonitrile such as 3,3'- or 4,4'-bis(phthalonitriles) (9), **Scheme 1.2**, or the corresponding naphthalene-containing bis(phthalonitrile) (12) (**Schemes 1.3**) may be used in the cross-condensation reaction with an excess of a phthalonitrile or substituted

isoindole-1,3-diylidenediamine precursor (**10**) to form an asymmetric type of a dimeric Pcs **11**, (**B3A-AB3**). Co-facial Pcs (**Scheme 1.3**) could be formed depending on the rigidity of the linking group in starting **A-A** phthalonitrile (**12**) to form **13** [78]. This is a strategy employed in this thesis for clam shell Pcs. Another approach for preparing clam shell Pcs is by linking two pure Pcs of **AB3** type asymmetric Pc molecules with selective binding moieties in one of peripheral or nonperipheral positions [101]. One could design such a system in such a way that two different metals are inserted into the central cavity of each binding Pc.



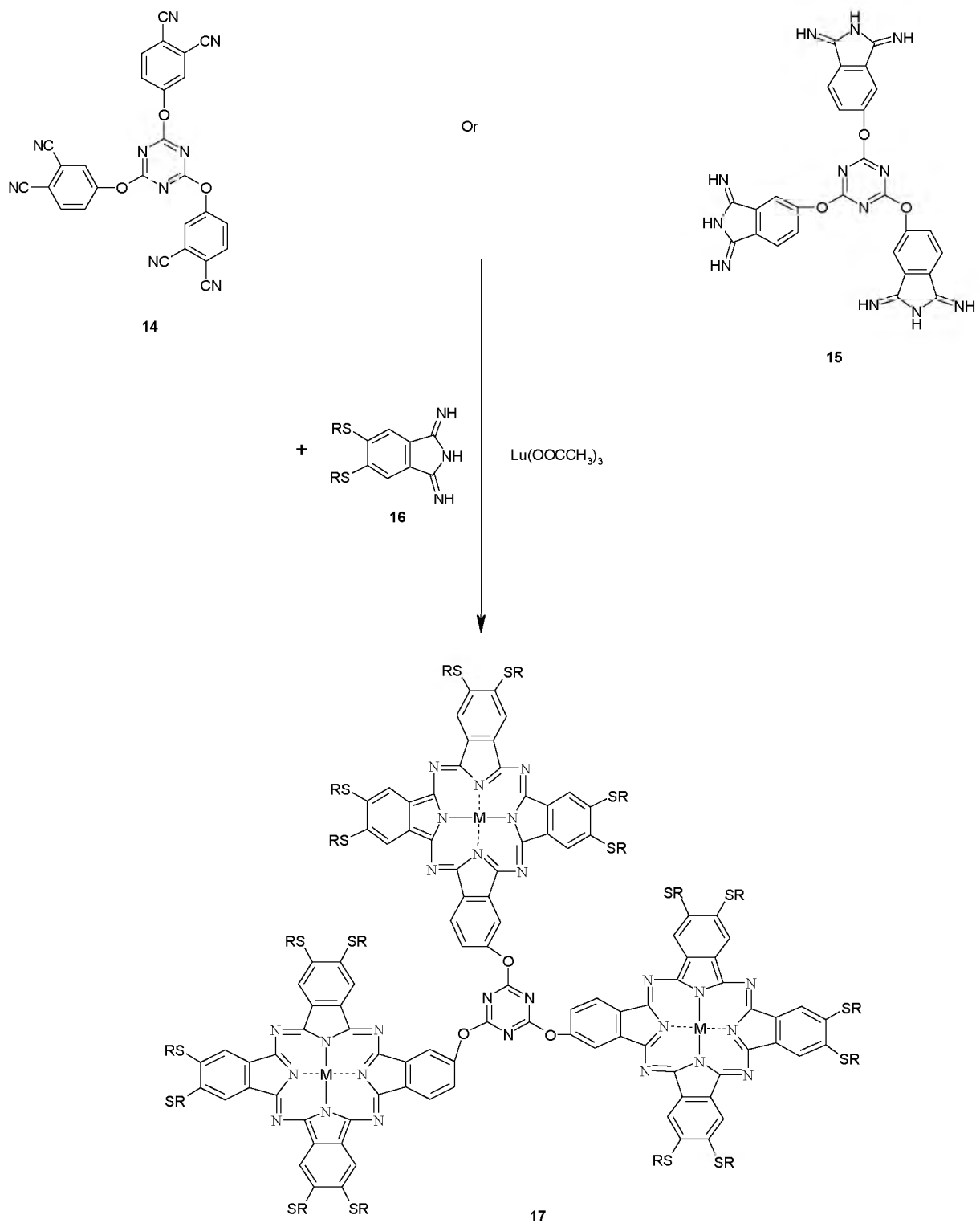
Scheme 1.2: Synthesis of a planar clamshell [78].



Scheme 1.3: Synthesis of a cofacial clamshell [79].

Another type of Pcs formed from the self-condensation involves the reaction of tris(phthalonitrile) with a substituted phthalonitrile [102,103] to form trinuclear Pcs. For example, a trinuclear lutetium-based Pc (17) was synthesized by self-condensation between 2,4,6-tris(2-oxaphthalonitrile)-s-triazine (14) or 2,4,6-tris[2-oxa(1,3-hexamino isoindoline)]-s-triazine (15) with 4,5-bis(hexylthio)-1,2-diimino-isoindoline (16) [102],

Scheme 1.4.



Scheme 1.4: Synthesis of an s-triazine trimeric Pc [102]. $M = \text{LuOOCCH}_3$, $R = \text{C}_6\text{H}_{13}$.

Sub-aim of this thesis: Therefore the aim of this thesis, in part, is to present the synthesis of new neodymium based mononuclear (**18**) clam shell Pc (**19** in Table 1.1) with a carboxyl moiety attached to the bridge as well as new *s*-triazine trimeric ytterbium and lutetium phthalocyanines (**20** and **21** in Table 1.1). The latter are substituted with tert-butyl for improved solubility. To the best of the author's knowledge, the nonlinear optical (NLO) behavior of has been studied only indium- and gallium-based binuclear Pcs [104,105], using a Z-scan technique. The NLO behavior of *S*-triazine phthalocyanines has not received much attention [103]. It has been suggested that lanthanide bisphthalocyanines show improved optical nonlinearities due to their expanded π -electron system and the presence of the heavy lanthanide central metal [104,106-108] which enhances the rate of intersystem crossing (ISC) to the triplet state. Hence in this work, NLO and photophysical behavior of trimeric trilanthanide and clam shell Pcs which also have expanded π -electron system are studied. Previous reports have shown the importance of asymmetry on the photophysical, photochemical and optical limiting (OL) properties of phthalocyanines [69,109-112]. Thus complexes **20** and **21** are expected to show improved NLO properties due to their low symmetry. *S*-triazine oxygen (or nitrogen, sulfur, ethynyl and ethenyl) bridged trinuclear phthalocyanines have been reported for Zn, Co, Lu and Cu as central metals and containing long chain ring substituents [102,113-116]. This work reports for the first time on an *s*-triazine sulfur bridged Yb phthalocyanine and its Lu counterpart (**20** and **21**). For practical applications, phthalocyanine complexes are embedded in thin films of polymers such as poly (methyl methacrylate) (PMMA) [117,118] resulting in improved optical limiting behavior

compared to solution. Recently [119], poly (acrylic acid) (PAA) was shown to result in improved optical limiting behavior when compared to PMMA, hence the former is employed in this work. Poly (bisphenol A carbonate) (PBC) is also employed in this study.

Table 1.1: Structures of lanthanide Pc complexes synthesized in this thesis, with their names given below this table. Names of the complexes are shown at the end of the table.

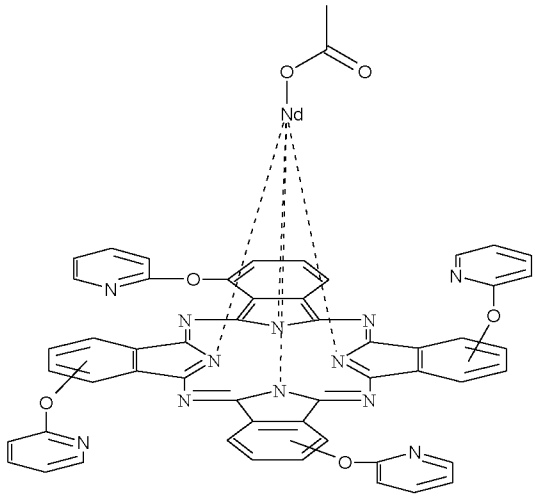
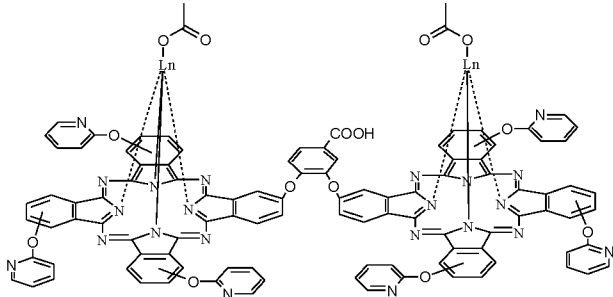
Complex	Lanthanide	Complex number
	Nd (α -substituted: 2-ylloxy pyridine)	(18)
	Ln (α -substituted: 2-ylloxy pyridine)	(19)

Table 1.1 continued...

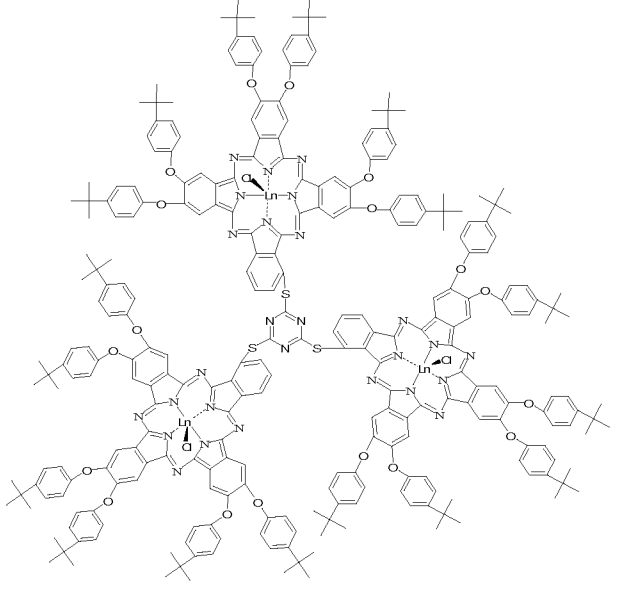
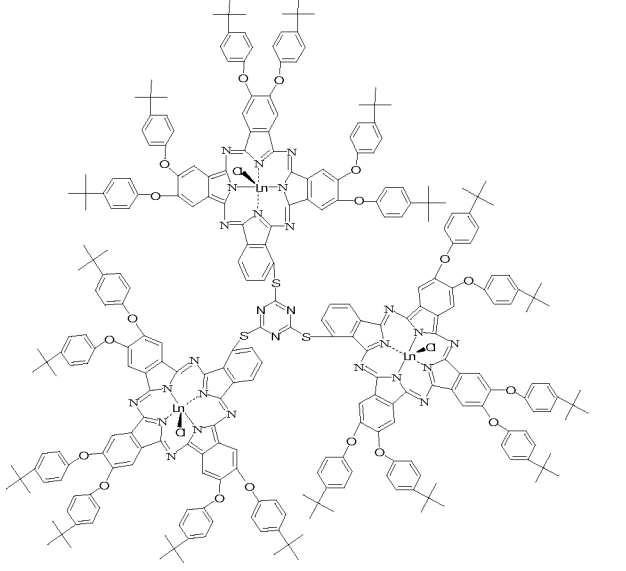
Complex	Lanthanide	Complex number
	Yb (β -substituted: tert-butyl phenoxy)	(20)
	Lu (β -substituted: tert-butyl phenoxy)	(21)

Table 1.1 continued...

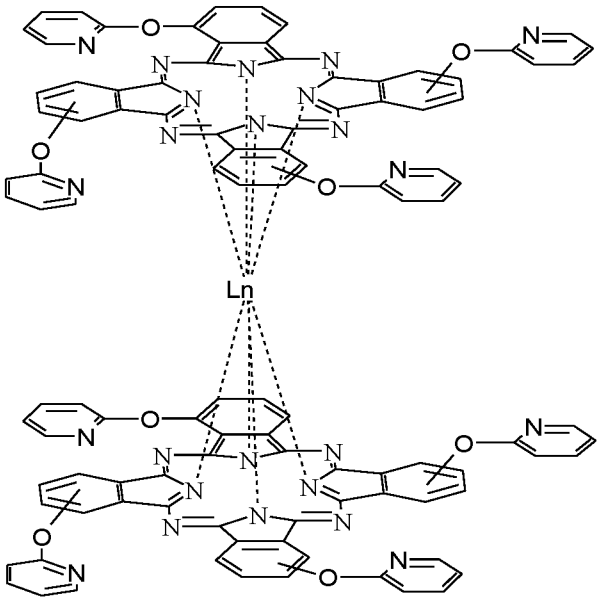
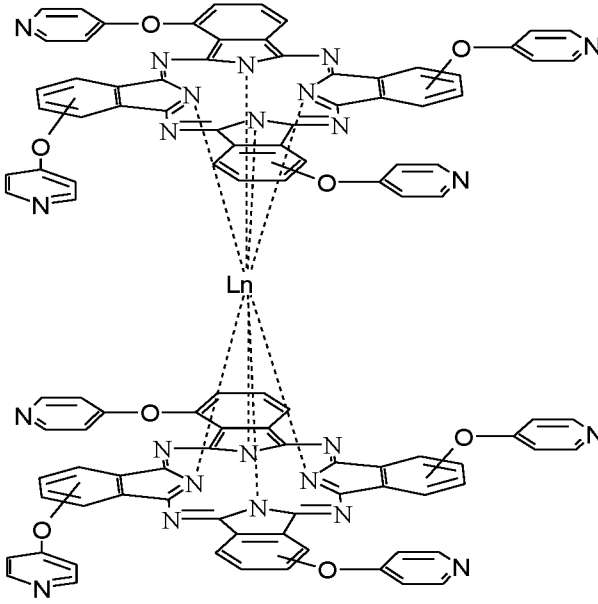
Complex	Lanthanide	Complex number
	Yb (α -substituted: 2-yloxy-pyridine)	(22)
	Yb (α -substituted: 4-yloxy-pyridine)	(23)

Table 1.1 continued...

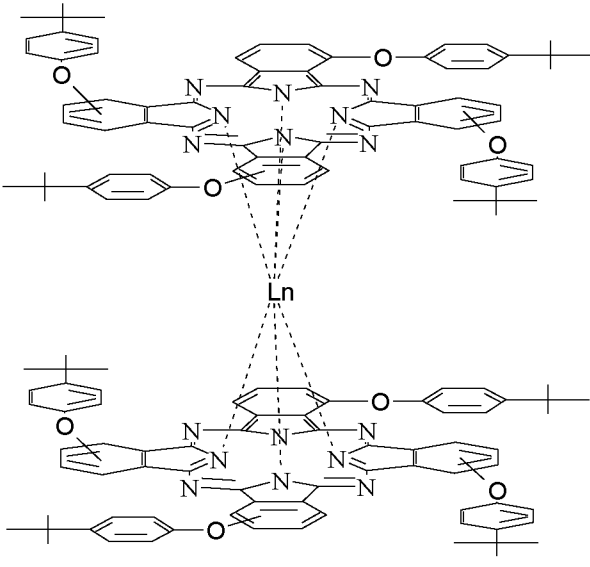
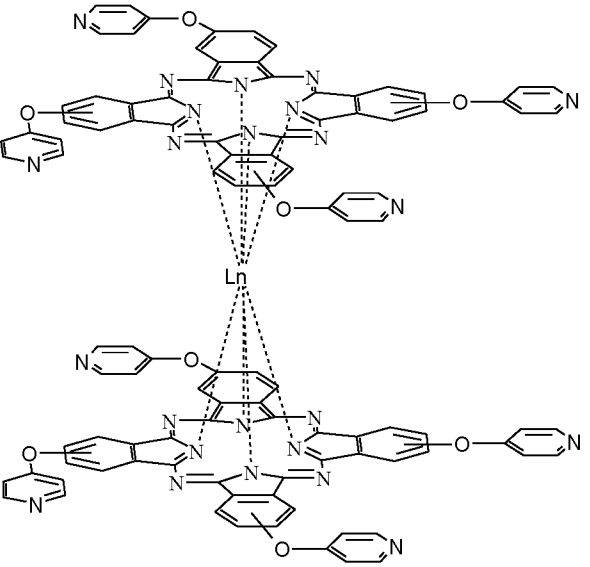
Complex	Lanthanide	Complex number
	Yb (α -substituted: tert-butyl phenoxy)	(24)
	Yb (β -substituted: 4-yloxy-pyridine)	(25)

Table 1.1 continued...

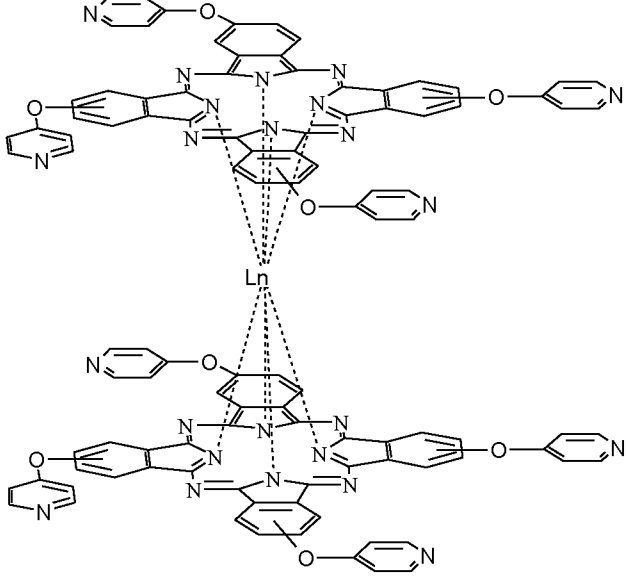
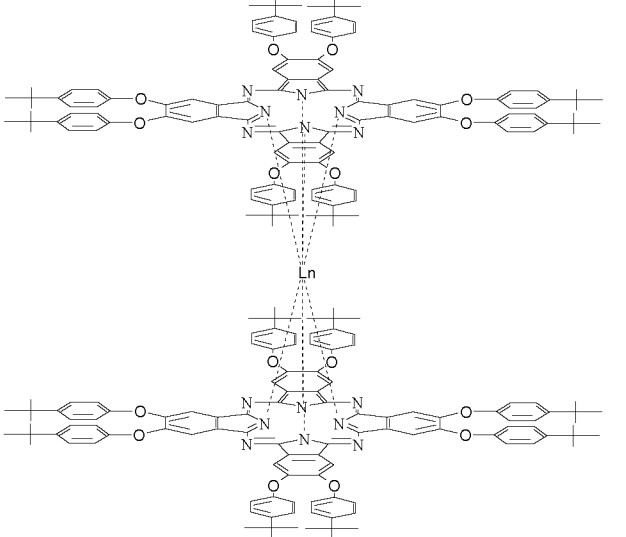
Complex	Lanthanide	Complex number
	La (β -substituted: 4-yloxy-pyridine)	(26)
	Ce (β -substituted: tert-butyl henoxy)	(27)

Table 1.1 continued...

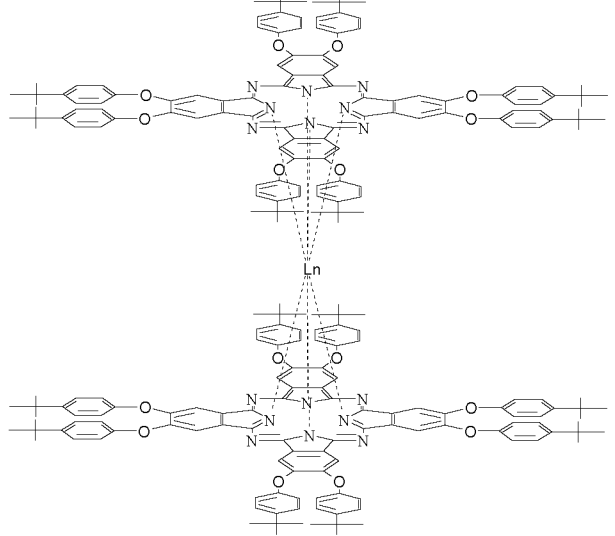
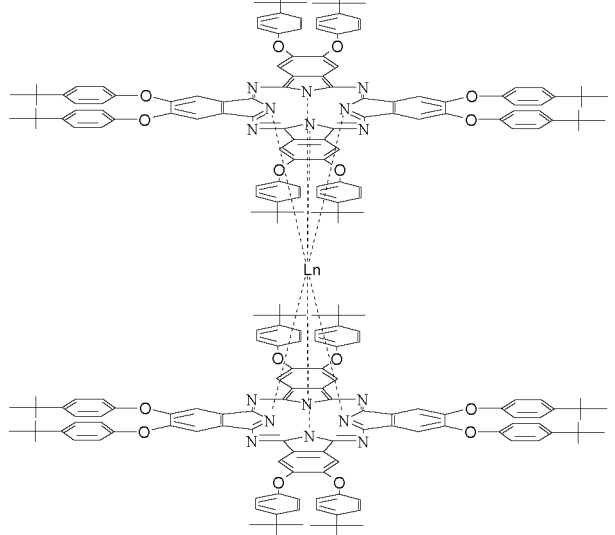
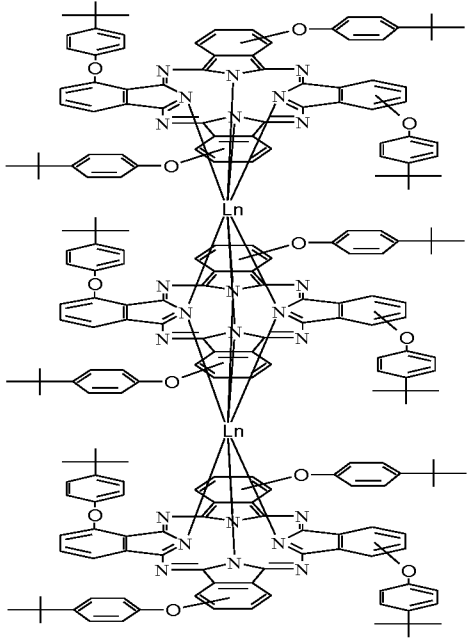
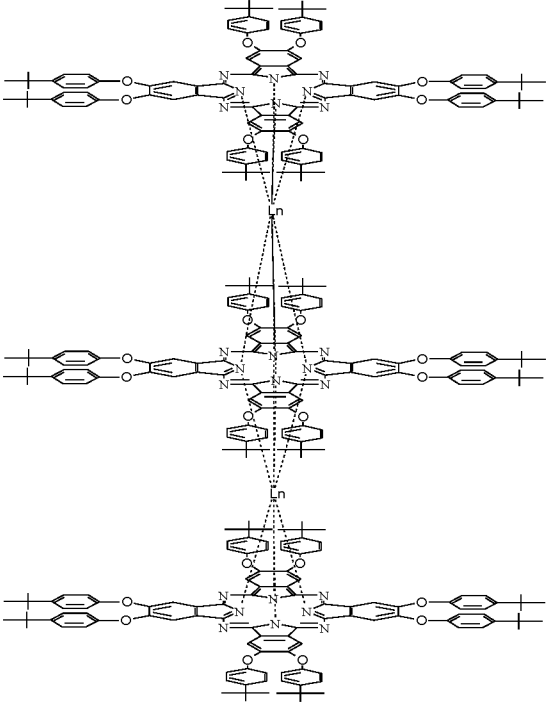
Complex	Lanthanide	Complex number
 <p>The structure shows a central Lu atom coordinated to two N2O2 ligands (top and bottom) and two phenoxide ligands (left and right). The N2O2 ligands are bis-imidazole derivatives with two phenoxide groups each. The phenoxide ligands are also bis-imidazole derivatives with two phenoxide groups each. The Lu atom is coordinated to the two nitrogen atoms of each N2O2 ligand and the two oxygen atoms of each phenoxide ligand. Dashed lines indicate the coordination bonds from the Lu atom to the nitrogen and oxygen atoms.</p>	Lu (β -substituted: tert-butyl phenoxy)	(28)
 <p>The structure is identical to complex (28), but the central lanthanide atom is Gd instead of Lu. It shows a central Gd atom coordinated to two N2O2 ligands (top and bottom) and two phenoxide ligands (left and right). The N2O2 ligands are bis-imidazole derivatives with two phenoxide groups each. The phenoxide ligands are also bis-imidazole derivatives with two phenoxide groups each. The Gd atom is coordinated to the two nitrogen atoms of each N2O2 ligand and the two oxygen atoms of each phenoxide ligand. Dashed lines indicate the coordination bonds from the Gd atom to the nitrogen and oxygen atoms.</p>	Gd (β -substituted: tert-butyl phenoxy)	(29)

Table 1.1 continued...

Complex	Lanthanide	Complex number
	Nd (α -substituted: tert-butyl phenoxy)	(30)
	Ce (β -substituted: tert-butyl phenoxy)	(31)

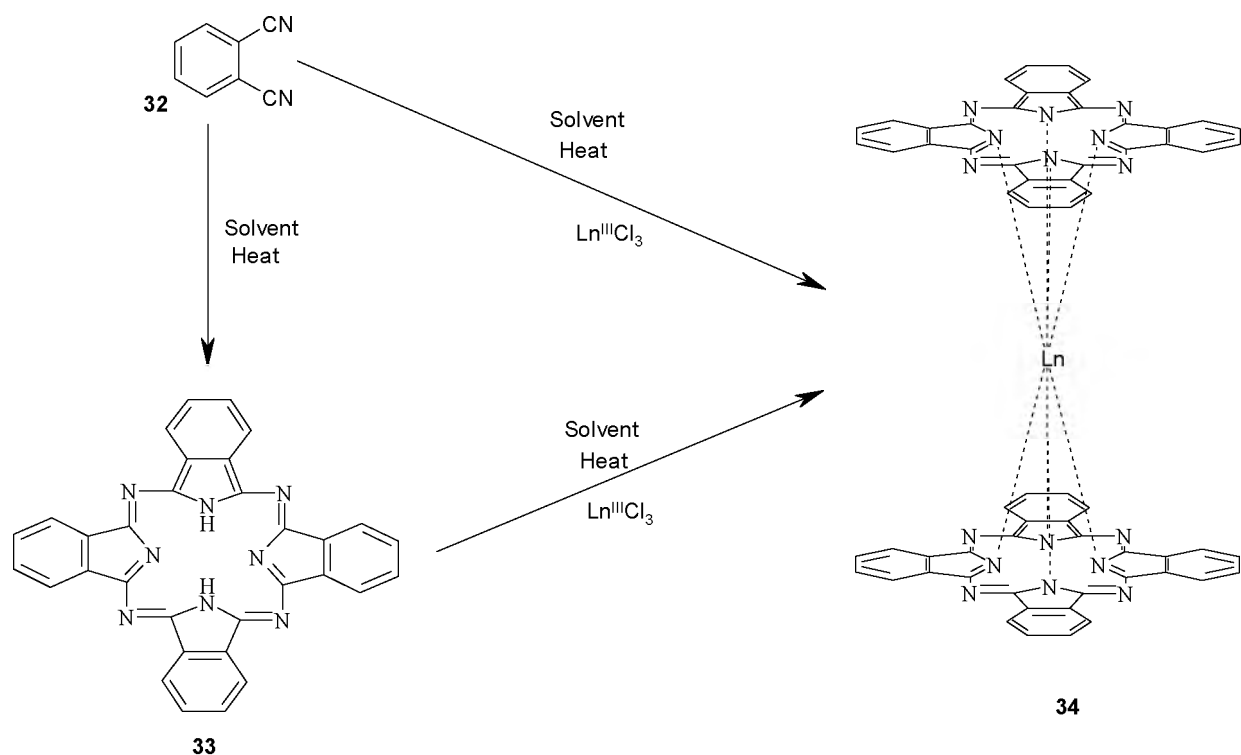
Names of the complexes in Table 1.1:

2(3), 9(10), 16(17), 23(24)-(tetrapyridin-3-yloxy phthalocyaninato) neodymium (III) acetate (18), bis{23-(3,4-di-yloxybenzoic acid)-(2(3), 9(10), 16(17), 23(24)-(hexakis-pyridin-3-yloxy phthalocyaninato))} dineodymium (III) acetate (19), 2,4,6-tris[3-thio-9,10,16,17,23,24-hexa(4-tertbutylphenoxy) phthalocyaninato ytterbium (III) chloride]-s-triazin (20), 2,4,6-tris[3-thio-9,10,16,17,23,24-hexa(4-tertbutylphenoxy) phthalocyaninato lutetium (III) chloride]-s-triazin (21), bis-{1(4), 8(11), 15(18), 22(25)-(tetrapyridin-2-yloxy phthalocyaninato)} ytterbium (III) (22), bis-{1(4), 8(11), 15(18), 22(25)-(tetrapyridin-4-yloxy phthalocyaninato)} ytterbium (III) (23), bis-{1(4), 8(11), 15(18), 22(25)-tetra(4-tertbutylphenoxy) phthalocyaninato} ytterbium (III) (24), bis-{2(3), 9(10), 16(17), 23(24)-(tetrapyridin-4-yloxy phthalocyaninato)} ytterbium (III) (25), bis-{2(3), 9(10), 16(17), 23(24)-(tetrapyridin-4-yloxy phthalocyaninato)} lanthanum (III) (26), bis-{2,3,9,10,16,10,16,17,23,24-octa(4-tertbutylphenoxy) phthalocyaninato} cerium (III) (27), bis-{2,3,9,10,16,10,16,17,23,24-octa(4-tertbutylphenoxy) phthalocyaninato} lutetium (III) (28), bis-{2,3,9,10,16,10,16,17,23,24-octa(4-tertbutylphenoxy) phthalocyaninato} gadolinium (III) (29), tris-{1(4),8(11),15(18),22(25)-tetra(4-tertbutylphenoxy) phthalocyaninato} dineodymium (III) (30) and tris-{2,3,9,10,16,10,16,17,23,24-octa(4-tertbutylphenoxy) phthalocyaninato} dicerium(III) (31).

1.1.2.3 Multi-decker phthalocyanines

1.1.2.3.1 Double-decker phthalocyanines

Like all the normal Pcs, double-decker or lanthanide bis(phthalocyanines) (LnPc_2) may be prepared directly from a phthalonitrile (**32**) in the presence of a lanthanide salt, organic solvent and a catalyst, **Scheme 1.5**. The ratio of a lanthanide salt to a phthalonitrile is very important since monophthalocyanines are also highly likely to form in the same reaction mixture. A ratio of 1:8 of a lanthanide salt to a phthalonitrile is normally employed to eliminate the formation of monophthalocyanines [**120**], and enhance the likelihood of the formation of LnPc_2 complexes. Another synthetic strategy is to prepare an LnPc_2 complex (**34**) is by sandwiching of a lanthanide ion with an H_2Pc molecule (**33**) in organic solvents with high boiling points in the presence of a catalyst, **Scheme 1.5** [**121**]. This strategy could be time-consuming, considering that an H_2Pc molecule, on its own, requires extensive purification. These two methods are employed in this thesis.



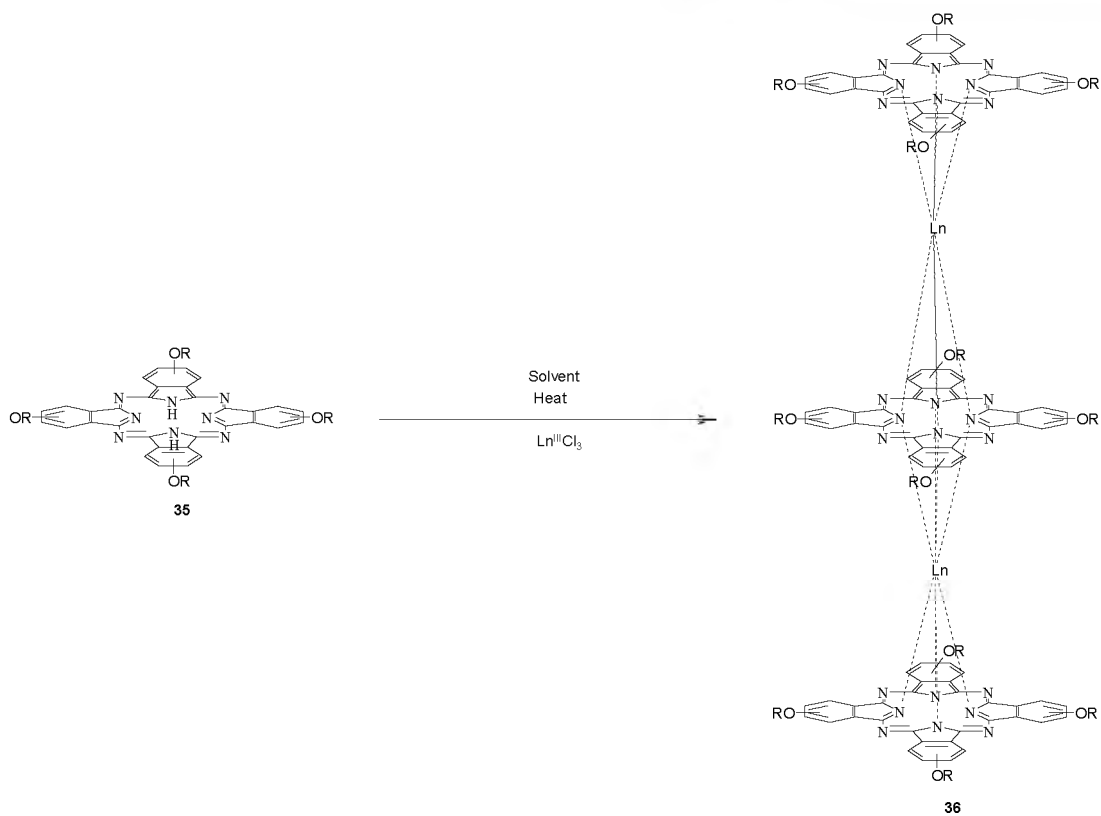
Scheme 1.5: Synthesis of LnPc₂ complex via two routes.

Studies for the Ce derivatives are nonexistent, hence are subject of this work. As stated above, LnPc₂ complexes show improved optical nonlinearities due to their expanded π -electron system and the presence of the heavy lanthanide central metal [106,107,106] which enhances the rate of intersystem crossing (ISC) to the triplet state [108]. The reported NLO behavior of LnPc₂ complexes has concentrated on unsubstituted or peripherally substituted derivatives [106,122-127]. This work presents YbPc₂ derivatives substituted at non-peripheral positions (complexes **22**, **23** and **24** in Table 1.1), which will result in reduced aggregation. Peripherally tetra substituted Pcs containing the same substituents as **23** are also presented as complexes **25** and **26**. Also to date, the studies on the NLO behavior of LnPc₂ have concentrated on the neutral green form, despite the

paramagnetic nature, which shortens triplet state lifetimes. This thesis also compares the NLO behavior of green and blue forms of LnPc_2 complexes based on ytterbium and lutetium, complexes **24** and **28** in **Table 1.1**. NLO parameters such as third order optical susceptibility and hyperpolarizability have been extensively reported for monomeric Pcs, but are still limited for LnPc_2 and are thus reported in this work. The work also reports on the octa substituted derivatives containing Ce, Lu and Gd (complexes **27**, **28** and **29** respectively)

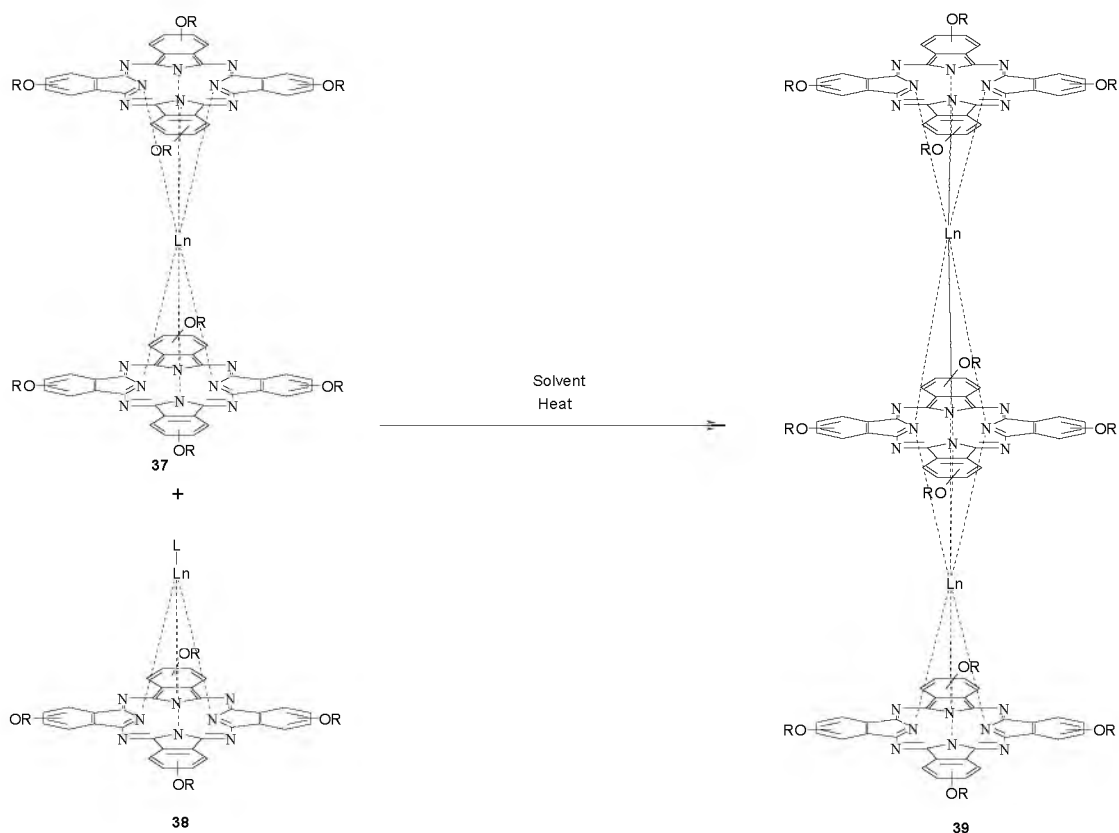
1.1.2.3.2 Triple-decker phthalocyanines

Triple-decker or dilanthanide tris(phthalocyanines) (Ln_2Pc_3) are a family of LnPc_2 complexes. The difference between the two is the number of coordinating lanthanide ions and Pc molecules, with the former having two lanthanide ions and three Pc rings while the latter has one lanthanide ion and two Pc rings. The preparation of Ln_2Pc_3 complexes (**36**) involves many synthetic strategies. One simplest approach involves refluxing one coordinating Pc (**35**) entity in the presence of a lanthanide salt, appropriate solvent and a catalyst [128], **Scheme 1.6**. Normally a 1:1.5 molar ratio of a Pc and a lanthanide salt would result in a successful formation of Ln_2Pc_3 complex, though 1:1 molar ratio may also be used. This strategy is as time-consuming as that of preparing LnPc_2 complexes from Pc entities mentioned above.



Scheme 1.6: Synthesis of an Ln₂Pc₃ complex.

Another approach involves coordinating an LnPc₂ complex (37) to a lanthanide phthalocyanine (LnPc, 38) [129,130] by employing a molar of 1:1 in an appropriate organic solvent with the addition of a catalyst to form an Ln₂Pc₃ complex (39), **Scheme 1.7.**



Scheme 1.7: Synthesis of an Ln_2Pc_3 complex from LnPc_2 and LnPc complexes.

Unlike the LnPc_2 counterparts which are paramagnetic, the positive charge on the two Ln (III) in Ln_2Pc_3 balances the negative charge in the three Pc ligands, hence Ln_2Pc_3 complexes are neutral. The neutral Ln_2Pc_3 complexes are expected to show improved NLO characteristics compared to LnPc_2 or monomeric derivatives. Apart from very limited reports on hetero phthalocyanine-porphyrin tris derivatives [131], the NLO behavior of Ln_2Pc_3 complexes has been un-explored. A number of Ln_2Pc_3 has been synthesized with substituents at the peripheral positions [132-136], but no reports on their NLO behavior. This work presents a Ln_2Pc_3 derivative substituted at non-peripheral positions with tert-butylphenoxy substituents (complex 30, Table 1.1) and an octa substituted Ce containing

Ln_2Pc_3 (complex **31**, Table 1.1) and reports on their NLO behavior. In summary, this thesis compares the following Pc molecules for their NLO behavior:

1. The effects of π -electron system (complexes **18** and **19**; **27** and **31**).
2. Effects of central metals (complexes **20** and **21** or **25** and **26** or **27**, **28** and **29**).
3. The effects of substituents (complexes **22**, **23** and **24**; **23** and **25**).
4. Complex **30** is independently investigated.
5. The effects of thin films against solutions.

In this work, PBC, PAA and PMMA are employed, with PBC chosen because it has been used as a material for making safety visors in the past and has great affinity for modification [137].

1.1.3 Electronic absorption spectra of phthalocyanines

1.1.3.1 Monomeric phthalocyanines

Monophthalocyanines absorb strongly in the near infrared region of the visible spectrum due to transitions from the a_{1u} of the highest occupied molecular orbital (HOMO) to the e_g of the lowest unoccupied molecular orbital (LUMO), Fig. 1.2, resulting in the Q band. The B band occurs at higher energy and is due to transitions $e_g \leftarrow a_{2u}$ (B_1) and $e_g \leftarrow b_{2u}$ (B_2).

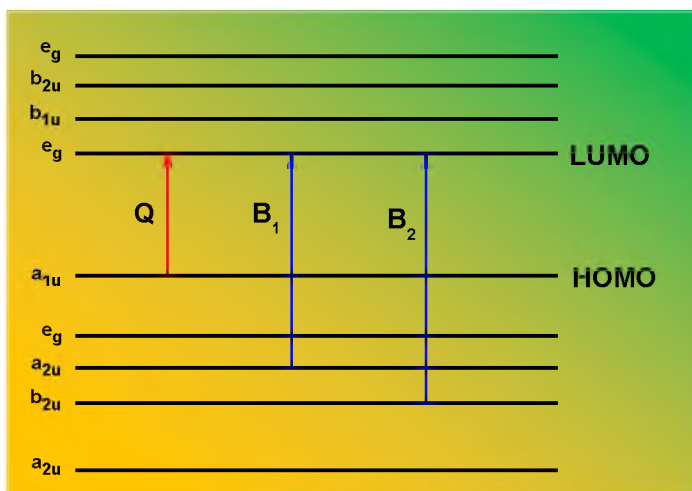


Fig. 1.2: Electronic transitions in phthalocyanines.

The Q band of monophthalocyanine splits into two in the absence of a central metal [138], **Fig. 1.3**, due to D_{2h} symmetry and when there is a lack of symmetry [139]. The metallated Pc shows an unsplit Q band as a result of a D_{4h} symmetry and the degeneracy of the LUMO.

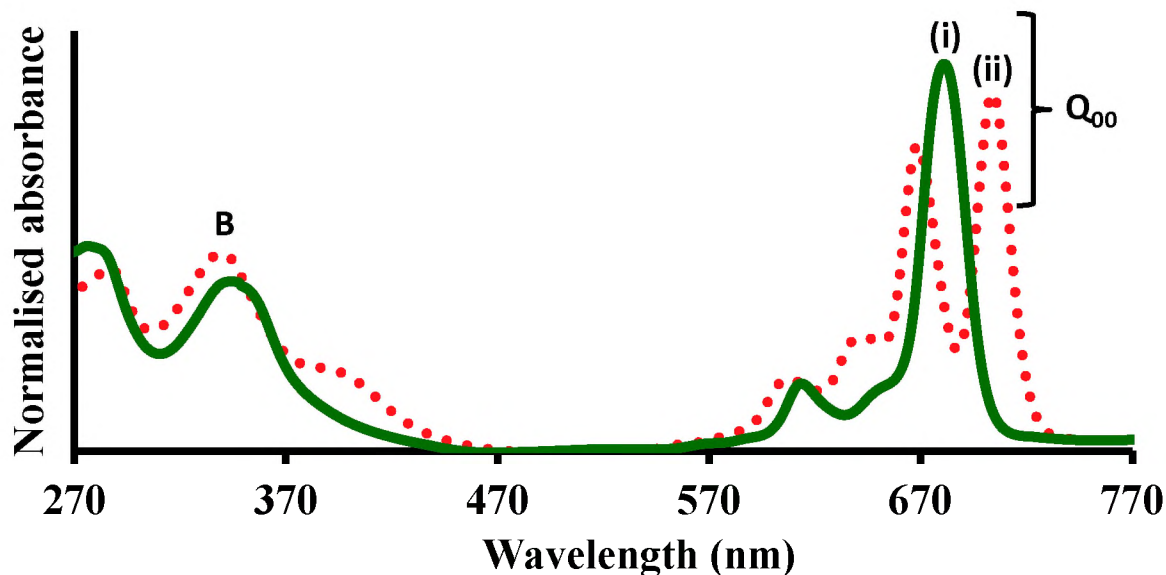


Fig. 1.3: Ground state absorption spectra of metallated ((i) black) and unmetallated ((ii) red) Pc

1.1.3.2 Multi-decker phthalocyanines

The neutral or green forms of LnPc_2 complexes are designated as $(\text{Pc}^{-1}\text{LnPc}^{-2})$. The electronic absorption transitions of LnPc_2 complexes were not understood until Orti et al [140-142] made the first theoretical attempt to interpret the spectrum of LuPc_2 as a delocalized system, using a molecular orbital (MO) model based on a valence effective Hamiltonian (VEH) calculation. The B or Soret band is associated with various inter-phthalocyanine allowed transitions [140-149] assigned to $6e_1(\pi) \leftarrow 4a_1(\pi^*)$, **Fig. 1.4**. Next is the characteristic absorption band in the 400-500 nm region for the green form referred to as the blue valence band (BV) [144,148-154] arising from the electronic excitations $2a_2(\pi^*) \leftarrow 5e_1(\pi)$. Using VEH calculations, the Q band was assigned to the electronic

transitions [148] arising from the excitation $6e_3(\pi^*) \leftarrow 2b_1(\pi)$. The red valence (RV) band is assigned to the vibronically activated forbidden transition $6e_3(\pi^*) \leftarrow 2a_2(\pi)$ involving semi occupied molecular orbital (SOMO) [150,155], Fig. 1.4. The RV slightly red shifts with decreasing the size of the metal center.

With the exception of Ce and Pm, all other neutral LnPc_2 complexes (La – Tm) exhibit split Soret bands with maxima around 335-343 and 369-374 nm, an intense Q-band at 672-699 nm, BV band at 485-513 and RV band 900-915 nm, and the ring-to-ring charge transfer transition band(s) in the near IR region (NIR band) between 1416 and 2250 nm [120] due to excitation $2a_1 \leftarrow 2b_1$, Fig. 1.4. The absorptions are sensitive to the metal center. Most of the absorptions, particularly the longest-wavelength ring-to-ring charge transfer transition bands, are monotonically blue-shifted with the decrease of the ionic radius from La^{3+} to Tm^{3+} .

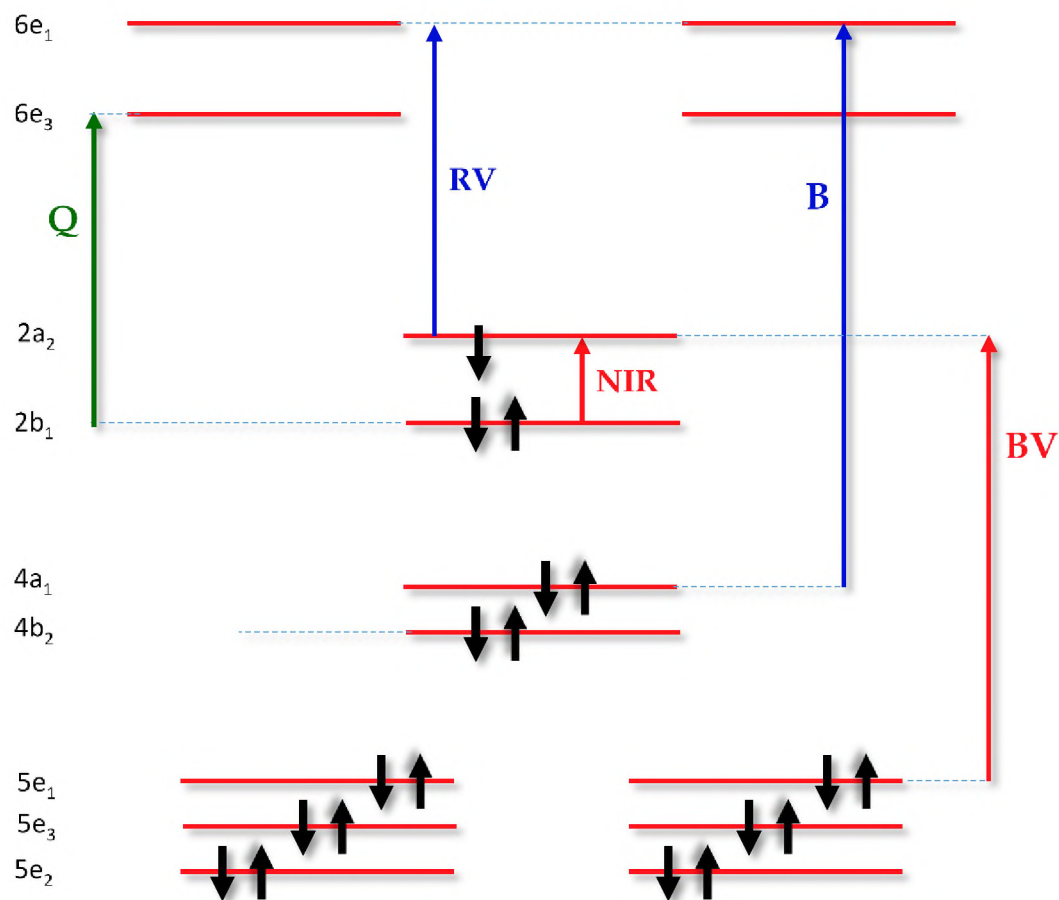


Fig. 1.4: Electronic excitation transitions observed in LnPc₂ complexes in accordance with VCH calculations [126,140-155].

Fig. 1.5 therefore shows the absorption spectra of green (Pc⁻¹LnPc⁻²) and blue (Pc⁻²LnPc⁻²) forms of LnPc₂ in CHCl₃. The absorption bands corresponding to the electronic transitions discussed above are labeled. It is noteworthy that the Q band of Pc⁻²LnPc⁻² is split. This is attributed to an electron accepted by the Pc ring which was Pc⁻¹ in Pc⁻¹LnPc⁻².² The radical-related BV band also disappears. It has been discovered that the polarity of the solvent plays huge role on the character of the LnPc₂ ultra violet-visible (UV-Vis)

spectra, with the LnPc_2 solutions blue in the polar dimethyl formamide (DMF) and green both in low-polarity dichloromethane and non-polar nujol [156,157].

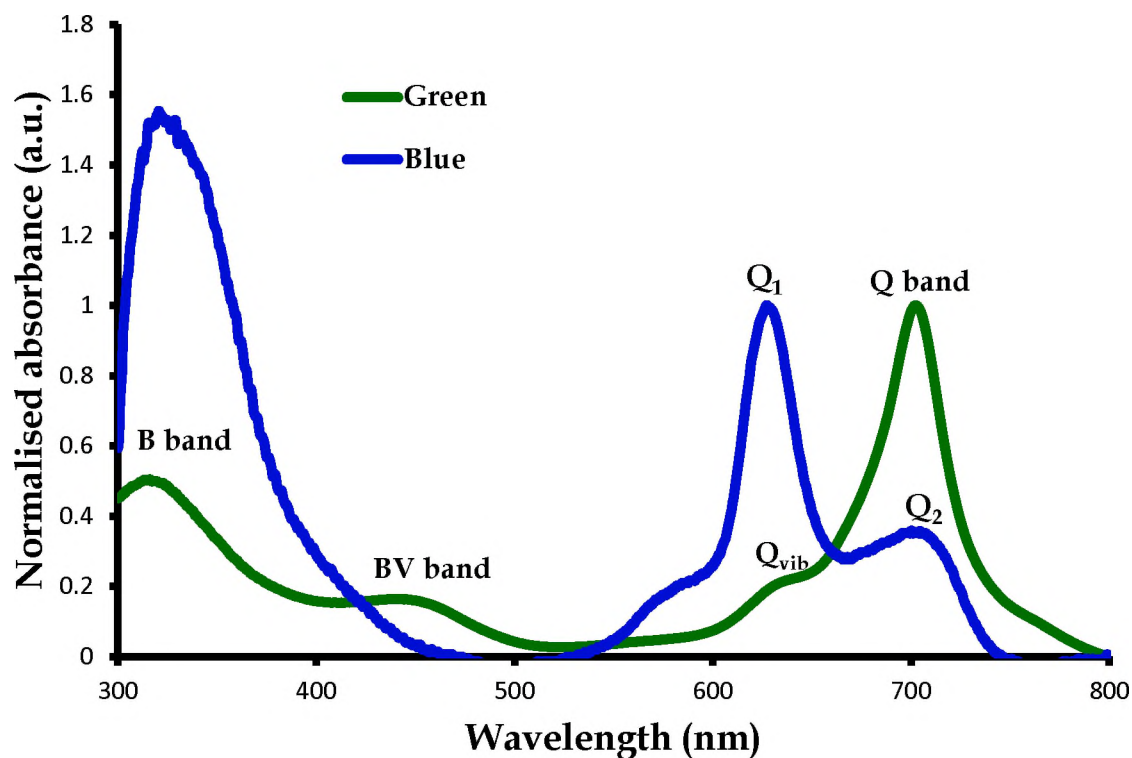


Fig. 1.5: The absorption spectra of YbPc_2 complexes (unpublished) in green form (no Q band split) and blue form (indicating splits in the Q bands, resulting in Q_1 and Q_2).

1.2 Nonlinear optical limiting

1.2.1 Definition of optical limiting

Nonlinear optics was observed for the first time about six decades ago when the invention of the laser provided enough light intensity [158]. This was followed by theoretical examination of interactions between light waves in a nonlinear dielectric [159]. The birth of nonlinear optics is often associated with J. Kerr, who observed that the refractive index of organic liquids and glasses in the presence of an electric field could change [160-162]. Ideally, the output intensity (transmitted by a material) should be a linear function of the input intensity. However, with lasers providing highly illuminating intensities, the transmitted intensity may cease to behave linearly as a function of the input intensity, allowing the occurrence of optical nonlinearities. Optical limiting (OL) is therefore viewed as an important phenomenon that can be useful for applications in nonlinear optics in which devices decrease transmission with increasing excitation. Such devices are referred to as the optical limiters. For Pcs, the 18 π -electron system contributes to strong NLO response as a measure of optical limiting of nanosecond [163], picosecond [74] and femtosecond laser pulses [164] due to easy modification of their physical, optoelectronic and chemical parameters in a broad range, resulting in exceptional stability and processability features [64,66,165-167].

1.2.2 Nonlinear optical mechanisms

Nonlinear absorption (NLA), nonlinear scattering (NLS) and nonlinear refraction (NLR) are the most important mechanism for optical limiting [168-170]. Highly illuminating lasers provide higher input energies to the NLO material with a positive nonlinear absorption coefficient, thus exhibiting reverse saturable absorption (RSA). RSA is an NLO process characterized by a decrease in transmission under high intensity or high fluence illumination but would not occur at normal light intensities due to higher transmission. When the transmission increases with increasing input intensity of the laser beam, saturable absorption (SA) occurs. Fig. 1.6 illustrates both RSA and SA.

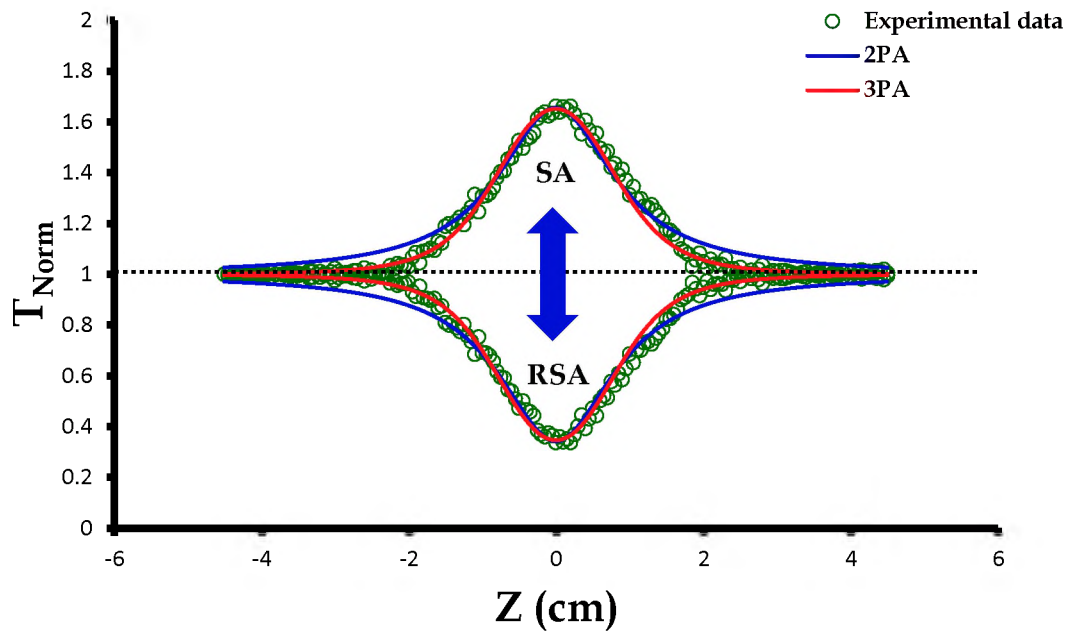


Fig. 1.6: Illustration of RSA and SA occurring when high input energies of light are pumped in the NLO material. Red and blue lines are the fits used to predict which mechanism is dominant in a material. This data was obtained from the Z-scan but remains unpublished.

Negative nonlinear absorption coefficient is normally observed in the materials that undergo SA [163]. Two photon absorption (2PA) [171] and three photon absorption (3PA) [172-175] associated with the imaginary part of the third-order susceptibility, are known as the two out of many mechanisms accounting for optical limiting.

Upon receiving the energy, NLO material undergoes transitions that can be explained in terms of a five-level diagram [176,177], Fig. 1.7. The system absorbs the energy that results in the transitions [S_0 to S_1] (ground state absorption), [S_1 to S_2] (singlet excited state absorption) and [S_2 to S_1] excited state emission (ESE). The molecule then undergoes intersystem crossing (ISC) [S_1 to T_1] and re-absorbs the energy through the transition [T_1 to T_2] (triplet excited state absorption). In the five-level system, the following assumptions are made:

- Energy levels are non-degenerate
- ISC transition [S_1 to T_1] is fast
- Emission from the upper excited states: [S_2 to S_1] and [T_2 to T_1] is fast
- Larger excited state cross sections (σ_2 and σ_3) than the ground state cross section (σ_1)

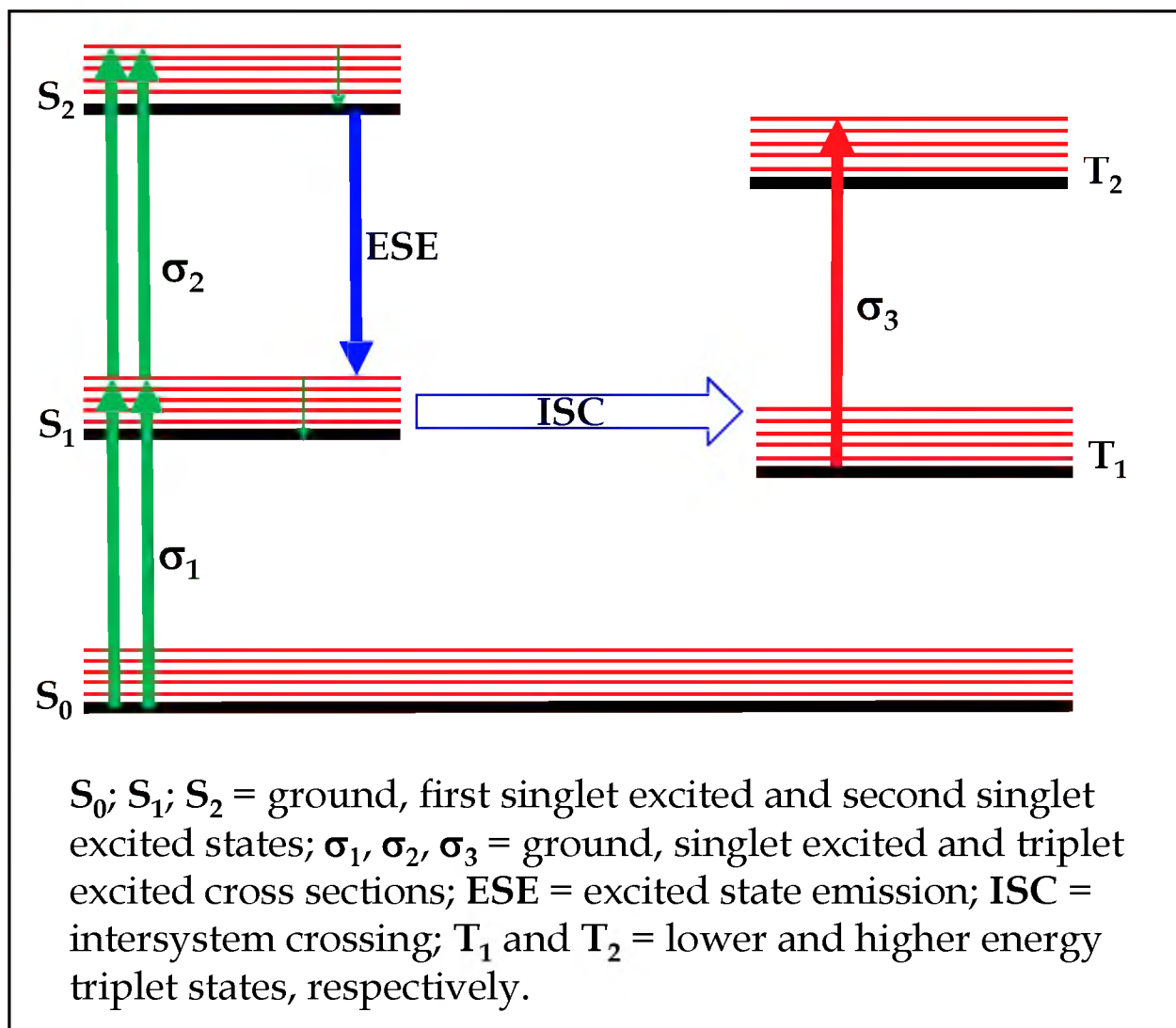


Fig. 1.7: A model used to describe the interaction of light with a molecular compound in terms of electronic transitions in the NLO materials, particularly phthalocyanines.

Large σ_2 and σ_3 and a long excited state lifetime are prerequisites for the largest nonlinear absorption [163]. Organic and organometallic materials, including porphyrins, MPcs, fullerenes, organometallic cluster compounds and other materials are known to exhibit

large excited state cross sections with large difference between the ground and excited state absorption cross sections [178-182].

Good optical limiters are characterized by low limiting thresholds (I_{lim}), with large nonlinear response over a wide range of fluences before the saturation of nonlinearity occurs [163]. High concentrations of the nonlinear material in the optical beam are required in the case of high saturation fluence.

The optical limiting (OL) effect of a NLO material is shown by a response to the intense beams in the form of a strong attenuation when the input intensity has passed the I_{lim} value, Fig. 1.8A and B. By definition, the I_{lim} value ($J.cm^{-2}$) is the input fluence at which the output fluence is 50% of the linear transmission [172,183].

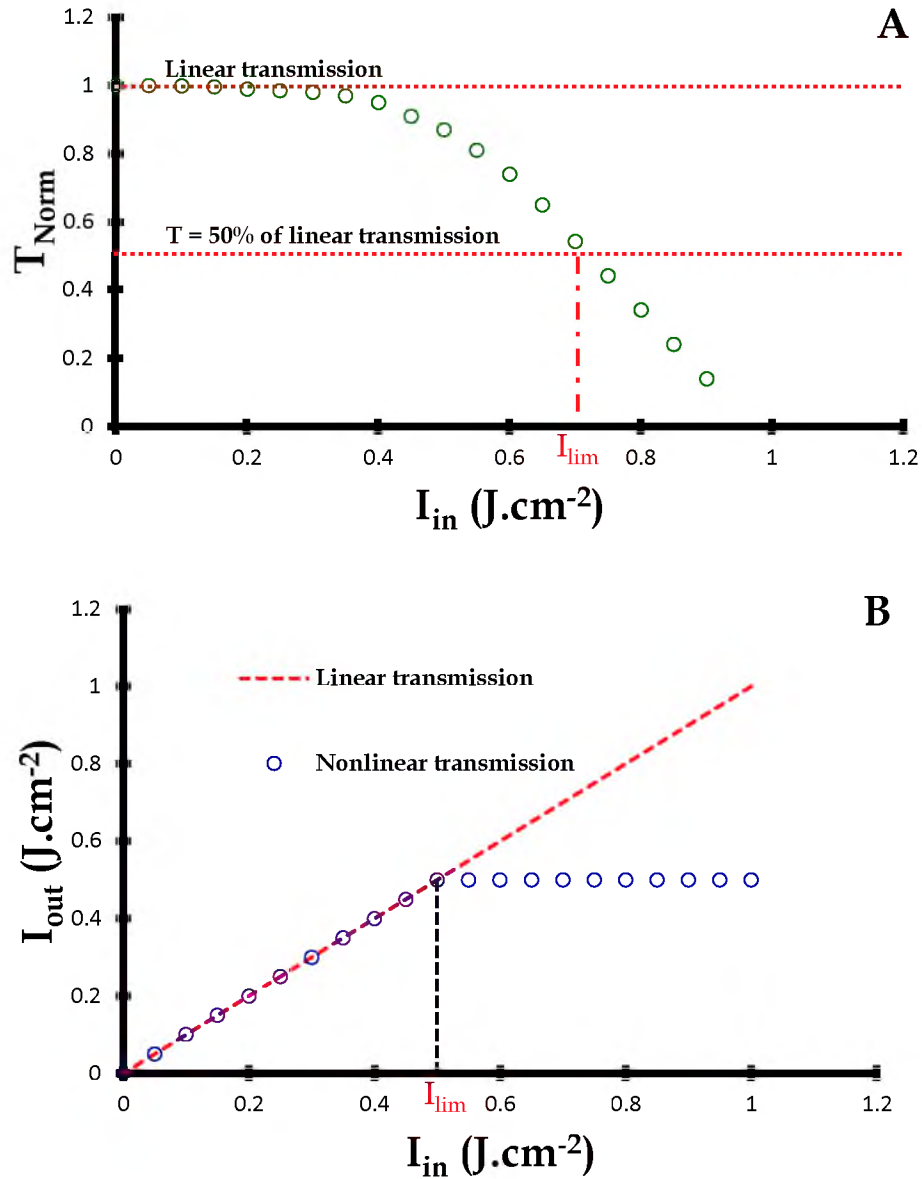


Fig. 1.8: The behavior of (A) transmission against input intensity (I_{in}) and (B) (the output intensity (I_{out}) transmitted by an optical limiter vs I_{in} from the light source. These two figures were modified in accordance with reference [163].

I_{out} and I_{in} respectively, are the intensity of light beam transmitted by the NLO material and the intensity of the incoming light beam from the light source. The most important feature of the plot in **Fig. 1.8B** is the flattening of the curve called “effect of residual absorption” [184], due to a reduced transmittance once $I_{\text{in}} > I_{\text{lim}}$.

1.2.3 Calculations of nonlinear optical parameters

Using nonlinear regression technique, all open aperture Z-scan data based on two photon absorption may be fitted with Eq. 1.1, where the normalized transmittance ($T_{\text{Norm}}(z)$) is defined as a function of position [185-188] as described by Sheik-Bahae and co-workers.

$$T_{\text{Norm}}(z) = \frac{1}{\sqrt{\pi q_0(z)}} \int_{-\infty}^{\infty} \ln[1 + q_0(z)e^{-\tau^2}] d\tau \quad 1.1$$

$$\text{In Eq. 1.1, } q_0(z) = \frac{\beta_{\text{eff}} I_0 L_{\text{eff}}}{1 + (z/z_0)^2} \quad 1.2$$

where β_{eff} and I_0 are the effective intensity dependent nonlinear absorption coefficient and the intensity of the beam at focus, respectively. z and z_0 are sample position with respect to the input intensity and Rayleigh length (defined by $\pi w_0^2 / \lambda$; λ = wavelength of the laser beam and w_0 = beam waist). L_{eff} is referred to as the effective thickness of the sample and is given by Eq. 1.3 [185]:

$$L_{\text{eff}} = \frac{1 - e^{-\alpha L}}{\alpha} \quad 1.3$$

Here α and L are the linear absorption coefficient and the thickness of the sample respectively.

The imaginary component of the third order optical susceptibility ($\text{Im}[\chi^{(3)}]$ in esu) is directly proportional to β_{eff} via Eq. 1.4 [163,189]:

$$\text{Im}[\chi^{(3)}] = \frac{(n^2 \varepsilon_0 c \lambda \beta_{\text{eff}})}{(2\pi)} \quad 1.4$$

In Eq. 1.4, c and n , respectively, are the speed of light in vacuum and the linear refractive index. ε_0 is the permittivity of free space and λ is the wavelength of the laser light.

At a molecular level, there is a direct correlation of $\text{Im}[\chi^{(3)}]$ with the hyperpolarizability γ (which provides the nonlinear absorption per mole of the sample) via the relationship shown in Eq. 1.5 [163,190,191]:

$$\gamma = \frac{\text{Im}[\chi^{(3)}]}{N^* f^4} \quad 1.5$$

where $N^* = C_{\text{mol}} N_A$ (C_{mol} is the concentration active species in the excited state in mol) and f represents Lorenz local field factor and is given by Eq. 1.6:

$$f = \frac{n^2 + 2}{3} \quad 1.6$$

1.2.4 Nonlinear optical behavior of phthalocyanines

The electronic energy levels mainly account for the NLO response of a molecule [64]. The Q band of a Pc is more intense than the B band. Between these two bands is an optical region in which the nonlinear optical mechanisms take place with the involvement of effective excited state absorption stronger than the ground state absorption [163], resulting in reverse saturable absorption (RSA) due to MPA. The investigation of the third-order NLO properties of Pcs stretches back to 1987 when chlorogallium and fluoroaluminium Pcs were reported for the first time [66]. Table 1.2 [107,123,192-196] lists LnPc₂ complexes have been studied for NLO behaviors.

Table 1.2: Nonlinear absorption properties of LnPc₂ complexes.

Sample	Solvent	Concentration (M)	β_{eff} (m.W ⁻¹)	$\text{Im}[\chi^{(3)}]$ (esu)	γ (esu)	I_{lim} (J.cm ⁻²)	Ref.
EuPc ₂	THF	2.20 x10 ⁻⁴	3.27 x10 ⁻¹¹	^b 1.94 x10 ⁻²⁰	3.3 x10 ⁻³⁰	-	[192]
α -EuPc ₂	THF	2.16 x10 ⁻⁴	1.88 x10 ⁻¹¹	^b 1.11 x10 ⁻²⁰	1.98 x10 ⁻³⁰	-	[192]
β -EuPc ₂	THF	2.16 x10 ⁻⁴	1.24 x10 ⁻¹¹	^b 0.738 x10 ⁻²⁰	1.31 x10 ⁻³⁰	-	[192]
β_2 -EuPc ₂	THF	2.08 x10 ⁻⁴	2.23 x10 ⁻¹¹	^b 1.33 x10 ⁻²⁰	2.45 x10 ⁻³⁰	-	[192]
EuPc ₂	THF	2.20 x10 ⁻⁴	3.27 x10 ⁻¹¹	^b 1.94 x10 ⁻²⁰	3.3 x10 ⁻³⁰	-	[192]
SmPc ₂	DMF	-	-	1.8 x10 ⁻¹³	55 x10 ⁻³²	-	[193]
EuPc ₂	DMF	-	-	1.7 x10 ⁻¹³	4.1 x10 ⁻³¹	-	[194]
LuPc ₂	CHCl ₃	^a	1.42 x10 ⁻¹⁰	-	-	-	[195]
GdPc ₂	Pyridine	^a	4.54 x10 ⁻¹⁰	-	-	-	[195]

Table 1.2 continued....

Sample	Solvent	Concentration (M)	$\beta_{\text{eff}} (\text{m.W}^{-1})$	$\text{Im}[\chi^{(3)}] (\text{esu})$	$\gamma (\text{esu})$	$I_{\text{lim}} (\text{J.cm}^{-2})$	Ref.
Eu[Pc(OC ₅ H ₁₁) ₈] ₂	CHCl ₃	9.7 x10 ⁻⁶	-	-	-	0.3	[196]
Eu[Pc(C ₇ H ₁₅) ₈] ₂	CHCl ₃	8.6 x10 ⁻⁶	-	-	-	0.45	[196]
LuPc ₂	DMSO	2 x10 ⁻³	7.76 x10 ⁻¹⁰	-	-	1.8	[197]
LuPc ₂	-	-	-	-	-	5	[123]

b = values in m²/v², a = 1 g/L.

Most of the studied NLO of LnPc₂ complexes do not indicate susceptibility, hyperpolarizability and I_{lim} values but predict how these molecules behave in both ground and excited states [122,192]. Nonlinear optical data for Ln₂Pc₃ complex is limited. Furthermore, to the best of the author's knowledge, LnPc₂ linked to or mixed with either polymers or nanoparticles have not been studied in nonlinear optics.

The aim, in part, therefore is to characterize by Z-scan both LnPc₂ and Ln₂Pc₃ complexes in detail.

1.2.5 Nonlinear optical limiting of phthalocyanines in the presence of carbon nanotubes

Carbon nanotubes (CNTs) are considered as a new form of pure carbon [197]. There are two types of common carbon tubes, namely: single-walled (SWCNTs (comprising only one cylinder)) and multi-walled (two or more concentric graphene cylinders) carbon nanotubes (MWCNTs). Historically speaking, CNTs were discovered in the mid-1970s by Endo [198]. Ijima [199] employed the arc-discharge fullerene reactor (operating at low direct current) to generate the helical carbon microtubules (today also called nanotubes) which were comprised of graphene tubules, **Fig. 1.9**, and used the high resolution transmission electron microscopy (HRTEM) and electron diffraction to prove the existence of MWCNTs.

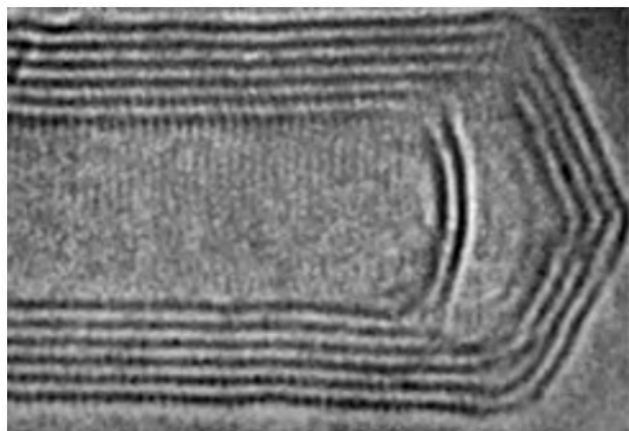


Fig. 1.9: HRTEM image of a multi-walled carbon nanotube [200].

Due to their superior mechanical, thermal, and electrical properties, CNTs can be employed as nanocomposites [200-202], supercapacitors [203-207], in lithium batteries [208-213], electrochemical sensors [214,215] and nonlinear optics [216-218]. The optical limiting properties of MWCNTs have therefore been taken advantage of by linkage to monophthalocyanines [219], with reasonably high β_{eff} values obtained. SWCNTs were also studied in the presence of Pcs [220]. However, it is only when embedded in PMMA that extremely high β_{eff} values were obtained [221,222]. The data in which clam shell Pcs are covalently linked to MWCNTs or SWCNTs is non-existent. In this thesis, the surface of MWCNTs was modified with diaminomaleonitrile for covalent linkage to a neodymium clamshell. Even though both MWCNTs and Pcs are optical limiting materials, their combination does not always lead to improved NLO behavior [223]. It has been reported that since solutions of CNTs are in the form of a dispersion, their optical limiting is due to scattering combined with possible electronic absorption

contributions [223,224]. The aim of this work is to elucidate the mechanism used for NLO for a clamshell Pc in the presence of MWCNTs.

1.2.6 Nonlinear optical limiting of phthalocyanines in the presence of graphene oxide nanosheets

Graphene is a basic building block for all graphitic forms [225]. It consists of a single atomic layer of sp^2 two-dimensional hybridized carbon atoms arranged in a honeycomb structure [226]. Graphite oxide, which contains abundant oxygen-based groups, can be easily exfoliated to graphene oxide nanosheets (GONS), **Fig. 1.10**, by employing ultrasonic devices [227-229]. On reduction using standard procedures involving temperatures and chemical reagents [230-235], the amount of oxygen decreases and therefore GONS are viewed as the precursor to produce reduced graphene oxide nanosheets (rGONS). Despite challenges such as production at large scale and difficulty to incorporate and distribute homogeneously into various matrices for applications, graphene finds its applications based on its electronic properties [236-238] such as nonlinear optics [239-241]. Graphene possesses other exciting properties, such as high stiffness and strength, excellent thermal properties and promising biocompatibility [242]. When monophthalocyanines were covalently linked to GONS and rGONS, a good optical limiting behavior was obtained [243]. However, NLO studies in which GONS or rGONS are covalently linked to low symmetry clam shell Pcs are non-existent. As stated already, low symmetry improves NLO behavior of Pcs.

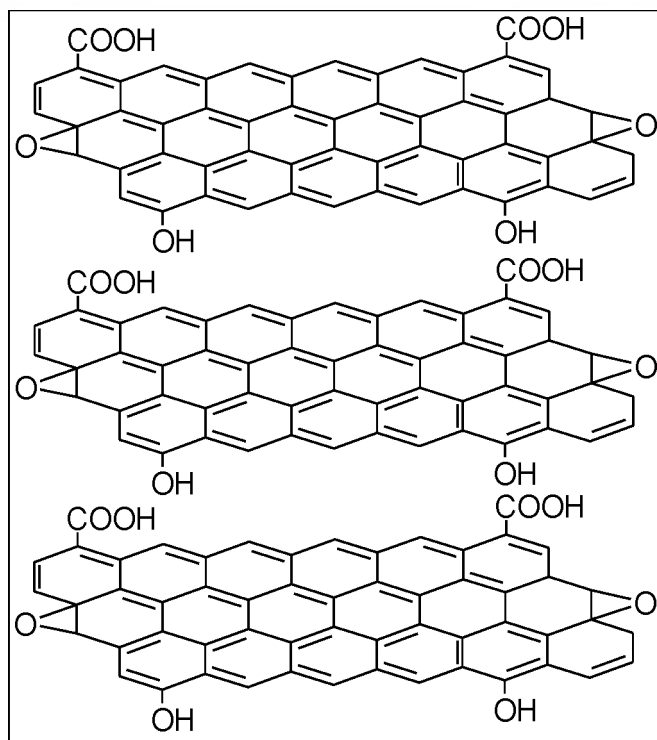


Fig. 1.10: Structure of graphene oxide nanosheets.

This research thesis presents the surface modification of GONS and rGONS with diaminomaleonitrile. The linking of GONS and rGONS to a clam shell Pc is reported for the first time. Conjugates with GONS and rGONS are embedded in PAA, which help to form thin films for solid state Z-scan laser characterization to determine their potential in optical limiting. In general, this study is aimed at investigating the optical limiting processes induced by 2PA.

1.2.7 Nonlinear optical limiting of phthalocyanines in the presence of zinc oxide nanoparticles

Nanoparticles are defined as particulate dispersions or solid particles with a size in the range of 10-1000 nm [244]. Gold, silver and bismuth nanoparticles exhibit a strong nonlinear scattering [245-247], while zinc oxide show strong 2PA [248]. In this work, the Pc complexes are linked to zinc oxide nanoparticles (ZnO NPs) since the latter show good NLO due to two photon absorption [249]. The combination of the two NLO materials (Pc and ZnO NPs) is expected to improve NLO behavior. Conjugates of low symmetry clam shell Pcs covalently linked to ZnO NPs do not exist. In this thesis, ZnO NPs are linked to an Nd clam shell Pc complex (**19**) using different strategies in order to compare the effects of different linkages on the photophysical and NLO behavior. This thesis presents the photophysics and NLO behavior of neodymium based clam shell Pc (alone or linked to ZnO NPs). The NLO behavior is studied in solution or when embedded in thin films of poly (acrylic acid). As stated above, zinc oxide nanoparticles exhibit 2PA. Since neodymium based clam shell Pc also shows 2PA, the nonlinear optical mechanisms are not expected to change. The heavy atom effect of zinc will aid in increasing the triplet state population.

1.3 Photophysico-chemical parameters

1.3.1 Fluorescence quantum yields and lifetimes

Fluorescence quantum yield (Φ_F) is the number of emitted photons relative to the number of absorbed photons. The emission rates of fluorescence are typically 10^8 s^{-1} , so that a typical fluorescence lifetime is near 10 ns [250]. Fluorescence lifetime (τ_F) is the average time an excited fluorophore spends in the excited state before it releases energy and decays to its basic ground state [250,251]. Fluorescence lifetime may be determined by a time correlated single photon counting method [252] and this is employed in this work. Fluorophores decay with various exponential processes. For those that decay with multi-exponential mechanism, Eq. 1.7 may be used to calculate the amplitude weighted fluorescence lifetimes.

$$\tau_{F(Av)} = \sum_i \alpha_i \tau_i \quad 1.7$$

In Eq. 1.7, α_i is the relative amplitude contribution to the lifetime τ . The data obtained from a fluorescence lifetime measuring equipment is judged by a goodness of fit (χ^2) close to one, with good residuals.

By comparing with a standard using Eq. 1.8 [253], fluorescence quantum yield (Φ_F) may be determined:

$$\Phi_F = \Phi_{F_{std}} \frac{F \cdot A_{std} n^2}{F_{std} \cdot A \cdot n_{std}^2} \quad 1.8$$

F and F_{Std} denote the areas under the fluorescence curves for sample and standard, respectively. A and A_{Std} represent the absorbances of the sample and reference at the excitation wavelength respectively, in the solvents of the refractive indices n and n_{Std} for the sample and the reference, respectively.

1.3.2 Triplet quantum yields and lifetimes

Laser flash photolysis technique is used to determine the triplet lifetime and the change in absorbance in the triplet state, which is directly related to the triplet quantum yield [254]. The efficiency of the triplet state is quantified by the use of the triplet quantum yield (Φ_T) and the triplet lifetime (τ_T). The triplet absorption is ~ 500 nm for phthalocyanines. This is far from the ground singlet state absorption, making it possible to conduct these measurements. One may determine Φ_T values either by using the triplet absorption or singlet depletion method. In this work the triplet absorption method was employed hence its discussion below.

A comparative method [255] using standard may be employed for the calculations of Φ_T ,

Eq. 1.9

$$\Phi_T = \Phi_T^{Std} \frac{\Delta A_T \cdot \epsilon_T^{Std}}{\Delta A_T^{Std} \cdot \epsilon_T} \quad 1.9$$

where ΔA_T and ΔA_T^{Std} are the changes in the triplet state absorbances of the sample and the standard respectively; ϵ_T and ϵ_T^{Std} , the triplet state molar extinction coefficients for

the sample and the standard respectively; Φ_T^{Std} , the triplet quantum yield for the standard.

ε_T and ε_T^{Std} are determined from the molar extinction coefficients of their respective ground singlet state (ε_S and ε_S^{Std}), the changes in absorbances of the ground singlet states (ΔA_S and ΔA_S^{Std}) and changes in the triplet state absorptions,

(ΔA_T and ΔA_T^{Std}) in accordance with Eqs 1.10a and 1.10b:

$$\varepsilon_T = \varepsilon_S \frac{\Delta A_T}{\Delta A_S} \quad 1.10a$$

$$\varepsilon_T^{Std} = \varepsilon_S^{Std} \frac{\Delta A_T^{Std}}{\Delta A_S^{Std}} \quad 1.10b$$

1.3.3 Singlet oxygen quantum yield

In this thesis, singlet oxygen quantum yields (Φ_Δ) are determined as a side study to determine the fate of the excited triplet state in the presence of singlet oxygen (1O_2).

There are different experimental procedures employed in the determination of Φ_Δ . The singlet-oxygen quantum yields for the MPc complexes may be conveniently determined using a singlet-oxygen quencher such as 1,3-diphenylisobenzofuran (DPBF) in organic solvents or by using the singlet-oxygen luminescence method (SOLM) [256].

Employing the comparative method, the singlet oxygen quantum yield of the phthalocyanine can be determined according to Eq. 1.11 [257-259]:

$$\Phi_{\Delta} = \Phi_{\Delta}^{Std} \frac{WI_{Abs}^{Std}}{W^{Std}I_{Abs}} \quad 1.11$$

where Φ_{Δ}^{Std} is the singlet oxygen quantum yield for the standard, W and W^{Std} are the photobleaching rates of a quencher such as DPBF in the presence of MPC derivatives under examination and the standard, respectively. I_{Abs}^{Std} and I_{Abs} are the rates of light absorption by the MPC derivative and standard, respectively.

For the SOLM method, the dynamic course of 1O_2 concentration can be clearly recorded, following Eq. 1.124 as described theoretically in the literature [260]:

$$I(t) = B \frac{\tau_D}{\tau_T - \tau_D} [e^{-t/\tau_T} - e^{-t/\tau_D}] \quad 1.12$$

where $I(t)$ is the phosphorescence intensity of $O_2(^1\Delta_g)$ at time t , τ_D is the lifetime of $O_2(^1\Delta_g)$ phosphorescence decay, τ_T is the triplet state lifetime of standard or sample and B is a coefficient involved in sensitizer concentration and singlet oxygen quantum yield. The Φ_{Δ} of the phthalocyanine is then determined by a comparative method using Eq 1.13 [260]:

$$\Phi_{\Delta} = \Phi_{\Delta}^{Std} \cdot \frac{B \cdot OD^{Std}}{B^{Std} \cdot OD} \quad 1.13$$

where Φ_{Δ}^{Std} is the singlet oxygen quantum yield for the standard usually unsubstituted zinc phthalocyanine. B and B^{Std} refer to coefficient involved in sensitizer concentration

and $^1\text{O}_2$ quantum yield for the sample and standard respectively. OD and OD^{Std} are the optical density of the sample and standard correspondingly at the excitation wavelength. In the family of lanthanides, only lanthanum and lutetium are diamagnetic. The rest are paramagnetic due to unpaired f-orbital electrons. **Table 1.3** shows LnPc_2 complexes whose physico-chemical properties are known [72,76,261,262]. Even though Yb and Nd are paramagnetic, this thesis explores their physico-chemical behavior.

Table 1.3: Photophysico-chemical parameters of lanthanide complexes.

MPc	Type	Φ_F (τ_F /ns)	Φ_T	Φ_Δ	Ref.
LuPc	monomer	<0.01	0.83	0.71	[76]
ErPc	monomer	<0.01	-	-	[76]
DyPc ₂	dimer	<0.01	-	-	[76]
[(acac)Er{Pc(β -OC ₅ H ₁₁) ₄ }]	monomer	--	--	--	[72]
[(acac)Er{Pc(β -C ₄ H ₉) ₄ }]	monomer	--	--	--	[72]
Er{Pc(β -OC ₅ H ₁₁) ₄ } ₂	Dimer	--	--	--	[72]
Er{Pc(β -C ₄ H ₉) ₄ } ₂	Dimer	--	--	--	[72]
Eu(acac)Pc	monomer	--	--	--	[261]
Eu(q)Pc	monomer				[261]
[(Ac)Lu{Pc(β -HPTCP) ₄ }]	monomer	0.01(0.07)	--	0.66	[261]
Lu{Pc(HPCP) ₄ } ₂	Dimer	0.03(0.03)	--	0.10	[262]

Summary of the aims of this thesis is given below:

1. To design
 - new lanthanide bisphthalocyanines
 - new lanthanide based mono and clam shell phthalocyanines
 - new lanthanide trimeric phthalocyanines
 - new dilanthanide triphthalocyanes
2. To carry out extensive characterization of these molecules using, among other techniques, NMR, elemental analysis, mass spectrometry, Fourier transformer infrared spectroscopy, time-correlated single photon counting, ultra-violet visible absorption spectroscopy, transmission electron microscopy, etc.
3. To modify the surface of multi-walled carbon nanotubes and graphene oxide nanosheets.
4. To covalently link neodymium monophthalocyanines and clamshelled (via carbonyl moieties and carboxyl groups available on the bridge) to zinc oxide nanoparticles, multi-walled carbon nanotubes and graphene oxide nanosheets.
5. To study photophysics and photochemistry of the designed molecules
6. To incorporate the new molecules into polymers for thin film formation.
7. To carry out nonlinear optical studies and determine the mechanisms of the new molecules and conjugates in solution and thin films.

Chapter 2

Experimental

2. Experimental

2.1 Materials

2.1.1 Solvents

1-Pentanol, deuterated dimethylsulfoxide (DMSO- d_6) and deuterated chloroform ($CDCl_3$) were purchased from Sigma Aldrich. Dichloromethane (DCM), dimethyl sulfoxide (DMSO), and dimethyl formamide (DMF) were purchased from Merck. Tetrahydrofuran (THF) and chloroform were purchased from MINEMA. Diethyl ether, ethanol, methanol, formamide and n-hexane were purchased from SAARCHEM.

2.1.2 Synthesis reagents

Ammonia (25%), dicyclohexylcarbodiimide (DCC) (99%), 3-diphenylisobenzofuran (DPBF), ytterbium (III) chloride hexahydrate, ytterbium (III) chloride, lutetium(III) chloride, cerium chloride, neodymium (III) acetate hydrate, gadolinium (III) chloride, thiocyanuric acid, graphene oxide, diaminomaleonitrile, multi-walled carbon nanotubes (diam. = 110-170 nm; length = 5-9 micron), sodium borohydride, poly (acrylic acid) (PAA), poly (methyl methacrylate) (PMMA), poly (bisphenol A carbonate) (PBC), p-toluenesulfonic acid (*p*-TSA), potassium carbonate, trifluoroacetic acid (TFA), hydrazine (HZ) and sodium azide were purchased from Sigma-Aldrich. 3,4-Dihydroxybenzoic acid, 2,5-dihydroxybenzoic acid, alpha-cyano-4-hydroxycinnamic acid and 1,8-

diazabicyclo[5.4.0]undec-7-ene (DBU) were purchased from Fluka. Silica gel 60PF₂₅₄ was purchased from Merck.

2.1.3 Previously synthesized phthalonitriles, phthalocyanines and nanoparticles

2.1.3.1 Phthalonitriles

The syntheses of 4-nitrophthalonitrile (40) [263-265], 3-nitrophthalonitrile (41) [263], 3-(pyridine-2-yloxy)-phthalonitrile (42) [266], 4,5-bis-{4-tert-butylphenoxy}-phthalonitrile (43) [267] 3-(pyridine-4-yloxy)-phthalonitrile (44) [268-272] and 4-(pyridin-4-yloxy)-phthalonitrile (45) [273] have been reported before.

2.1.3.2 Phthalocyanines

1(4),8(11),15(18),22(25)-Tetra(4-tertbutylphenoxy) phthalocyanine (46) [274] and 2,3,9,10,16,10,16,17,23,24-octa(4-tertbutylphenoxy) phthalocyanine (47) [275,276] were prepared according to literature methods.

2.1.3.3 Nanoparticles

ZnO NPs employed in this work have been synthesized elsewhere [277].

2.2 Instrumentation

❖ Infrared spectra were recorded on a Perkin Elmer 100 ART FT-IR spectrometer.

- ❖ Ultraviolet-visible spectra (UV-Vis) were recorded on a Shimadzu UV-Vis 2550 spectrophotometer.
- ❖ The emission spectra were recorded on a Varian Cary Eclipse fluorescence spectrophotometer.
- ❖ Luminescence lifetimes were measured using time correlated single photon counting setup (TCSPC) (PicoQuant FluoTime 200), Fig. 2.1. The excitation source was a diode laser (LDH-P-C-485, 480 nm, 10 MHz repetition rate for excitation of QDs, or LDH-P-670 with PDL 800-B, 670 nm, 20 MHz repetition rate Picoquant GmbH, for excitation of Pcs. Fluorescence was detected under the magic angle with a peltier cooled photomultiplier tube (PMT) (PMA-C 192-N-M, Picoquant) and integrated electronics (PicoHarp 300E, Picoquant GmbH). A monochromator with a spectral width 4 nm was used to select the required emission wavelength. The response function of the system, which was measured with a scattering Ludox solution (DuPont), had a full width at half-maximum (FWHM) of 300 ps. All luminescence decay curves were measured at the maximum of the emission peak and the lifetimes obtained by deconvolution of the decay curves using the FluoFit Software program (PicoQuant GmbH, Germany). The support plane approach [278] was used to estimate the errors of the decay times.

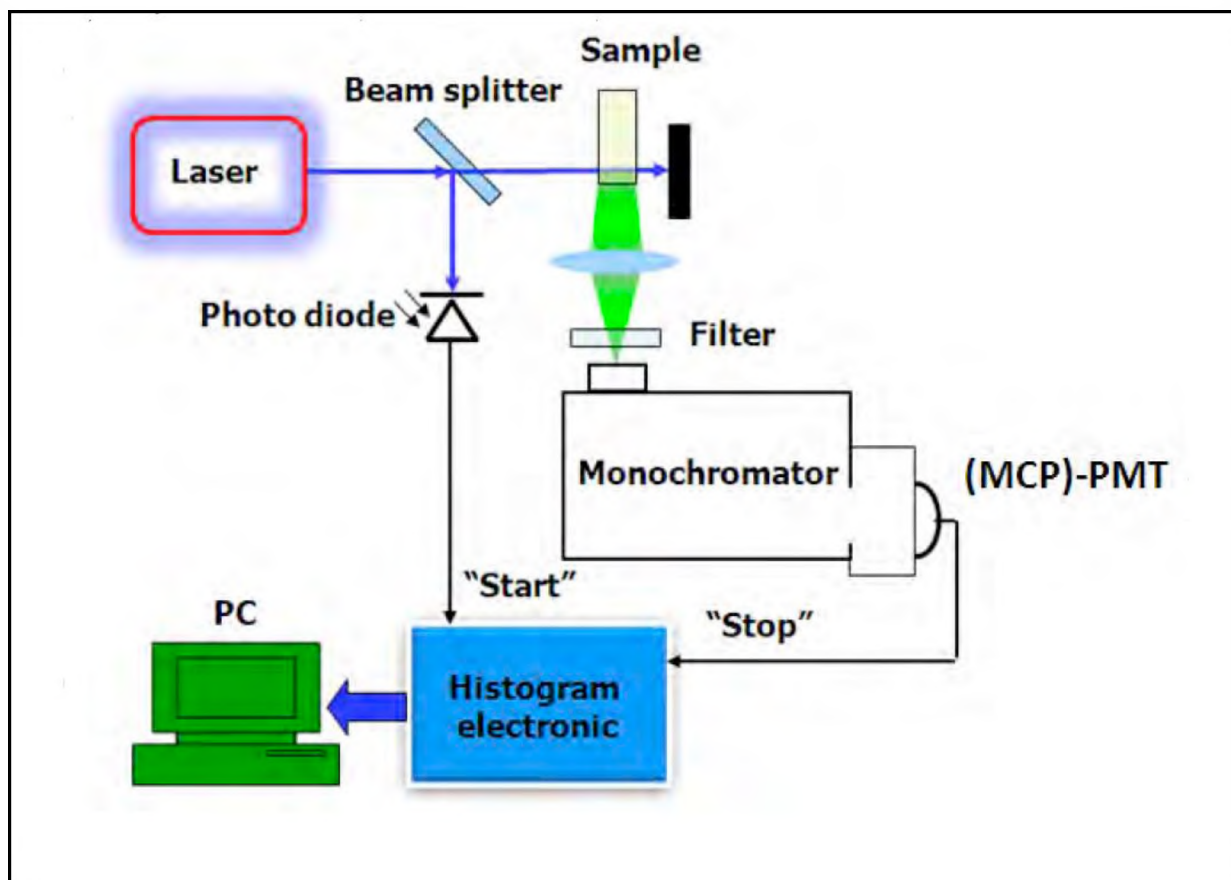


Fig. 2.1: Schematic diagram of time-correlated single photon counting (TCSPC) setup. (MCP)-PMT = Monochromator photomultiplier tube, PC = Personal computer.

- ❖ ^1H NMR nuclear magnetic resonance signals were recorded on a Bruker AMX 600 NMR spectrometer.
- ❖ Raman spectra were obtained using a Bruker Vertex 70-Ram II spectrometer equipped with an Nd:YAG laser that emit at 1064 nm and liquid nitrogen cooled germanium detector.
- ❖ Mass spectral data were collected with a Bruker AutoFLEX III Smart beam TOF/TOF Mass spectrometer. The spectra were acquired using 2,5-dihydroxy

benzoic acid or alpha-cyano-4-hydroxycinnamic acid as the MALDI matrices, and a 355 nm Nd:YAG laser as the ionizing source. Elemental analyses were carried out on a Vario EL III MicroCube CHNS instrument Analyzer.

- ❖ All Z-scan experiments described in this study were performed using a frequency-doubled Nd:YAG laser (Quanta-Ray, 1.5 J/10 ns fwhm (full width at half maximum) pulse duration) as the excitation source. The laser was operated in a near Gaussian transverse mode at 532 nm (second harmonic), with a pulse repetition rate of 10 Hz and energy range of 0.1 μ J – 0.1 mJ, limited by the energy detectors (Coherent J5-09). The low repetition rate of the laser prevents cumulative thermal nonlinearities. The beam was spatially filtered to remove the higher order modes and tightly focused with a 15 cm focal length lens. The Z-scan system size (l x w x h) used was 600 mm x 300 mm x 350 mm (excluding the computer, energy meter, translation stage driver and laser system). The liquid samples were placed in a cuvette (internal dimensions: 2 mm x 10 mm x 55 mm, 0.7 mL) and a path length of 0.2 cm while thin films were run on a thin glass slide, making a total average path length of 0.005 cm (Starna 21-G-2). The Z-scan setup is shown in Fig. 2.2.

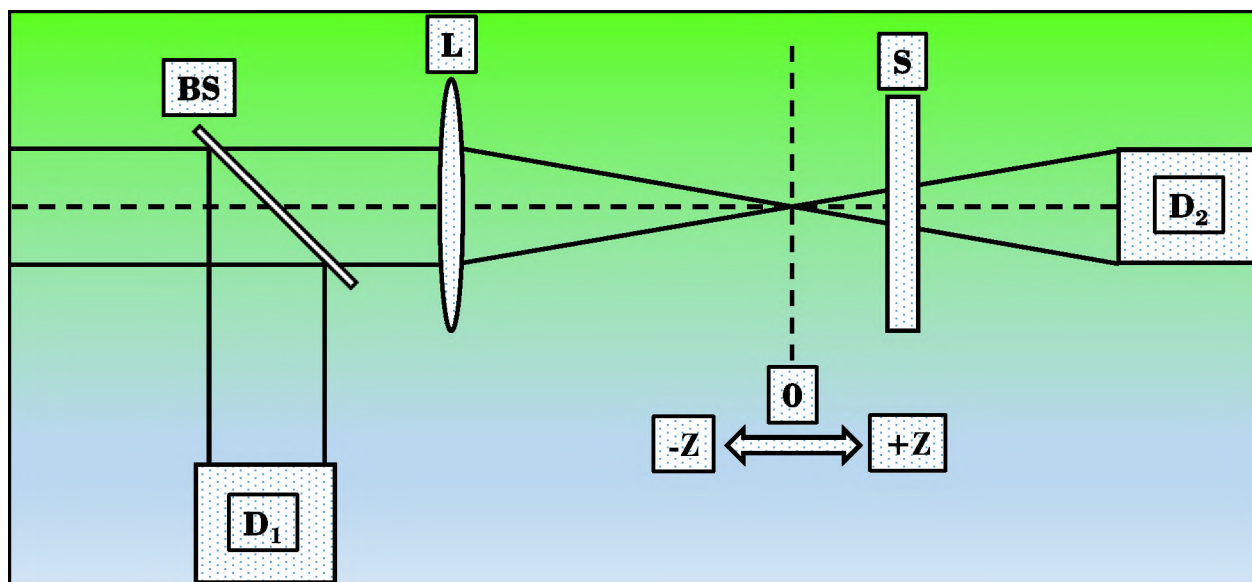


Fig. 2.2: Schematic representation of the open-aperture Z-scan setup. BS = beam splitter; L = lens; D_1 and D_2 = photodetectors; S = sample.

- ❖ Laser flash photolysis experiments were performed with light pulses produced by a Quanta-Ray Nd:YAG laser providing 400 mJ, 9 ns pulses of laser light at 10 Hz, pumping a Lambda-Physik FL3002 dye laser (Pyridin 1 dye in methanol), **Fig. 2.3**. Single pulse energy ranged from 2 to 7 mJ. The analyzing beam source was from a Thermo Oriel Xenon arc lamp, and photomultiplier tube (a Kratos Lis Projekte MLIS-X3) was used as a detector. Signals were recorded with a two-channel 300 MHz digital real time oscilloscope (Tektronix TDS 3032C); the kinetic curves were averaged over 256 laser pulses.

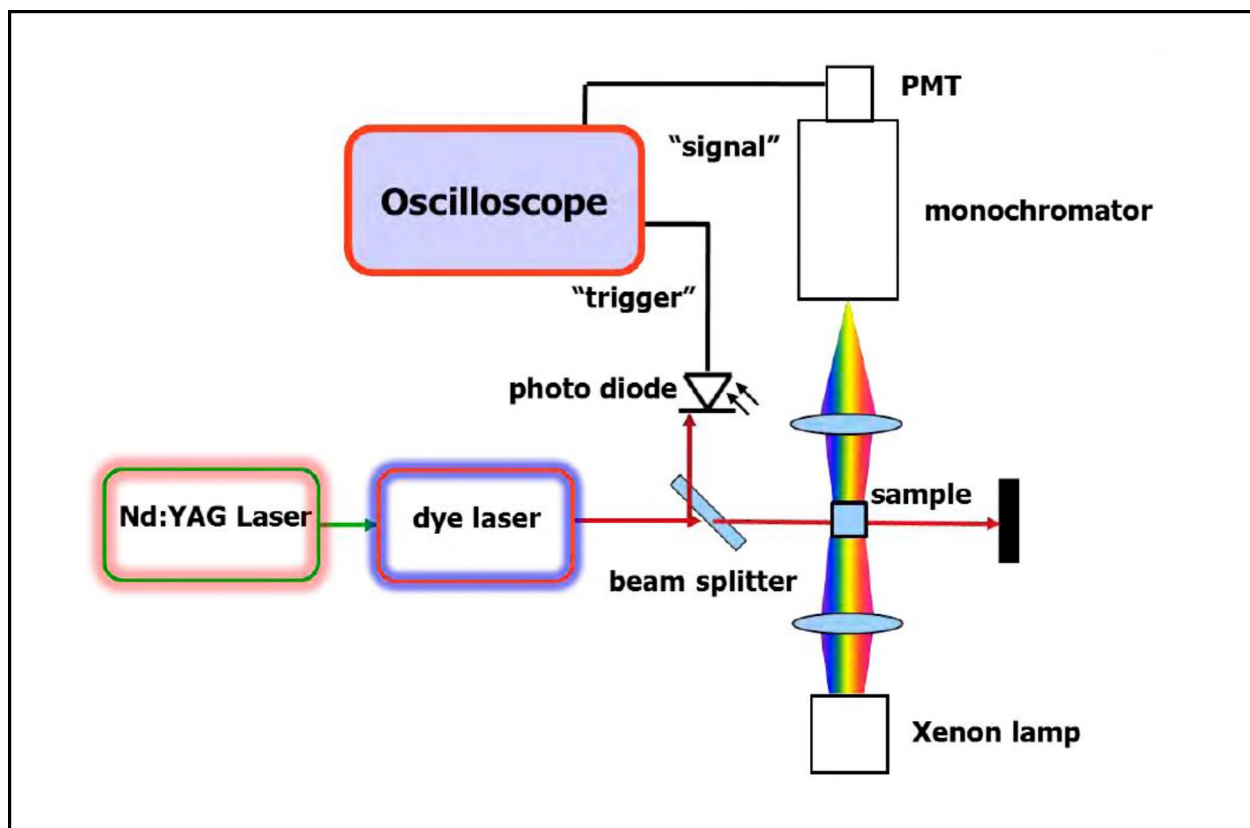


Fig. 2.3: Schematic diagram for a laser flash photolysis setup.

- ❖ Time resolved phosphorescence decay of singlet oxygen at 1270 nm was used to determine singlet oxygen quantum yield. The dynamic phosphorescence decay of singlet oxygen ($O_2(^1\Delta_g)$), was demonstrated using time resolved phosphorescence of $O_2(^1\Delta_g)$ at 1270 nm. For these studies an ultra sensitive germanium detector (Edinburgh Instruments, EI-P) combined with a 1000 nm long pass filter (Omega, RD 1000 CP) and a 1270 nm band-pass filter (Omega, C1275, BP50) (Fig. 2.4) was used to detect $O_2(^1\Delta_g)$ phosphorescence under the excitation using Quanta-Ray Nd:YAG laser providing 400 mJ, 90 ns pulses of laser light at 10 Hz pumping a Lambda-Physik FL3002 dye laser (Pyridin 1 dye in methanol), with a pulse period

of 7 ns and repetition rate of 10 Hz. The near-infrared phosphorescence of the samples were focused onto the germanium detector by a lens (Edmund, NT 48-157) with detection direction perpendicular to the excitation laser beam. The detected signals were averaged with a digital oscilloscope (Tektronics, TDS 360) to show the dynamic decay of $O_2(^1\Delta_g)$.

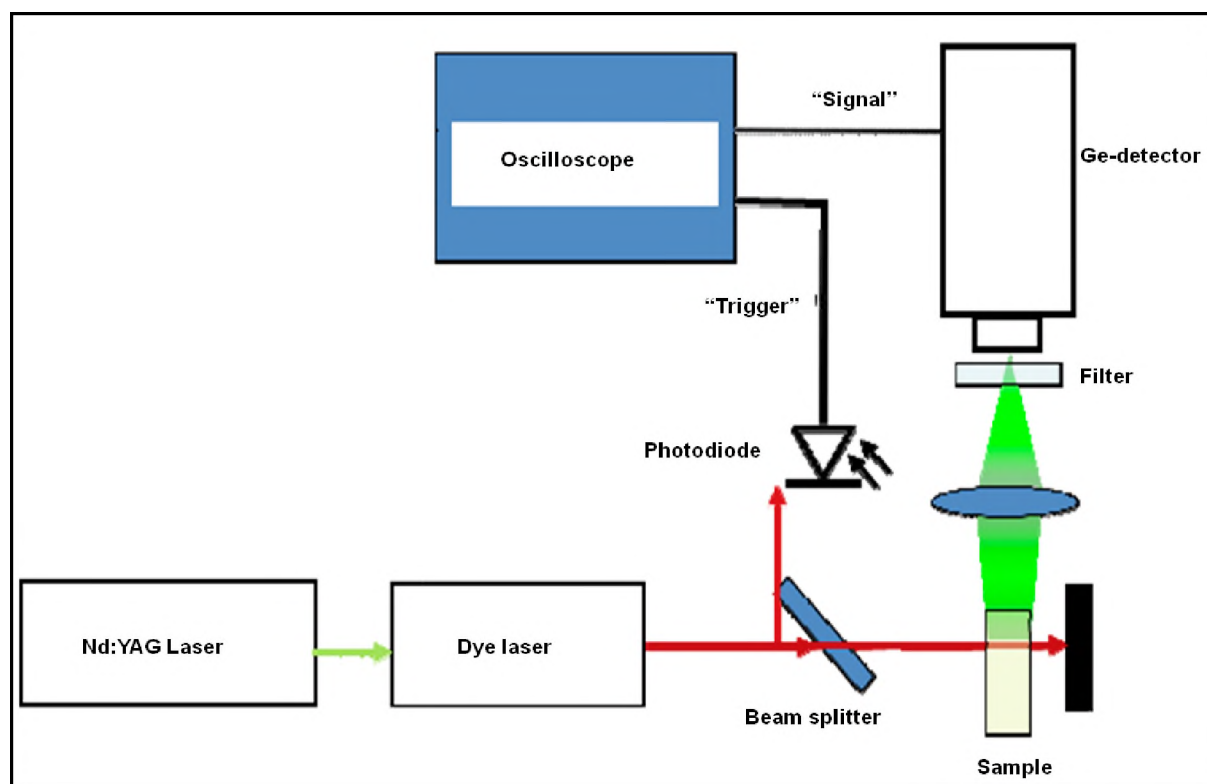


Fig. 2.4: Schematic diagram for the singlet oxygen detection setup using its phosphorescence.

- ❖ Photo-irradiations for singlet oxygen quantum yields were done using a General Electric Quartz line lamp (300 W), **Fig. 2.5**. A 600 nm glass cut off filter (Schott) and a water filter were used to filter off ultraviolet and infrared radiations respectively. An interference filter (Intor, 670 nm with a band width of 40 nm) was additionally

placed in the light path before the sample. Light intensities were measured with a POWER MAX 5100 (Molelectron Detector Inc.) power meter.

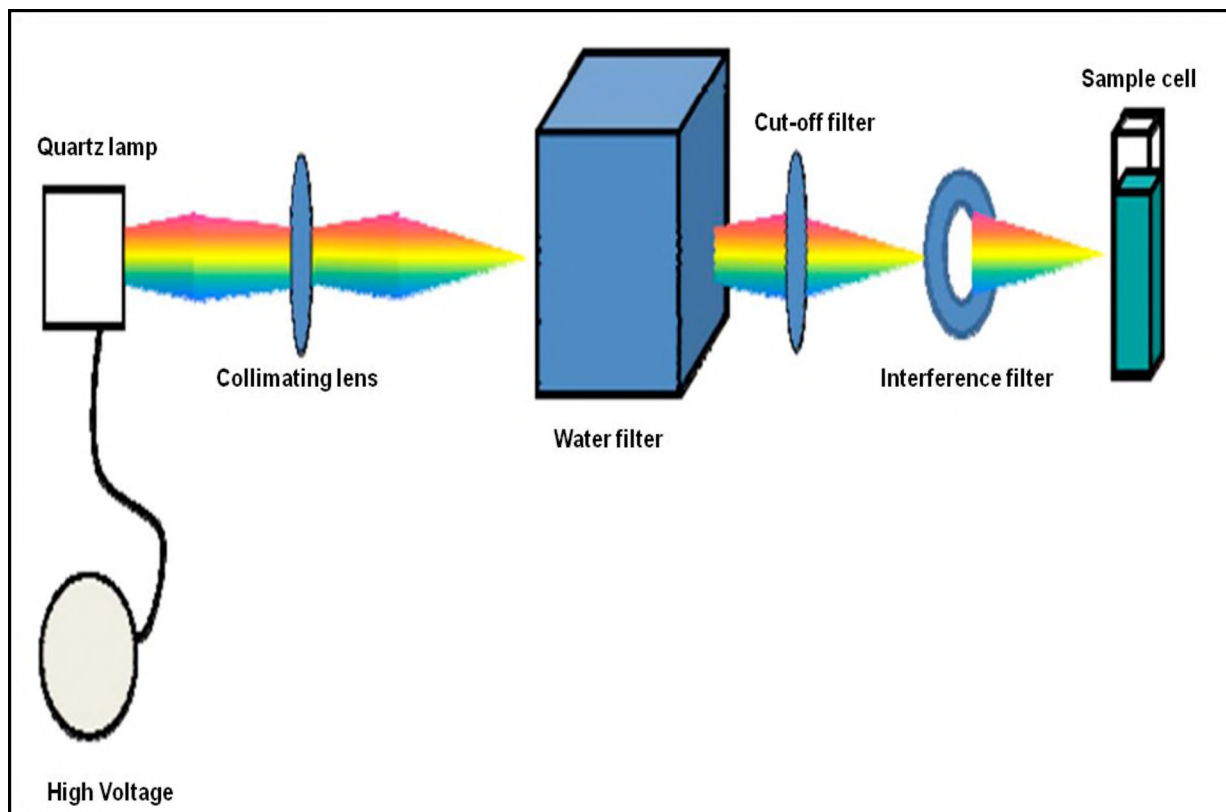


Fig. 2.5: Schematic diagram of photolysis setup.

- ❖ Electron spin resonance (ESR) spectra were recorded on a Bruker EPR 300E X-band (10 GHz) spectrometer equipped with a TM probe with a flat quartz cell. The spin Hamiltonian parameters were obtained by simulation of the spectra. The static field (2500–3486 G), the center field (3488–3500 G), the modulation amplitude (5.44–8.10 G), the time constant (10.24 ms), the conversion time (5.12 ms), the resolution (1024–2048 pts), power (2.00 mW) and the modulation frequency (100 kHz) were used as the experimental parameters at 298 K with one to five scans.

- ❖ Film thickness (~10 μm) was determined by utilization of the knife edge attachment of the Bruker D8 Discover X-ray diffraction (XRD) following removal of the films from the glass slides.

2.3 Synthesis

2.3.1 Synthesis of phthalonitriles

2.3.1.1 Synthesis of 3,4-Bis-(3,4-dicyano-phenoxy)-benzoic acid (**48**) (Scheme 3.1)

4-Nitrophthalonitrile (**40**) (2.00 g; 9.75 mmol), 3,4-dihydroxybenzoic acid (751 mg; 4.87 mmol) and DMF (25 mL) were added together in a round bottom flask (250 mL). The reaction mixture was purged with argon for 10 min before the addition of potassium carbonate (20.00 g; 144.71 mmol), followed by constant stirring under inert atmosphere at room temperature for 48 h. The product was then poured into ice water, followed by addition of concentrated hydrochloric acid. The precipitate was washed several times with water and methanol and dried at 60 $^{\circ}\text{C}$ in the oven.

Yield: 17%. IR: [KBr, ν , cm^{-1}] 776, 804, 844, 860, 881, 904, 921, 950, 961, (benzene ring) 1092, 1110, 1171, 1197, 1242, 1273, 1372, 1414, 1436, 1482, 1497 (C-O-C), 1568, 1592 (C=O), 1722, 1740 (-C=N-), 2232 ($\text{C}\equiv\text{N}$) 3033, 3078 (C-H, aromatic), 3247 (OH). ^1H NMR (DMSO- d_6): δ , ppm 13.44 (1H, s, COOH), 8.09-8.05 (2H, q, Ar-H), 7.97-7.97 (1H, d, Ar-H), 7.87-7.83 (3H, m, Ar-H), 7.50-7.45 (3H, m, Ar-H).

2.3.1.2 Synthesis of 2,4,6-tris(3-thiophthalonitrile)-s-triazine (49) (Scheme 3.2)

3-Nitrophthalonitrile (**41**) (4.40 g; 25.4 mmol) and thiocyanuric acid (1.50 g; 8.46 mmol) were added into round a bottom flask (100 mL). After 10 min of purging with argon, DMF (50 mL) was added to the mixture. The mixture was stirred for another 10 min and then potassium carbonate (3.50 g; 25.42 mmol) was added all at once before heating the mixture at 65 °C for 48 h as explained by Şen et al [103]. The reaction mixture was cooled to room temperature and then poured into ice water before slowly filtering and washing with water. The obtained product was washed four times with ethanol. The crude yellow product was dried in open air. Yield: 59%. IR: [KBr, ν , cm^{-1}] 1002, 1147, 1199, 1278, 1429, 1445 (Benzene ring), 1570, 1666, 1729 (-C=N-), 2232 ($\text{C}\equiv\text{N}$), 3075 (CH).

^1H NMR (DMSO-d_6): δ , ppm 8.14-8.12 (3H, d, Ar-H), 7.85-7.84 (3H, t, Ar-H), 7.82-7.81 (3H, d, Ar-H). ^{13}C NMR (CHCl_3): δ , ppm 113.21 (3C, s, Ar-C), 114.56 (3C, s, Ar-C), 118.61 (3C, s, Ar-C), 119.45 (6C, s, $\text{C}\equiv\text{N}$), 133.55 (3C, s, Ar-C), 133.70 (3C, s, Ar-C), 137.84 (3C, s, S-Ar-C), 138.42 (3C, s, N-C=N).

2.3.2 Synthesis of phthalocyanines

2.3.2.1 Synthesis of 2(3), 9(10), 16(17), 23(24)-(tetrapyrroline-3-yl)oxy phthalocyaninato neodymium (III) acetate (18) (Scheme 3.3)

Complex **18** was prepared as follows: Compound **42** (160 mg, 0.78 mmol), neodymium acetate hydrate (220 mg; 0.68 mmol), DBU (0.5 mL) and 1-pentanol (10 mL) were added to a round bottom flask, and the mixture was heated at reflux temperature with constant stirring for 21 h. The product obtained was centrifuged at 3000 rpm several times in THF and methanol, respectively. The pure green solid was dried in oven at 110 °C.

Yield: 23%. IR: [KBr, ν , cm^{-1}] 667, 726, 750, 814, 851, 891, 933 (Pc skeleton), 1018, 1046, 1082, 1130, 1193, 1236, 1283, 1343, 1399, 1485 (C-O-C), 1538 (C=O) 1634 (-C=N-), 3325 (OH). UV-Vis (DMSO): λ_{max} nm (log ϵ), 335 (4.21), 385 (3.94), 630 (3.86), 695 (4.45). Anal. Calc. for $\text{C}_{54}\text{H}_{31}\text{N}_{12}\text{O}_6\text{Nd}$: C, 59.60; H, 2.87; N, 15.45. Found: C, 58.92; H, 2.32; N, 14.93%. ^1H NMR (DMSO- d_6): δ , ppm 9.81 (2H, s, Ar-H), 9.50 (3H, m, Ar-H), 9.17-9.15 (2H, m, Ar-H), 8.84-8.76 (2H, m, Ar-H), 8.61-8.50 (5H, m, Ar-H), 8.35-8.29 (3H, m, Ar-H), 8.03-8.00 (1H, m, Ar-H), 7.89-7.86 (2H, m, Ar-H), 7.39-7.28 (4H, m, Ar-H), 7.08-6.99 (4H, m, Ar-H), 1.43 (3H, m, CH_3). MS (MALDI-TOF): (m/z): Calc. 1087 amu. Found: 1091 amu [M+4H+].

2.3.2.2 Synthesis of bis{23-(3,4-di-yloxybenzoic acid) (2(3), 9(10), 16(17), 23(24)-(hexakis-pyridin-3-yloxy phthalocyaninato)} dineodymium (III) acetate (19) (Scheme 3.4)

Complex **19** was synthesized by refluxing compounds (**42**) (400 mg; 1.95 mmol) and **48** (132 mg; 0.325 mmol) in 1-pentanol (15 mL) and DBU (0.5 mL) in the presence of neodymium acetate hydrate (229 mg; 0.713 mmol) for 21 h in open air. The green solution which formed was cooled to room temperature and centrifuged several times at 3000 rpm in THF and methanol to obtain a green solid. After drying at 100 °C, the product was subjected to Soxhlet extraction using THF as a solvent. The Soxhlet extraction vessel was cooled to room temperature to obtain a green solid which was dried in open air. Further purification was achieved by subjecting the green product to a reverse phase column first using THF and DMSO solvent system (4:1; *v/v*), followed by DMSO containing TFA (5 drops at a time). Ice water was added to the obtained green solution and neutralized with ammonia to get a green precipitate which was washed in water and methanol respectively. The product was dried at 110 °C.

Yield: 60%. IR: [KBr, *v*, cm⁻¹] 747, 810, 837, 872, 888, 900, 953, 974 (Pc skeleton), 1038, 1080, 1123, 1213, 1236, 1269, 1287, 1325, 1374, 1388, 1481, 1553, 1573 (C-O-C), 1655 (C=O), 1712, 1773 (-C=N-), 2850, 2924 (C-H, aromatic), 3326 (OH). UV-Vis (DMSO): λ_{max} nm (log ϵ) 336 (4.66), 564 (3.82), 656 (4.60). Anal. Calc. for C₁₀₅H₅₈N₂₂O₁₂Nd₂. C, 58.93; H, 2.73; N, 14.45. Found: C, 59.35; H, 3.40; N, 15.12%. ¹H NMR (DMSO-d₆): δ , ppm 8.21 (1H, s, COOH), 8.03 (3H, s, Ar-H), 7.90 (16H, s, Ar-H), 7.66-6.64 (16H, m, Ar-

H), 7.58-7.56 (16H, m, Ar-H), 1.36-1.19 (6H, m, methyl). MS (MALDI-TOF): (m/z):
Calc. 2140 amu. Found: 2144 amu [M+4H⁺].

2.3.2.3 *Synthesis of 2,4,6-tris[3-thio-9,10,16,17,23,24-hexa(4-tertbutylphenoxy) phthalocyaninato ytterbium (III) chloride]-s-triazin (20) (Scheme 3.2)*

Complex **20** was synthesized as follows: compound **43** (687.7 mg; 1.62 mmol), compound **49** (100 mg; 0.180 mmol) and ytterbium (III) chloride hexahydrate (216.2 mg; 0.558 mmol) were added into a round bottom flask. After the addition of DBU (5 drops) and 1-pentanol (15 mL), the reaction mixture was heated at reflux in open air for 21 h and then cooled to room temperature. The obtained green product was subjected to silica column chromatography, using chloroform and hexane solvent mixture (*v/v*; 1:1) as an eluent to give the first green layer which was not the desired product. The second green layer (the desired product) was obtained by further eluting with ethanol and chloroform solvent mixture (*v/v*; 1:3). Yield: 77%. IR: [KBr, *v*, cm⁻¹] 723, 750, 769, 829, 890, 989, 1013 (Pc skeleton), 1064, 1083, 1172, 1207, 1240, 1290, 1322, 1363, 1389, 1430, 1462, 1487, 1506 (C-O-C), 1599, 1728 (-C=N-), 2871, 2926, 2952 (CH₃ (t-Butyl) and C-H (aromatic)), UV-Vis (DMF): λ_{max} nm (log ε), 345 (4.03), 647 (4.78), 680 (4.07). Anal. Calc. for C₂₇₉H₂₆₁N₂₇O₁₈S₃Yb₃Cl₃: C, 66.99; H, 5.26; N, 7.56, S, 1.92. Found: C, 66.01; H, 5.35; N, 7.60; S, 1.52%. ¹H NMR (DMSO-d₆): δ, 7.67-7.29 (36H, m, Ar-H), 7.24-6.94 (33H, m, Ar-H), 6.92-6.70 (21H, m, Ar-H), 6.69-6.50 (9H, m, Ar-H), 1.43-1.24 (162H, m, t-Butyl). MALDI-TOF MS, m/z: Expected: 5001 [M]⁺; found: 5002 [M+H]⁺

2.3.2.4 Synthesis of 2,4,6-tris[3-thio-9,10,16,17,23,24-hexa(4-tertbutylphenoxy) phthalocyaninato lutetium (III) chloride]-s-triazin (21) (Scheme 3.2)

Complex **21** was prepared and purified as explained for **20**, using compound (**43**) (150 mg; 0.35 mmol), compound **49** (21.8 mg; 0.039 mmol) and lutetium (III) chloride (34.3 mg; 0.122 mmol). Yield: 69%. IR: [KBr, ν , cm^{-1}] 718, 747, 831, 890, 986, 1013 (Pc skeleton), 1083, 1082, 1172, 1206, 1243, 1290, 1363, 1391, 1434, 1484, 1504 (C-O-C), 1623, 1712, 1729 (-C=N-), 2866, 2930 (CH_3 (t-Butyl) and C-H (aromatic)). UV-Vis (DMF): λ_{max} nm ($\log \epsilon$), 332 (5.00), 633 (4.74), 677 (4.63). Anal. Calc. for $\text{C}_{279}\text{H}_{261}\text{N}_{27}\text{O}_{18}\text{S}_3\text{Lu}_3\text{Cl}_3$: C, 66.92; H, 5.25; N, 7.49; S, 1.90. Found: C, 67.07; H, 5.59; N, 7.29; S, 1.53%. ^1H NMR (DMSO- d_6): δ , ppm 7.44-7.32 (54H, m, Ar-H), 7.01-6.97 (45H, m, Ar-H), 1.43 (162H, m, t-Butyl). MALDI-TOF MS, m/z: Expected: 5006 [M] $^+$, found: 5006 [M] $^+$.

2.3.2.5 Synthesis of bis-{1(4), 8(11), 15(18), 22(25)-(tetrapyrroline-2-yl)oxy phthalocyaninato} ytterbium (III) (22) (Scheme 3.5)

Compound **42** (400 mg, 1.95 mmol) and ytterbium (III) chloride hexahydrate (94.4mg, 0.244 mmol) were added into a round bottom flask and heated for a three minutes. DBU (2 mL) and 1-pentanol (15 mL) were added to the reaction mixture, followed by heating under reflux for 21 h to obtain a green product of **22**. The product obtained was transferred to a centrifuge tube, followed by addition of THF. After centrifugation at 3500 rpm for several minutes, the supernatant obtained was evaporated under reduced pressure. The product was further purified with column chromatography packed with

silica and C18 reverse phase column using DMF and THF (*v/v*; 1:2) solvent mixture as an eluent, yielding complex **22**. Yield: 23%. IR: [KBr, *v*, cm⁻¹] 809, 825, 840, 825, 892, 1006 (Pc skeleton), 1046, 1072, 1111, 1136, 1158, 1225, 1244, 1286, 1316 (Pc•- IR marker), 1496, 1530 (C-O-C), 1574, 1658, 1728 (-C=N-), 2856, 2924, 3068 (C-H, aromatic), 3291, 3397 (OH). UV-Vis (DMSO): λ_{\max} nm (log ϵ), 395 (4.23), 612 (4.03), 675 (4.73). Anal. Calc. for C₁₀₄H₅₆N₂₄O₈Yb: C, 64.30; H, 2.91; N, 17.30. Found: C, 63.28; H, 3.96; N, 16.53%. ¹H NMR (DMSO-d₆): δ , ppm 9.94 (1H, s, Pc-H), 8.16-7.53 (13H, m, Pc-H), 7.07-6.82 (10H, m, Pyr-H), 6.48 (1H, s, Pyr-H), 6.33 (1H, s, Pyr-H), 5.35 (1H, s, Pyr-H), 3.75-3.22 (29H, m, Pyr-H). MS (MALDI-TOF): (*m/z*): Calc. 1942 amu. Found: 1949 amu [M+7H⁺].

2.3.2.6 *Synthesis of bis-{1(4), 8(11), 15(18), 22(25)-(tetrapyrroline-4-yl)oxy phthalocyaninato} ytterbium (III) (23) (Scheme 3.6)*

Complex **23** was prepared as described for complex **22** except that compound **44** (200 mg, 0.975 mmol) and ytterbium (III) chloride hexahydrate (47.2 mg, 0.112 mmol) were employed. Once obtained, the complex was subjected to centrifugation in acetone and DCM (1:1). After drying the supernatant, the Soxhlet method was employed to further purify the complex, using acetone as a solvent. The product was then centrifuged in a mixture of ethanol and THF (2:3), with the supernatant giving a green product on drying in open air. The product was further purified with column chromatography and C18 reverse phase column as described for **22** above to give complex **23**.

Yield: 57%. IR: [KBr, ν , cm^{-1}] 663, 680, 750, 811, 847, 892, 974 (Pc skeleton), 1044, 1080, 1127, 1189, 1264, 1322 (Pc•- IR marker), 1403, 1482, (C-O-C), 1562, 1633 (-C=N-), 2924, 3058 (C-H, aromatic), 3230 (OH). UV-Vis (DMSO): λ_{max} nm ($\log \epsilon$), 655 (3.98), 694 (4.21). Anal. Calc. for $\text{C}_{104}\text{H}_{56}\text{N}_{24}\text{O}_8\text{Yb}$: C, 64.30; H, 2.91; N, 17.30. Found: C, 63.78; H, 4.04; N, 16.91%. ^1H NMR (DMSO- d_6): δ , ppm 8.23-8.22 (4H, s, Pyr), 7.92 (12H, s, Pyr), 7.81-7.71 (3H, m, Pc), 7.63-7.56 (11H, m, Pc), 7.52-7.49 (6H, m, Pc), 7.39-7.38 (4H, d, Pc), 6.45-6.38 (8H, m, Pyr), 6.28-6.18 (8H, m, Pyr). MS (MALDI-TOF): (m/z): Calc. 1942 amu. Found: 1945 amu [$\text{M}+3\text{H}^+$].

2.3.2.7 *Synthesis of bis-{1(4), 8(11), 15(18), 22(25)-tetra(4-tert-butylphenoxy) phthalocyaninato} ytterbium (III) (24) (Scheme 3.7)*

Complex **46** (100 mg, 0.090 mmol) and ytterbium chloride (23.00 mg; 0.082 mmol) were transferred into a round bottom flask. 1-Pentanol (15 mL) and DBU (0.5 mL) were added into the reaction vessel. The reaction mixture was heated at reflux temperature for 21 h and then cooled down to room temperature. The green product was eluted as a second band from a column chromatography packed with silica, using chloroform and hexane (v/v ; 3:2) as a solvent mixture, and dried in vacuum. Yield: 13%. IR: [KBr, ν , cm^{-1}] 747, 776, 802, 826, 878, 933, 958, 969, 999, 1011, 1044 (Pc skeleton), 1072, 1108, 1173, 1247, 1290, (C-O-C), 1318 (Pc•- IR marker), 1360, 1391, 1411, 1477, 1504, 1588, 1729 (benzene, pyrrole, isoindole and aza), 2866, 2927, 2954 (C-H, aromatic or CH_3 , t-butyl). UV-Vis (DMF): λ_{max} nm ($\log \epsilon$), 324 (4.78), 631 (4.54), 701 (4.96). Anal. Calc. for $\text{C}_{144}\text{H}_{128}\text{N}_{16}\text{O}_8\text{Yb}$: C, 72.56; H,

5.41; N, 9.40. Found: C, 72.27; H, 5.15; N, 9.15%. $^1\text{H NMR}$ (CDCl_3): δ , ppm: 6.86-6.85 (28H, m, Ar), 6.29-6.28 (28H, m, Ar), 1.72-1.58 (72H, m, t-Butyl). MS (MALDI-TOF): (m/z): Calc. 2384 amu. Found: 2390 amu [$\text{M}+6\text{H}^+$].

2.3.2.8 *Synthesis of bis-{2(3), 9(10), 16(17), 23(24)-(tetrapyrroline-4-yl)oxy phthalocyaninato} ytterbium (III) (25) (Scheme 3.8)*

Compound **45** (215.7 mg, 0.975 mmol) and ytterbium chloride hexahydrate (47.3 mg; 0.122 mmol) were added to a round bottom flask. DBU (0.5 mL) and 1-pentanol (15 mL) were added to the reaction mixture, followed by heating under reflux for 21 h in open air to obtain a green product of **25**. The product obtained was transferred to a centrifuge tube, followed by addition of THF. After centrifugation at 3500 rpm for several minutes, supernatant obtained was evaporated under reduced pressure, yielding a green product which was subjected to a column packed with silica and eluted with a mixture of DMF and THF (*v/v*; 2:3). After evaporation, the product was subjected to a reverse phase column to give complex **25** after eluting with a mixture of DMF and THF (*v/v*; 3:1).

Yield: 19%. IR: [KBr , ν , cm^{-1}] 663, 680, 750, 811, 847, 892, 974 (Pc skeleton), 1044, 1080, 1127, 1189, 1264, 1322 (Pc•- IR marker), 1403, 1482, (C-O-C), 1562, 1633 (-C=N-), 2924, 3058 (C-H, aromatic), 3230 (OH). UV-Vis (DMSO): λ_{max} nm ($\log \epsilon$), 354 (4.79), 621 (4.40), 687 (4.99). Anal. Calc. for $\text{C}_{104}\text{H}_{56}\text{N}_{24}\text{O}_8\text{Yb}$: C, 64.30; H, 2.91; N, 17.30. Found: C, 63.71; H, 3.13; N, 17.22%. $^1\text{H NMR}$ (DMSO-d_6): δ , ppm 8.47-7.69 (39H, m, Ar-H), 6.47-6.32 (17H, d, Ar-H). MS (MALDI-TOF): (m/z): Calc. 1943 amu. Found: 1947 amu [$\text{M}+4\text{H}^+$].

2.3.2.9 Synthesis of bis-{2(3), 9(10), 16(17), 23(24)-(tetrapyrroline-4-ylidene phthalocyaninato)} lanthanum (III) (26) (Scheme 3.8)

Complex **26** was synthesized and purified as explained for **25**, except that lanthanum (III) chloride (29.89 mg; 0.122 mmol) was employed in the place of ytterbium (II) chloride in the reaction. Yield: 26%. IR: [KBr, ν , cm^{-1}] 809, 825, 840, 825, 892, 1006 (Pc skeleton), 1046, 1072, 1111, 1136, 1158, 1225, 1244, 1286, 1316 (Pc•- IR marker), 1496, 1530 (C-O-C), 1574, 1658, 1728 (-C=N-), 2856, 2924, 3068 (C-H, aromatic), 3291, 3397 (OH). UV-Vis (DMSO): λ_{max} nm (log ϵ) 400 (4.36), 618 (4.46), 683 (4.78). Anal. Calc. for $\text{C}_{104}\text{H}_{56}\text{N}_{24}\text{O}_8\text{La}\cdot\text{H}_2\text{O}$: C, 64.83; H, 3.03; N, 17.45. Found: C, 64.13; H, 2.73; N, 16.69%. ^1H NMR (DMSO- d_6): δ , ppm 8.72-8.70 (2H, d, Ar-H), 8.19-7.56 (41H, m, Ar-H), 7.25-7.16 (2H, m, Ar-H), 6.79-6.77 (2H, d, Ar-H), 6.55 (1H, s, Ar-H), 6.30-6.14 (8H, m, Ar-H). MS (MALDI-TOF): (m/z): Calc. 1907 amu. Found: 1912 amu [M+5H $^+$].

2.3.1.10 Synthesis of bis-{2,3,9,10,16,10,16,17,23,24-octa(4-tertbutylphenoxy) phthalocyaninato} cerium(III) (27) (Scheme 3.9)

A mixture of compound **43** (150 mg, 0.35 mmol) and cerium (III) chloride (7.75 mg, 0.044 mmol) was added into a round bottom flask. After addition of DBU (2 mL) and 1-pentanol (15 mL), the reaction mixture was heated at reflux temperature for 21 h in open air to obtain complex **27** as a green product. The crude product was purified by silica gel column chromatography using chloroform and distilled hexane (v/v ; 4:1) as an eluent.

Yield: 17%. IR: [KBr, ν , cm^{-1}] 689, 724, 743, 782, 827, 854, 866, 890, 990, 1013 (Pc skeleton), 1063, 1109, 1170, 1205, 1240, 1308, 1364, 1385, 1433, 1487, 1506 (C-O-C), 1599 (-C=N-), 2868, 2927, 2956 (C-H, aromatic). UV-Vis (CHCl_3): λ_{max} nm ($\log \epsilon$), 352 (4.42), 652 (4.42), 663 (4.40), 702 (4.20). Anal. Calc. for $\text{C}_{224}\text{H}_{224}\text{N}_{16}\text{O}_{16}\text{Ce}$: C, 76.08; H, 6.38; N, 6.34. Found: C, 76.21; H, 6.16; N, 6.55%. ^1H NMR (CDCl_3): δ , ppm 8.99-8.85 (15H, m, Ar-H), 8.34 (15H, m, Ar-H), 7.75-7.65 (15H, m, Ar-H), 7.60-7.28 (35H, m, Ar-H), 1.50-1.43 (144H, m, t-Butyl). MS (MALDI-TOF): (m/z): Calc. 3536 amu. Found: 3537 amu [$\text{M}+\text{H}^+$].

2.3.2.11 Synthesis of bis-{2,3,9,10,16,10,16,17,23,24-octa(4 *tert*-butylphenoxy) phthalocyaninato} lutetium (III) (28) (Scheme 3.9)

Complex **28** was prepared as explained for complex **27**, except that compound **43** (300 mg, 0.71 mmol) and lutetium (III) chloride (24.9 mg, 0.088 mmol) were employed. The crude green product was purified by silica gel column chromatography using THF as an eluent.

Yield: 50%. IR: [KBr, ν , cm^{-1}] 830, 886, 985, 1013 (Pc skeleton), 1083, 1098, 1171, 1287 (Pc•-), 1359, 1390, 1429, 1505 (C-O-C), 1601, 1728 (-C=N-), 2955, 3090 (C-H, aromatic). UV-Vis (DMSO): λ_{max} nm ($\log \epsilon$), 635 (4.40), 676 (4.77). Anal. Calc. for $\text{C}_{224}\text{H}_{224}\text{N}_{16}\text{O}_{16}\text{Lu}\cdot 3\text{H}_2\text{O}$: C, 74.21; H, 6.41; N, 6.18. Found: C, 73.91; H, 6.92; N, 7.47%. ^1H NMR (DMSO-d_6): δ , ppm 8.42 (4H, s, Pc), 7.94-7.89 (4, m, Pc), 7.69-7.63 (8H, m, Pc), 7.45-7.41 (32H, m, Ar), 7.08-7.6.99 (32H, m, Ar), 1.31-1.25 (144H, m, t-Butyl).

2.3.2.12 *Synthesis of bis-{2,3,9,10,16,10,16,17,23,24-octa(4-tertbutylphenoxy) phthalocyaninato} gadolinium (III) (29) (Scheme 3.10)*

Complex **47** (90.00 mg; 52.93 μmol) and gadolinium (III) chloride (6.98 mg; 26.48 μmol) were added together into a round bottom flask. DBU (2 mL) and 1-pentanol (10 mL) were added, followed by heating reaction mixture at reflux temperature with constant stirring for 21 h in open air to obtain complex **29** as a blue product. The purification of the crude product was achieved as reported for complex **27** above.

Yield: 14%. IR: [KBr, ν , cm^{-1}] 685, 723, 750, 781, 826, 852, 865, 892, 990, 1012 (Pc skeleton), 1067, 1095, 1108, 1170, 1205, 1235 (C-O-C), 1317 (Pc⁻), 1363, 1380, 1424, 1444, 1482, 1506 (C-O-C), 1598 (-C=N-), 2861, 2927, 2954 (C-H). UV-Vis (CHCl_3): λ_{max} nm (log ϵ), 333 (5.43), 356 (5.34), 483 (4.69), 615 (4.93), 681 (5.53). Anal. Calc. for $\text{C}_{224}\text{H}_{224}\text{N}_{16}\text{O}_{16}\text{Gd}$: C, 75.71; H, 6.35; N, 6.31 %. Found: C, 75.43; H, 6.42; N, 3.01%. ^1H NMR (CDCl_3): δ , ppm 12.42 (66H, m, Ar-H), 8.67 (12H, m, Ar-H), 7.21 (1H, s, Ar-H), 7.11 (1H, s, Ar-H), 1.54-1.26 (144H, m, t-Butyl). MS (MALDI-TOF): (m/z): Calc. 3554 amu. Found: 3556 amu [$\text{M}+2\text{H}^+$].

2.3.2.13 *Synthesis of tris-{1(4), 8(11), 15(18), 22(25)-tetra(4-tert-butylphenoxy) phthalocyaninato} dineodymium (III) (30) (Scheme 3.11)*

Complex **46** (50.6 mg, 0.0457 mmol) and neodymium acetate hydrate (9.89 mg; 0.0305 mmol) were transferred into a round bottom flask. 1-Pentanol (15 mL) and DBU (0.5 mL) were added into the reaction vessel. The reaction mixture was heated at reflux for 8 h and then cooled down to room temperature. The green product was eluted as a second band

from a column chromatography packed with silica, using chloroform and hexane (*v/v*; 1:1) as a solvent mixture, and dried in vacuum. Yield: 71%. IR: [KBr, *v*, cm^{-1}] 745, 826, 966, 996, 1013, 1041 (Pc skeleton), 1073, 1108, 1173, 1214, 1247, 1290, 1327, 1363, 1391, 1411, 1478, 1506 (C-O-C), 1584, 1646, 1731 (-C=N-), 2866, 2956 (C-H, aromatic or CH₃, t-butyl). UV-Vis (DMF): λ_{max} nm (log ϵ), 468 (3.67), 662 (4.47). Anal. Calc. for C₂₁₆H₁₉₂N₂₄O₁₂Nd₂: C, 71.97; H, 5.37; N, 9.33. Found: C, 71.88; H, 6.08; N, 9.39%. ¹H NMR (CDCl₃): δ , ppm: 7.52-7.32 (45H, m, Ar), 7.06-6.92 (39H, m, Ar), 0.96-0.82 (108H, m, t-Butyl). MS (MALDI-TOF): (*m/z*): Calc. 3604 amu. Found: 3608 amu [M+4H⁺].

2.3.2.14 *Synthesis of tris-{2,3,9,10,16,10,16,17,23,24-octa(4-tertbutylphenoxy)phthalocyaninato} cerium(III) (31) (Scheme 3.12)*

Complex **47** (90.00 mg; 52.93 μmol) and cerium (III) chloride (9.78 mg; 39.70 μmol) were added together into a round bottom flask. DBU (2 mL) and 1-pentanol (10 mL) were added, followed by heating reaction mixture at reflux temperature with constant stirring for 21 h in open air to obtain complex **31** as a blue product. The crude product was subjected to silica gel column chromatography ethanol and distilled hexane (*v/v*; 4:1) as eluent. The open air dried product was further purified using chloroform and distilled hexane (*v/v*; 4:1) as an eluent in silica column chromatography and dried in vacuum.

Yield: 13%. IR: [KBr, *v*, cm^{-1}] 690, 724, 745, 781, 827, 854, 890, 990, 985, 1012 (Pc skeleton), 1063, 1109, 1170, 1204, 1240, 1307, 1348, 1364, 1385, 1433, 1487, 1506 (C-O-C), 1598 (-C=N-), 2867, 2921, 2955 (C-H, aromatic). UV-Vis (CHCl₃): λ_{max} nm (log ϵ), 352 (5.84), 653 (5.87),

698 (5.51). Anal. Calc. for $C_{336}H_{336}N_{24}O_{24}Ce_2$: C, 75.09%; H, 6.30; N, 6.25. Found: C, 74.83; H, 6.19; N, 6.95 %. 1H NMR ($CDCl_3$): δ , ppm 9.15-8.80 (22H, m, Ar-H), 8.45-8.23 (23H, m, Ar-H), 7.66-7.61 (24H, m, Ar-H), 7.60-7.30 (51H, m, Ar-H), 1.49-1.42 (216H, m, t-Butyl). MS (MALDI-TOF): (m/z): Calc. 5375 amu. Found: 5375 amu [M^+].

2.4 Functionalization of nanomaterials

2.4.1 Functionalization of MWCNTs with diaminomaleonitrile to form NH-MWCNTs (Scheme 3.13)

MWCNTs were functionalized with acid as reported before for SWCNTs [279]. Acid functionalized MWCNTs were linked to diaminomaleonitrile for further attachment to complex **19** as follows: acid functionalized MWCNTs (50 mg) were transferred into a clean vial containing DMSO (15 mL). DCC (70 mg; 0.34 mmol) was added to the mixture and stirred in an airtight vial at room temperature for 24 h to activate the carboxyl groups, followed by addition of diaminomaleonitrile (70 mg; 0.65 mmol) to obtain diaminomaleonitrile functionalized MWCNT (represented as NH-MWCNTs) whose purification was achieved by centrifugation at 3000 rpm in methanol and then ethyl acetate and drying at 110 °C in the oven. IR: [KBr, ν , cm^{-1}] 3783 (NH).

2.4.2 Graphene oxide nanosheets

2.4.2.1 Reduction of GONS to form rGONS (Scheme 3.14) and their functionalization with diaminomaleonitrile to form NH-rGONS (Scheme 3.15)

Following literature methods [233] graphene oxide nanosheets (GONS) were reduced as follows (Scheme 3.14): 1 g of GONS were dispersed in 100 ml Millipore water through ultrasonication. NaBH_4 (0.57 g, 15 mmol) was added and the mixture stirred for 3 h at 70 °C to reduce the GONS. The black solid product was obtained by filtration over a fritted glass funnel, washed with copious amounts of water (5 x 50 ml), and dried in an oven at 70 °C. The resulting sample was further treated with 98% H_2SO_4 and is designated as rGONS [233].

rGONS were linked to diaminomaleonitrile to form NH-rGONS as explained below for the formation of NH-GONS. IR: [KBr, ν , cm^{-1}] 1636, 1578 (amide), Scheme 3.15.

2.4.2.2 Functionalization of GONS with diaminomaleonitrile to give NH-GONS (Scheme 3.15)

GONS (which contain COOH in addition to other oxygen containing groups) were linked to diaminomaleonitrile for further attachment to complex **19** as follows: acid functionalized GONS (50 mg) were transferred into a clean vial containing DMSO (15 mL). DCC (70 mg; 0.34 mmol) was added to the mixture and stirred in an airtight vial at room temperature for 24 h to activate the carboxyl groups, followed by addition of diaminomaleonitrile (70 mg; 0.65 mmol) to obtain diaminomaleonitrile functionalized

GONS (NH-GONS) whose purification was achieved by centrifugation at 3000 rpm in methanol and then ethyl acetate and drying at 110 °C in the oven. IR: [KBr, ν , cm^{-1}] 1623, 1569 (Amide), 3323 (NH).

2.5 Preparation of conjugates

2.5.1 Coordination of phthalocyanines with ZnO NPs

2.5.1.1 Covalent linking of complex 18 to ZnO NPs (Scheme 3.16)

Complex **18** (20 mg; 18.4 μmol) and ZnO NPs (20 mg) were added into a round bottom flask containing ethanol (10 mL) and *p*-TSA (20 mg; 0.12 mmol) and stirred at 60 °C for 24 h. The product was centrifuged several times at 3000 rpm in methanol and water solvent mixture (4:1; *v/v*) and ethyl acetate and dried in open air to obtain **18-ZnO NPs** (Scheme 3.16). IR: [KBr, ν , cm^{-1}] 1548 (C-N).

2.5.1.2 Covalent linking of complex 19 to ZnO NPs (Schemes 3.17 and 3.18)

Complex **19** was linked to ZnO NPs in two ways to form **19-ZnO NPs_A** (Scheme 3.17) and **19-ZnO NPs_B** (Scheme 3.18) as follows:

Method (a): Complex **19** (20 mg; 9.34 μmol) was dissolved in DMSO (10 ml) in a vial. DCC (30 mg; mmol) and TFA (5 drops) were added to the solution of complex **19** and constantly stirred in a sealed vial for 24 h to activate the carboxyl moiety. ZnO NPs (20 mg) was added to the carboxyl-activated solution of **19**. After sealing the reaction vessel,

the reaction mixture was stirred for another 24 h after which ice water and ammonia solution (25%) were added and followed by centrifugation at 3000 rpm. The formed solid was further centrifuged in methanol and ethyl acetate. On drying at 110 °C, **19-ZnO NPs_A** (Scheme 3.17) was obtained. IR: [KBr, ν , cm^{-1}] 1626 (amide), 3324 (NH).

Method (b): **19-ZnO NPs_B** (Scheme 3.18) was prepared as explained for **18-ZnO NPs**, except that complex **19** (20 mg; 9.34 μmol) and ZnO NPs (20 mg) were employed in the reaction. IR: [KBr, ν , cm^{-1}] 1704 (C-N).

2.5.2 Coordination of complex 19 to NH-GONS or NH-rGONS (Schemes 3.19)

Complex **19** (20 mg; 9.34 μmol) was dissolved in DMSO (10 ml) in a vial. DCC (30 mg; 0.15 mmol) and TFA (5 drops) were added into the solution of complex **19** and the mixture was constantly stirred in a sealed vial for 24 h to activate the carboxyl moiety. NH-GONS or NH-rGONS were separately added to the carboxyl-activated solution of **19**. After sealing the reaction vessel, the reaction mixture was stirred for another 24 h after which ice water and ammonia solution (25%) were added and followed by centrifugation at 3000 rpm. The formed solid was further centrifuged in ice water, methanol and ethyl acetate, respectively. On drying at 110 °C, **19-NH-GONS** or **19-NH-rGONS**, respectively, were obtained. **19-NH-GONS**; IR: [KBr, ν , cm^{-1}] 1563, 1536 (amide), 3696 (NH). **19-NH-rGONS**; IR: [KBr, ν , cm^{-1}] 1656, 1533 (amide), 3697 (NH).

2.5.3 Coordination of complex 19 to NH-MWCNTs to form 19-NH-MWCNTs (Scheme 3.20)

19-NH-MWCNTs was prepared as explained for 19-NH-GONS or 19-NH-rGONS, except that NH-MWCNTs (20 mg) were used in the place of NH-GONS or NH-rGONS in the reaction.

2.6 Preparation of thin films (TFs)

Different polymers were employed for different complexes to match solubilities as explained below.

2.6.1 Using poly(bisphenol A carbonate) (PBC) – complexes 20 and 21

Thin films were prepared by adding poly(bisphenol A carbonate) (110 mg) and complex **20** or **21** (~ 2.48 mg; $\sim 5 \times 10^{-7}$ mol) into a vial containing DCM (1.5 mL). The mixture was sonicated for fifteen minutes to dissolve the polymer and the complexes. Three drops from the mixture were then placed on a glass substrate placed in a 100 mL beaker. The solvent was allowed to evaporate at room temperature. The beaker was then covered with aluminum foil for thirty minutes to allow for the uniform drying of thin films. The TFs prepared from complexes **20** and **21** are presented as **20-TF** and **21-TF** respectively.

2.6.2 Using poly (methyl methacrylate) (PMMA) – complexes 23, 25 and 26

PMMA (200 mg) was added to DMF (2.5 mL) and the mixture stirred at room temperature in an airtight vial. Each of the LnPc₂ complexes (**23**, **25** or **26**; 1.65 mg each) (used as

examples) was transferred into a well dissolved PMMA solution and stirred for another 24 h. The mixture was then transferred onto a clean thin glass slide and dried in the oven at 110 °C. The thin films prepared from complexes **23**, **25** or **26** are presented as **23-TF**, **25-TF** and **26-TF**, respectively.

2.6.3 Using poly (acrylic acid) (PAA) - 18, 19, 18-ZnO NPs, 19-ZnO NPs_A, 19-ZnO NPs_B, 19-NH-MWCNTs, 24, 27, 29 and 31

PAA (200 mg) was added to DMSO (2.5 mL) and the mixture stirred at room temperature in an airtight vial. Each of the neodymium Pc complexes (**18** or **19**; 0.86 μmol) as well as **19-ZnO NPs_A** (1.8 mg), **19-ZnO NPs_B** (1.8 mg) or **18-ZnO NPs** (0.92 mg) were transferred into a well dissolved PAA solution and stirred for another 24 h. Each mixture was then transferred onto a clean thin glass slide and dried as explained for **23-TF**, **25-TF** and **26-TF**. The thin films prepared from complexes **18** or **19** are presented as **18-TF** and **19-TF** and, from **18-ZnO NPs**, **19-ZnO NPs_A** and **19-ZnO NPs_B**, as **18-ZnO NPs-TF**, **19-ZnO NPs_A-TF** and **19-ZnO NPs_B-TF** respectively.

The same technique was used to form TFs from conjugates of complex **19** and MWCNTs. Briefly, a mixture of PAA (200 mg) and DMSO (2.5 mL) was stirred at room temperature in an airtight vial followed by addition of **19-NH-MWCNTs** (1.8 mg) into a solution of PAA (200 mg) dissolved in DMSO and stirring continued for 24 h. The TF prepared from **19-NH-MWCNTs** is presented as **19-NH-MWCNTs-TF** throughout this thesis. Those prepared from **NH-GONS**, **NH-rGONS**, **19-NH-GONS**, **19-NH-rGONS** (1.8 mg for all

four) and PAA (200 mg) in DMSO (2.5 L) are referred to as NH-GONS-TF, NH-rGONS-TF, 19-NH-GONS-TF and 19-NH-rGONS-TF. Similarly complex **24** and PAA were used as explained above, except that PAA (200 mg) and DMF (2.5 mL) **24** (2.02 mg, 0.86 μmol) were employed. The TF prepared from **24** is represented as **24-TF**.

Complexes **27** (3.01 mg), **29** (3.02 mg) and **31** (4.57 mg) were employed in TF preparation as explained for TFs prepared from PAA (200 mg) in DMSO (2.5 L) above. The thin films prepared from complexes **27**, **29** and **31** are presented as **27-TF**, **29-TF** and **31-TF**, respectively, throughout this thesis.

2.7 Photophysical and photochemical conditions

2.7.1 Fluorescence quantum yields (Φ_F)

Φ_F values of the Pcs were determined in either DMF, CHCl_3 or DMSO by a comparative method, Eq. 1.8. Unsubstituted zinc phthalocyanine (ZnPc) {(ZnPc in DMSO, $\Phi_F^{\text{Std}} = 0.2$) [280]} was employed as the standard, with the same wavelength chosen for excitation of both the samples and standard. The absorbances of the solutions at the excitation wavelength were between 0.1 and 0.05 to avoid any inner filter effects.

2.7.2 Triplet quantum yields (Φ_T) and lifetimes (τ_T)

The absorbance of sample solutions and that of the standard were adjusted to be nearly 1.5 at their Q-band maximum. All samples were introduced into a 1 cm quartz cell and then bubbled with argon for 10 min to remove dissolved oxygen before taking readings. The triplet quantum yields of the sample phthalocyanines alone and in the presence of ZnO NPs were determined using Eq. 1.9. ZnPc was employed as a standard {ZnPc in DMF ($\Phi_T^{Std} = 0.68$ [281]) and DMSO ($\Phi_T^{Std} = 0.65$ [255])}. Triplet lifetimes were determined from the kinetic data obtained, using ORIGIN Pro 8 software to fit the kinetics decay curves.

2.7.3 Singlet oxygen quantum yields (Φ_Δ)

The determination of Φ_Δ was achieved by employing both the optical and chemical methods. Sodium azide (NaN_3) was used as singlet oxygen quencher for the optical method. The dynamic course of the singlet oxygen concentrations were clearly recorded following Eq. 1.12. The Φ_Δ values were then determined using Eq. 1.13, and employing ZnPc in DMF ($\Phi_\Delta^{Std} = 0.56$ [256]) as a standard.

A chemical method was also used in the determination of Φ_Δ of Pcs and their conjugates in solution (DMF or DMSO). The experiments based on the chemical method were carried out in air using Pcs, conjugates and ZnPc standard (absorbance of 2 at its Q band) and mixed with DPBF (absorbance of 2 at 414 nm), resulting in approximate absorbance of 1

at the Q band (when mixed with equal volume of a solution of DPBF). The resulting solution was irradiated and the degradation of the DPBF monitored by recording the UV-vis spectra of the sample solution at 30 s time intervals. Eq. 1.11 was employed and ZnPc in DMF ($\Phi_{\Delta}^{Std} = 0.56$ [256]) or DMSO ($\Phi_{\Delta}^{Std} = 0.56$ [282]) was used as a standard. The two methods have been compared [256] and give similar results. Hence the differentiation in the results section is not made between the two.

Chapter 3

Synthesis and Characterization

Publications

This thesis is based on peer-reviewed papers published and submitted for publication in international journals

1. **Kutloano E. Sekhosana**, Tebello Nyokong, *Synthesis of ytterbium bisphthalocyanines: Photophysical properties and nonlinear absorption behavior*, *Optical Materials* 37 (2014) 139–146.
2. **Kutloano Edward Sekhosana**, Edith Amuhaya, John Mack, Tebello Nyokong, *Optical nonlinearities and photophysical behavior of green and blue forms of lutetium bisphthalocyanines*, *J. Mater. Chem. C*, 2014, 2, 5431–5437.
3. **Kutloano E. Sekhosana**, Edith Amuhaya, Tebello Nyokong, *Nanosecond nonlinear optical limiting properties of new trinuclear lanthanide phthalocyanines in solution and as thin films*, *Polyhedron* 85 (2015) 347–354.
4. **Kutloano E. Sekhosana**, Edith Amuhaya, Samson Khene, Tebello Nyokong, *Synthesis, photophysical and nonlinear optical behavior of neodymium based trisphthalocyanine*, *Inorganica Chimica Acta* 426 (2015) 221–226.
5. **Kutloano Edward Sekhosana**, Tebello Nyokong, *The nonlinear absorption in new lanthanide double decker pyridine based phthalocyanines in solution and thin films*, *Optical Materials* 47 (2015) 211–218.
6. **Kutloano Edward Sekhosana**, Edith Amuhaya, Tebello Nyokong, *Nonlinear optical behavior of neodymium mono- and bi-nuclear phthalocyanines linked to zinc oxide nanoparticles and incorporated into poly acrylic acid*, *Polyhedron* 105 (2016) 159–169.
7. **Kutloano Edward Sekhosana**, Jonathan Britton, Tebello Nyokong, *The optical limiting of blue and green ytterbium double-decker phthalocyanines in solution and in poly (acrylic acid) as thin films*, *Inorganica Chimica Acta* 450 (2016) 87–91.
8. **Kutloano Edward Sekhosana**, Tebello Nyokong, *Optical limiting response of multi-walled carbon nanotube-phthalocyanine nanocomposite in solution and when in poly (acrylic acid)*, *Journal of Molecular Structure* 1117 (2016) 140–146.

9. **Kutloano Edward Sekhosana**, Munyaradzi Shumba, Tebello Nyokong, *Optical limiting response of phthalocyanine-graphene nanosheet (oxidized and reduced) conjugates embedded in poly (acrylic acid)*, In preparation.
10. **Kutloano Edward Sekhosana**, Meloddy Hlatini Manyeruke, Tebello Nyokong, *Synthesis and optical limiting properties of new lanthanide bis and tris(phthalocyanines) based on two-photon absorption mechanisms*, Journal of Molecular Structure 1121 (2016) 111-118.

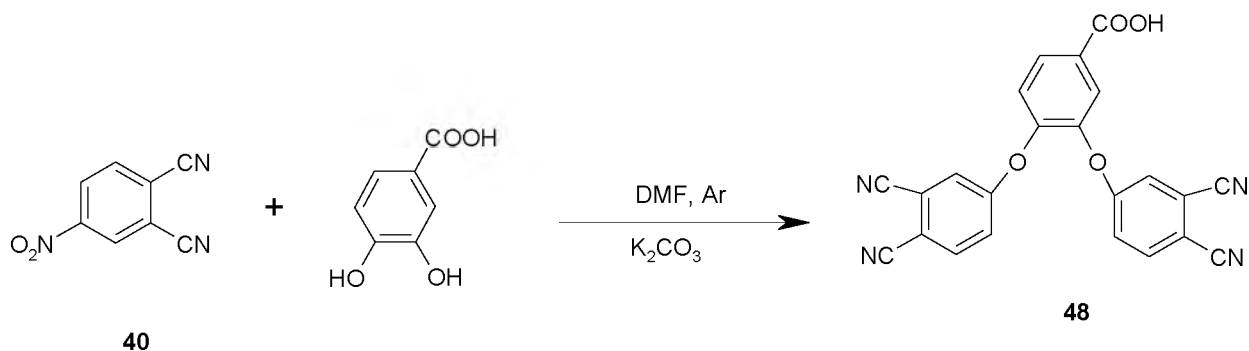
Side publication:

11. Weronika Kuzyniak, Oluwasesan Adegoke, **Kutloano Sekhosana**, Sarah D'Souza, Sesethu Charmaine Tshangana, Björn Hoffmann, Eugeny A. Ermilov, Tebello Nyokong, Michael Höpfner, *Synthesis and characterization of quantum dots designed for biomedical use*, International Journal of Pharmaceutics 466 (2014) 382–389.

3.1 Phthalocyanines

3.1.1 Phthalonitriles (48 and 49; Schemes 3.1 and 3.2)

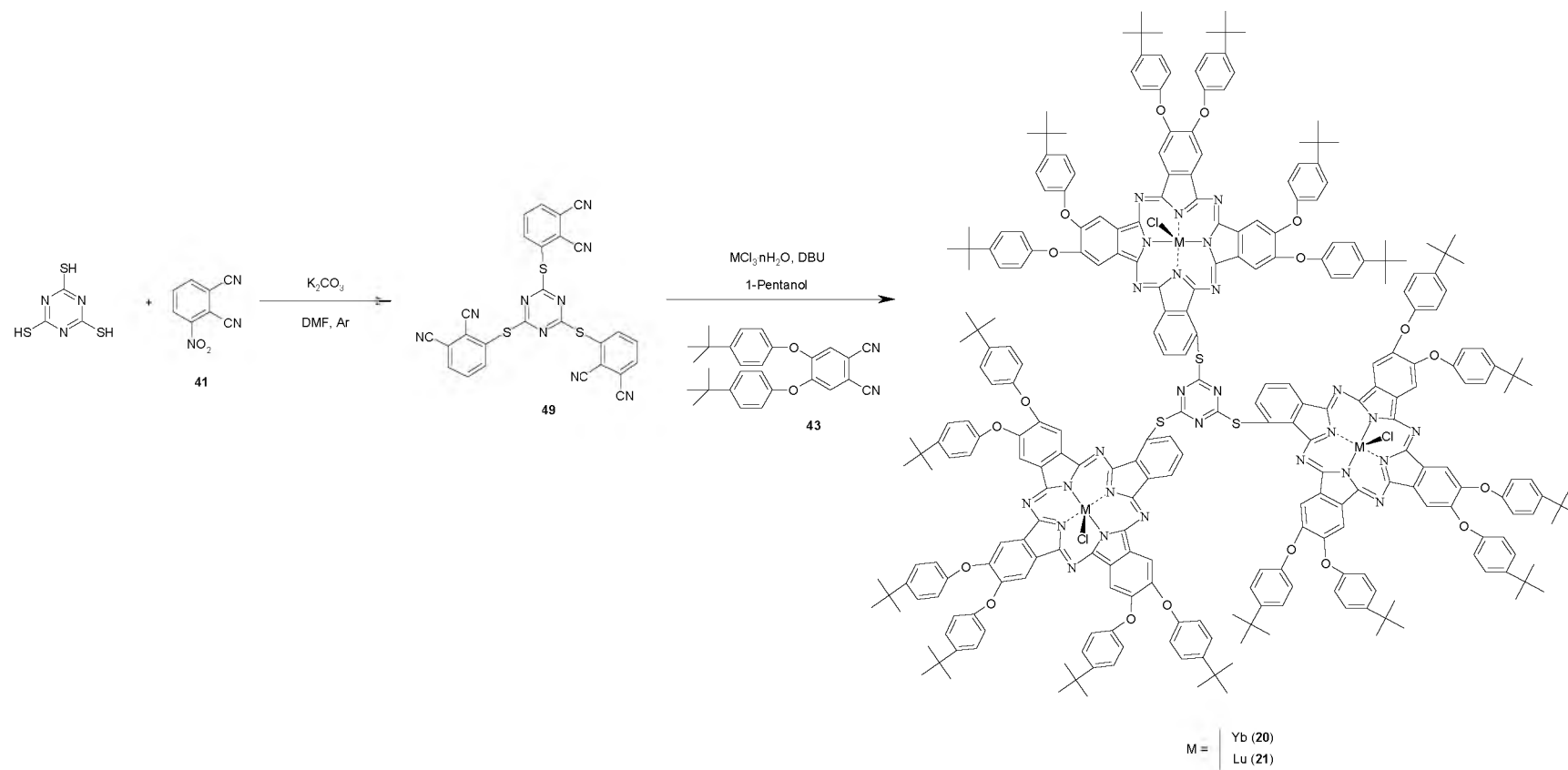
Compound **48** was synthesized by double substitution on 4,5-dihydroxybenzoic acid with compound **40** through base catalyzed reaction using excess K_2CO_3 (Scheme 3.1), yielding 17%. Compound **48** is expected to show nine aromatic protons and one from the carboxyl group. On analysis with 1H NMR, nine aromatic protons (two appearing at 8.09-8.05 ppm, one at 7.97-7.97 ppm, three at 7.87-7.83 ppm and another three at 7.50-7.45 ppm), making up the predicted number of the proposed structure for the aromatic protons. A broad 1H NMR peak appearing at 13.44 showed the presence of a single proton resulting from the carboxyl group. IR also confirmed the presence of $C\equiv N$ at 2232 cm^{-1} and (OH) at 3247 cm^{-1} .



Scheme 3.1: Synthetic route for the preparation of compound **48**.

Compound **49** was synthesized as a precursor for complexes **20** and **21** by displacing nitro groups of three molecules of 3-nitrophthalonitrile (**41**) with the thiol groups of thiocyanuric acid, yielding 59%. The 1H NMR spectrum was in good agreement

with the structure of the compound **49** in DMSO. The aromatic protons gave two doublets: 8.12–8.14 ppm (3H, d, Ar-H) and 7.82–7.81 ppm (3H, d, Ar-H) and a triplet at 7.85–7.84 ppm (3H, t, Ar-H) which, on integration, yielded 3 protons each adding up to the expected 9 protons. ^{13}C NMR spectrum for compound **49** was recorded in CDCl_3 , and gave aliphatic carbon atoms as the expected eight signals at: δ , ppm 113.21, 114.56, 118.61 (Ar-C), 119.45 ($\text{C}\equiv\text{N}$), 133.55, 133.70 (Ar-C), 137.84 (S-Ar-C), 138.42 (N-C=N).

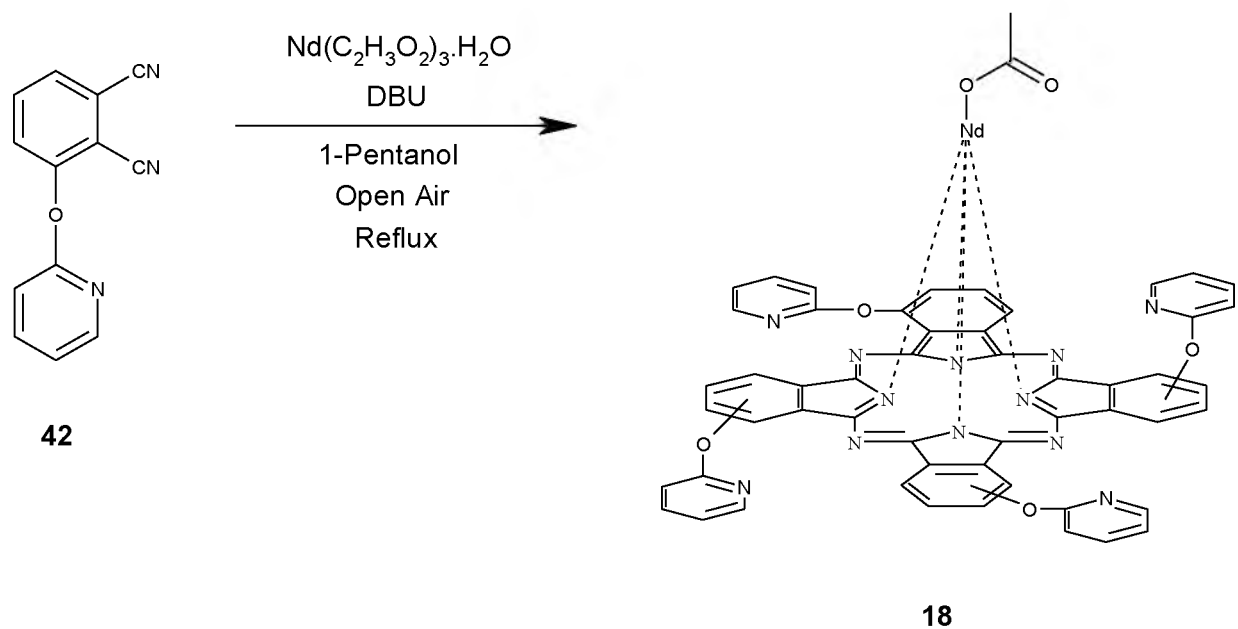
Scheme 3.2: Synthesis of complexes **49**, **20** and **21**.

3.1.2 Mononuclear and clamshell phthalocyanines (18 and 19; Schemes 3.3 and 3.4)

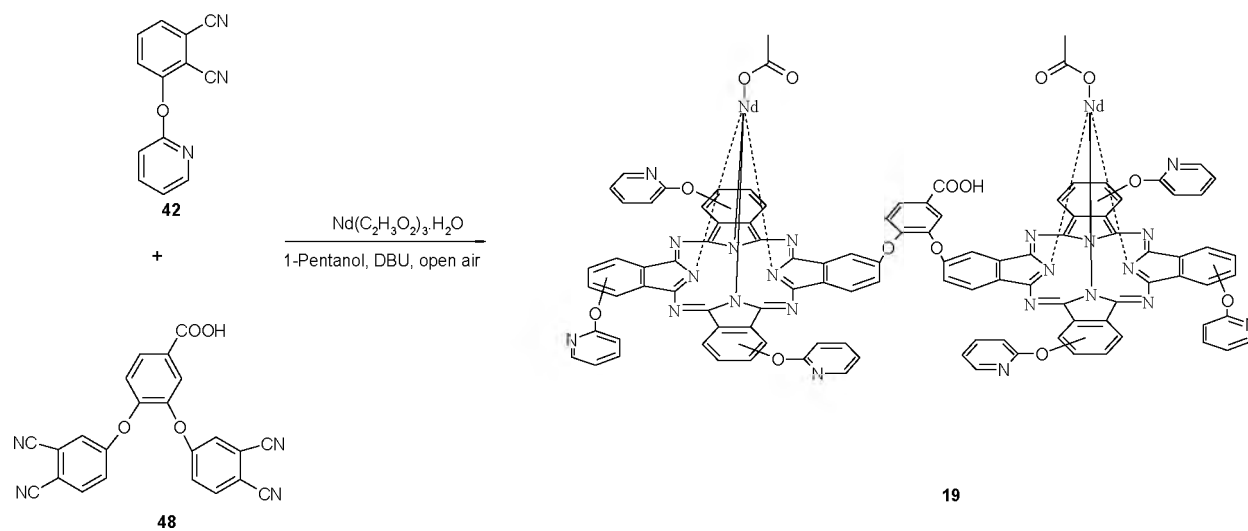
The formation of complex **19** is a result of statistical condensation reaction between compounds **42** and **48** in the presence of neodymium acetate hydrate (Scheme 3.4). Since complex **19** is asymmetrical, purification is a challenge because monophthalocyanines such as complex **18** also form in the same reaction pot in small amounts. Complex **18** (Scheme 3.3) was prepared separately in order to obtain high yields (about 23%), even though these are low compared to **19** (about 60%). The results obtained from elemental analysis corresponded well with the proposed structures. The ^1H NMR spectra of complex **19** and **18** recorded in DMSO-d_6 gave results that were in agreement with their proposed structures. Broad signals were obtained due to the paramagnetic nature of Nd [283].

Mass spectrum of complex **19** gave a signal at 2144 amu. This value differs slightly with the calculated value (2140 amu) for complex **19** by four protons, confirming its proposed structure. Similarly, the calculated value for complex **18** (1087 amu) corresponded to the experimental value (1091 amu). MPc complexes have been observed to degrade with molecular ion peaks $[\text{M}]^+$, $[\text{M}+\text{nH}]^+$ or $[\text{M}-\text{nH}]^+$ ($n = 1-3$) [284]. The matrix employed in this work is 2,5-dihydroxybenzoic acid, which is known [284] to intensify the fragmentation process, hence the observed mass spectral data.

The C≡N stretch (2232 cm^{-1} , Fig. 3.1 for 48) of compounds 42 and 48 disappears on formation of complexes 19 and 18. There are some shifts in the rest of the IR vibrations for 42 and 48 on formation of 19 and 18.



Scheme 3.3: Preparation of complex 18.



Scheme 3.4: Preparation of complex 19.

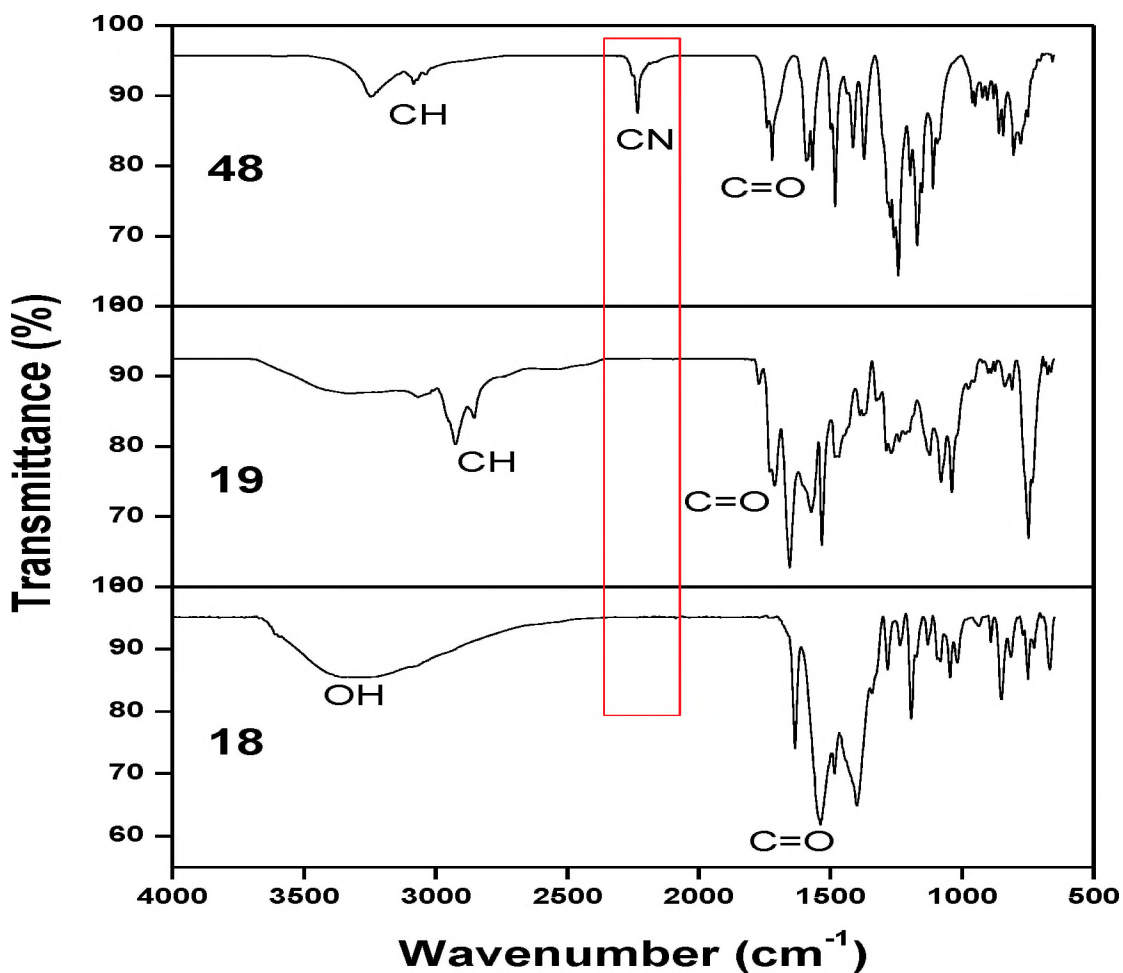


Fig. 3.1: IR spectra of complexes 48, 18 and 19 in solid state.

Neodymium ion has open f-shell orbitals with unpaired electron and is therefore paramagnetic. Both complexes 18 and 19 have Nd³⁺ ion as a central metal. Electron spin resonance (ESR) spectra for complexes 18 and 19 (Fig. 3.2) confirmed the paramagnetic nature as a result of an unpaired electron. The g-values were the same at 2.000 with a band width around 5.44 G and 6.25 G for both 18 and 19, respectively.

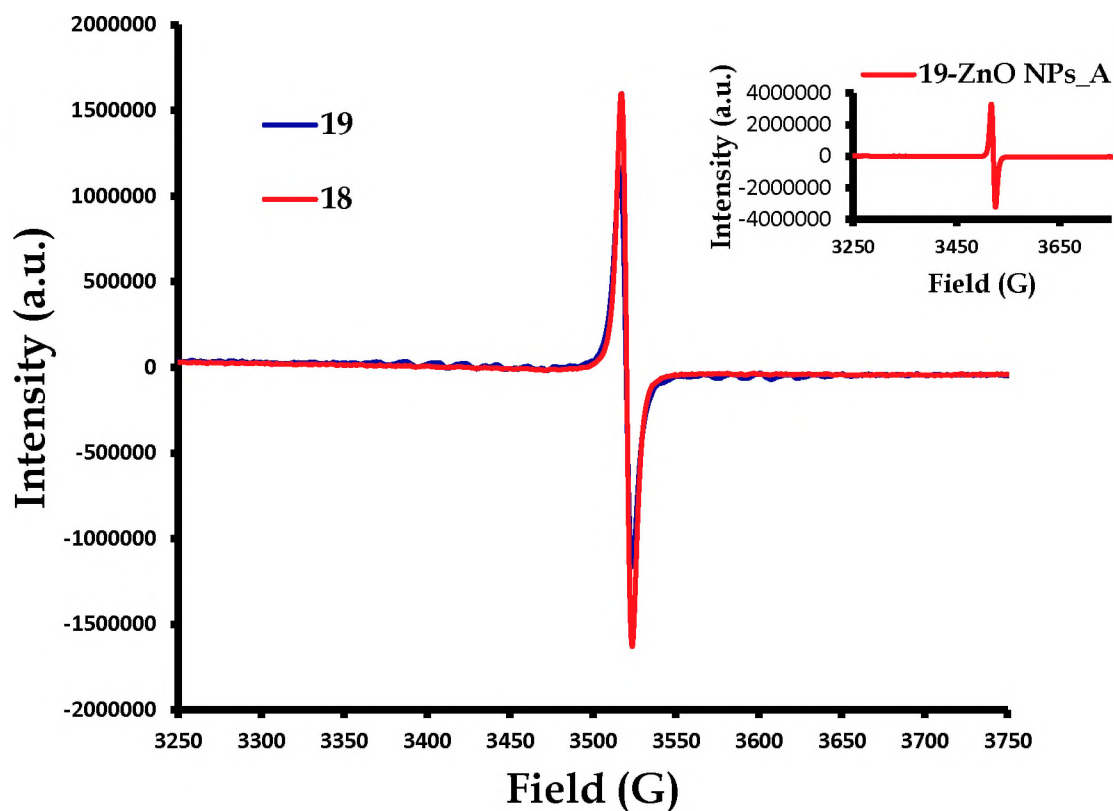


Fig. 3.2: ESR spectral signals of complexes 18, 19 and 19-ZnO NPs_A in solid state.

3.1.3 Trinuclear phthalocyanines (20 and 21; Scheme 3.2)

The new s-triazine based trinuclear ytterbium and lutetium phthalocyanine complexes (20 and 21 respectively) were prepared statistically by condensing compounds 49 and 43 (Scheme 3.2) in the presence of a metal salt ($\text{YbCl}_2 \cdot 6\text{H}_2\text{O}$ or LuCl_3) in 1-pentanol for 21 h in open air, yielding 77% (complex 20) and 69% (complex 21) upon purification via a silica column chromatography. Complexes 20 and 21 are soluble in THF, DMF, chloroform and dichloromethane, but less soluble in DMSO.

The ^1H NMR spectra for complexes **20** and **21** were also taken in DMSO-d_6 , with **20** being paramagnetic due to an Yb metal. The paramagnetism of a compound is known to perturb the proton signals situated in the vicinity of the aromatic core [285]. It was therefore difficult to detect the individual protons situated in the aromatic region. The ^1H NMR

spectrum for complex **20** was broad in the aromatic region, but added up to the expected number of protons on integration, with aromatic protons at 7.67–7.29 ppm (36H, m, Ar-H), 7.24–6.94 ppm (33H, m, Ar-H), 6.92–6.70 ppm (21H, m, Ar-H) and 6.69–6.50 ppm (9H, m, Ar-H). Complex **21** contains a diamagnetic central metal ion (Lu) and hence shows better resolved protons at 7.44–7.32 ppm (54H, m, Ar-H) and 7.01–6.97 ppm (45H, m, Ar-H). The protons resulting from t-butyl group for complex **20** appear as a broad signal at 1.43–1.24 ppm (162H, m, t-Butyl) compared to the resolved t-butyl protons for complex **21** at 1.43 ppm (162H, m, t-Butyl).

The IR spectra for complex **20** and **21** show the disappearance of the $\text{C}\equiv\text{N}$ stretching vibration at 2232 cm^{-1} (for **49**) confirming the formation of complex **20** and **21**. The $-\text{C}=\text{N}-$ vibration for complexes **20** and **21** appear at 1728 and 1729 cm^{-1} , respectively. The IR spectra for both complexes **20** and **21** show the similarities in terms of appearance of stretching vibrations such as CH and CH_3 at 2871 , 2926 and 2952 cm^{-1} (for complex **20**) and 2866 , 2930 cm^{-1} (for complex **21**). Small shifts of such vibrations (CH and CH_3) in complex **20** compared to **21** are due to the paramagnetic nature of Yb^{3+} ion. Complex **20** showed an ESR signal while **21** did not show any signal.

3.1.4 Lanthanide bis(phthalocyanines)

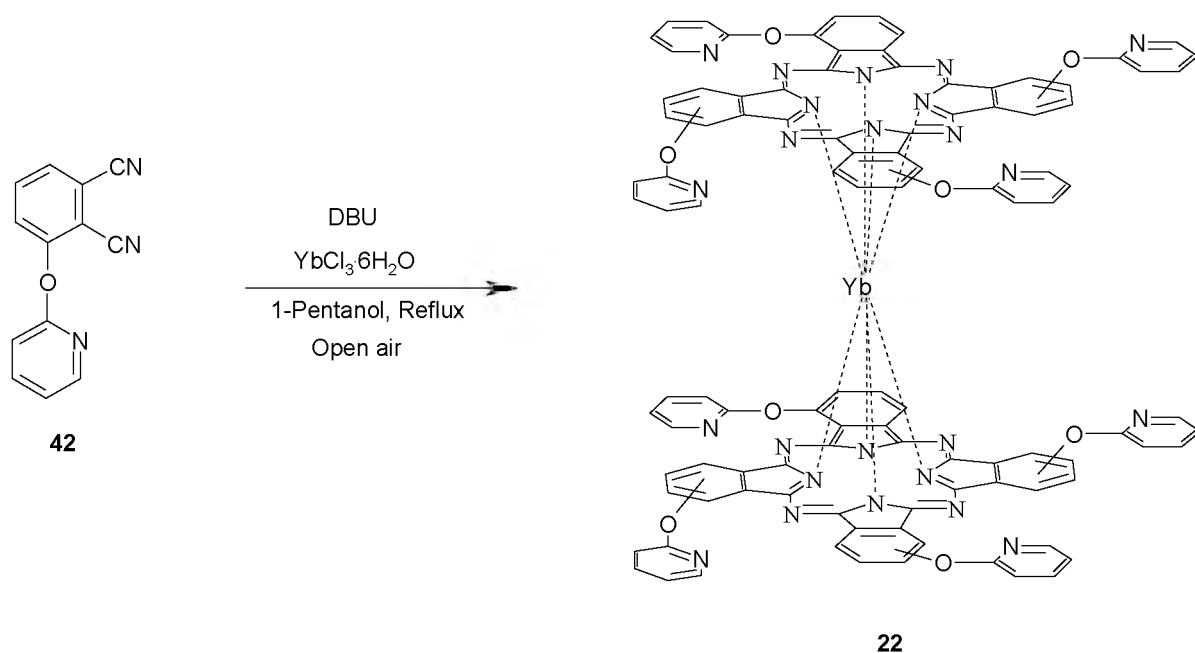
The synthesis of YbPc₂ complexes **22** (Scheme 3.5) and **23** (Scheme 3.6) was achieved by employing literature methods [120], using compounds (42) and (44) as starting materials. After purification via centrifugation and column chromatography, a yield of 23% was obtained for complex **22**. The low yield was expected since monophthalocyanes have been reported to form in the same reaction vessel during the preparation of LnPc₂ complexes [286]. The desired product was obtained after extensive purification. The yield for complex **23** was higher at 57% through Soxhlet extraction, centrifugation, column chromatography and C18 reverse phase column purification.

The ¹H NMR data obtained were in agreement with the structure of complexes **22** and **23**. Results obtained from elemental analysis corresponded with the proposed structure of complexes **22** and **23**. Both complexes were soluble in polar organic solvents such as DMF, DMSO, methanol and ethanol. MALDI -TOF mass spectra also provided results that corresponded to the proposed structures as detailed in the experimental section.

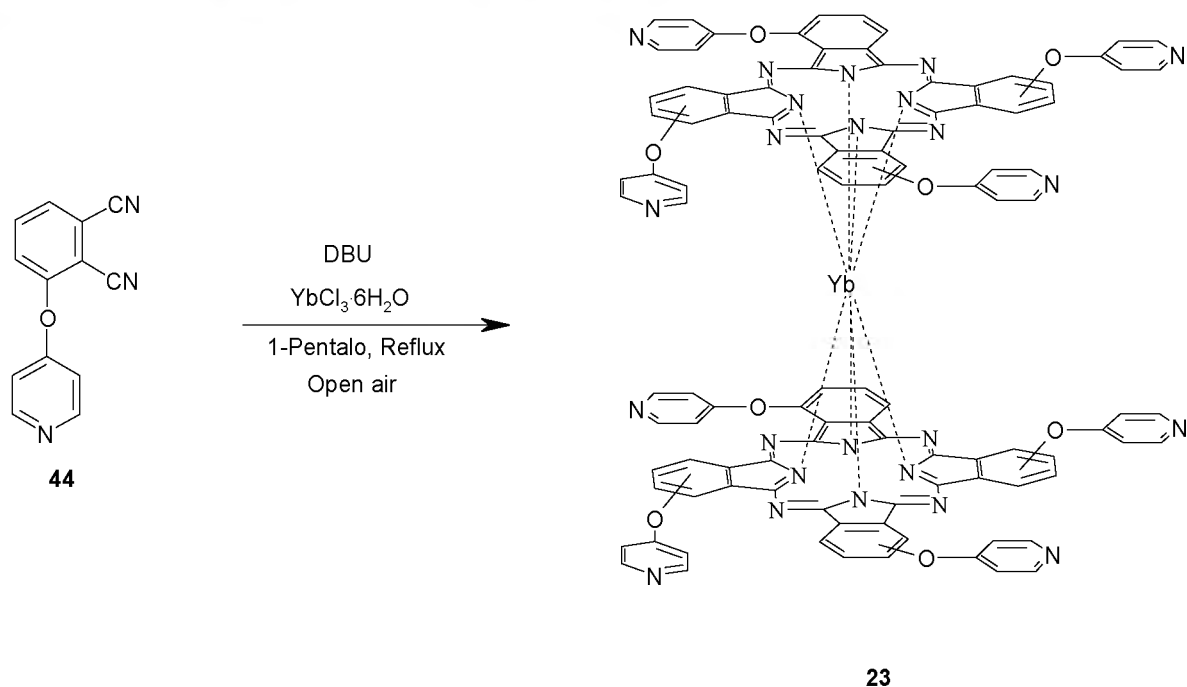
The disappearance of C≡N modes for complexes **42** and **44** on formation of **22** and **23**, confirms cyclization. Overall, the aromatic regions of complexes **42** and **44** are maintained in the IR spectra of complexes **22** and **23**, respectively. The IR marker band for the Pc monoanion radical, Pc^{•-}, usually appears in the range 1311 cm⁻¹ to 1324 cm⁻¹ [287,288]. Pc^{•-} IR marker band was observed at 1316 cm⁻¹ for complex **22** and at 1322 cm⁻¹ for **23**. A broad OH⁻ stretch was also observed at 3397 cm⁻¹ for complex **22** and 3230

cm^{-1} for complex **23**. The OH^- peaks can be attributed to the fact that the salt used contained water.

The OH^- stretching vibration appeared at 3241 cm^{-1} in the Raman spectra of complex **22**. The weak bands in Raman in the region: $2700\text{--}2900 \text{ cm}^{-1}$ are assigned to C-H on complexes **22** and **23** [289]. The bands appear to have shifted to lower energies compared to other C-H stretching modes reported elsewhere [289].



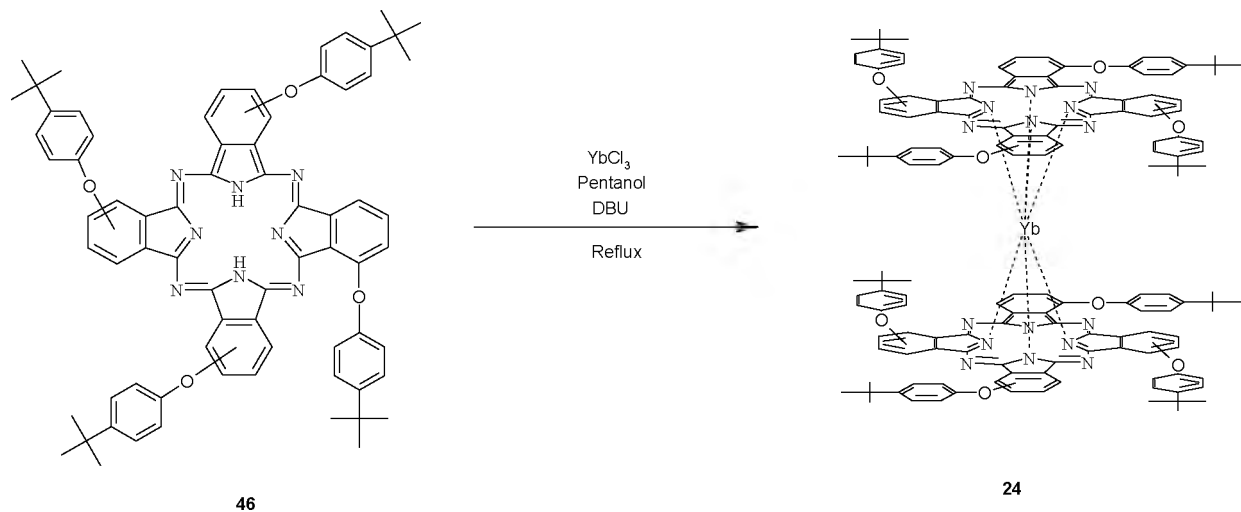
Scheme 3.5: Synthesis of bis-{1(4), 8(11), 15(18), 22(25)-(tetrapyrrodi-2-yloxy phthalocyaninato)} ytterbium (III) (**22**).



Scheme 3.6: Synthesis of bis-{1(4), 8(11), 15(18), 22(25)-(tetrapyrroline-4-yloxy phthalocyaninato)} ytterbium (III) (23).

Reasonable but relatively low yield of 13% was obtained for **24** (Scheme 3.7) on purification via a column packed with silica and using chloroform-hexane solvent mixture (*v/v*: 3:2) as an eluent. The ¹H NMR data obtained was in agreement with the structure of complex **24**. Results obtained from elemental analysis are in agreement with the proposed structure of complex **24**. Complex **24** is soluble in organic solvents such as DMF, ethanol, toluene, tetrahydrofuran, chloroform and dichloromethane. Aromatic C=C peak for complex **24** is observed at 1588 cm⁻¹. A weak band in the region 2866 cm⁻¹ to 2954 cm⁻¹ is due to the aromatic C-H stretches on the Pc rings. For complex **24**, the Pc•-

IR marker was observed as a strong vibration at 1318 cm^{-1} . In general, the in-plane C-H bending dominate the IR spectra in the range 958 cm^{-1} to 1290 cm^{-1} .

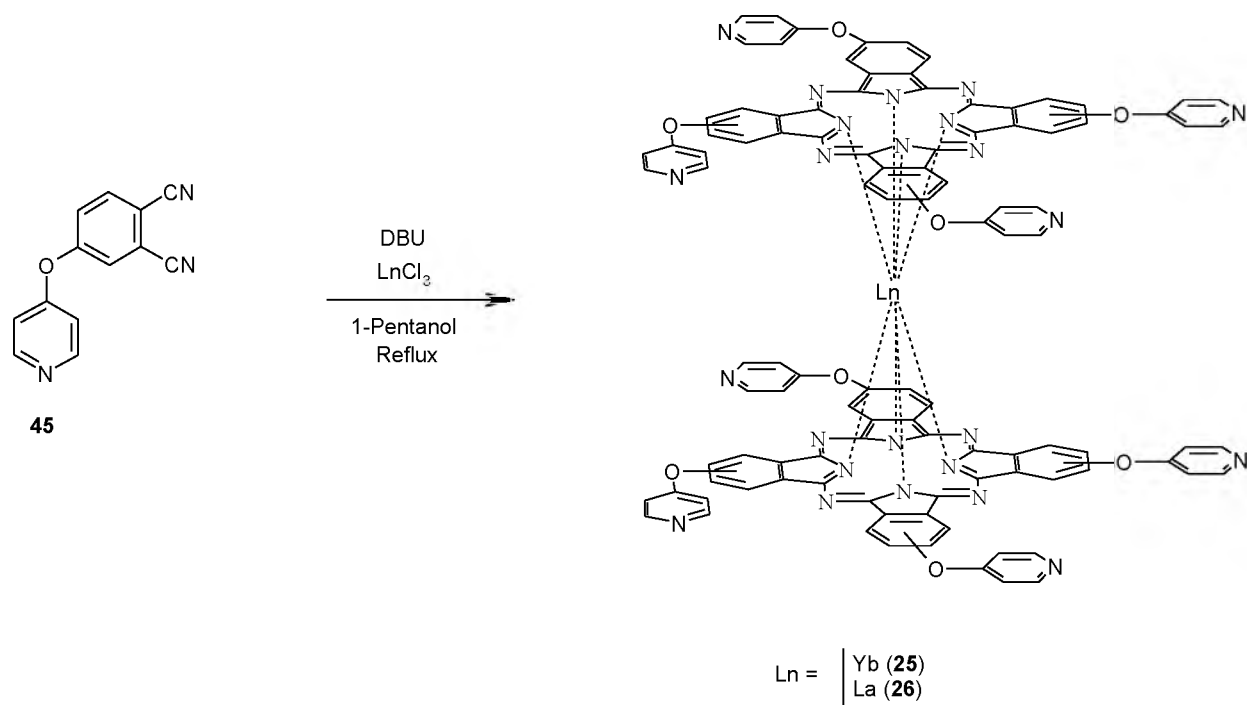


Scheme 3.7: Synthesis of complex **24**.

The yields obtained for complexes **25** and **26** were 19% and 26%, respectively. ^1H NMR, IR and mass spectroscopies as well as elemental analysis techniques were employed for the characterization of LnPc_2 complexes (**25** and **26** (Scheme 3.8)). In general, the obtained ^1H NMR data was in agreement with the proposed structures of complexes **25** and **26**. The ^1H NMR data for complex **26** integrated for two protons at 8.72-8.70 ppm, forty one protons at 8.19-7.56 ppm, two protons at 7.25-7.16 ppm, two protons at 6.79-6.77 ppm, one proton at 6.55 ppm and eight protons at 6.30-6.14 ppm. For complex **25**, the ^1H NMR data showed a broad but split signal at 8.47-7.69 ppm integrating for thirty nine protons. The signal at 6.47-6.32 ppm was also broad and split into two and integrating for seventeen protons. As shown by the ^1H NMR data, complexes **25** and **26** are of different

nature in terms of their magnetic properties that result from lanthanum and ytterbium, though structurally they are the same. Prominent ^1H NMR signals are obtained for **26** are due to diamagnetism. However, the ^1H NMR data for complex **25** reveals broadness and splitting of signals around the same chemical shift range observed for **26**, leading to speculation that paramagnetism due to ytterbium results in deshielding and overlapping of protons.

Results obtained from elemental analysis, IR and MALDI-TOF spectrometer also corresponded with the proposed structure of complexes **25** and **26**. Both complexes were soluble in organic solvents such as DMF and DMSO.



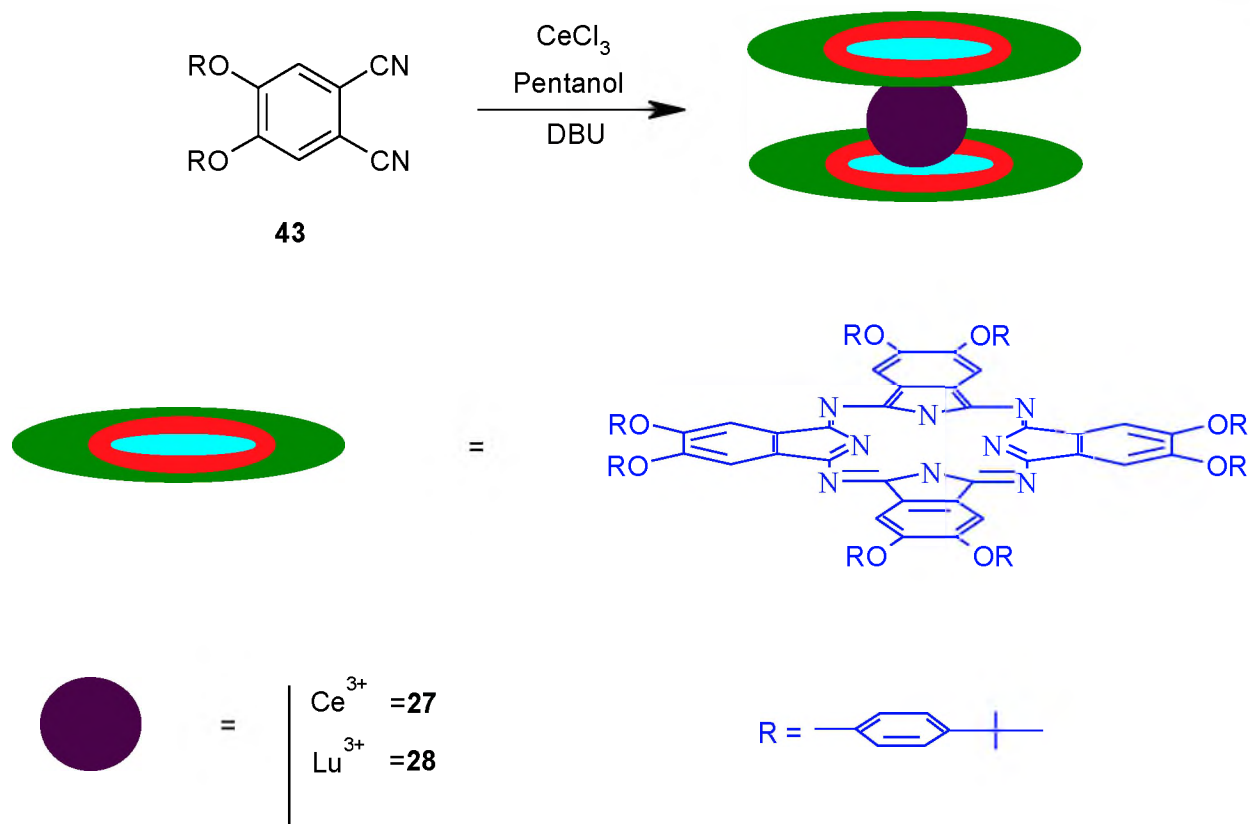
Scheme 3.8: Synthesis of bis-{2(3), 9(10), 16(17), 23(24)-(tetrapyridin-4-yloxy phthalocyaninato)} ytterbium (III) (25) and bis-{2(3), 9(10), 16(17), 23(24)-(tetrapyridin-4-yloxy phthalocyaninato)} lanthanum (III) (26).

The literature method [120] was employed to synthesize complexes 27 and 28 using compound 43 as a starting material (Scheme 3.9), while 29 was achieved by sandwiching gadolinium ion with two Pc rings of complex 47 (Scheme 3.10). Low yields in the range of 13-17% were obtained for complexes 27 and 29 and 50% for complex 28. The triple decker version of 29 (Gd derivative) was obtained as a bi-product for the synthesis of 29, but with very low yields, hence was not employed further.

The ^1H NMR data obtained were in agreement with the structure of complex **28**. Results obtained from elemental analysis corresponded with the proposed structure of complex **28**. Pcs are often isolated as solvates [290], hence the observed results. Complex **28** is soluble in organic solvents such as DMF, ethanol, toluene, THF, chloroform and dichloromethane. The ^1H NMR spectrum is consistent with what would be anticipated for the structure of the synthesized complex, **28**. The aromatic region exhibited peaks at 8.42 ppm, 7.94–7.89 ppm and 7.69–7.63 ppm. These were assigned to the protons on the Pc ring because of their close proximity to the deshielding region of the ring. The two other sets of signals in the region, 7.45–7.41 and 7.08–6.99 ppm (each representing 32 protons), were assigned to the protons on the benzyloxy substituent of the Pc. These were found at a slightly stronger field due to presence of the electron donating oxygen atoms as well as the tert-butyl groups. A peak at 1.31–1.25 ppm for **28** was assigned to the tert-butyl substituents. The ^1H NMR signature for complex **29** was not obtainable in its green neutral form, as compared to complex **27**, due to its paramagnetic nature [283]. Addition of hydrazine (reducing agent) resulted in appropriate ^1H NMR data. The challenge in the synthesis of LnPc_2 complexes is the formation of both the blue and green forms. The blue GdPc_2 complex obtained by MacKay et al. [291] was proposed to contain a proton to balance the charge of the Pc ligand. The green form of LuPc_2 complex was reduced using hydrazine in the presence of tetrabutylammonium perchlorate to yield the blue salt, $\text{NBu}_4[\text{LuPc}_2]$ [292]. Electrochemical processes [293,294] can also be employed to reduce the green forms of LnPc_2 into their blue counterparts. ^1H NMR spectra of

samarium, europium, and erbium derivatives, $\text{NBu}_4[\text{LnPc}_2]$ [295], and $\text{NBu}_4[\text{LuPc}_2]$ [292] salts have been obtained in DMSO-d_6 and deuterated acetonitrile, respectively. Due to challenges in obtaining reasonable ^1H NMR spectra of green LnPc_2 complexes, many researchers [296-298] prefer to study the blue forms whose paramagnetism could only result from the type of a lanthanide ion.

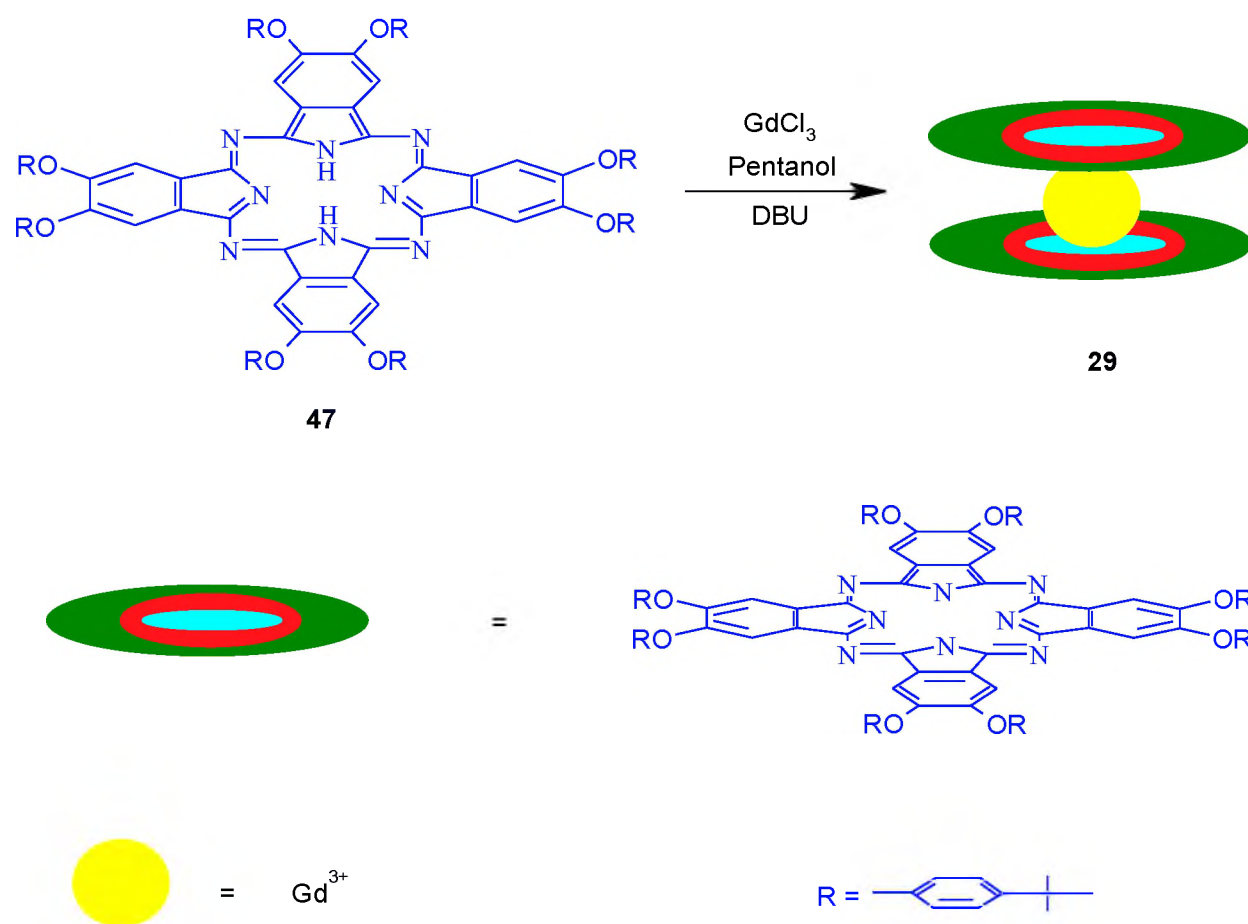
It seems that the blue salts of LnPc_2 complexes exhibit two significant ^1H NMR signals in the aromatic region with different chemical shifts in neutral forms [295]. As stated above, the ^1H NMR spectrum for complex **29** analyzed in the neutral form using DMF in the presence of hydrazine, giving two prominent and two weak ^1H NMR signals. This observation of two significant ^1H NMR signals is in agreement with ^1H NMR spectra of the other blue LnPc_2 complexes [295]. Elemental analysis as well as the mass spectroscopic signatures for all the three complexes, **27**, **28** and **29** are in agreement with their proposed structures.



Scheme 3.9: Synthesis of bis-{2,3,9,10,16,10,16,17,23,24-octa(4-tertbutylphenoxy) phthalocyaninato} cerium (III) (**27**) and bis-{2,3,9,10,16,10,16,17,23,24-octa(4-tertbutylphenoxy) phthalocyaninato} lutetium (III) (**28**). Ln = lanthanide (representing Ce^{3+} or Lu^{3+}).

This $\text{Pc}^{\bullet-}$ IR marker is observed at 1317 cm^{-1} for **29**. Complex **27** does not possess the $\text{Pc}^{\bullet-}$ IR marker, as is typical of Ce sandwich complexes [286]. The other IR vibrations (for complexes **27** and **29**) such as those from the aromatic $\text{C}=\text{C}$, $\text{C}-\text{H}$ from t-butyl or aromatic groups and $\text{C}=\text{N}$ are characteristic for phthalocyanines.

The IR spectrum for **28**, the region of fundamental frequencies, is characteristic of the phthalocyanine ligand. Aromatic in-plane C-H bending vibrations are observed in the region of 1000–1300 cm^{-1} [299]. An aromatic C=C peak is observed at 1601 cm^{-1} . A weak band around 3090 cm^{-1} is due to the aromatic C-H stretches on the phthalocyanine rings [299]. The vibrations at 1505 cm^{-1} indicate the presence of C-O-C groups in the structure for **28**. The marker IR band for the phthalocyanine monoanion $\text{Pc}^{\bullet-}$ radical was observed at 1287 cm^{-1} .



Scheme 3.10: Synthesis of bis-{2,3,9,10,16,10,16,17,23,24-octa(4-tertbutylphenoxy)phthalocyaninato} gadolinium (III) (**29**).

The paramagnetic nature was also obtained using ESR for all neutral LnPc_2 complexes, except **24**. It is known that LnPc_2 complexes can be regarded as single-hole complexes in which an unpaired electron is present in one of the macrocyclic ligands [300]. The ESR spectra are comparable to those obtained elsewhere for LuPc_2 [301]. On reduction with NaBH_4 and recrystallization, no EPR signal was observed for **28**. This provides direct spectroscopic evidence for the absence of an unpaired electron in the reduced neutral $[\text{Pc}^{-2}\text{LuPc}^{-2}]^-$ and confirms that the reduction was successful.

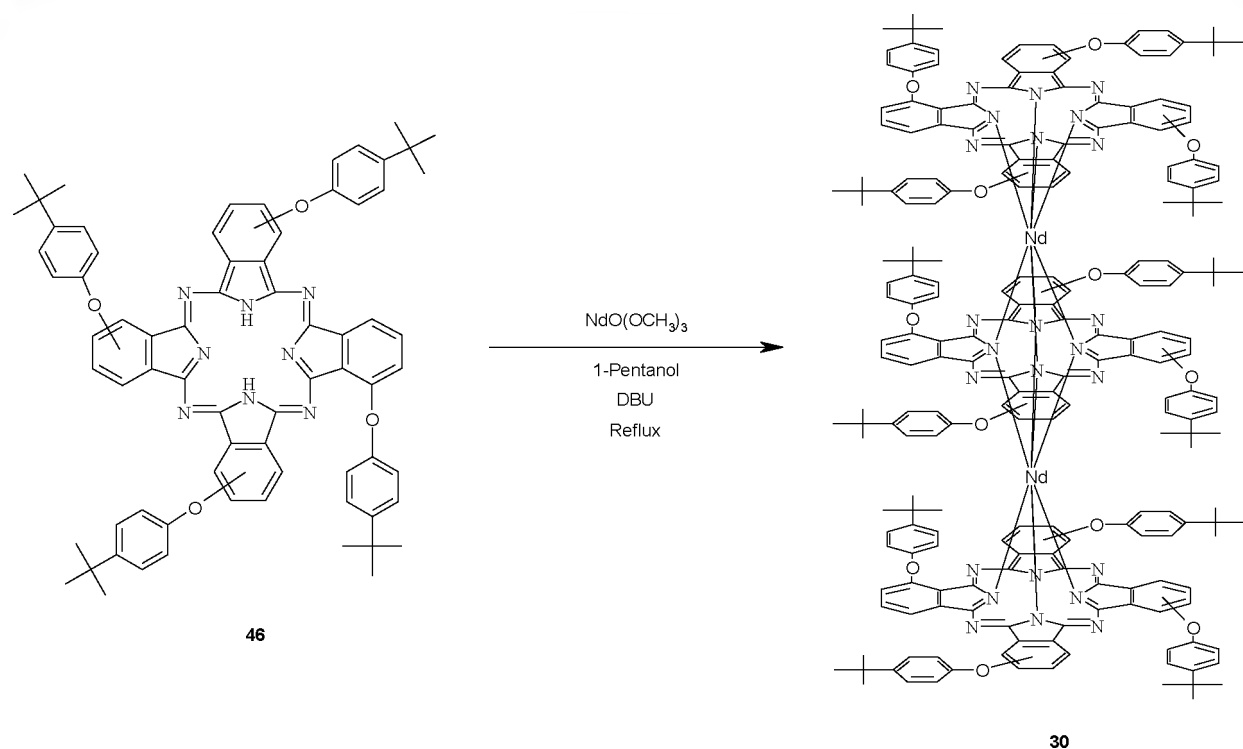
Even though Yb^{3+} is paramagnetic, no signal appears in the EPR spectrum for complex neutral **24**. This has been attributed to the strong interaction between the spins of the unpaired electron in $\text{Pc}^{\bullet-}$ and those of the central Yb ion [302].

3.1.5 Dilanthanide tris(phthalocyanines)

On refluxing a mixture of complex **46** and neodymium acetate hydrate in 1-pentanol in the presence of DBU, complex **30** (Scheme 3.11) was formed, yielding about 71% upon purification. The results obtained from elemental analysis were in agreement with the proposed structure of complex **30**. The yields were moderate. The ^1H NMR spectrum of **30** was taken in CDCl_3 and was also in agreement with the proposed structure, though the signals in the aromatic region were broad probably due to paramagnetism in Nd^{3+} ion or structural distortion of Pc rings. The ^1H NMR spectra of the MPc complexes containing paramagnetic lanthanides, are shifted from their positions in the spectra of the diamagnetic analogs [283,303]. This is the so called so called lanthanide induced shift.

Since this thesis presents the study on complex **30**, which was prepared from complex **46** whose ^1H NMR data is known [274], the comparison can be made between the two complexes **46** and **30**. Complex **46** is unmetallated and hence diamagnetic, whereas complex **30** contains a paramagnetic central metal. In the ^1H NMR signals for complex **46**, the skeleton and the phenyl groups in the aromatic region were found in the ranges: 7.95-7.57 and 7.62-7.03 ppm [274]. Complex **30** also showed two ^1H NMR signal ranges 7.52-7.32 and 7.06-6.92 ppm. The ^1H NMR data for complex **30** in the aromatic region showed broad signals due to paramagnetism from Nd ions, making it difficult to compare the chemical shifts of **46** and **30**. However, the ranges for the chemical shifts in ^1H NMR signals for complex **30** differ from those of complex **46**. If only the first resonance signals within the ranges above are considered, $\Delta\delta$ values obtained are: -0.43 ppm and -0.56 ppm. The δ values for the t-butyl groups for complex **30** (0.96–0.82 ppm) are shifted upfield as compared to those of complex **46** (1.69–1.21 ppm [274]).

Mass spectrum of complex **30** gave a signal at 3608 amu. This value differs slightly with the calculated value (3604 amu) for complex **30** by four protons. This data corresponds to the mass of complex **30**, confirming the proposed structure.



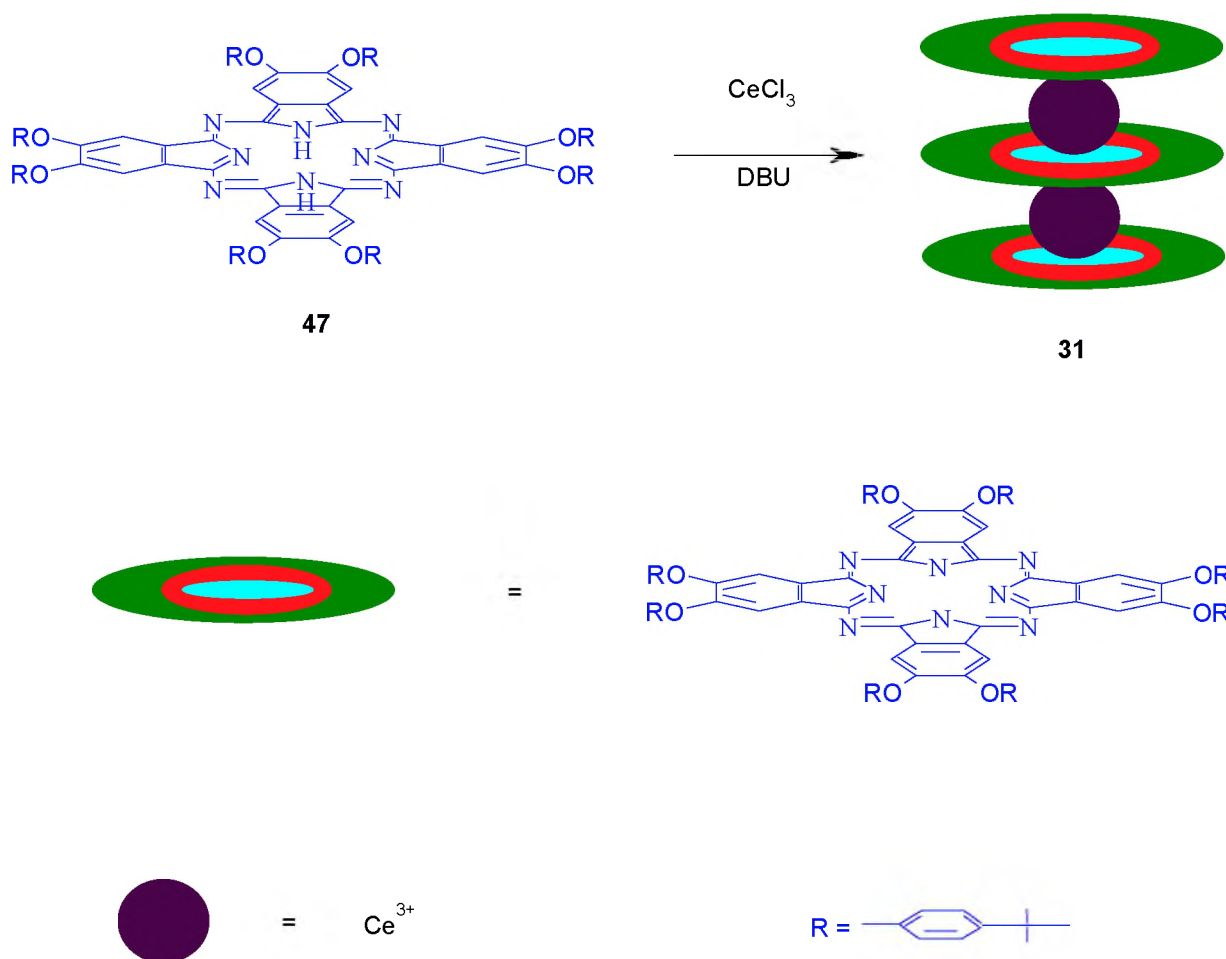
Scheme 3.11: Synthesis of tris-{1(4), 8(11), 15(18), 22(25)-tetra(4-tertbutylphenoxy)phthalocyaninato} dineodymium (III) (30).

Complex 31 was prepared by refluxing complex 47 in 1-pentanol in the presence of DBU and CeCl_3 . The yields obtained for complex 31 (Scheme 3.12) were low (about 13%). The ^1H NMR signature obtainable for complex 31 corresponded with the expected number of protons. Similarly, the elemental composition and mass spectral data gave the results that corresponded with the calculated ones to confirm the proposed structure of complex 31.

IR spectra for complexes 46 and 30 are expected to be the same because of similar Pc ligands. However, any distortion in the Pc rings may shift the IR bands. IR vibrational frequencies ranging from $745\text{--}1041\text{ cm}^{-1}$ (attributed to a Pc skeleton), $1073\text{--}1506\text{ cm}^{-1}$

(resulting from C-O-C vibrations), 1584–1731 cm^{-1} (representing the $-\text{C}=\text{N}-$ IR modes) and 2866–2956 cm^{-1} (showing the IR stretching for C-H, aromatic or CH_3 , t-butyl) were obtained.

Complexes **30** and **31** do not possess the $\text{Pc}^{\bullet-}$ IR marker. This observation is also reported elsewhere [287], and is associated with the neutrality of Ln_2Pc_3 complexes and lack of Pc rings with one charge.



Scheme 3.12: synthesis of tris-{2,3,9,10,16,10,16,17,23,24-octa(4-tertbutylphenoxy) phthalocyaninato} cerium(III) (**31**).

Sub-summary: ^1H NMR, ^{13}C NMR and elemental analysis data corresponded to the proposed structures of the Pc molecules presented in this work. All IR spectral data of LnPc_2 complexes showed the $\text{Pc}\bullet$ - IR marker, except complex **27**.

3.1.6 Ultra violet-visible spectral data

3.1.6.1 Effects of π -electron system and symmetry

The ground state electronic absorption spectra for complexes **18** and **19** in DMSO are shown in **Fig. 3.3**. The Q band of complex **19** is blue-shifted compared to **18**, **Table 3.1**. The lack of symmetry is known to result in blue shifting of the Q band [304], hence the blue-shifting of the Q band for **19** compared to **18**, is due to the low symmetry of the former.

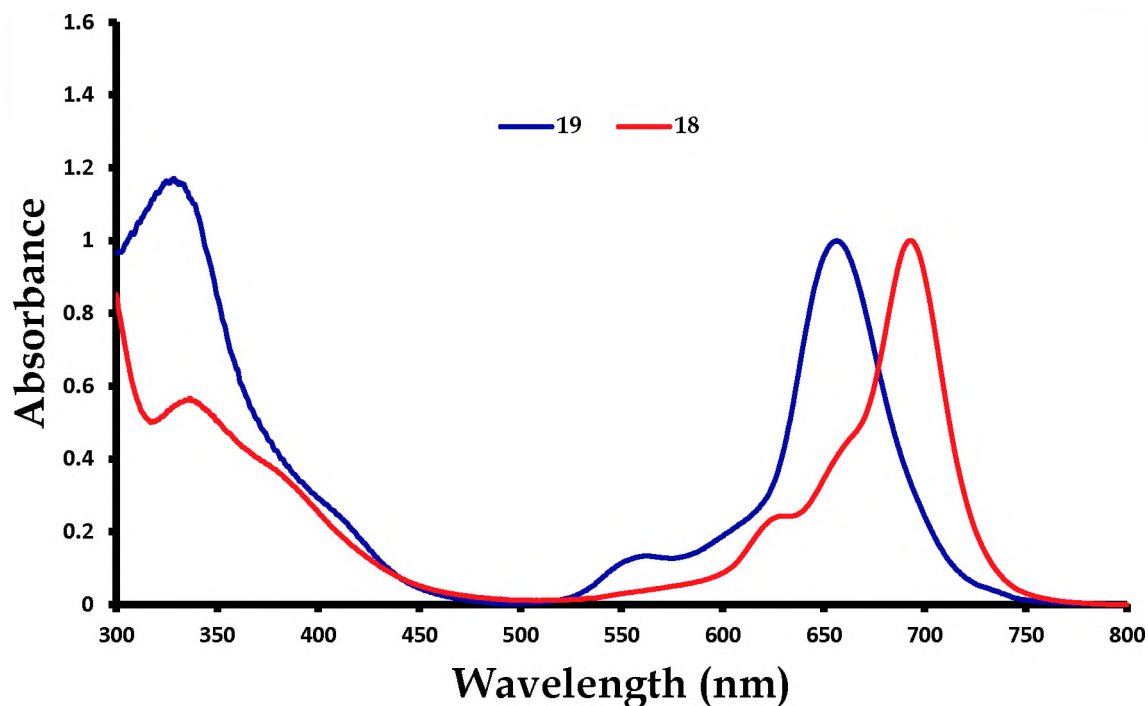


Fig. 3.3: Absorption spectra of complexes **18** and **19** in DMSO ($C = 1.6 \times 10^{-5}$ M).

The ground state electronic absorption spectra for complexes **27**, **29** and **31** in chloroform are shown in **Fig. 3.4**. Complexes **27** and **31** contain the same coordinating metal but differ in the number of Pc entities and lanthanide ions, hence different π -electron systems. As can be observed, the Q bands for **27** and **31** are split as is typical of Ce sandwich complexes [305]. A split in the Q band into two components may be observed in LnPc_2 complexes depending on the solvent and the central metal. For example splitting has been observed in DMF but not in dichloromethane for some LnPc_2 derivatives [306]. The presence of the unsymmetrical spectral pattern as well as splitting of peaks suggests a degree of distortion of one of the Pc rings which is typical of

bis(phthalocyaninato) lanthanides [307,308]. For complex **29** the π -radical-anion band is observed near 500 nm as expected for lanthanide double-deckers which contain a hole in one of the rings [151-154]. For complex **27**, there is no $\text{Pc}^{\bullet-}$ IR marker as stated above. The B bands are split as is typical of double and triple decker phthalocyanines [128]. Despite different π -electron systems in **27** and **31**, with **31** having more π -electrons, no change was observed in the Q band maxima, Table 3.1. The Q bands for **27** and **31** are also split.

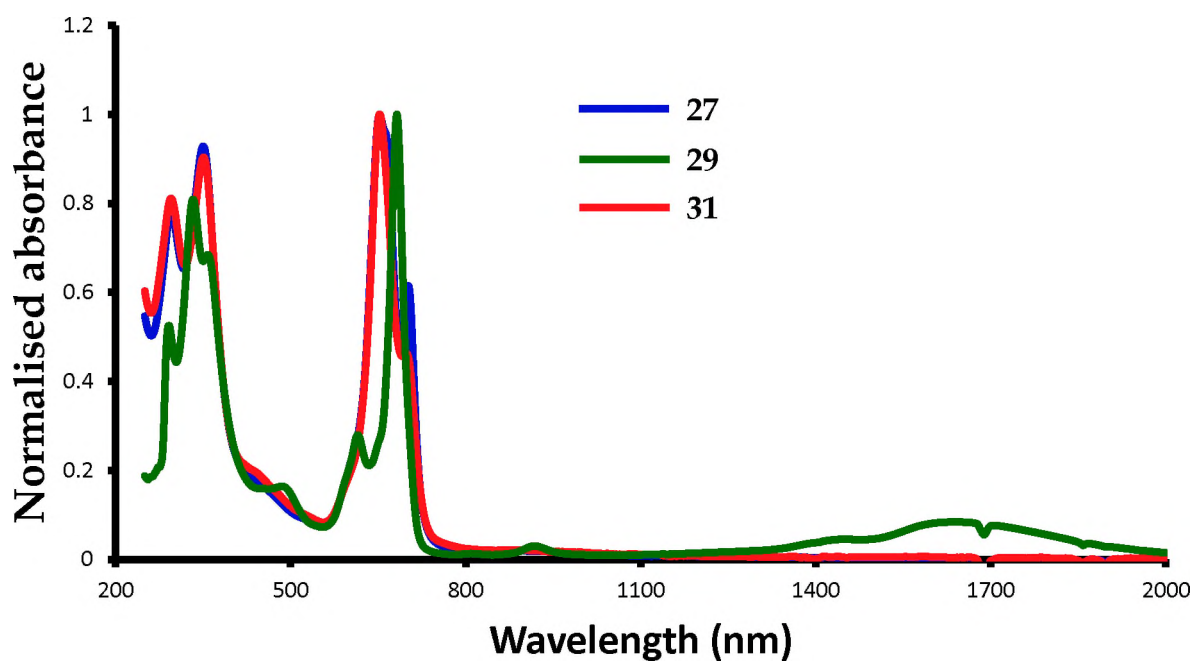


Fig. 3.4: Absorption spectra of complexes **27**, **29** and **31** in CHCl_3 ($C = 1.2 \times 10^{-5}$ M).

In the case of complex **27**, the split is a result of blue sandwich-type Pc like behavior as a result of stable +IV oxidation state of cerium which allows both Pc rings to have the overall charge of -2 each, i.e., $\text{Pc}(2-)$, which causes the splitting in the Q band due to the

exciton interaction between the two Pc rings that adopt an almost staggered orientation in neutral CePc₂ complexes. Complex **28** was studied in detail to compare the neutral and reduced forms. The ground state electronic absorption spectrum for complex **28** in DMF is shown in Fig. 3.5. The Q band lies at 676 nm, Table 3.1. Solutions of the reduced form [Pc²⁻LnPc²⁻]⁻ were obtained by reducing Pc¹⁻LuPc²⁻ with hydrazine, resulting in a split Q band with a shoulder appearing at 710 nm, and a blue shift as shown in Fig. 3.5. The Q band for reduced **28** appeared at 632 nm, Table 3.1.

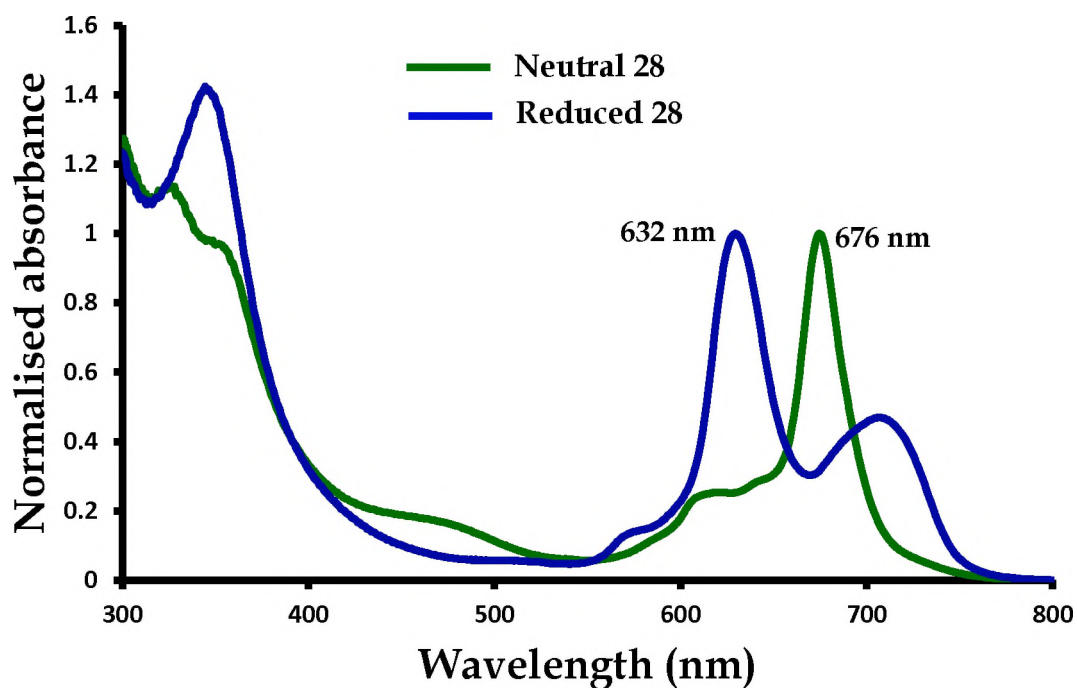


Fig. 3.5: Absorption spectra of neutral **28** in CHCl₃ and reduced **28** in CHCl₃ in the presence of hydrazine (C = 1.3 × 10⁻⁵ M).

Table 3.1: Photophysical parameters of phthalocyanines alone and conjugates presented in this thesis.

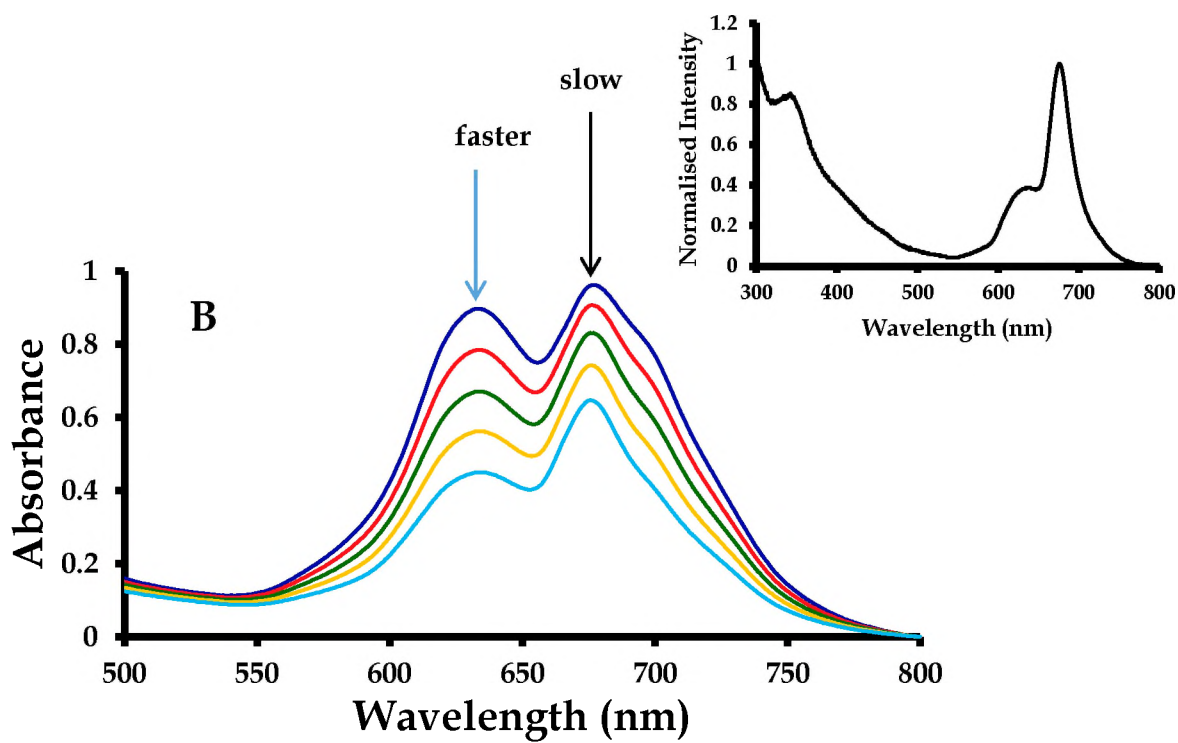
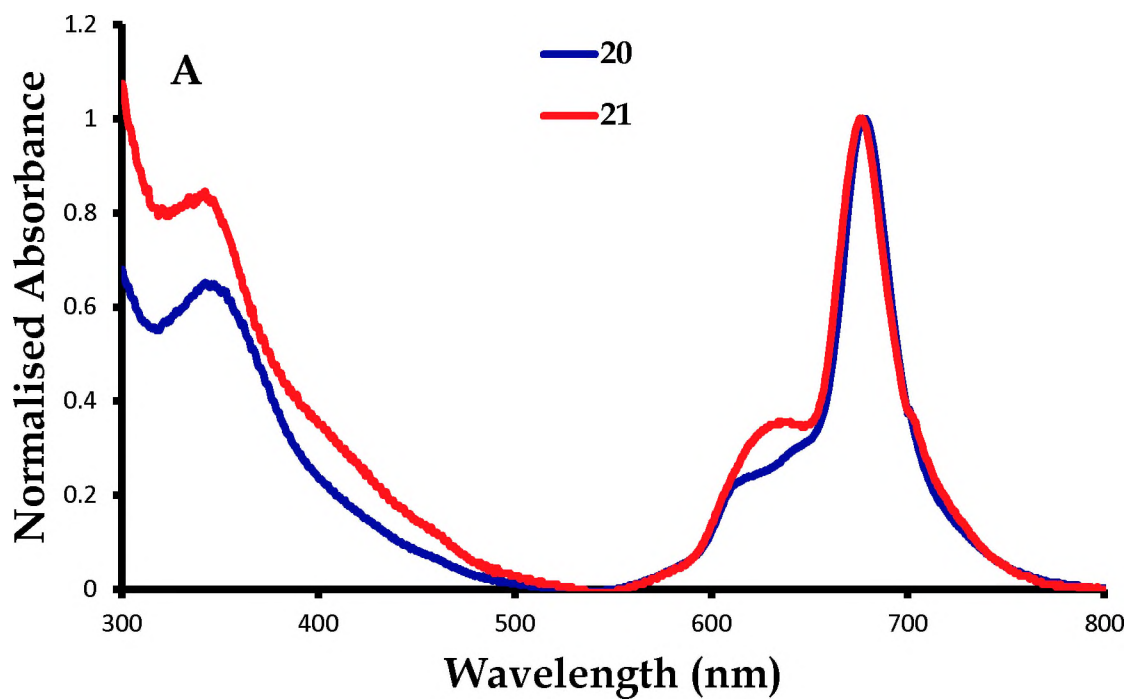
Complex	$\lambda_{\text{abs}}/\text{nm}$	Solvent
18	695	DMSO
19	656	DMSO
18-ZnO NPs	685	DMSO
19-ZnO NPs_A	651	DMSO
19-ZnO NPs_B	655	DMSO
19-NH-MWCNTs	660	DMSO
19-NH-GONS	656	DMSO
19-NH-rGONS	656	DMSO
20	680	DMF
21	677	DMF
22	675	DMSO
23	694	DMSO
Neutral 24	701	CHCl ₃
Reduced 24	652	CHCl ₃
25	687	DMSO
26	685	DMSO
27	652	CHCl ₃
Neutral 28	676	DMF
Reduced 28	632	DMF
29	681	CHCl ₃
30	665	DMF
31	653	CHCl ₃

3.1.6.2 Effects of central metals

The ground state electronic absorption spectra for complexes **20** (M = Yb) and **21** (M = Lu) in DMF are shown in **Fig. 3.6A**. The Q band for **20** is observed at 680 nm while **21** has the Q band at 677 nm, **Table 3.1**. The B band for complex **20** was observed at 345 and 332 nm for complex **21**. There is a slight red shift for **20** compared to **21**. It was also observed that complex **21** is more aggregated compared to **20**. Phthalocyanines form H- and J-type aggregates depending on the orientation of the induced transition dipoles of their monomers [309-311]. In the more common H-aggregates, the component monomers are arranged into a face-to-face conformation. In general, aggregation depends mainly on parameters such as concentration, temperature, nature of the substituents, nature of solvents and complexed metal ions [312]. H aggregation is evidenced by a broad (or split) Q band with peaks due to the aggregate around 630 nm and the monomer peak near 680 nm (depending on the nature of the Pc) [313].

Aggregation studies were done in DMF for complex **21**, **Fig. 3.6B**, in which serial dilutions were carried out. It was observed that the dimer band decreases faster than the monomer band, leaving a narrower the Q band at low concentrations (**Fig. 3.6B**, insert). The broadening and split in the Q band could also be related to lack of symmetry in these complexes [116]. Complex **20** did not show aggregation (the changes shown in **Fig. 3.6B** were not observed for **20**), but the Q band was broadened probably due to lack of symmetry, **Fig. 3.6A**.

Fig. 3.6C shows the absorption spectra of TFs for complexes **20** (**20-TF**) and **21** (**21-TF**) respectively. The absorption spectrum of **20-TF** is broader compared to that of complex **20** in solution. The broadness is due to aggregation in solid state which is more enhanced than in solution, as expected. For **21-TF**, the dimer band was higher than the monomer band Fig. 3.6C. It can be observed that **21** is more aggregated than **20** in solid state as was the case in solution.



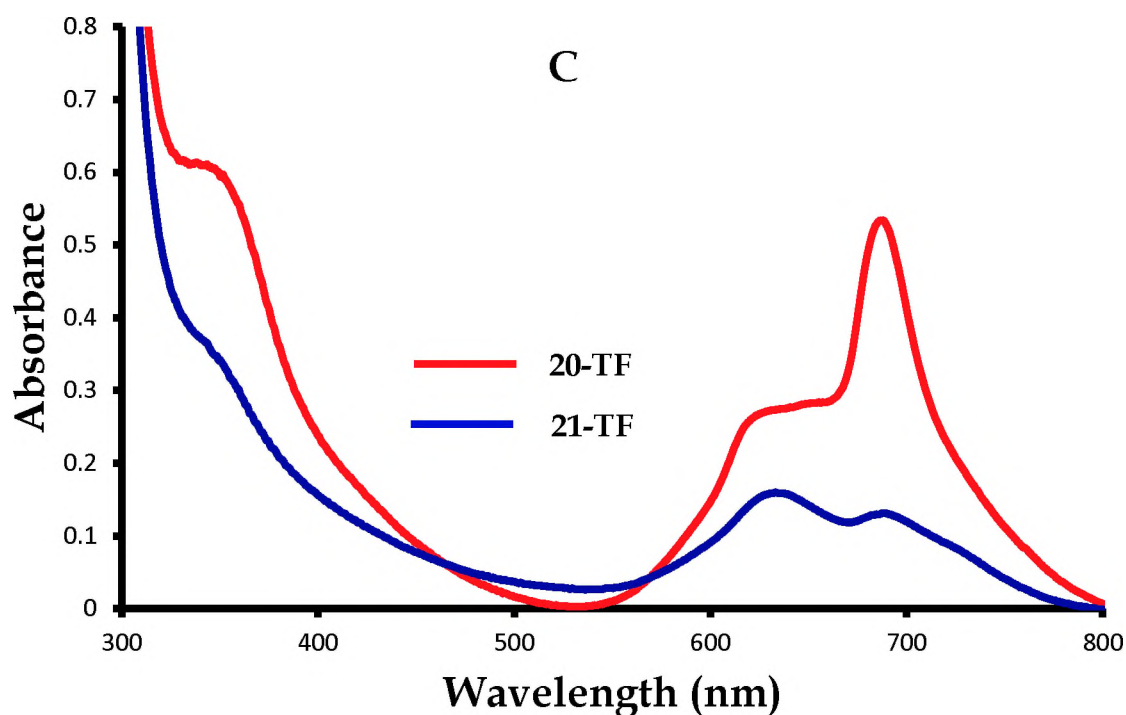


Fig. 3.6: (A) Normalized absorption spectra of complexes **20** (2.77×10^{-5} M) and **21** (4.21×10^{-6} M) in DMSO. (B) Absorption spectra of complex **21** in DMSO at different concentrations 2.19×10^{-5} – 1.45×10^{-5} M. (C) Absorption spectra of thin films in **20-TF** and **21-TF**.

The ground state electronic absorption spectra for complexes **25** (M = Yb) and **26** (M = La) in DMSO are shown in Fig. 3.7. The Q band of complexes **25** and **26** are observed at 687 nm and 685 nm, respectively, Table 3.1. The Q band for complex **25** is slightly red shifted compared to **26**. This is due to the larger central Yb metal in **25**. Larger central metals result in red shifting in Pcs [314]. Complex **23** is more red-shifted than **25** due to non-peripheral substitution, which results in the red-shifting of the Q band in

phthalocyanines [314]. The peaks beyond the Q band (around 900 nm) are typical of bisphthalocyanines containing Pc(1-) rings, and they are due to transitions from the semi-occupied orbital to the degenerate highest unoccupied molecular orbital (LUMO) [155]. A shoulder in the 400–500 nm region of the absorption spectrum characteristically designates a radical phthalocyanine anion [315,316]. The absorption spectra of complexes **25** and **26** show a shoulder within this range. The absorption spectra are broad for complex **26**, suggesting aggregation. Complex **26** showed extensive aggregation (at concentration higher than 6×10^{-6} M) with a monomer peak at 685 nm and peaks due to aggregation between 650 and 630 nm, Fig. 3.8A. On dilution, the peaks at high energy decreased faster than the peaks due to the monomer, thus confirming that the split in the Q band is due to aggregation and not due to low symmetry.

There was no clear aggregation for **25** (at the same concentration as complex **26**), Fig. 3.8B. Aggregation is expected to be enhanced in peripherally substituted Pcs. The extensive aggregation observed for **26** needs some explanation. It can be speculated that the nature of the coordinating lanthanide could encourage aggregation. La (III) is a much smaller ion than Yb (III) and hence the former may allow more interactions of the rings, hence resulting in aggregation.

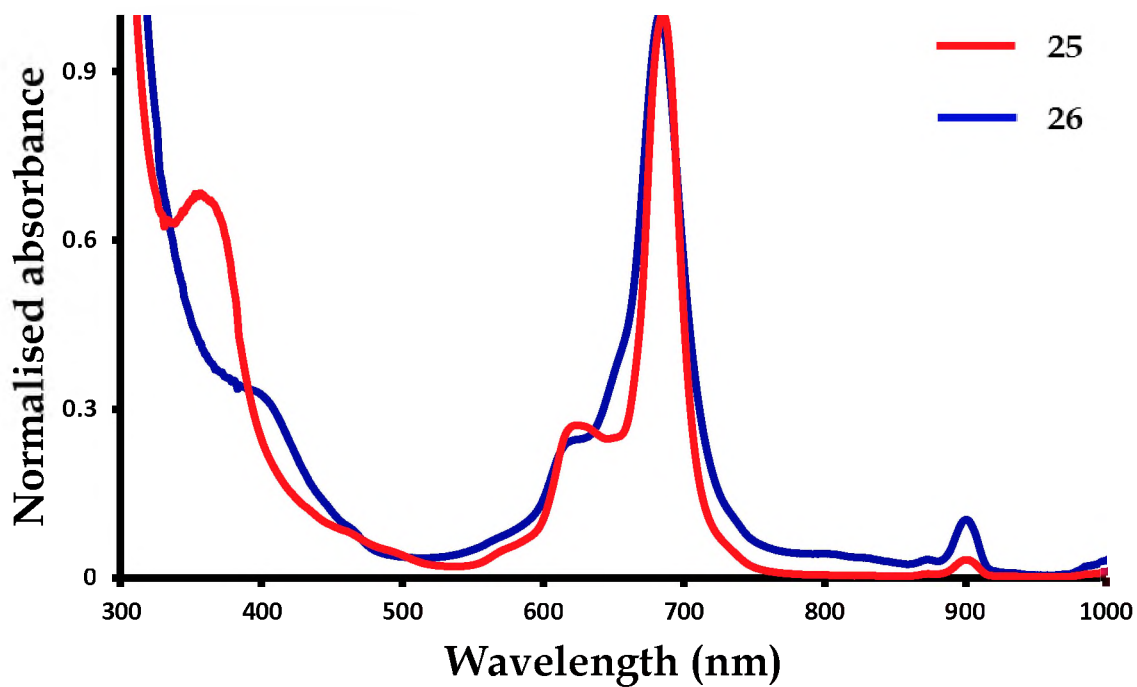
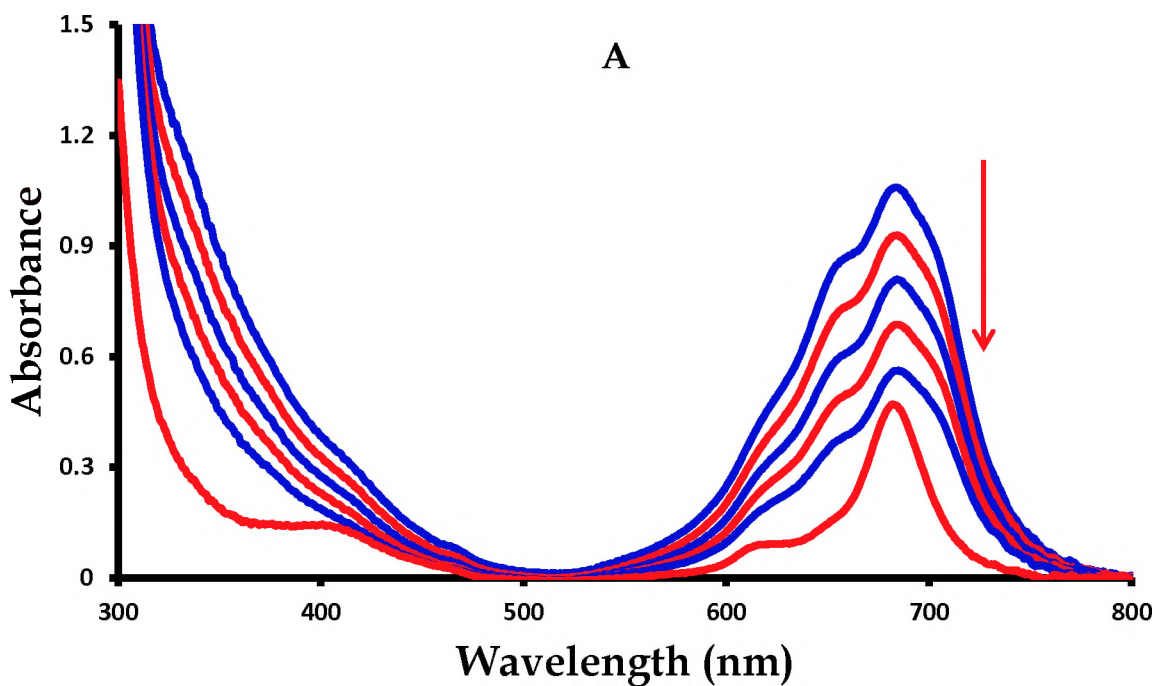


Fig. 3.7: Ground state electronic absorption spectra for complexes 25 (1.3×10^{-5} M) and 26 (6×10^{-6} M) in DMSO.



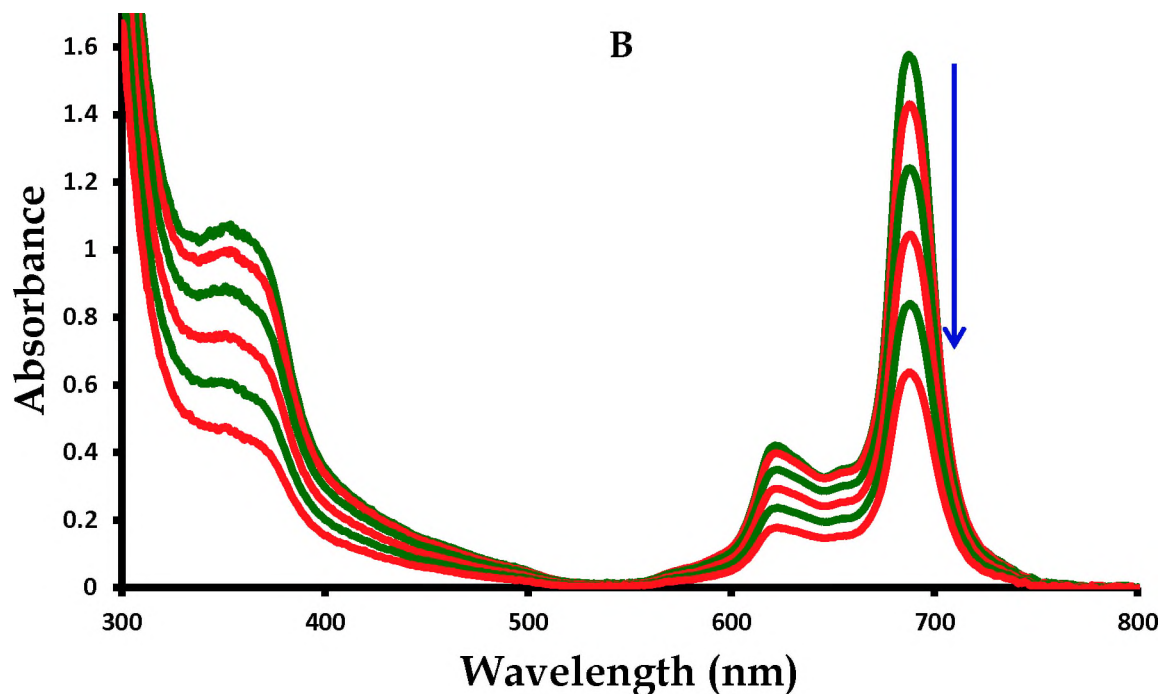
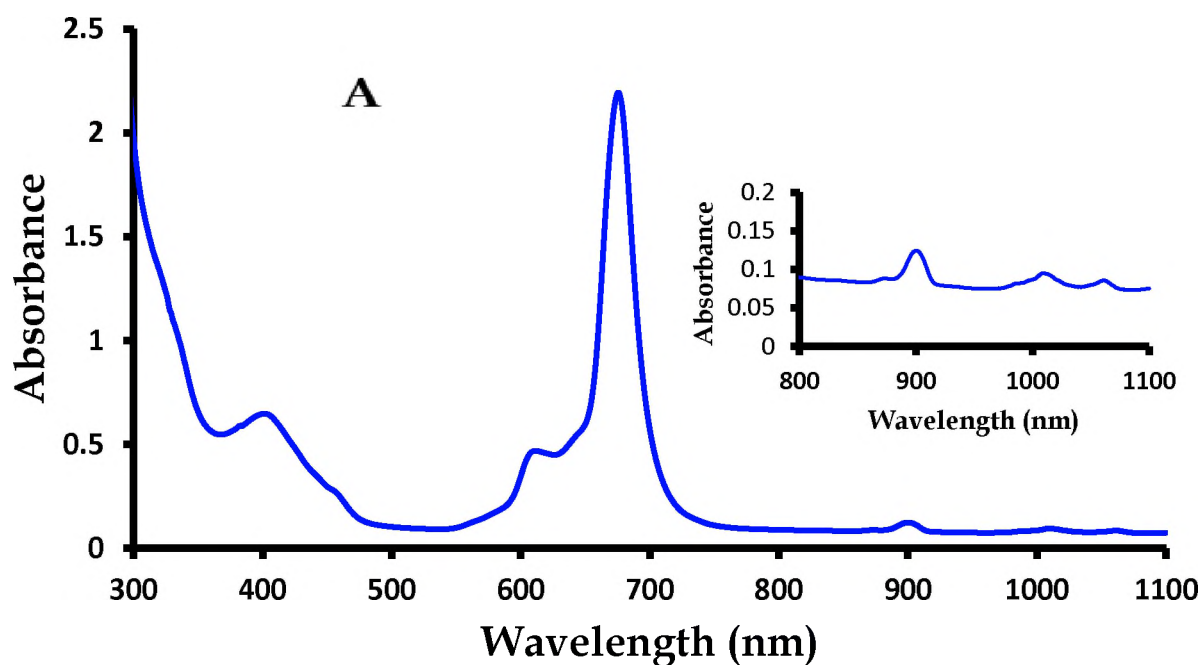


Fig. 3.8: Absorption spectral changes of complex 26 (A) and complex 25 (B). Concentration range = 1.6×10^{-5} – 6×10^{-6} M for both (A) and (B).

3.1.6.3 Effects of natures of substituents

The ground state electronic absorption spectrum for complex 22 and 23 in DMSO is shown in Fig. 3.9A and B. The Q band of complex 22 is at 675 nm and 694 nm for 23, Table 3.1. Thus complex 23 is red shifted compared to 22. Nitrogen containing groups result in the red shifting of the Q band in phthalocyanines [317]. It has also been reported and it is possible that the overlap of bulky groups located at the non-peripheral positions of the ring (such as phenyl groups) causes substantial deformation of the phthalocyanine [318]. This results in splitting and red shift is observed in the Q band, which can be observed in complex 23. The distortion seems to be related to the position of the nitrogen

group on the pyridine substituent. This broadening or splitting in the Q band was also observed in porphyrins and was attributed to out-of-plane deformation [319]. Spectral changes observed for complex **23** on changing its concentration, Fig. 3.9C, did not give evidence for aggregation, since both peaks decreased equally on dilution, showing that the presence of the two peaks is not due to aggregation and confirms the possibility of deformation discussed above. The peaks beyond the Q band (Fig. 3.9, inserts) are typical of bisphthalocyanines containing Pc(1-) rings as stated above.



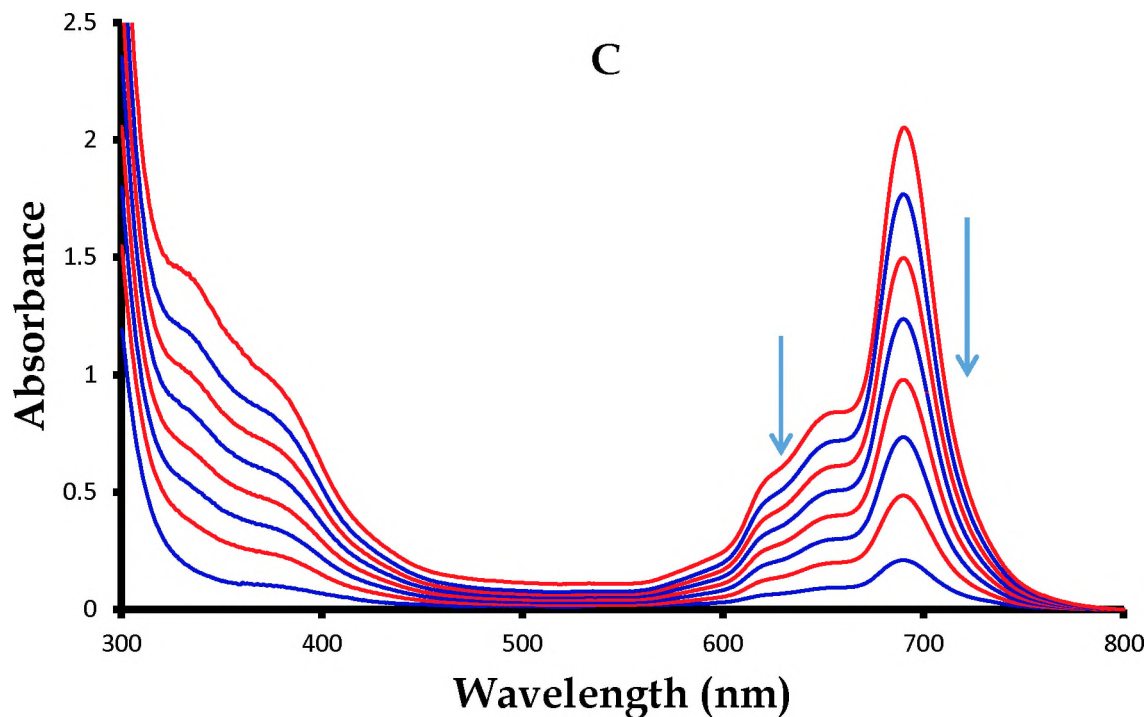
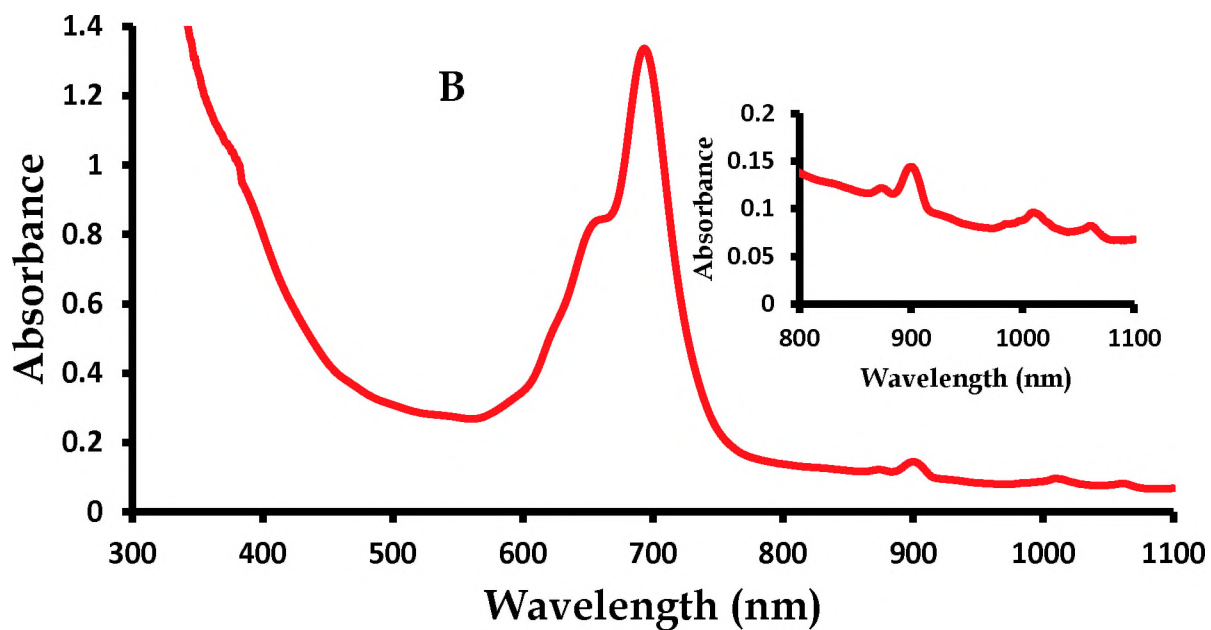


Fig. 3.9: Absorption spectra of (A) complex 22 and (B) complex 23 in DMSO at $\sim 4.0 \times 10^{-6}$ M and 8.23×10^{-6} M. Inserts = NIR spectra. (C) Changes in absorbance spectra of 23 on change in concentration. Starting concentration $\sim 1 \times 10^{-5}$ M.

3.1.6.4 Ultra violet-visible spectral data of dilanthanide tris(phthalocyanines)

The ground state electronic absorption spectra for complex **30** in DMF and DMSO are shown in **Fig. 3.10** with the Q-bands at 662 nm and 665 nm, respectively. Compared with neodymium bisphthalocyanines [**320**] whose intense absorption band was recorded at 705 nm in DMF, the absorption spectrum of complex **30** is blue-shifted. The blue-shifting as well as the nature of absorption spectrum for complex **30** is typical of neodymium based tris(phthalocyanines) [**321**] and other Ln_2Pc_3 [**128**]. **31** is also blue shifted compared to LnPc_2 complexes. It has been shown in literature that the absorption spectrum of a tris(phthalocyanine) is similar to that of a reduced LnPc_2 complexes with a split in the Q-band [**322**], hence the appearance of a shoulder at ~687 nm for complex **30**. The B band is broad in **Fig. 3.10**. A split B-band has been reported for europium based tris(phthalocyanines) [**128**]. Thus, the broad B band in **Fig. 3.10** is a result of overlap of split components.

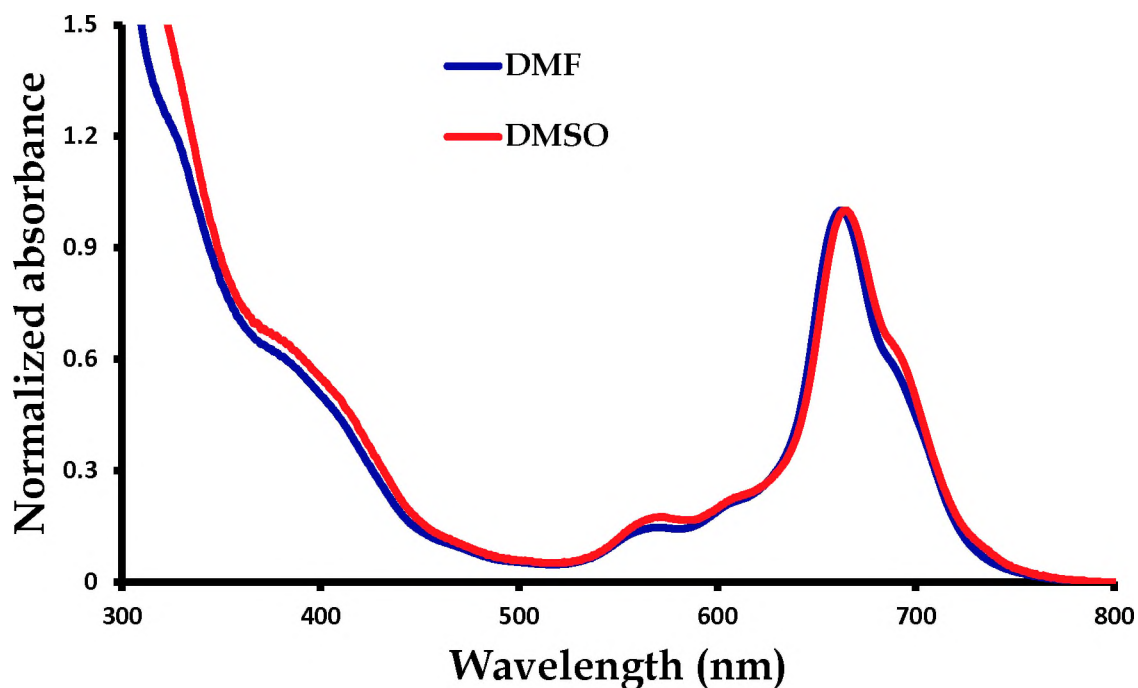


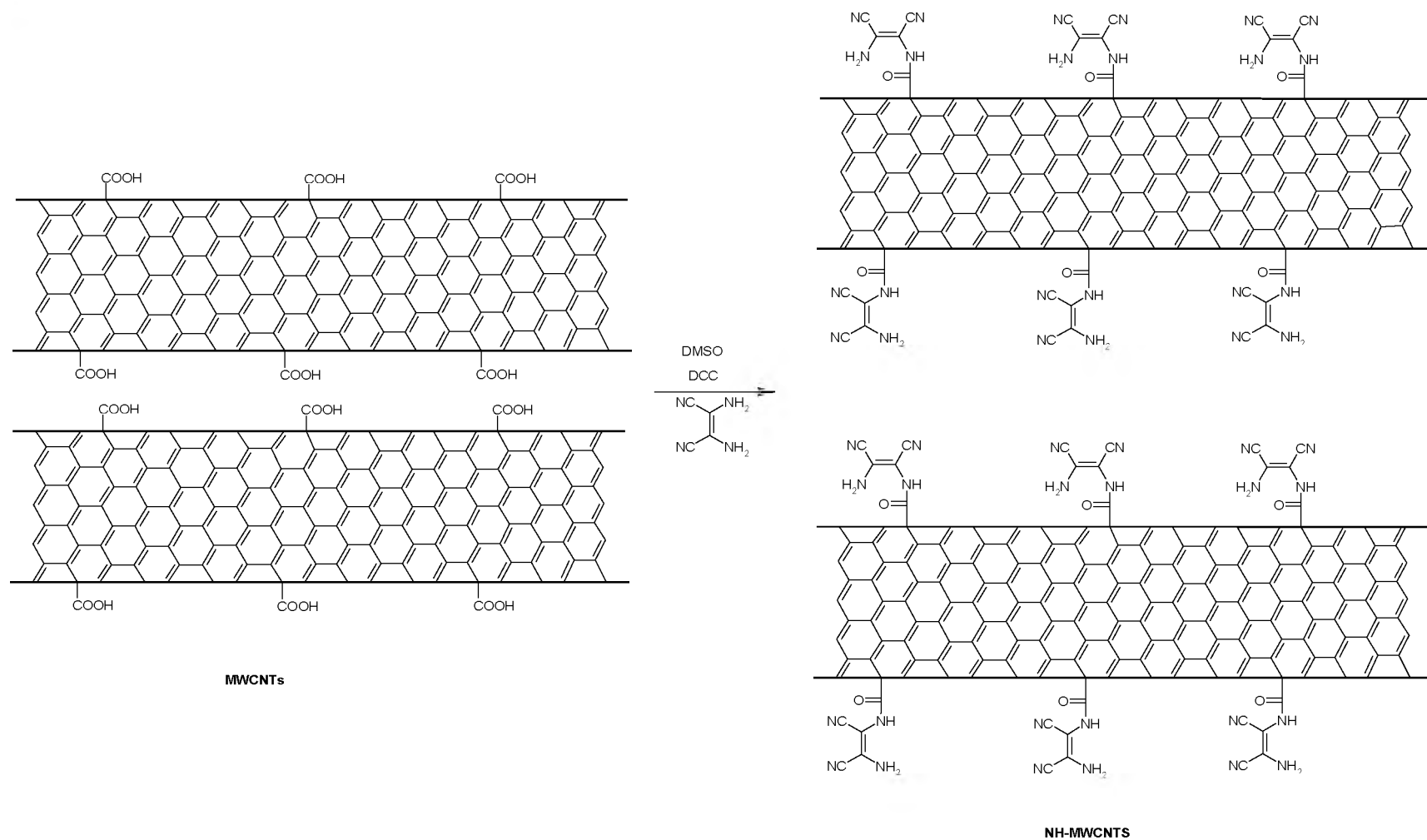
Fig. 3.10: Absorption spectra of complex 30 in DMF and DMSO ($C = 1.6 \times 10^{-5}$ M).

Sub-summary: it was observed that the low symmetry binuclear Pc (19) is blue shifted compared to its symmetrical monomer Pc (18). The LnPc_2 complex (for example, complex 23) can be structurally distorted, depending on the nature of substituent. On addition of a reductant (for example, neutral 28 and reduced 28), the Q band of an LnPc_2 complex blue shifts, leaving a shoulder in the NIR. CePc_2 (27) was found as existing without π -radicals. The UV-Vis spectra of 30 and 31 are typical of Ln_2Pc_3 complexes.

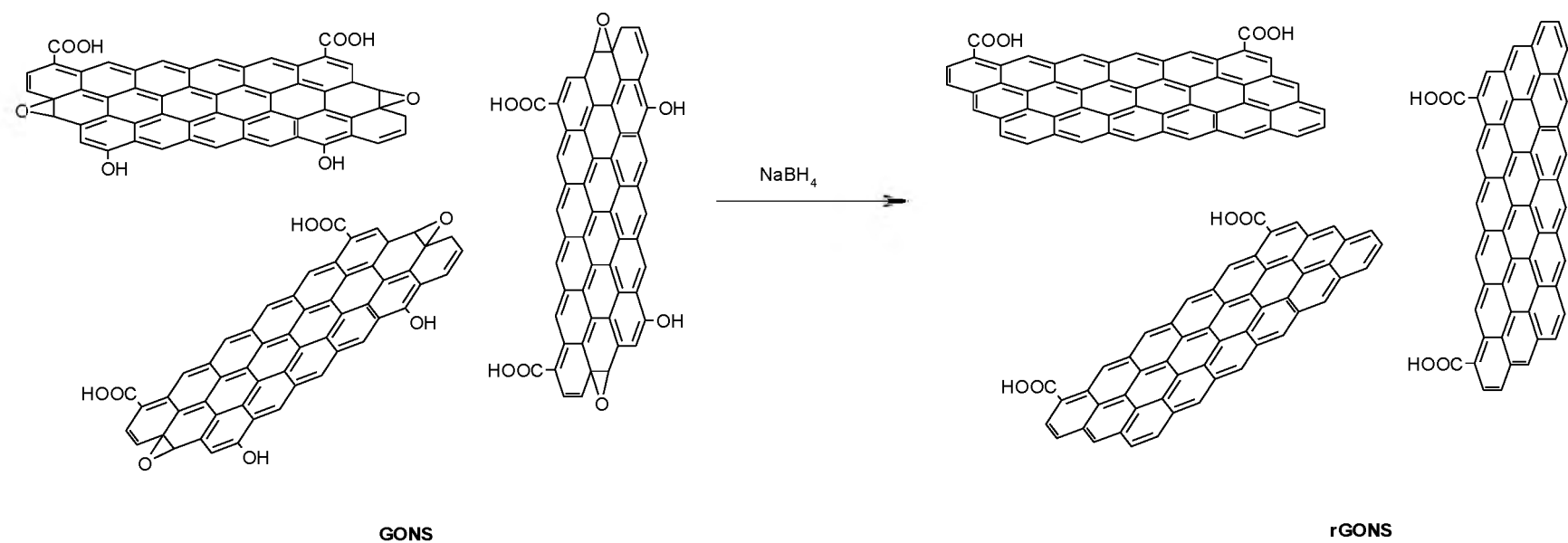
3.2 Characterization of nanomaterials and conjugates

3.2.1 Functionalization of multi-walled carbon nanotubes and graphene oxide nanosheets

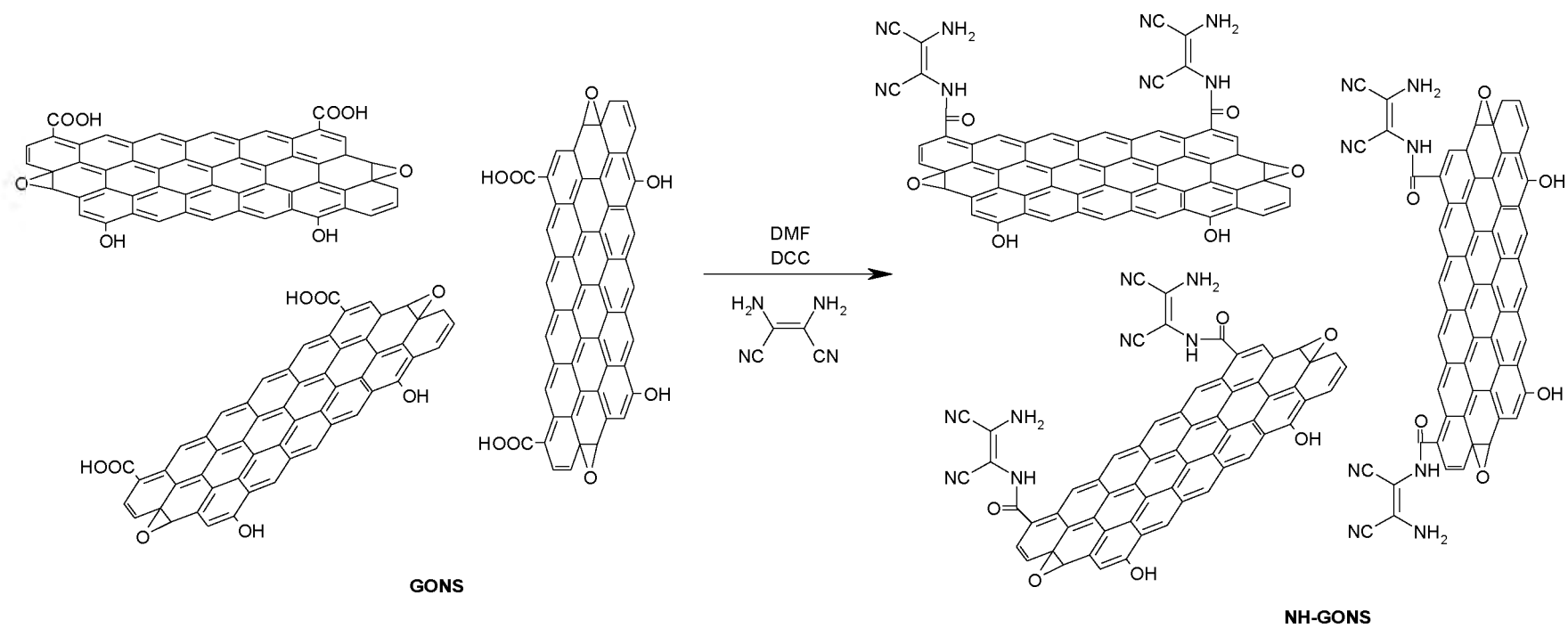
Multi-walled carbon nanotubes (MWCNTs) were functionalized with diaminomaleonitrile after activating the COOH groups on MWCNTs using DCC as a coupling agent in DMSO to form NH-MWCNTs (**Scheme 3.13**). Graphene oxide nanosheets (GONS) were reduced with NaBH_4 to form reduced GONS (**rGONS**; **Scheme 3.14**). NH-GONS (**Scheme 3.15**) was formed from GONS whose COOH groups were activated by DCC in DMSO and linked to diaminomaleonitrile. DCC was added to the solution of **rGONS** in DMSO to activate the COOH groups for coordination with diaminomaleonitrile to form NH-**rGONS** (same as **Scheme 3.15**).



Scheme 3.13: Synthesis of diaminomaleonitrile-functionalized MWCNTs (NH-MWCNTs).



Scheme 3.14: Reduction of GONS to form rGONS.



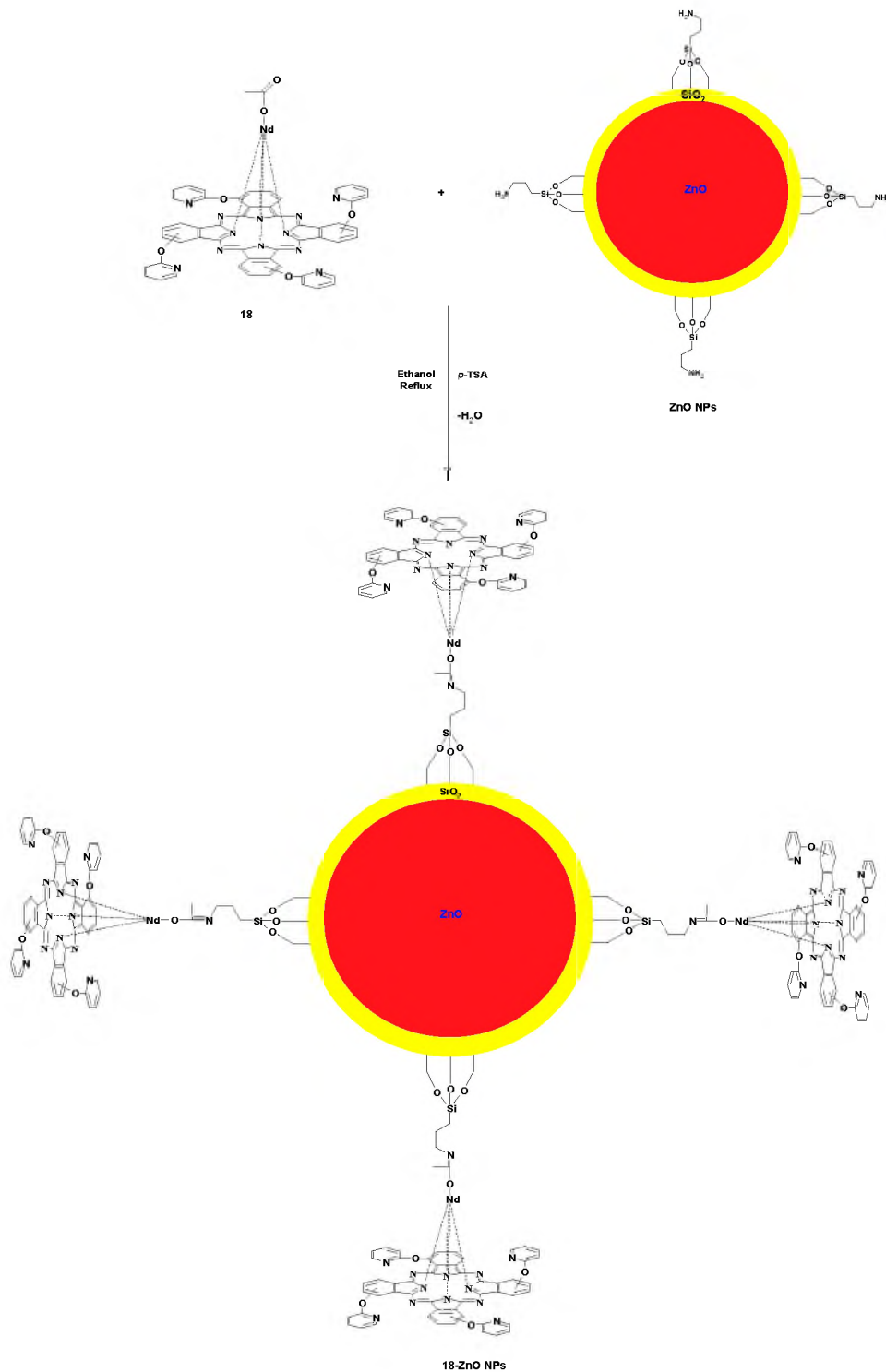
Scheme 3.15: Surface modification of GONS with diaminomaleonitrile to form NH-GONS.

3.2.2 Linking of phthalocyanines to nanomaterials

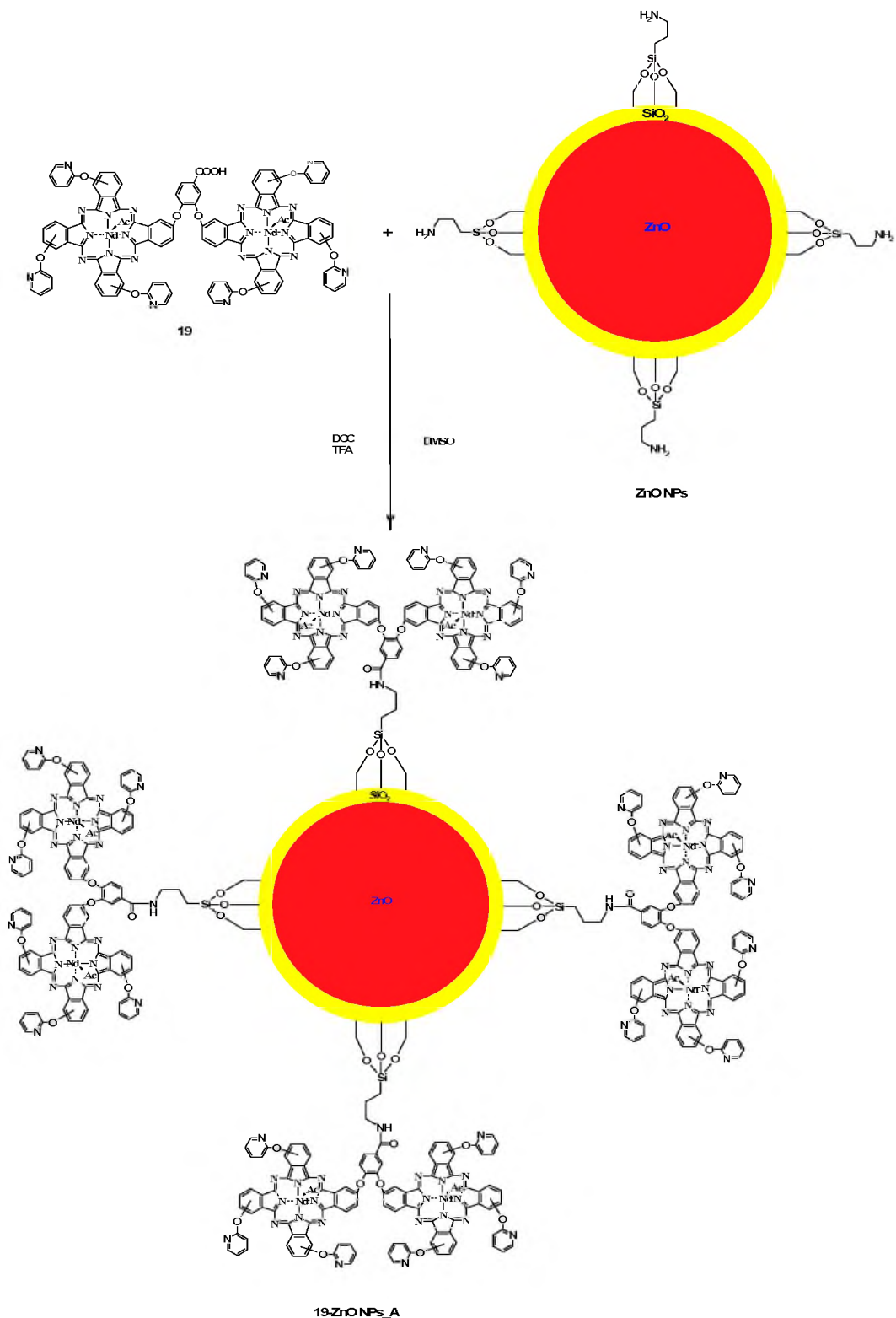
The formation of **18-ZnO NPs** (Scheme 3.16) involved refluxing complex **18** and ZnO NPs in ethanol at moderate temperatures and axially linking the two entities (**18** and ZnO NPs). *p*-TSA was employed as a catalyst for the dehydration reaction between ZnO NPs and complex **18** to form **18-ZnO NPs**, with ethanol used as solvent medium. The amide bond formation between the COOH group of the bridging ligand of complex **19** and the amino group the ZnO NPs was facilitated by DCC as a coupling agent in the presence of TFA to form **19-ZnO NPs_A** (Scheme 3.17). **19-ZnO NPs_B** (Scheme 3.18) was formed as explained for **18-ZnO NPs** above.

The number of Pc molecules bonded to the ZnO NPs were estimated following literature methods, but using absorption instead of fluorescence [323]. This involves comparing the Q band absorbance intensity of the Pcs in the conjugate with that of the initial Pcs before conjugation. By measuring the absorption intensities of complexes **18**, **19**, **19-ZnO NPs_A**, **19-ZnO NPs_B** and **18-ZnO NPs** with gravimetrically equal amounts of Pcs and the conjugates, the number of Pcs bonded to ZnO NPs were estimated as Pcs: ZnO NPs ratio, to be: 2:1 (for complex **19-ZnO NPs_A**), 3:1 (for complex **19-ZnO NPs_B**) and 4:1 (for complex **18-ZnO NPs**). Complex **18** is smaller than **19**, so there are more molecules of **18** linked to ZnO NPs in **18-ZnO NPs** than for **19-ZnO NPs_A** or **19-ZnO NPs_B**. Conjugate **19-ZnO NPs_B** is bonded to ZnO NPs through the axial ligand and accommodates slightly more Pcs on ZnO NPs than

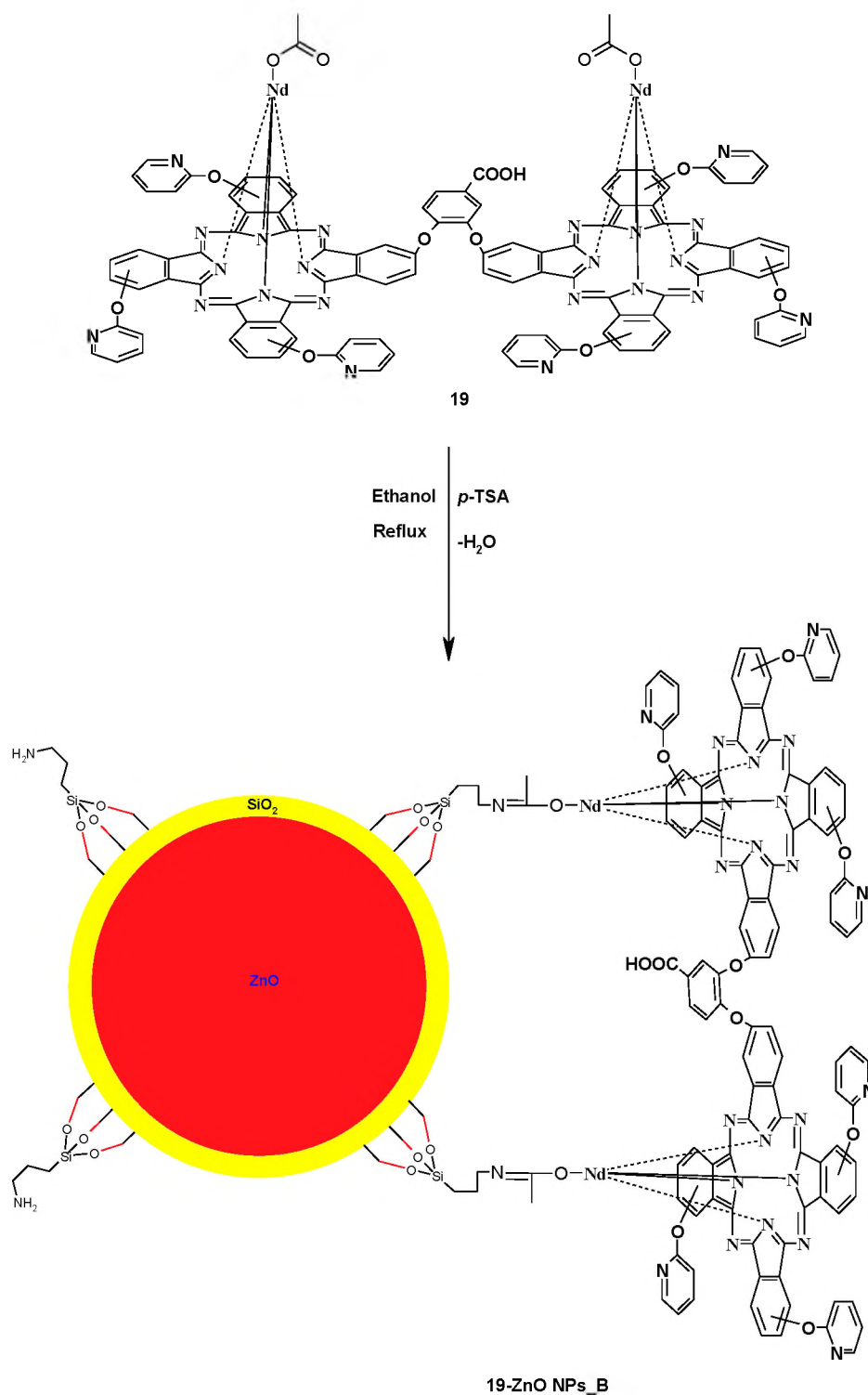
conjugate **19-ZnO NPs_A**, using a bridging ligand for conjugation.



Scheme 3.16: Schematic representation of complex **18** linked to **ZnO NPs**. This molecule is presented as **18-ZnO NPs** throughout this thesis.

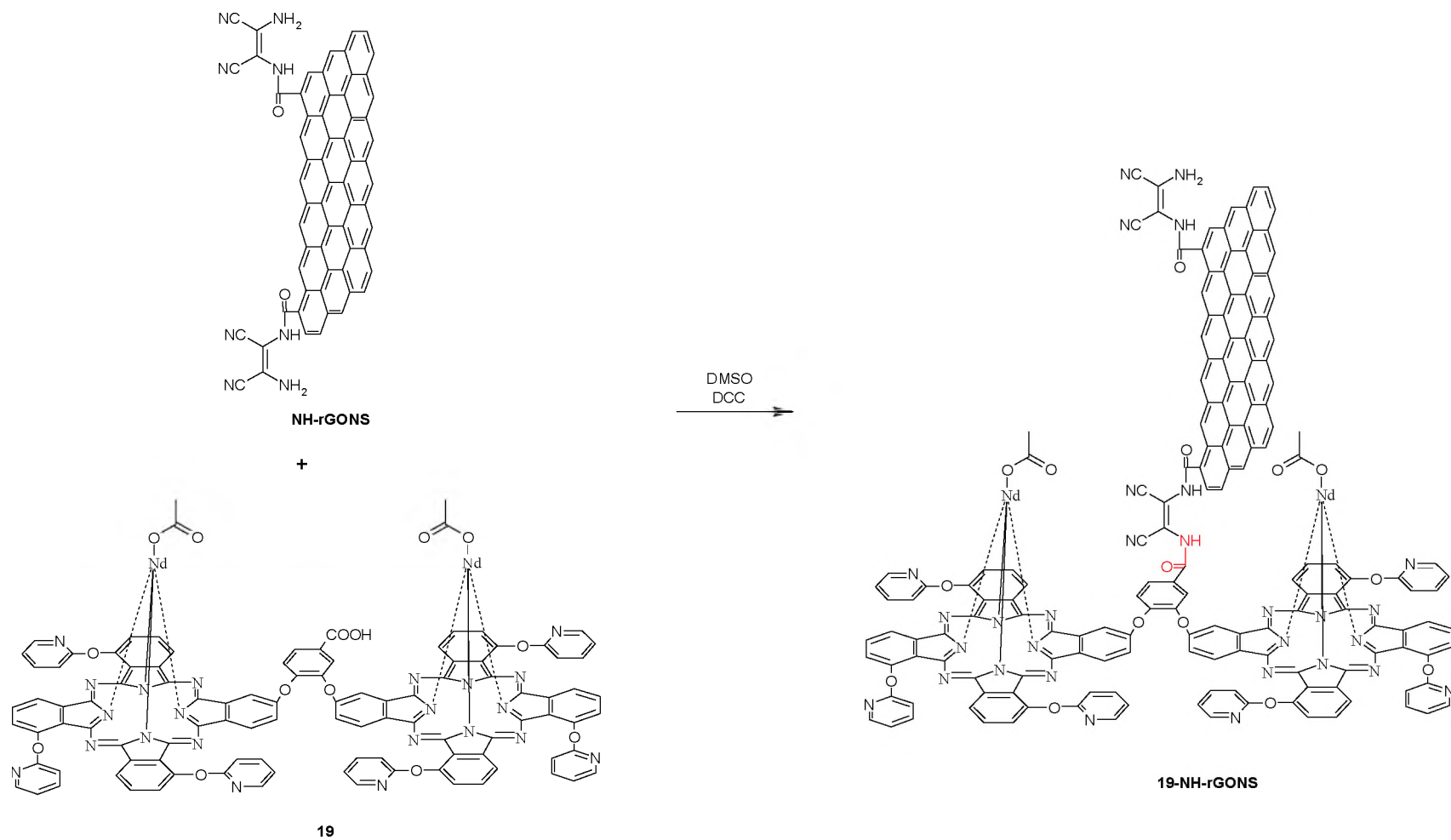


Scheme 3.17: Schematic representation of complex **19** linked to ZnO NPs. This molecule is presented as **19-ZnO NPs_A** throughout this thesis. Ac = C₂H₃O₂.

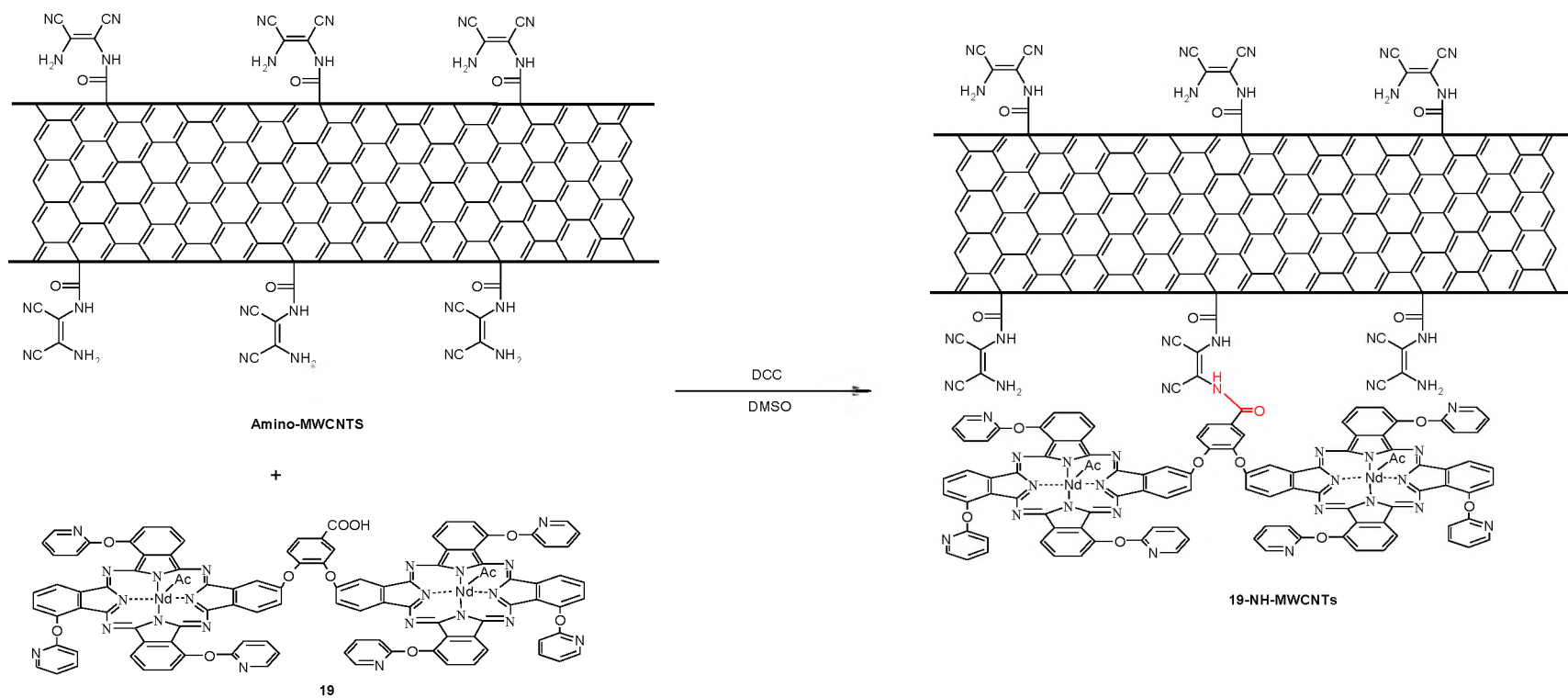


Scheme 3.18: Schematic representation of complex **19** linked to ZnO NPs via axial ligand. This molecule is presented as **19-ZnO NPs_B** throughout this thesis.

19-NH-GONS, **19-NH-rGONS** (Scheme 3.19) and **19-NH-MWCNTs** (Scheme 3.20) were formed by linking **NH-GONS**, **NH-rGONS** and **NH-MWCNTs**, respectively, to complex **19** through the use of DCC as a coupling agent, as explained for **19-ZnO NPs_A** above.



Scheme 3.19: Covalent linking of complex 19 to NH-rGONS to form 19-NH-rGONS.



Scheme 3.20: Covalent linking of complex 19 to NH-MWCNTs to form 19-NH-MWCNTs.

3.2.3 Transmission electron microscopy

Fig. 3.11 shows the TEM images of complexes ZnO NPs, 19-ZnO NPs_A, 19-ZnO NPs_B and 18-ZnO NPs. Samples were prepared in ethanol for the image capturing using TEM. As shown in Fig. 3.11A, nanoparticles of complex ZnO NPs are mono dispersed and have a size average of 10 nm. For complex 19-ZnO NPs_A, the average size was found to be about 13 nm. This increase in size for complex 19-ZnO NPs_A suggests aggregation of the Pcs. The sizes obtained for complexes 19-ZnO NPs_B and 18-ZnO NPs are averaged at 27 nm and 45 nm respectively. The increase in the size corresponds to the number of Pcs bonded to the ZnO NPs and the resulting aggregation.

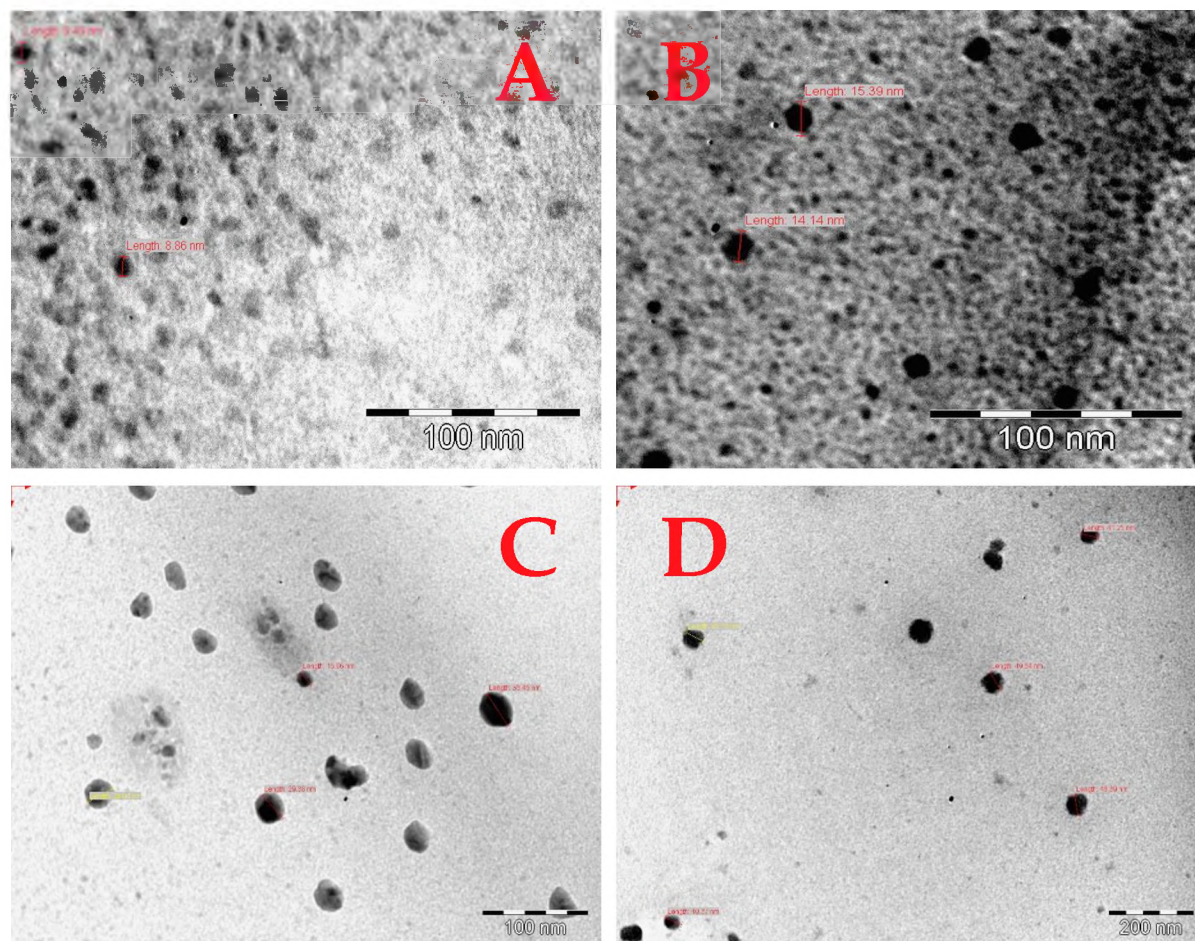


Fig. 3.11: TEM images of (A) ZnO NPs, (B) 19-ZnO NPs_A, (C) 19-ZnO NPs_B and (D) 18-ZnO NPs.

Fig. 3.12 shows the TEM images of NH-MWCNTs and 19-NH-MWCNTs. The TEM image of NH-MWCNTs alone (Fig. 3.12A) shows well dispersed NH-MWCNTs with relatively smooth surface. However, there are clusters towards the ends of some NH-MWCNTs. These clusters may be due to organic functionality, impurities or agglomeration, as also observed elsewhere for single-walled carbon nanotubes [266,324]. However, on linking NH-MWCNTs to complex 19 (to form 19-NH-MWCNTs) there is a huge change on the images of NH-MWCNTs (Fig. 3.12B). The tubes are well dispersed

with much smoother surface. Clusters, impurities and agglomeration are not evident. This observation is a confirmation of structural changes occurring on formation of 19-NH-MWCNTs.

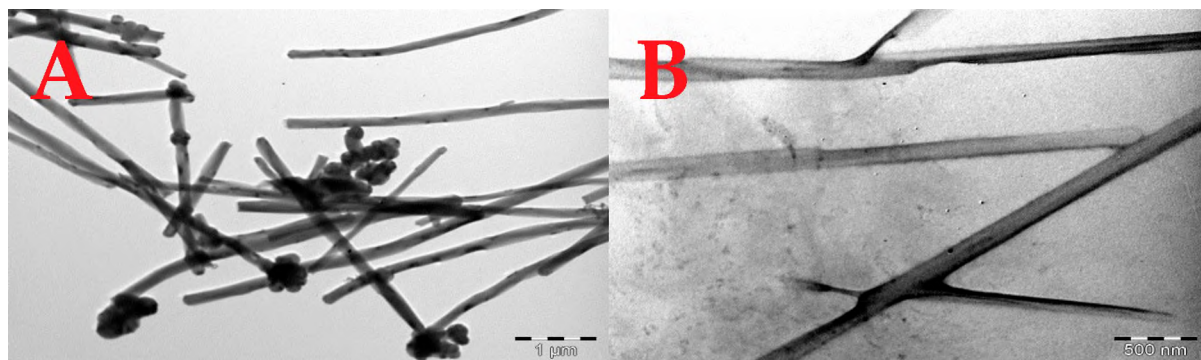


Fig. 3.12: TEM images of (A) NH-MWCNTs alone and (B) 19-NH-MWCNTs.

The TEM image of NH-GONS alone are shown in Fig. 3.13A. As can be seen in Fig. 3.13A, NH-GONS are not aggregated and are similar to TEM images of NH-rGONS (Fig. 3.13B), confirming that the reduction method employed for the preparation of NH-rGONS was not destructive and did not encourage π - π stacking. As stated above, organic functionality, impurities or agglomeration cause cluster-like structures on carbon-based nanomaterials. Therefore the black spots on NH-GONS and NH-rGONS are due to diaminomaleonitrile which acts as an impurity on the surface of GONS.

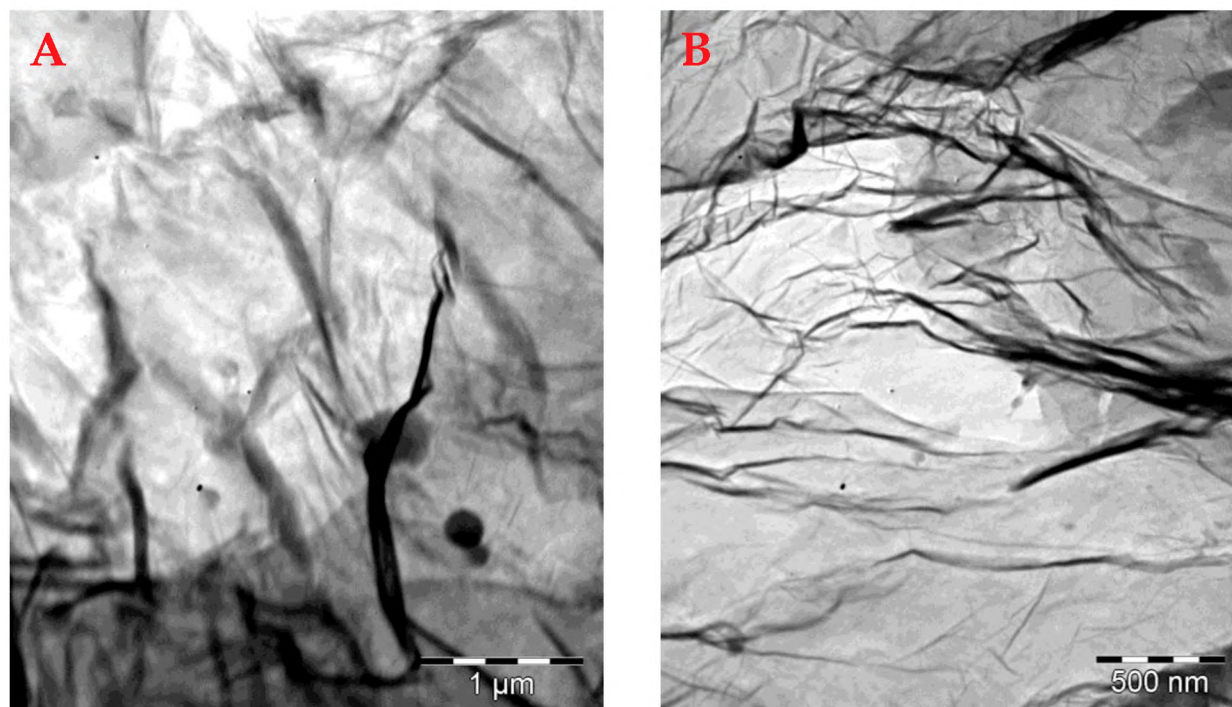


Fig. 3.13: TEM images of (A) NH-GONS and (B) NH-rGONS.

Sub-summary: TEM images showed changes on the surface of the modified molecules.

3.2.4 FTIR spectral data

ZnO NPs show two C-O stretches at 923 and 976 cm^{-1} , Fig. 3.14, originating from the capping ligand. The vibrational stretches for amines appear in the same region as the OH stretches. Because of this overlapping, the NH_2 stretch can be buried inside the OH stretch that appears at 3267 cm^{-1} . When complex **19** is linked to ZnO NPs to form **19-ZnO NPs_A** via the carboxyl group, amide I and II stretches appear at 1651 cm^{-1} and 1625 cm^{-1} , Fig. 3.14. For **19-ZnO NPs_A**, the NH stretch appears at 3323 cm^{-1} as a sharp peak. All these stretches confirm successful formation of **19-ZnO**

NPs_A. On closely inspecting the vibrational frequencies, it is observed that the C=O stretches for **19-ZnO NPs_B** appear at 1704 cm^{-1} compared to **19** at 1712 cm^{-1} . The C=O stretch observed at 1654 cm^{-1} for **19**, which results from the COOH group, is maintained for **19-ZnO NPs_B** at 1656 cm^{-1} . The C=O observed at 1634 cm^{-1} and 1538 cm^{-1} for complex **18** are diminished in **18-ZnO NPs** and observed at 1636 cm^{-1} and 1548 cm^{-1} .

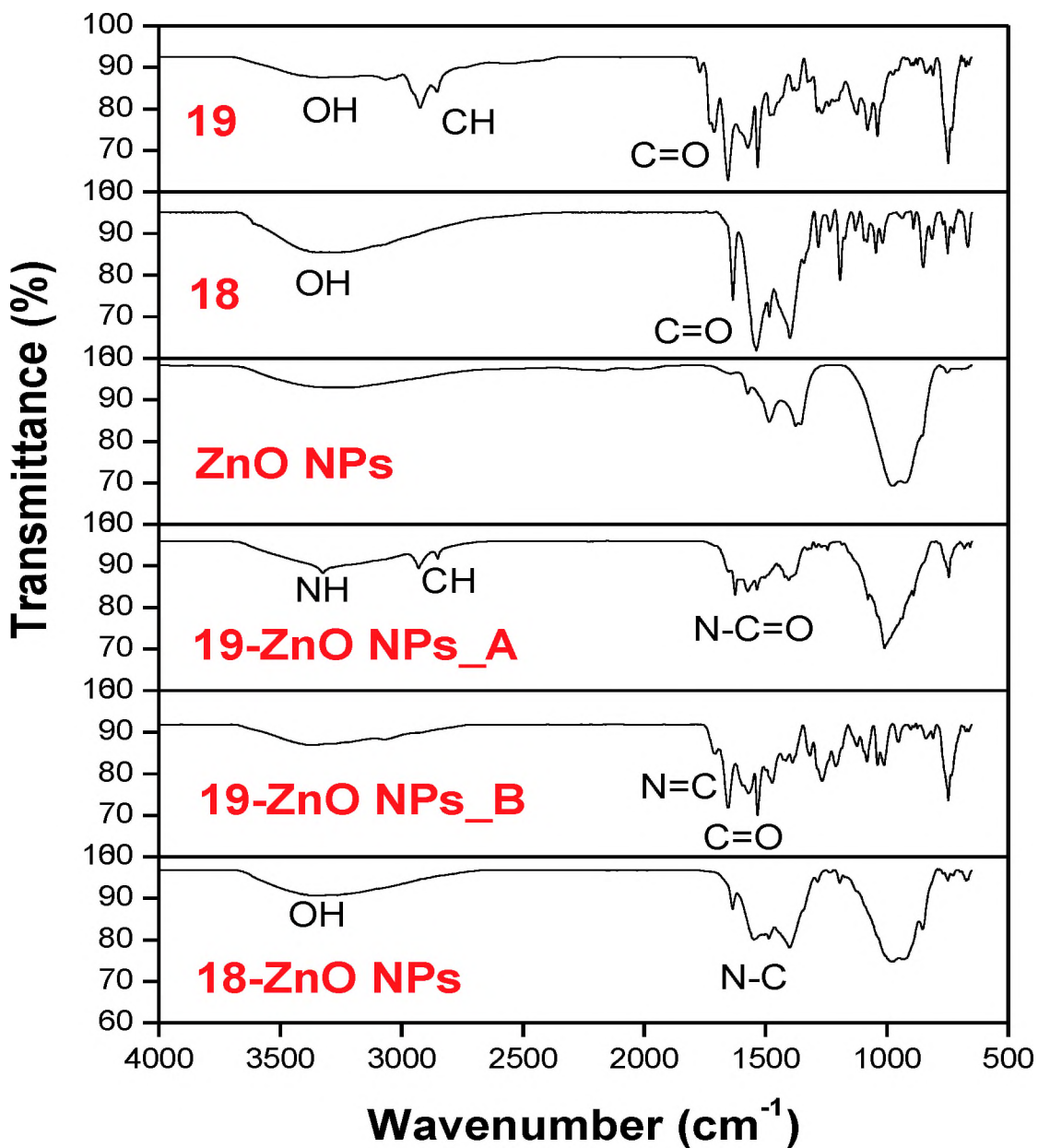


Fig. 3.14: IR spectra of complexes 19, 18, ZnO NPs, 19-ZnO NPs_A, 19-ZnO NPs_B and 18-ZnO NPs in solid state.

On functionalizing COOH-MWCNTs with diaminomaleonitrile, a sharp NH stretch (3783 cm^{-1}) appears. Amide I and amide II appeared at 1621 cm^{-1} and 1568 cm^{-1} thus confirming amide bond formation between **19** and NH-MWCNTs to form **19-NH-MWCNTs**, Fig. 3.15.

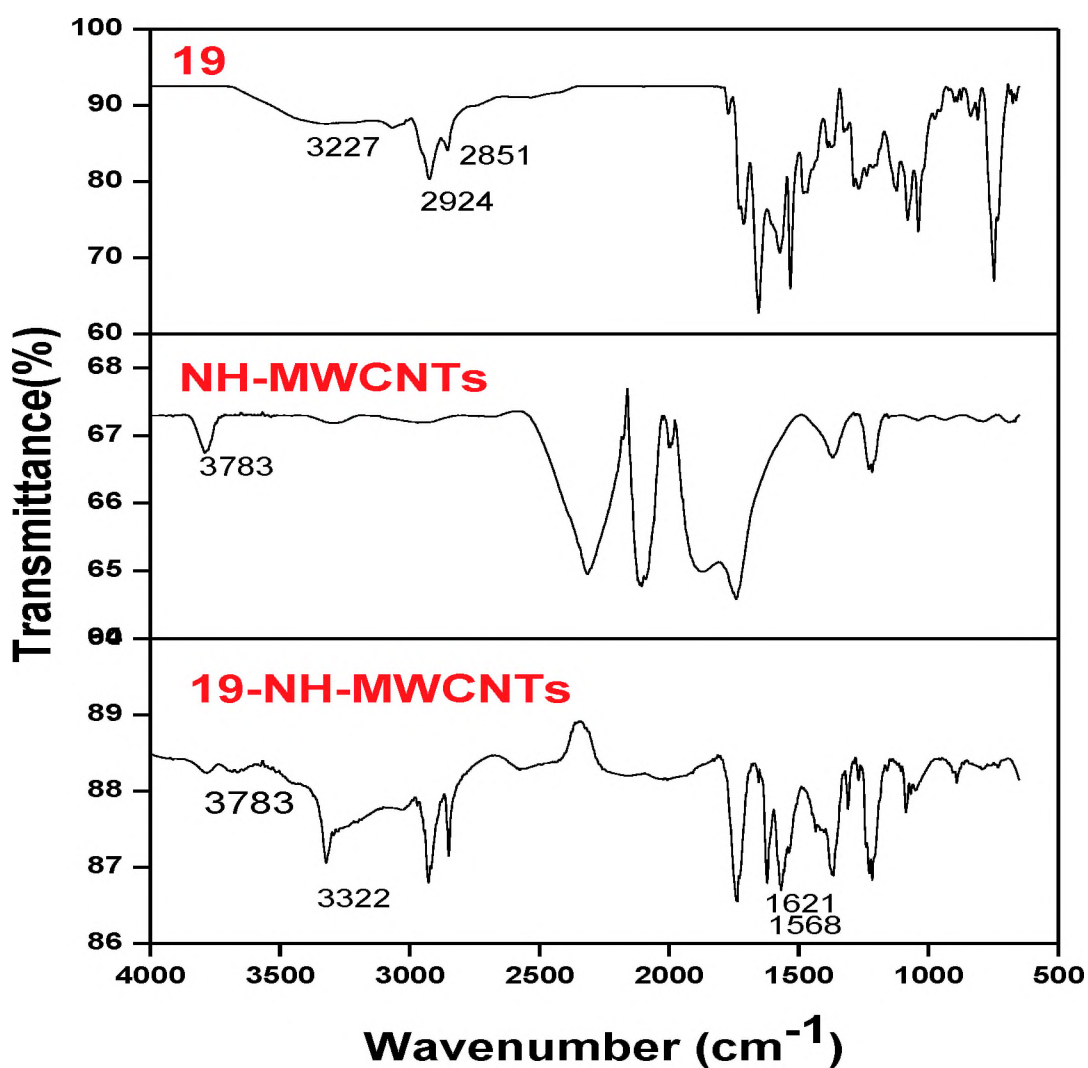


Fig. 3.15: FT-IR spectra for **19**, NH-MWCNTs and **19-NH-MWCNTs**.

Amide I and II appear at 1623 and 1569 cm^{-1} for NH-GONS and at 1635 and 1578 cm^{-1} for NH-rGONS, respectively. A sharp NH stretch appeared at 3323 cm^{-1} for NH-GONS, Fig. 3.16. All these characteristic frequencies confirm the amino functionalized of GONS surfaces. When further covalently linked to complex **19**, amide I and II appeared at 1656 and 1533 cm^{-1} , respectively, for **19-NH-rGONS**. For **19-NH-GONS**, amide I and II appeared at 1563 and 1536 cm^{-1} , respectively. All shifts in amide bond for GONS or rGONS confirm functionalization.

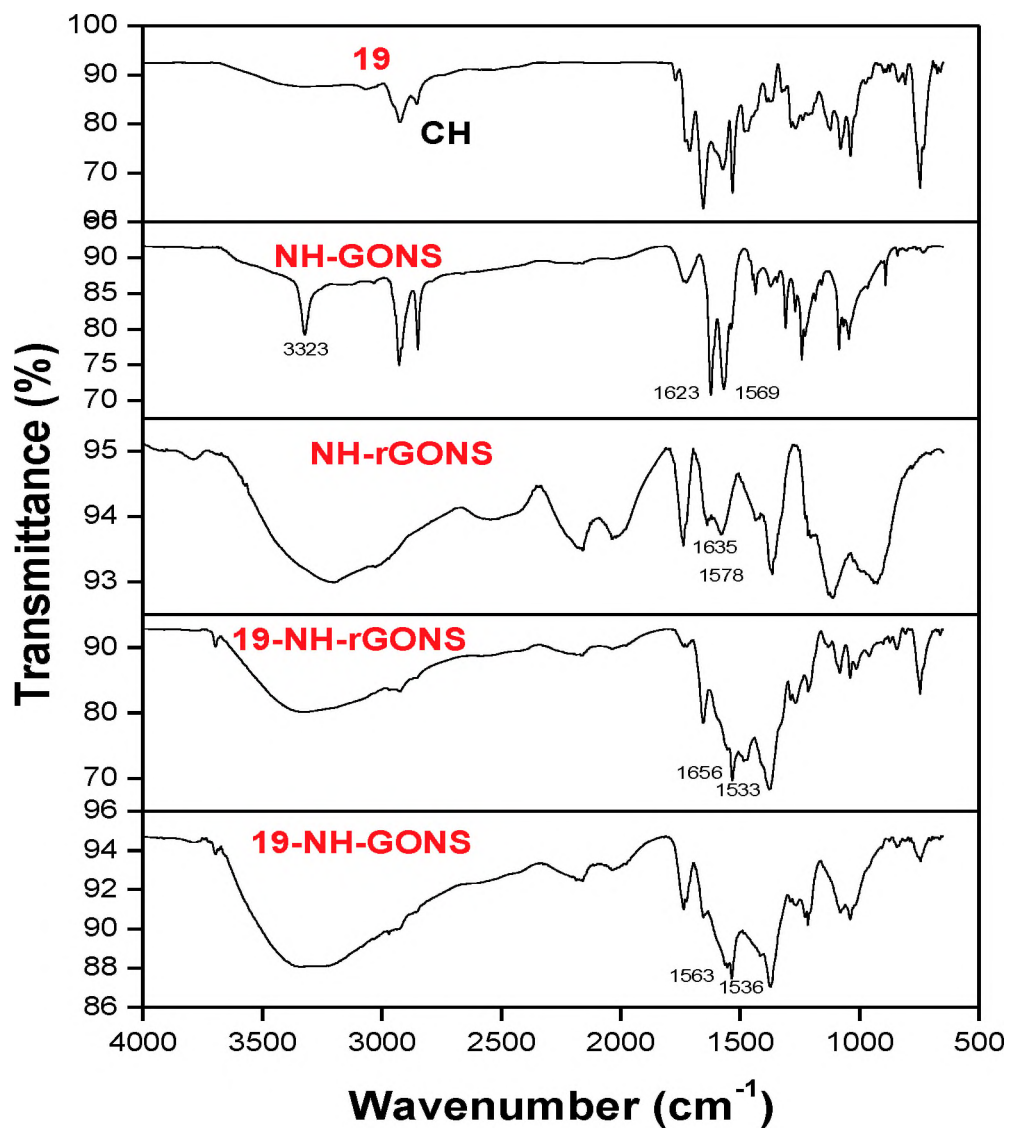


Fig. 3.16: IR Spectra of complex 19, NH-GONS, NH-rGONS, 19-NH-GONS and 19-NH-rGONS.

Sub-summary: IR spectral data for 18-ZnO NPs, 19-ZnO NPs_A, 19-ZnO NPs_B, NH-MWCTs, 19-NH-MWCNTs, NH-GONS, NH-rGONS, 19-NH-GONS and 19-NH-rGONS confirmed the amide bonds.

3.2.5 Electron spin resonance

The ESR signals were maintained in the conjugates with slight broadening as revealed by the band widths of **18-ZnO NPs** (7.26 G), **19-ZnO NPs_A** (8.00 G) and **19-ZnO NPs_B** (8.10 G) compared to 5.44 G for **18** and 6.25 G for **19**. The ESR spectrum of **19-ZnO NPs_A** is shown as an insert in **Fig. 3.2**.

3.2.6 Ultra violet-visible spectral data of nanomaterials and conjugates

The ground state electronic absorption spectra for **19-ZnO NPs_A**, **19-ZnO NPs_B** and **18-ZnO NPs** are compared with those of complexes **18** and **19** in DMSO, **Fig. 3.17**. There is a blue shift for **19-ZnO NPs_A** compared to **19** and a blue shift also for **18-ZnO NPs** compared to **18**. Shifts in the Q band maxima may be due to orientation of Pcs on the ZnO NPs as reported before for other chromophores [325].

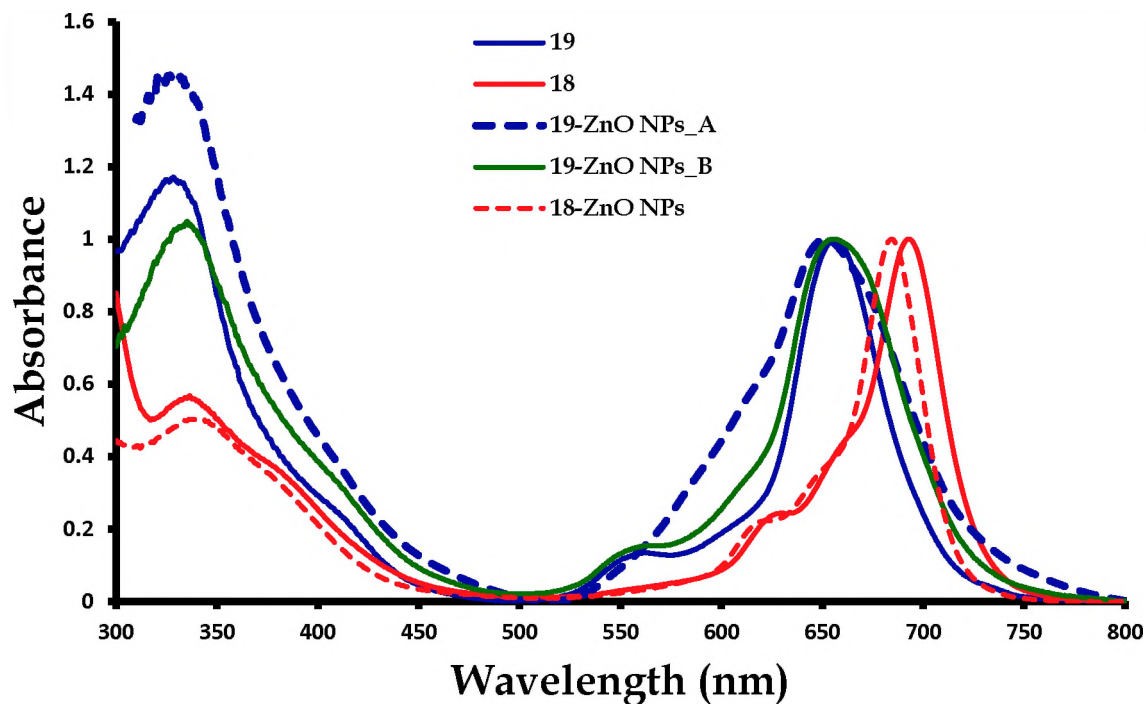


Fig. 3.17: absorption spectra of complexes 18, 19, 19-ZnO NPs_A, 19-ZnO NPs_B and 18-ZnO NPs in DMSO.

The ground state electronic absorption spectra for 19 and 19-NH-MWCNTs are shown in Fig. 3.18. There is an increase in the absorption below 500 nm due to the absorption of NH-MWCNTs. The Q band is also slightly red-shifted from 656 nm (for 19) to 660 nm (for 19-NH-MWCNTs) and broadened, Table 3.1.

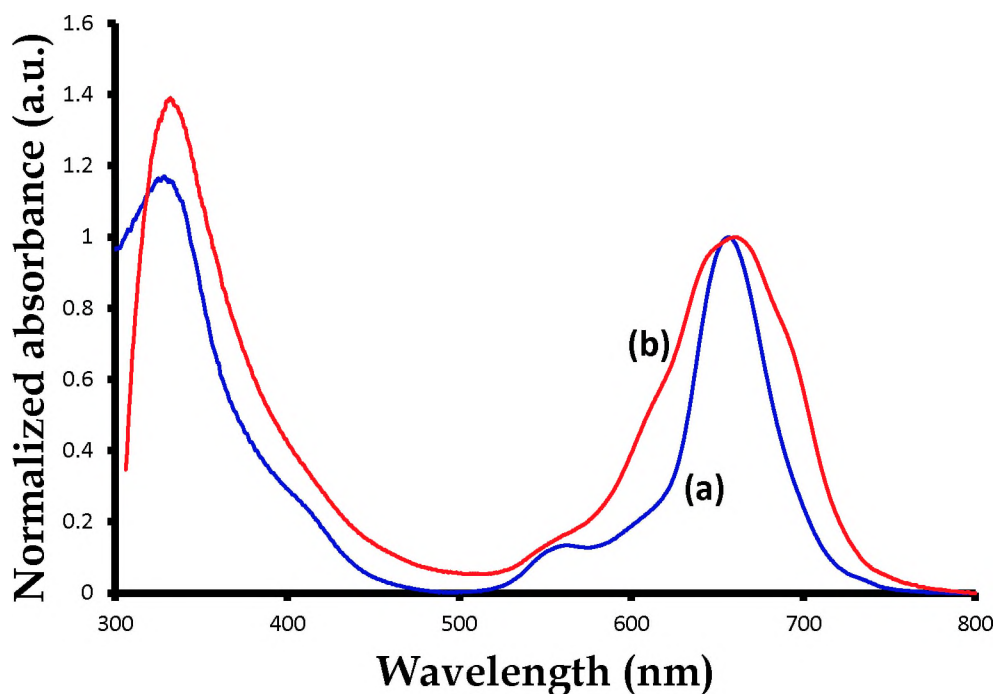


Fig. 3.18: UV-Vis spectra of (a) **19** ($C = 1.6 \times 10^{-5}$ M) and (b) **19-NH-MWCNTs** in DMSO.

The absorption spectra for NH-GONS or NH-rGONS (Fig. 3.19) are broad with a peak at 314 nm (NH-GONS) and 325 nm (NH-rGONS). **19-NH-GONS** and **19-NH-rGONS** show an increase in the absorption below 500 nm due to the absorption of NH-GONS or NH-rGONS. However, the position of the Q band remains unchanged at 656 nm (Fig. 3.19). The Q band is however broadened in the presence of GONS.

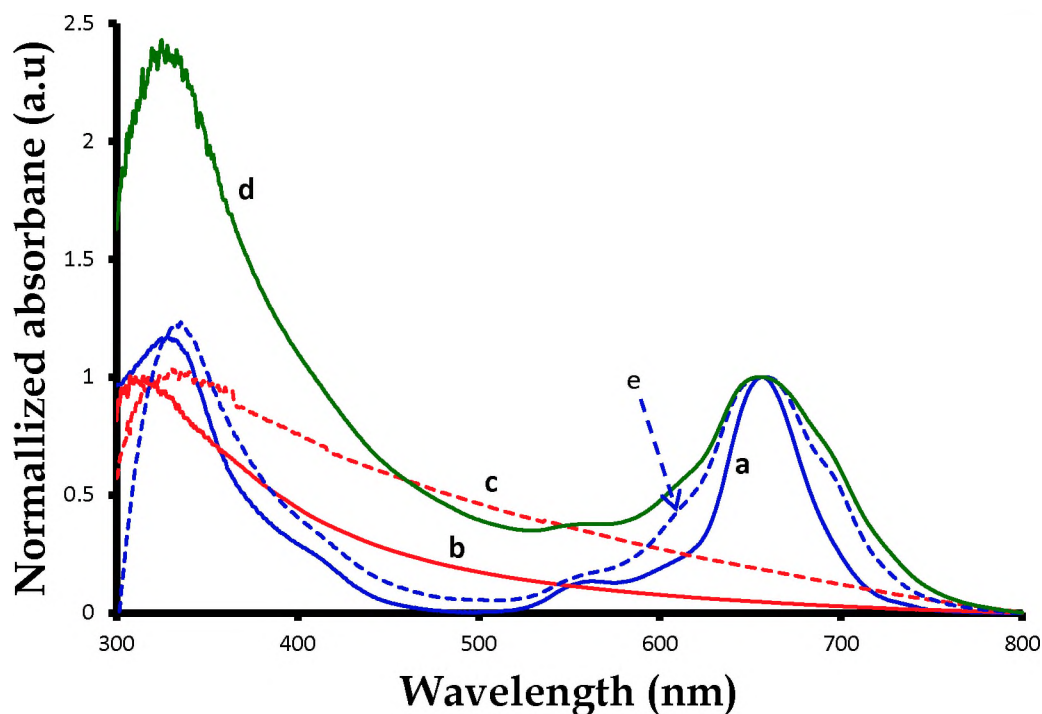


Fig. 3.19: Absorption spectra for (a) complex **19** ($C = 1.6 \times 10^{-5}$ M), (b) NH-GONS, (c) NH-rGONS, (d) **19**-NH-GONS and (e) **19**-NH-rGONS in DMSO.

Chapter summary: Synthesized Pcs and conjugates were characterized by various techniques. The success of conjugation was confirmed by IR, which revealed amide bonds. For LnPc_2 , the Pc^\bullet - IR marker (which is a radical) was proved by IR and UV-Vis spectroscopy, except for CePc_2 which does not possess any radical. The Q band maxima do not change on linking Pcs to nanomaterials. Similarly for CePc_2 and Ce_2Pc_3 , the Q band maxima remained the same despite the extended π -electron system in Ce_2Pc_3 .

Chapter 4

Photophysical and Photochemical Studies

4.1 Emission spectral data

Emission and excitation spectral data of complexes **18**, **19**, **24**, **27**, **29** and **31** as well as conjugates for complexes **18** and **19** are not discussed in this work due to lack fluorescence shown by such complexes. This applies to fluorescence quantum yields and lifetimes discussed below. Emission for complexes containing lanthanide is weak due to heavy atom effect and for LnPc₂ (neutral) also due to paramagnetic nature.

4.1.1 Trinuclear phthalocyanines

The excitation, absorption and emission spectra for complex **20** (Fig. 4.1 as an example) and complex **21** were recorded in DMSO. It was observed that complexes **20** and **21** behave in a similar way with weak emission spectra. The complexes showed broadening due to aggregation effects in the absorption spectra (which are more enhanced for complex **21**), which does not appear in the excitation spectra.

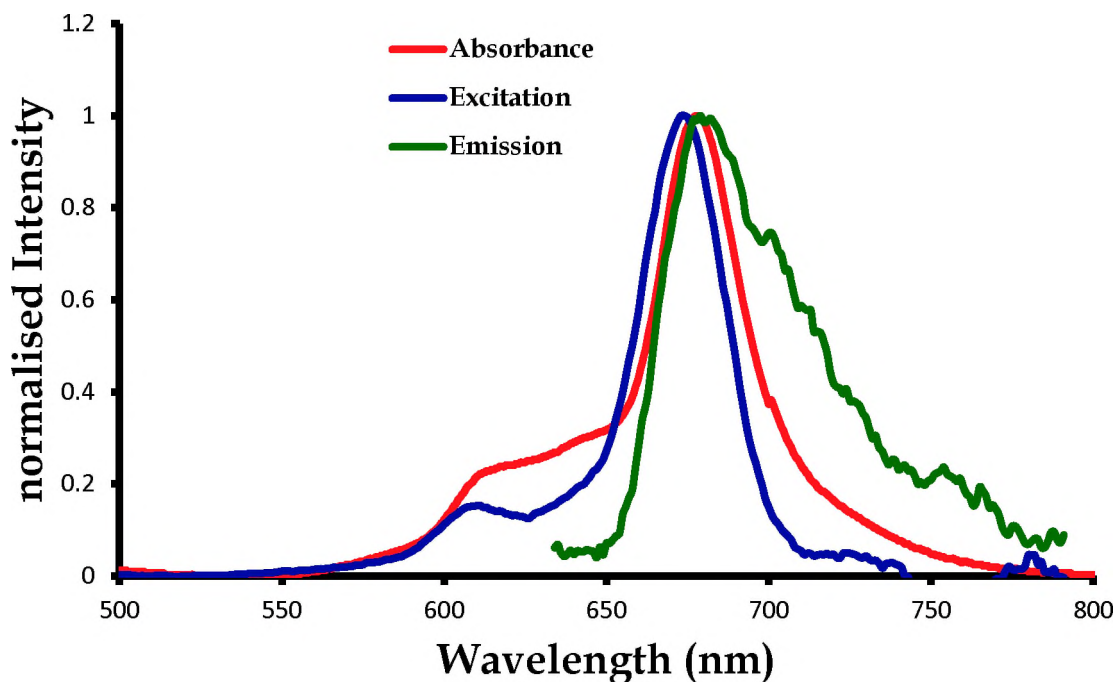


Fig. 4.1: Absorption and fluorescence spectra of complex **20** in DMSO.

4.1.2 Lanthanide bis(phthalocyanines)

YbPc₂ complexes are known to fluoresce [306], but fluorescence is expected to be weak as discussed above [326]. An emission in the IR region has also been reported for Yb phthalocyanine incorporated in silica gel [327].

The absorption, excitation and emission spectra of **22** are shown in Fig. 4.2 and used as an example. For **22**, the emission spectrum was broad compared to the excitation spectrum and the later was the same as the absorption spectrum except for the slight shift in the Q band maxima, which could be due to different equipment. Only a very weak emission was observed for **23** due to the deformation discussed above. The distortion in

the macrocycles such as porphyrins results in decrease in fluorescence [328]. Hence, the decrease in fluorescence for **23**.

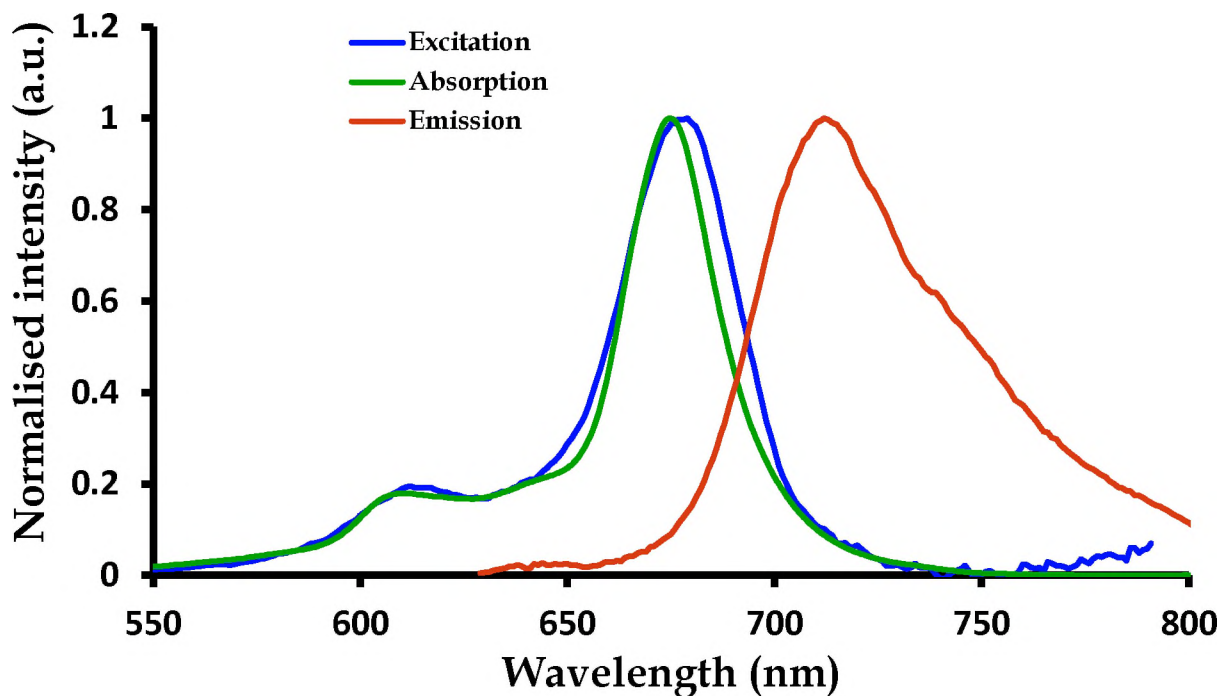


Fig. 4.2: Absorption, excitation and emission spectra of complex **22** in DMSO.

For the rest of the fluorescing LnPc₂ complexes (**25**, **26**, **27** and **28**), absorption and emission spectra were similar and mirror images of the emission spectra (figures not shown). Some were affected by aggregation, hence absorbances were broader than excitation spectra.

Table 4.1: Photophysico-chemical parameters of phthalocyanines alone and conjugates presented in this thesis.

Complex	Φ_F	Φ_T	τ_F (ns)	τ_T (μ s)	Solvent
19	-	0.08	-	79	DMSO
18	-	0.01	-	65	SMSO
19-ZnO NPs_A	-	0.34	-	89	DMSO
19-ZnO NPs_B	-	0.61	-	171	DMSO
18-ZnO NPs	-	0.70	-	225	DMSO
20	<0.01	0.65	^a 3.18	3.51	DMSO
21	~0.01	0.74	^a 3.86	52.7	DMSO
22	~0.01	0.89	^a 4.82	225	DMSO
23	<0.01	0.48	^a 2.60	4.91	DMSO
25	0.02	-	^a 2.26	-	DMSO
26	0.02	-	^a 2.59	-	DMSO
27	0.01	-	5.68	-	CHCl ₃
Neutral 28	0.03	-	^a 3.71	-	DMSO
Reduced 28	0.10	0.68	^a 2.18	375	DMSO
30	0.03	-	^a 4.31	-	DMSO
31	0.03	-	^a 5.88	-	CHCl ₃

a = average fluorescence lifetimes; - = photophysical parameter values not determined or that do not exist as discussed in the text.

4.2 Photophysical data

4.2.1 Fluorescence quantum yields (Φ_F) and lifetimes (τ_F)

Fluorescence studies were carried out in DMSO. Low Φ_F values were observed due to the paramagnetic nature (for complexes **20**, **22**, **23**, **25** and **27**) and the heavy atom effect that encourages intersystem crossing to the triplet state (for complexes **20**, **21**, **22**, **23**, **25**, **26**, **27**, neutral **28**, **30** and **31**). **Table 4.1**. Φ_F values lower than 0.01 have been reported for lanthanide phthalocyanines [76]. The fluorescence lifetime decay curves for complex **20**, **Fig. 4.3(i)**, and complex **21**, **Fig. 4.3(ii)** (as examples) were obtained by a bi-exponential fitting, with the calculated average fluorescence lifetimes ($\tau_{F(AV)}$) of each trinuclear lanthanide phthalocyanine listed in **Table 4.1**. The two lifetimes (average lifetimes shown in **Table 4.1**) could be due to the presence of small amounts of aggregates which may quench fluorescence [329]. Fluorescence lifetimes are within the range reported for monomeric phthalocyanines [330]. Complex **20** is shorter lived than **21** due to its paramagnetic nature.

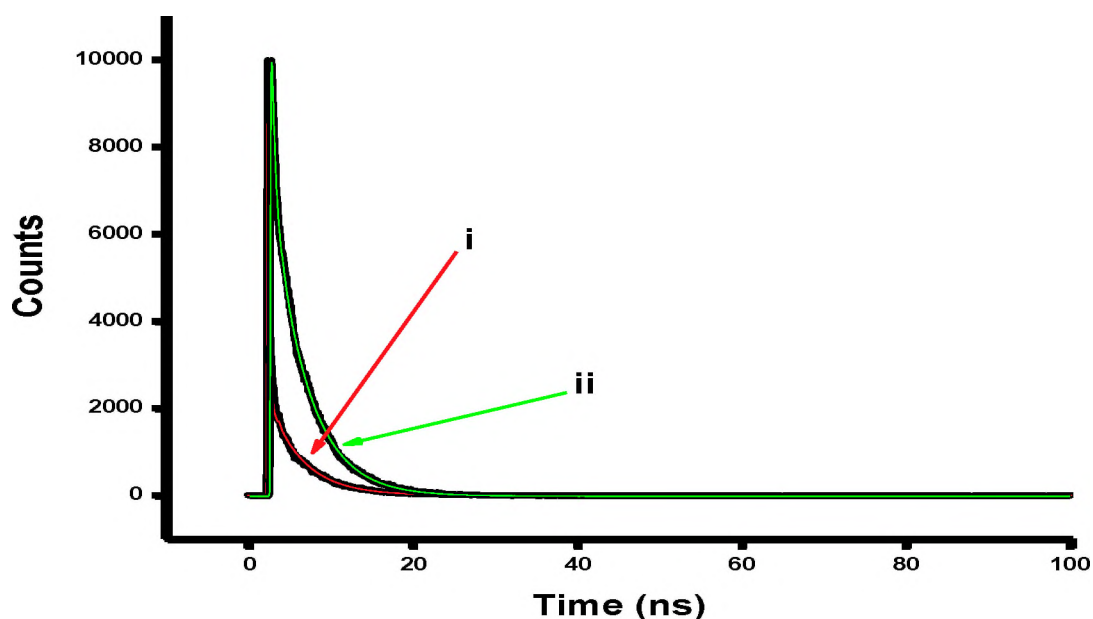


Fig. 4.3: Fluorescence lifetime decay curves of (i) complex 20 and (ii) complex 21 in DMSO.

As discussed above for absorption, low Φ_F values for complex 23 may be due to the distortion in the chemical structure on excitation. As stated above the out-of-plane deformations can quench the fluorescence lifetime [328], which is the case with complex 23 having shorter $\tau_{F(AV)}$ compared to complex 22, Table 4.1.

Φ_F value as low as 0.02 was obtained for 25 due to the paramagnetic nature of Yb which will encourage intersystem crossing to the triplet state [16]. This value is comparable to that of 26 which is aggregated, Table 4.1. The average lifetimes are longer for 26 compared to 25, Table 4.1. Φ_F values at 0.01 (for complex 27) and 0.03 (for

complexes **30** and **31**) were obtained. The Φ_F values were lower at 0.03 for neutral **28** compared to 0.10 for reduced **28**.

The fluorescence lifetime for complex **30**, was obtained by a bi-exponential fitting and expressed as an average to be 4.31 ns. A value of 5.88 ns was obtained for **31**, **Table 4.1**.

4.2.2 Triplet quantum yields (Φ_T) and lifetimes (τ_T)

Complexes **18** and **19** exhibited weak triplet decay curves as shown in **Fig. 4.4** (for complex **18**). The triplet decay curve was stronger for the conjugates (**Fig. 4.4**, using **18-ZnO NPs** as an example) compared to Pcs alone. The weak triplet decay curves observed for complexes **18** and **19**, are due to the heavy atom and paramagnetic nature of the central metal, which encourages intersystem crossing to the triplet state, but shortens triplet lifetimes. The triplet quantum yields were very low for **18** and **19** but improved when linked to **ZnO NPs**, possibly due to the external heavy atom effect of the latter. In addition to encouraging intersystem crossing to the triplet state, **ZnO NPs** may also form charged species in the presence of excited Pcs. Upon excitation with visible light, the electron hole pair is formed in the highest occupied molecular orbital (HOMO) and lowest unoccupied molecular orbital (LUMO) of the phthalocyanine. The electron in the LUMO is then injected into the conduction band of **ZnO** [331]. This could reduce the population of the excited states. However, the increase in triplet quantum yields show that the population of the triplet state

increased.

Conjugates **19-ZnO NPs_A** and **19-ZnO NPs_B** differ only in the mode of linking to the ZnO NPs, where **19-ZnO NPs_B** is linked via axial ligation and **19-ZnO NPs_A** is linked through the carboxy phenoxy bridge. The latter has a larger triplet quantum yield than the former. This could be related to the number of Pcs linked to ZnO NPs (2:1 for **19-ZnO NPs_A** and 3:1 for **19-ZnO NPs_B**).

The τ_T values are short for complexes **18** and **19** at 65 μs and 79 μs , respectively. However, on linking to ZnO NPs, the τ_T values increased to 89 μs , 171 μs and 225 μs for complexes **19-ZnO NPs_A**, **19-ZnO NPs_B** and **18-ZnO NPs**, respectively. The lengthening of triplet lifetimes could be due to the protection of the Pcs from the environment by ZnO NPs. **18-ZnO NPs** has the largest triplet quantum yield and longest triplet lifetimes of all the conjugates. This could be due to the largest number of Pcs on ZnO NPs.

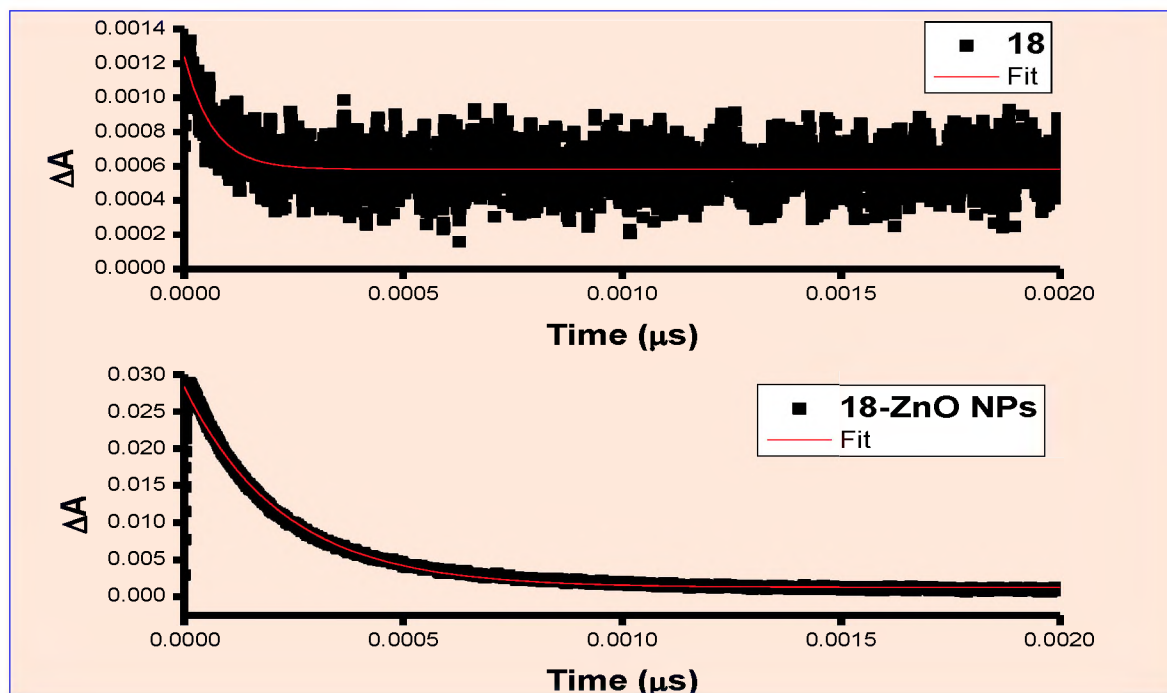


Fig. 4.4: Triplet decay curves of complexes **18** and **18-ZnO NPs** in DMSO.

The triplet quantum yield for **21** at $\Phi_T = 0.74$ was larger than for **20** at $\Phi_T = 0.65$. Both values were high due to the heavy atom effect.

Triplet quantum yield for **22** is large at $\Phi_T = 0.89$, Table 4.1 and a lifetime of 225 μs . However, for complex **23**, Φ_T value is 0.48 (nearly half the Φ_T value of **22**) while τ_T is 4.91 μs . This can be attributed to deformation in **23**.

4.2.3 Singlet oxygen quantum yields (Φ_{Δ})

Singlet oxygen decay curve in the form of changes in the absorption spectra of DPBF in DMSO in the presence of 18-ZnO NPs as a result of irradiation is shown in Fig. 4.5 and Φ_{Δ} values are summarized in Table 4.1. 18-ZnO NPs, 20, 21, 23 and reduced 28 were used as examples for Φ_{Δ} studies. Φ_{Δ} values were low for all complexes except for 20, 21 (which are trinuclear Pcs) and 23 (which is a bis(phthalocyanine)) at 0.13, 0.63 and 0.12, respectively. For reduced 28, Φ_{Δ} value obtained was 0.32. In all cases, Φ_{Δ} values were lower than Φ_T values, showing that not all triplet state species were converted to singlet oxygen. This is an inefficiency of $\Phi_T \rightarrow \Phi_{\Delta}$ transition.

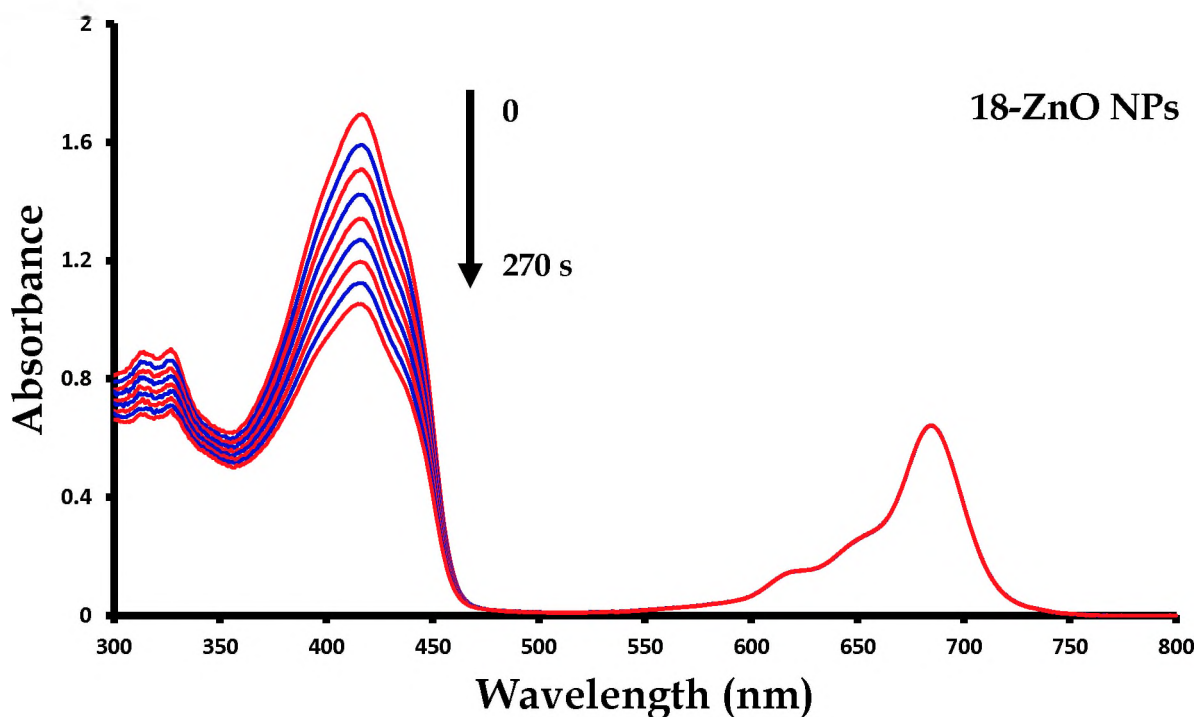


Fig. 4.5: Singlet oxygen absorption decay for 18-ZnO NPs.

Chapter 5

Optical limiting properties

5.1 Phthalocyanines alone

5.1.1 Effects of π -electron system and symmetry

This section compares complexes **18** and **19** as well as **27** and **31**, with each pair containing the same coordinating lanthanide ion but different π -electron system.

5.1.1.1 Complexes **18** and **19**

Reverse saturable absorption (RSA) is a cross-section dependent process [332-334], with the excited state cross section being larger than the ground state cross section for it to occur. As shown in **Fig. 5.1**, complexes **18** and **19** exhibited the RSA process at 3.4×10^{-4} M. However, there are differences in the reduction in transmittance (T_{Norm}). The lack of symmetry in **19** brought about a larger reduction in transmittance than **18**, **Fig. 5.1**. Low symmetry results in improved NLO behavior as stated above [104,110]. Although this phenomenon of asymmetric Pcs exhibiting low limiting threshold values has been observed many times, there is still lack of mechanisms drawn from such molecules to better understand the effects of low symmetry for NLO applications. It can be speculated, therefore, that the differences in the polarities of the substituents in Pcs reduce the scattering of electrons and favor a one-sided movement, resulting in their high concentration over one point. Therefore high active electron densities in low symmetry Pcs (complex **19**) would reduce higher laser beam intensities better than in symmetric molecules (complex **18**). The weak NLO behavior for **18** could be related to their

monomeric behavior (hence less π bonds) and to their symmetrical nature compared to complex **19**. As observed, the molecules with a large number of π electrons (complex **19**) exhibit good RSA when compared to monomeric **18**. The same trend of RSA was observed in thin films where **19-TF** showed enhanced reduction in transmittance compared to **18-TF** (figure not shown for the latter). It has been reported before that thin films improve NLO behavior of Pcs [118], hence more reduction in the transmittance of **19-TF** compared to **19** in solution, Fig. 5.2 (used as example to represent **18** and **18-TF** as well), or **18-TF** compared to **18** in solution. All thin films showed larger reduction in transmittance than for solution.

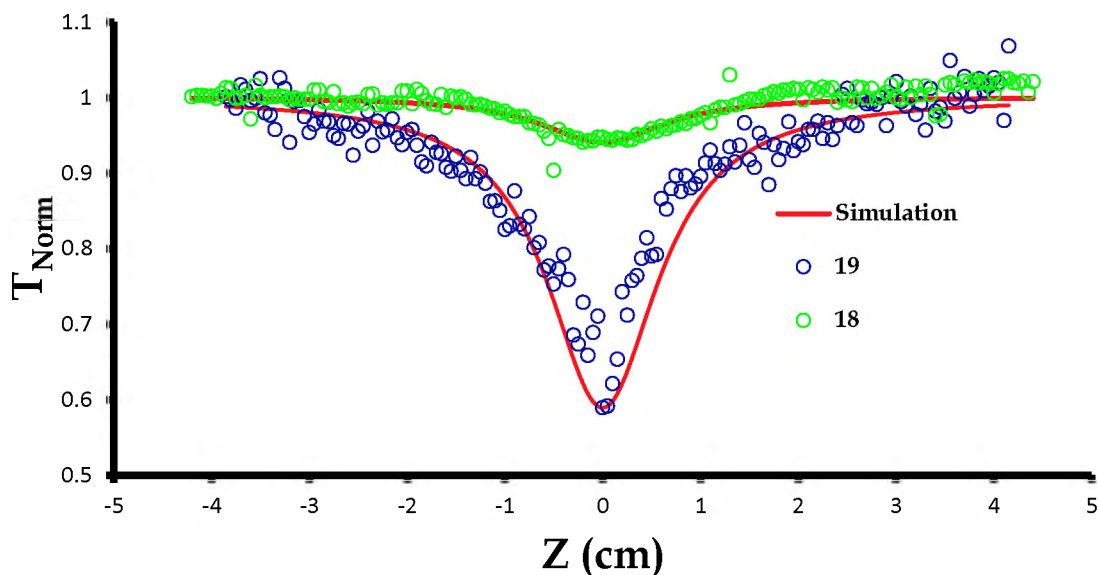


Fig. 5.1: Open aperture Z-scan curves for complexes **18** and **19** in DMSO registered at 532 nm using a 10 ns pulse length-based laser at $\sim 35 \mu\text{J}$.

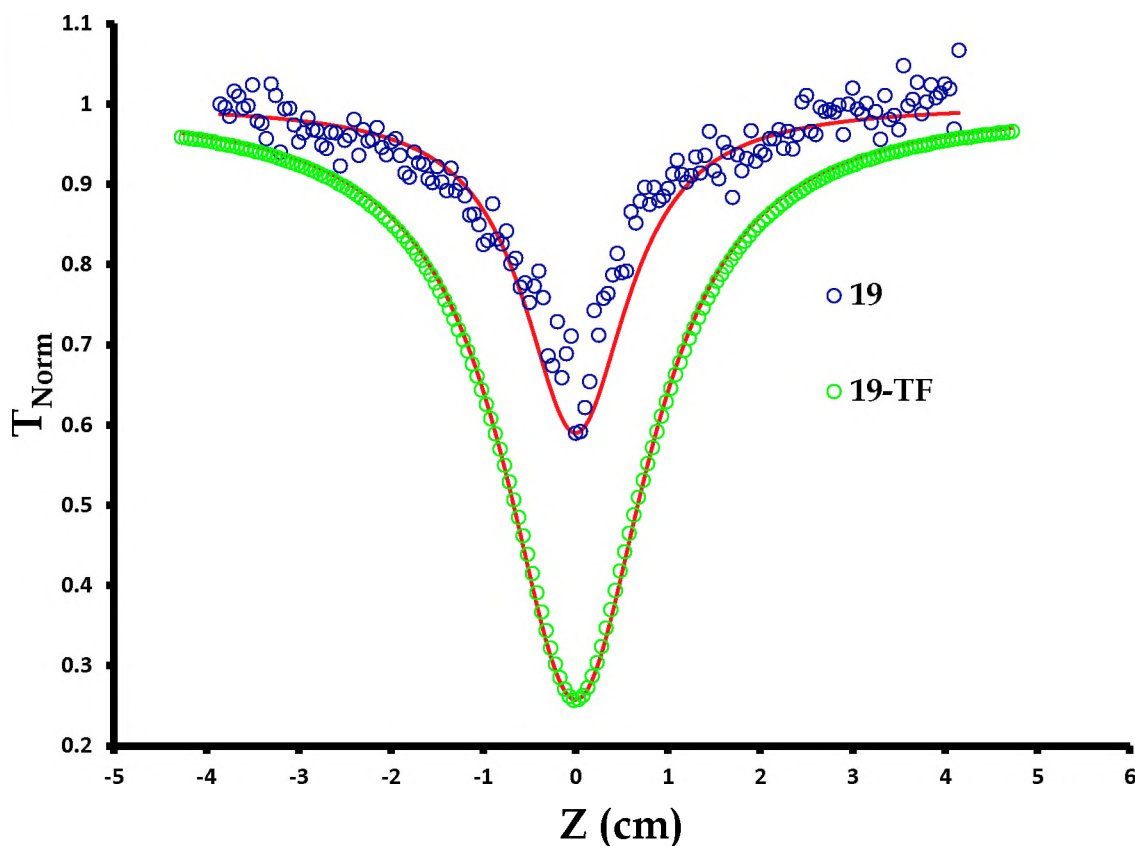


Fig. 5.2: Open aperture Z-scan curves for complexes **19** and **19-TF** registered in DMSO at 532 nm using a 10 ns pulse length-based laser at $\sim 35 \mu\text{J}$.

The transmittance reduction differences for Pcs are attributed to the amount of excited state absorption, which occurs in lanthanide Pcs as shown for GdPc elsewhere [74]. The excited state absorption, in turn, is associated with two photon absorption (2PA) [335-337], hence the employment of Eq. 1.1 for the simulation of mechanisms replicated by all complexes employed in this present study. The nonlinear absorption coefficients (β_{eff}) can be obtained from the Z-scan data but adjusted through Eq. 1.1 upon simulating, allowing for the determination of values of third order imaginary susceptibility ($\text{Im}[\chi^{(3)}]$) and the

second order hyperpolarizability (γ) using Eqs. 1.4 and 1.5. The $\text{Im}[\chi^{(3)}]$ values reported in this work for complexes **18** and **19** as well as all other complexes (Table 5.1), including conjugates, are larger than those reported for Yb, Gd and La polymeric phthalocyanines ($\sim 2.00 \times 10^{-13}$ to 2.52×10^{-13} esu) in DMF [289]. The γ values, Table 5.1, are also larger than those reported for In, Ga or Zn monomeric phthalocyanines [338] ($\gamma \sim 10^{-31}$ to 10^{-30} esu) in solution.

$\text{Im}[\chi^{(3)}]$ and γ values are larger for **19** compared to **18**, for reasons provided above, Table 5.1. The similar trend for $\text{Im}[\chi^{(3)}]$ and γ values of **18-TF** and **19-TF** was observed, with $\text{Im}[\chi^{(3)}]$ and γ values of the latter being larger than those of the former, Table 5.1. This observation is in agreement with the RSA behavior for **18**, **19**, **18-TF** and **19-TF** discussed for Fig. 5.1 and Fig. 5.2 above. While $\text{Im}[\chi^{(3)}]$ and γ values increase as an indication of better reduction of incident intensities by an optical limiter, the limiting threshold (I_{lim}) should decrease to show fast response of an optical limiter in terms of transmittance as a result of the RSA effect. As seen in Fig. 5.3, the extent of reduction of input intensities differs from one complex to another, with **19-TF** nonlinearly behaving better than and **19** alone in solution or **18-TF** better than **18** in solution. The I_{lim} values for **18**, **19**, **18-TF** and **19-TF** are indicated in Table 5.1 and follow the order: **19-TF**<**18-TF**<**19**<**18**. The I_{lim} values (in J cm^{-2}) presented in Table 5.1 are smaller than those reported for LuPc_2 whose I_{lim} was determined to be 1.8 J cm^{-2} [196].

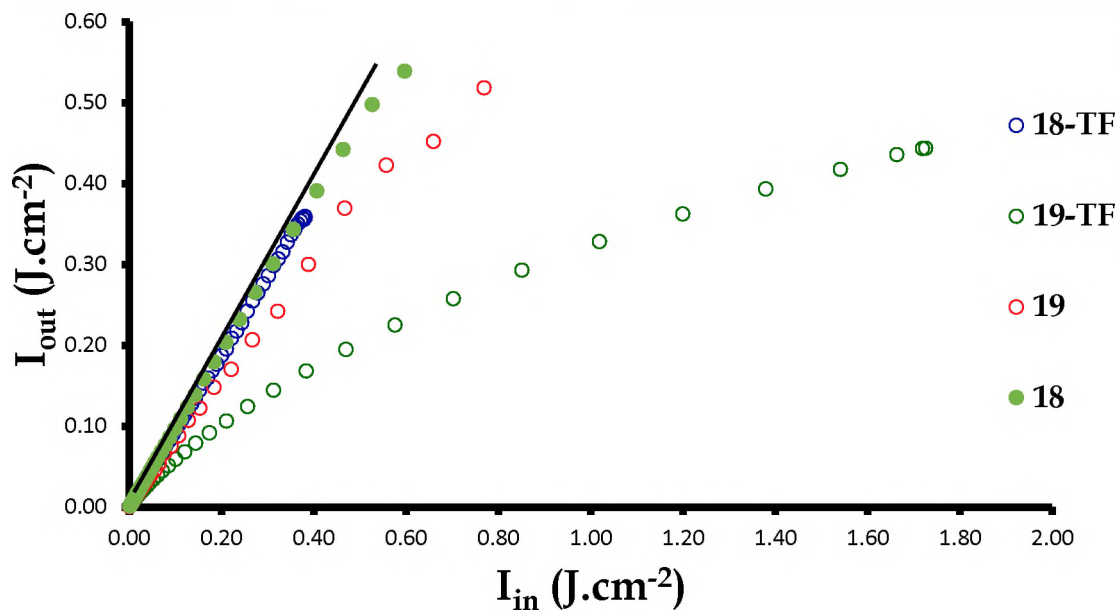


Fig. 5.3: Input against output intensity plot for complexes 18, 19 (in DMSO), 18-TF and 19-TF obtained at 532 nm using a 10 ns laser pulses when employing 35 μJ of energy.

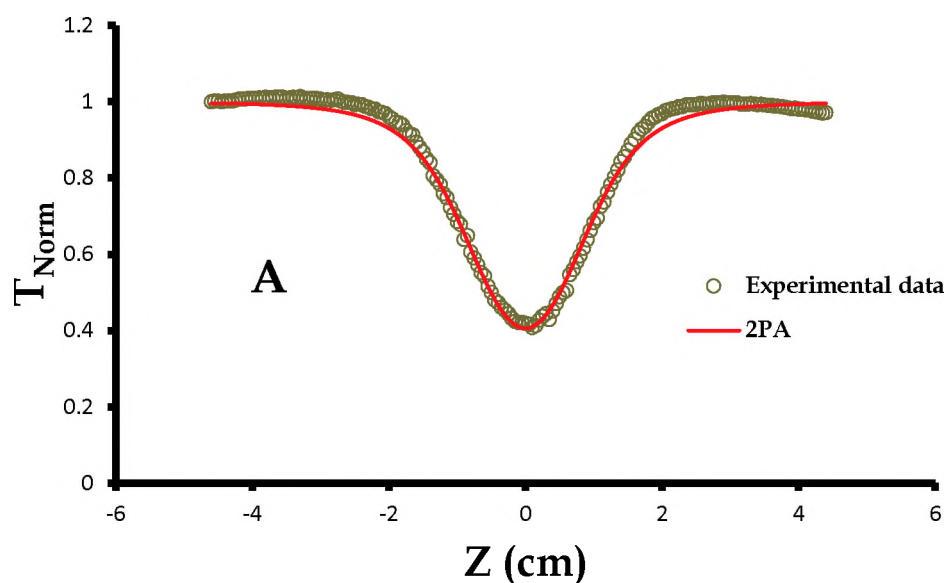
Table 5.1: Nonlinear optical parameters of lanthanide phthalocyanines alone and when embedded in PMMA, PBC and PAA.

Complex	Solvent/ Polymer	$\text{Im}[\chi^{(3)}]/\text{esu}$	γ/esu	$\sigma_{2\text{PA}} (\text{cm}^4 \text{s. photon}^{-1})$	$I_{\text{lim}} (\text{J.cm}^{-2})$
18	DMSO	1.10×10^{-10}	0.28×10^{-27}	-	0.99
19	DMSO	1.43×10^{-9}	3.69×10^{-27}	-	0.42
18-TF	PAA	3.35×10^{-9}	1.44×10^{-26}	-	0.36
19-TF	PAA	6.29×10^{-9}	2.70×10^{-26}	-	0.22
20	DMF	1.4×10^{-10}	2.60×10^{-28}	7.80×10^{-45}	0.31
21	DMF	8.10×10^{-11}	1.5×10^{-28}	4.60×10^{-45}	0.79
20-TF	PBC	90.4×10^{-10}	38.9×10^{-28}	5516.0×10^{-45}	0.11
21-TF	PBC	69.3×10^{-10}	29.9×10^{-28}	395.0×10^{-45}	0.26
22	DMSO	^a 3.43×10^{-10}	^a 3.64×10^{-27}	^a 1.03×10^{-45}	^a 0.3
23	DMSO	3.33×10^{-10}	1.77×10^{-27}	6.78×10^{-47}	0.27
23-TF	PMMA	7.48×10^{-8}	4.83×10^{-25}	-	0.033
Neutral 24	DMF	4.2×10^{-10}	1.1×10^{-27}	-	0.2
Reduced 24	DMF	3.52×10^{-9}	9.1×10^{-27}	-	0.18
24-TF	PAA	5.12×10^{-8}	1.23×10^{-25}	-	0.075
25	DMSO	5.30×10^{-10}	2.83×10^{-27}	-	0.22
26	DMSO	7.40×10^{-11}	5.17×10^{-28}	-	0.25
25-TF	PMMA	8.50×10^{-9}	5.49×10^{-26}	-	0.14
26-TF	PMMA	6.14×10^{-9}	3.96×10^{-26}	-	0.13
27	CH_2Cl_2	2.55×10^{-10}	6.59×10^{-28}	-	0.08
27-TF	PAA	1.79×10^{-10}	4.63×10^{-28}	-	0.08
Neutral 28	DMF	2.07×10^{-10}	4.50×10^{-28}	-	0.32
Reduced 28	DMF	2.44×10^{-10}	5.33×10^{-28}	-	0.09
29	CH_2Cl_2	2.12×10^{-10}	5.56×10^{-28}	-	0.09
29-TF	PAA	5.53×10^{-10}	1.43×10^{-27}	-	0.04
30	DMF	3.50×10^{-10}	7.60×10^{-28}	-	0.34
31	CH_2Cl_2	2.68×10^{-10}	6.93×10^{-28}	-	0.07
31-TF	PAA	1.66×10^{-10}	4.30×10^{-28}	-	0.08

a = values determined at 5.86×10^{-5} M. The concentration for the rest of the complexes is 3.4×10^{-4} M. - = values not determined due to absorption of Pcs or thin films around 532 nm.

5.1.1.2 Complexes 27 and 31

Fig. 5.4A shows an open aperture Z-scan curves obtained for complex 31 (as an example) at $0.19 \text{ GW}\cdot\text{cm}^{-2}$, as well the fitting to 2PA. The same nonlinear behavior was observed for complex 31. The Z-scan trace for Pcs in thin films is shown in Fig. 5.4B (using 31-TF as an example). It can be seen that transmittance of these thin films is much lower than that shown for complexes 27 and 31 in dichloromethane. The same applies for complex 27 and its thin film (27-TF) as well as all the Pcs and their thin films in this work.



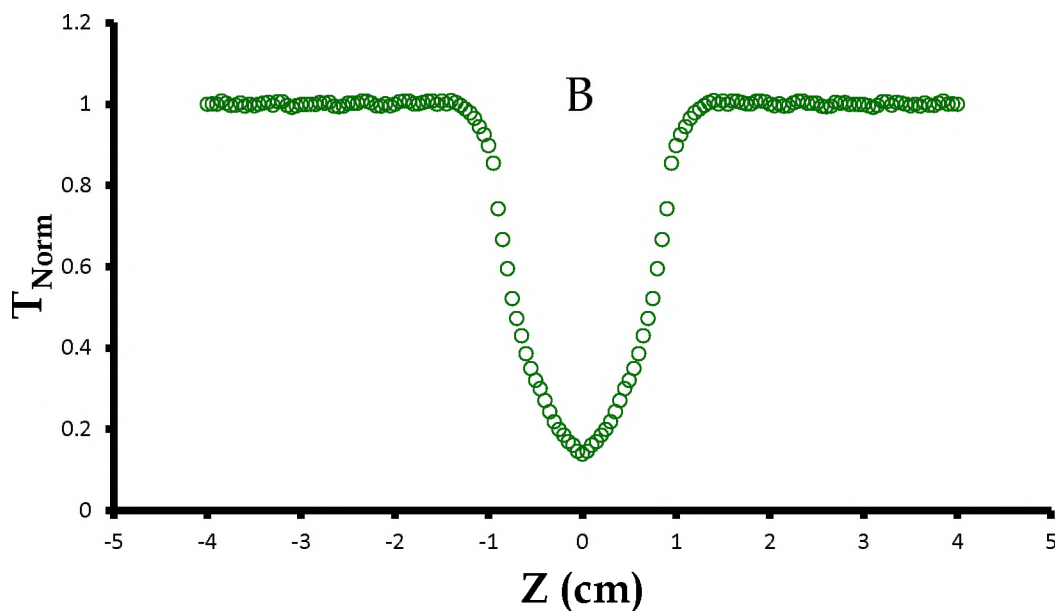


Fig. 5.4: Open aperture Z-scan signatures of (A) complex **31** obtained at $I_0 = 0.19 \text{ GW.cm}^{-2}$ in dichloromethane and (B) **31-TF** at $I_0 = 2.41 \text{ GW.cm}^{-2}$.

$\text{Im}[\chi^{(3)}]$ and γ values for are larger for **31** due to extended π -electron system compared to **27** both in solution, **Table 5.1**. Also **31** is neutral while **27** is paramagnetic. Similarly, **31-TF** exhibited larger $\text{Im}[\chi^{(3)}]$ and γ values compared to **27-TF**, **Table 5.1**. Plots of I_{in} against I_{out} are shown in **Fig. 5.5** for complexes **27** and **31**, and for **27-TF** and **31-TF**. These plots show a huge deviation from linearity as result of strong NLA. **27-TF** and **31-TF** showed similar I_{lim} values, **Table 5.1**.

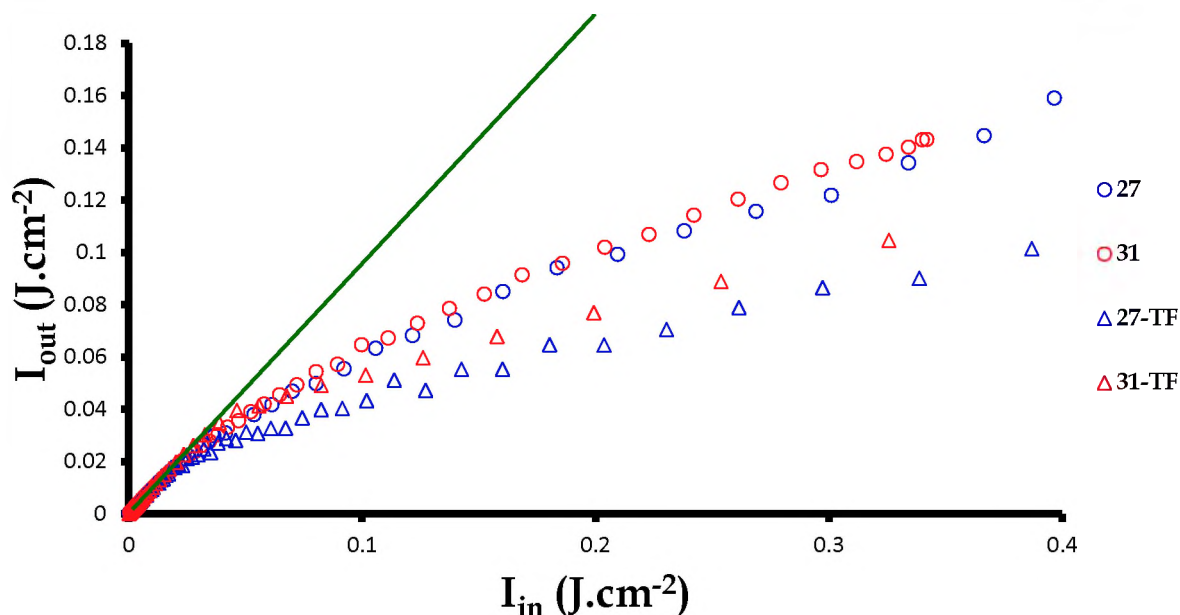


Fig. 5.5: Input against output intensity plots of complexes **27** and **31** (in dichloromethane), **27-TF** and **31-TF**.

To predict the extent of nonlinear behavior, the magnitudes of β_{eff} values are taken into account. These β_{eff} values are shown as a function of the on-focus intensity (I_0) in Fig. 5.6. Complex **31** which is a triple decker Pc shows a more positive slope of β_{eff} against I_0 . β_{eff} values for both complexes **27** and **31** increase with increasing I_0 values. Judging by the slopes of the plots, complex **31** is a better optical limiter. This shows that increased π -electron system in **31** improves NLO behavior. This brings about a conclusion that an increase in β_{eff} values with increasing I_0 is an indication of higher order nonlinear processes (2PA in the case of complexes **27** and **31** in solutions and thin films).

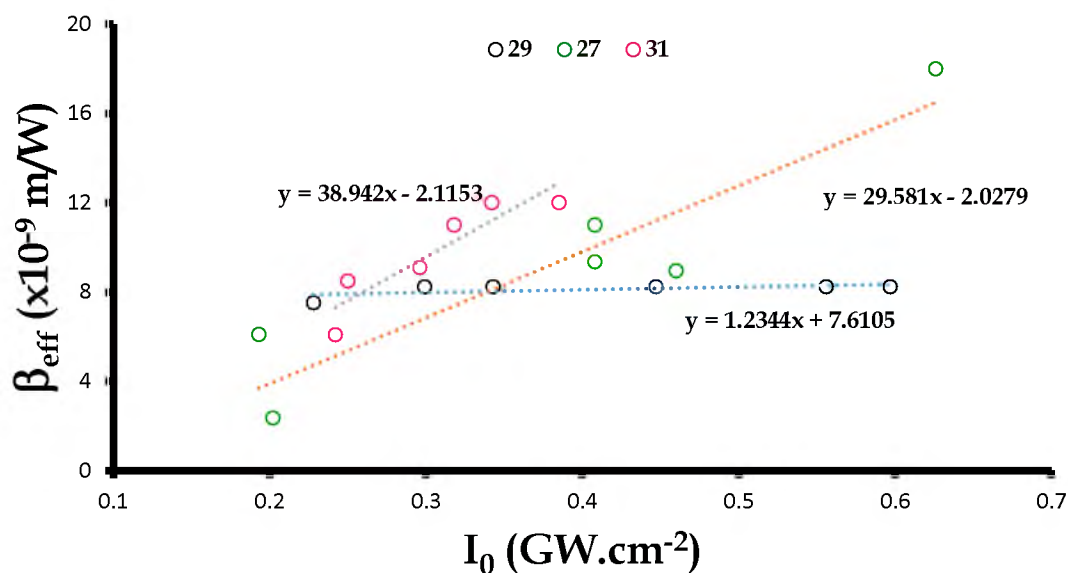


Fig. 5.6: β_{eff} against I_0 plots of complexes 27, 29 and 31 at various energies.

5.1.2 Effects of central metals

5.1.2.1 Complexes 20 and 21

Complex **20** is based on ytterbium while **21** comprises of lutetium as central metals. Varying the central metal atom in a Pc usually leads to considerable variation in the relevant NLO and OL properties [339]. Fig. 5.7 shows an open aperture Z-scan signals for **20** and **20-TF** fitted by Eq. 1.1 (for a 2PA process), showing RSA.

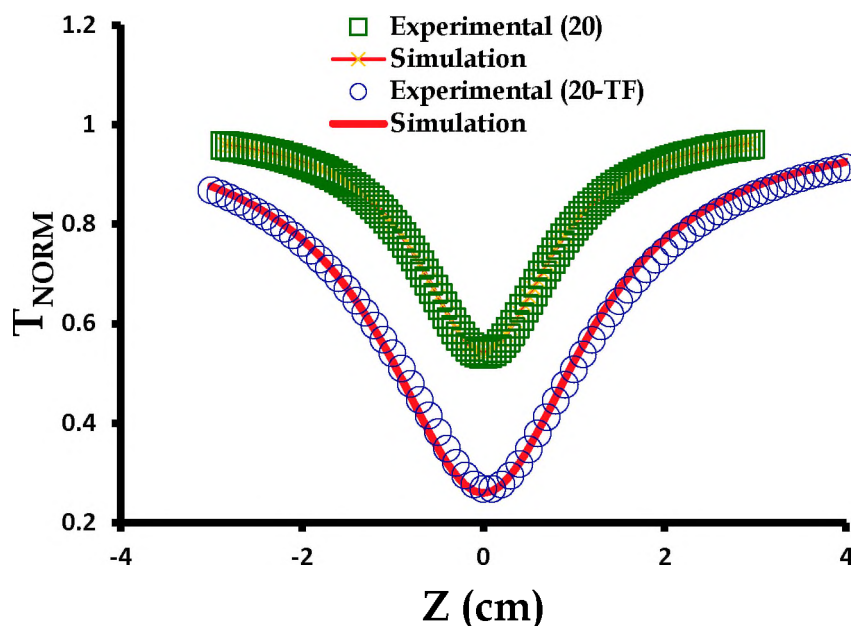


Fig. 5.7: Open-aperture Z-scan curve of complex **20** (in DMF) and **20-TF**.

As shown in Table 5.1, $\text{Im}[\chi^{(3)}]$ and γ values are higher for **20** compared to **21**, considering the same approximate concentrations in solution. The higher values suggest better optical limiting for the Yb_3Pc_3 derivative (**20**) due to lack of aggregation, even though it had a lower triplet quantum yield. The values are much higher in thin films, showing the importance of embedding Pcs in thin films for NLO applications. I_{lim} values were lower for **20** than for **21**. Similarly, **20-TF** showed lower I_{lim} value than **21-TF**. In general, the I_{lim} values for **20**, **21**, **20-TF** and **21-TF** follow the order: **20**<**21**; **20-TF**<**21-TF**, Table 5.1. Two photon cross section ($\sigma_{2\text{PA}}$) values were determined only for complexes **20-23** as examples using Eq. 5.1 [340].

$$\sigma_{2PA} = \frac{h\nu\beta_{eff}}{N \times 10^{-3}} \quad 5.1$$

where where h is Planck's constant, ν is the frequency of a laser excitation and N is defined as the system's number of active species per unit volume ($N = N_A C$; $N_A =$ Avogadro's number and $C =$ sample concentration). σ_{2PA} values are higher for complex **20** compared to **21**, **Table 5.2**. An increase in σ_{2PA} values was observed for **20-TF** and **21-TF** compared to solutions, as was the case for $\text{Im}[\chi^{(3)}]$ and γ in solution and the solid state.

5.1.2.2 Complexes 25 and 26

The coordinating lanthanide ion for complex **25** is Yb^{3+} while for **21** is Lu^{3+} . **Fig. 5.8 (A and B)** show of the open aperture Z-scan signals for complexes **26** and **25** best fitted by employing Eq. 1.1 at 2.6×10^{-4} M in DMSO. The lack of a deep valley below 50% for **26**, could be due to aggregation at the concentration of 2.6×10^{-4} M used for NLO. Complex **26** showed more aggregation than **25**. Thus aggregation in solution does not favor good NLO behavior. The spectrum for **25** still shows monomeric behavior at 3.4×10^{-4} M. **25-TF** and **26-TF** show better RSA processes (with a deep valley below 50%) in terms of open aperture Z-scan curves as shown in **Fig. 5.9** compared to solution as discussed above.

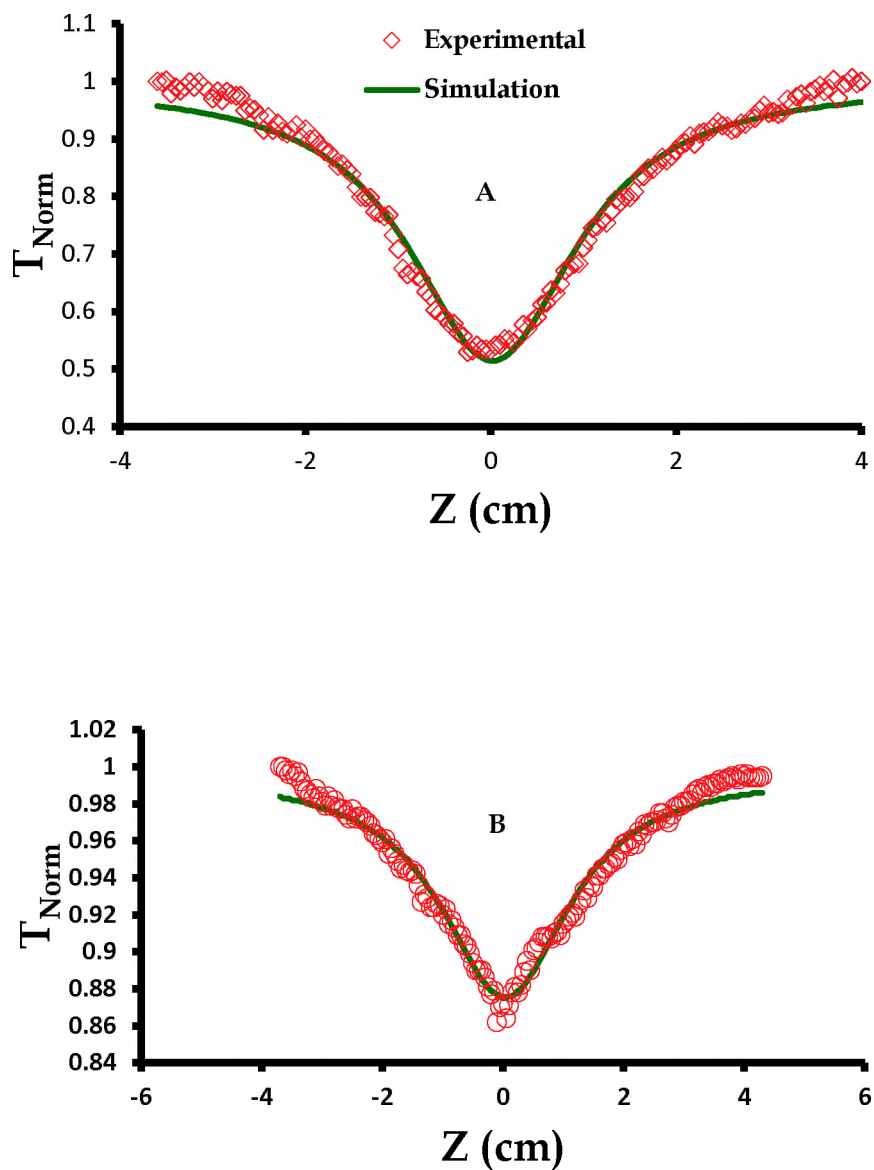


Fig. 5.8: Open aperture Z-scan signal for complex 25 (A) and 26 (B) in DMSO at 10 ns pulse duration.

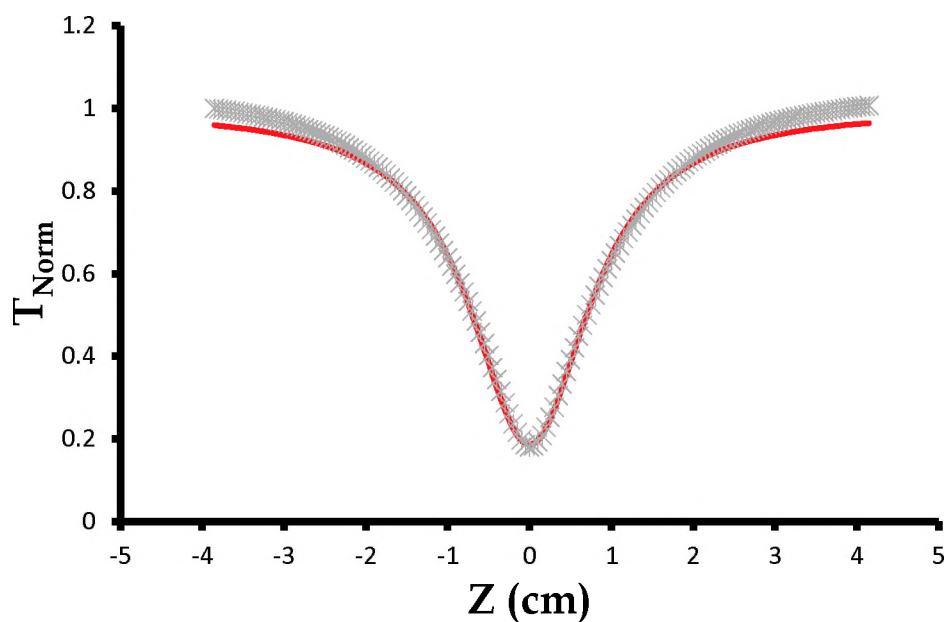


Fig. 5.9: Open aperture Z-scan curve for 26-TF at 10 ns pulse duration.

The $\text{Im}[\chi^{(3)}]$ and γ values are higher for **25** compared to **26** in solution. The low values for **26** are a result of aggregation, which does not favor triplet state population, hence NLO behavior. The $\text{Im}[\chi^{(3)}]$ and γ values are much larger in thin films than in solution, due to the rigidity of the media as already stated. The effect of aggregation is witnessed by slightly high I_{lim} values obtained for complex **26** compared to those for complex **25** in solution but not different in thin films. It was also observed that **25-TF** and **26-TF** possess even lower I_{lim} values ($\text{J}\cdot\text{cm}^{-2}$) than **25** and **26** in solution. In Fig. 5.10, a plot of the effective nonlinear absorption coefficient (β_{eff} in cm MW^{-1}) against the on-focus beam intensity (I_0 in GW cm^{-2}) is presented for complex **25** (as an example). It can be observed that the effective nonlinear absorption coefficient increases with I_0 . The same behavior was

observed **26**. This shows effects of high laser beam intensities which result in high β_{eff} values. Since this behavior is also dependent of concentrations, it can be observed that higher concentrations (related to the number of excited molecules) give better effective nonlinear absorption coefficients, **Fig. 5.11**.

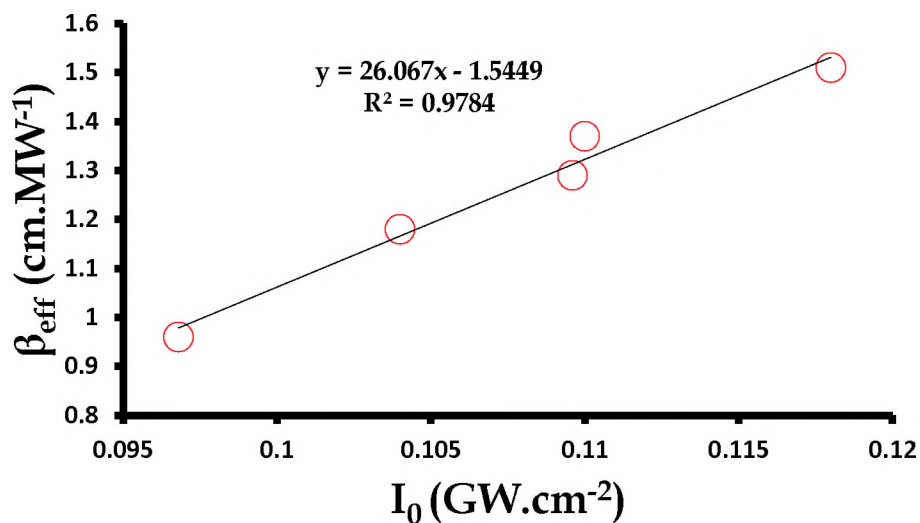


Fig. 5.10: A plot of the effective nonlinear absorption coefficient (β_{eff}) against the on-focus beam intensity (I_0) for complex **25** in DMSO.

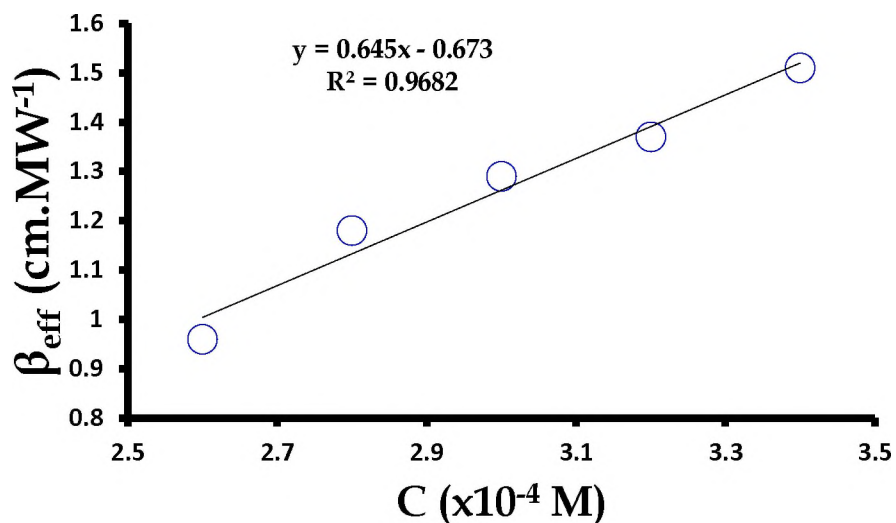


Fig. 5.11: Nonlinear absorption coefficient (β_{eff}) against concentration showing β_{eff} concentration dependence for complex **25**. This experiment was performed in DMSO.

5.1.2.3 Complexes **27**, **28** and **29**

When compared to **27**, complex **29** showed strong excited state saturation with increasing I_0 values. This is evidenced by constant β_{eff} values with changing on-focus input intensities, **Fig. 5.6**. It can be seen that complex **27** is more advantageous in terms of use as an optical limiter over complex **29** at very high intensities. Studies in which GdPc was employed in Z-scan measurements, with the excitation wavelengths ranging between 460 and 600 nm, revealed strong excited state absorption (ESA) [341]. Therefore the observed RSA can be associated with ESA for **29**, while not ruling out the triplet excited state cross-sections. This is explained by the proposed five-level diagram in **Fig. 1.7** (**chapter 1**), showing three cross sections contributing to NLA. **27** has larger $\text{Im}[\chi^{(3)}]$ and γ values

than **29** in solution due to lack of radical for **27**. However, due to solubility problems, complex **28** was studied in DMF while **27** and **29** in dichloromethane, making comparison with **28** inaccurate, but the superiority of **27** over **29** is confirmed in dichloromethane. This observation is reversed for thin films (**29-TF** > **27-TF**). **Table 5.1** summarizes the nonlinear optical properties of both the reduced and neutral forms of **28**. Both reduced and neutral forms of **28** showed RSA (figure not shown) as shown for other complexes above. At the same concentrations, the values of $\text{Im}[\chi^{(3)}]$ and γ are larger for reduced **28** compared to neutral **28**, showing that the reduced blue form is a better optical limiter than the charged green form. For the neutral **28** and reduced **28**, both the ligands and central metal are the same, hence similar optical limiting properties are expected. However, the two are different in that the neutral **28** is paramagnetic while the reduced **28** is not, resulting in improved photophysical behavior for the latter. The I_{lim} value obtained for reduced **28** (0.09 J.cm^{-2}) is smaller than for neutral **28** (0.32 J.cm^{-2}), **Table 5.1**, showing the positive influence of reduction.

Sub-summary: The $\text{Im}[\chi^{(3)}]$ and γ values for **20** and **25** were larger than those for **21** and **26**, while the I_{lim} values for **20** and **25** were lower than those of their counterparts (**21** and **26**), showing the superiority of paramagnetic lanthanide ions over the diamagnetic counterparts. The similar trend was observed for thin films.

5.1.3 Nature and position of substituents for complexes 22, 23, 24 and 25

Complexes **22**, **23** and **24** are all based on ytterbium as a coordinating lanthanide, but differ in substituents. In the case of **22** and **23**, only the position of nitrogen in pyridine is different, while neutral **24** is tert-butyl phenoxy-substituted. It has to be noted that **22**, **23** and **25** were studied in DMSO while neutral **24** in DMF. This makes comparison inaccurate when comparing complexes in different solvents as stated before. Also the thin film of **22** was not studied and therefore will not be discussed in this work. In summary, **22** will be compared to **23** due to same solvent but different substituent, while neutral **24** will be compared to reduced **24**. **23** and **25** will be compared due to same solvent and substituent, but different substitutional positions. As can be noted in **Table 5.1**, **23-TF** and **25-TF** are based on PMMA while **24-TF** was prepared from PAA and is only for neutral **24**. This compels the author of this work to discuss and draw conclusion both **23-TF** and **24-TF** independently.

Fig. 5.12 shows an open aperture Z-scan signal for complex **24**, indicating a decrease in transmitted beam as evidence of RSA effect. Such a Z-scan signal was also obtained for complexes **22**, **23** and **25** as stated already. 2PA has been especially effective at producing large nonlinear absorptions [62]. Complex **22** shows larger $\text{Im}[\chi^{(3)}]$, γ values and I_{lim} values compared to **23**, even at lower concentration for the former, showing the position of nitrogen in pyridine is important – which is closest to the Pc ring for **22**. $\sigma_{2\text{PA}}$ values are higher for **22** compared to **23**, **Table 5.1**. Complexes **23** and **25**, both contain Yb but are α - (complex **23**) and β -substituted (complex **25**). Complex **23** showed lower $\text{Im}[\chi^{(3)}]$

and γ values and higher I_{lim} values than **25** in solution showing the superiority of peripheral substitution in solution. However, **23-TF** gave $\text{Im}[\chi^{(3)}]$ and γ values which are larger than those of **25-TF**, but lower I_{lim} value ($0.033 \text{ J}\cdot\text{cm}^{-2}$), showing the superiority of non-peripheral substitution in thin films. However, $\sigma_{2\text{PA}}$ values for complex **23** are still indicative of an NLO material. **24** has an improved solubility and reduced aggregation due to tert-butyl phenoxy substituent.

As shown in Fig. 5.12, neutral and the reduced forms of **24** exhibited a reverse saturable absorption (RSA) process at $3.4 \times 10^{-4} \text{ M}$ as judged by the decrease in the transmittance. The normalized transmittance for reduced **24** exhibited deep valley to near 60% making it a better NLO material compared to neutral **24** at only $\sim 20\%$. Thus, as stated above for **28**, reducing the Pc ring in $\text{Pc}^{-1}\text{LnPc}^{-2}$ to form $[\text{Pc}^{-2}\text{LnPc}^{-2}]^{-}$ improves the NLO behavior even though the central Yb^{3+} is paramagnetic.

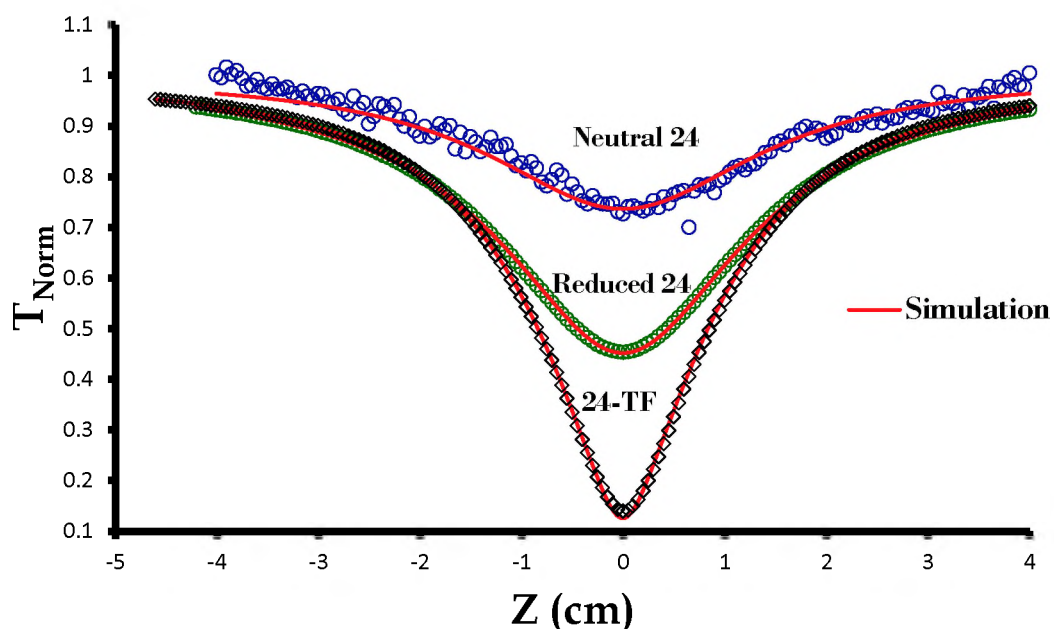


Fig. 5.12: Open aperture Z-scan curves for neutral **24** (in DMF), reduced **24** (in DMF in the presence of hydrazine) and **24-TF** at 532 nm.

In solid state, as shown in **Fig. 5.12**, **24-TF** shows better NLO as judged by the largest decrease in normalized transmittance. As indicated in the **Table 5.1**, the values of the NLO parameters ($\text{Im}[\chi^{(3)}]$ and γ) increase as follows: neutral **24**<reduced **24**<**24-TF**. Reduced **24** shows improved $\text{Im}[\chi^{(3)}]$ and γ as a result of the reduction of the Pc ring, as was the case for **28**.

Fig. 5.13 shows the input against output intensity plot for complexes neutral **24** (in DMF), reduced **24** (in DMF in the presence of hydrazine) and **24-TF**. As indicated in **Fig. 5.13**,

24-TF reaches a point of saturability much faster than neutral 24 and reduced 24, giving lower threshold values.

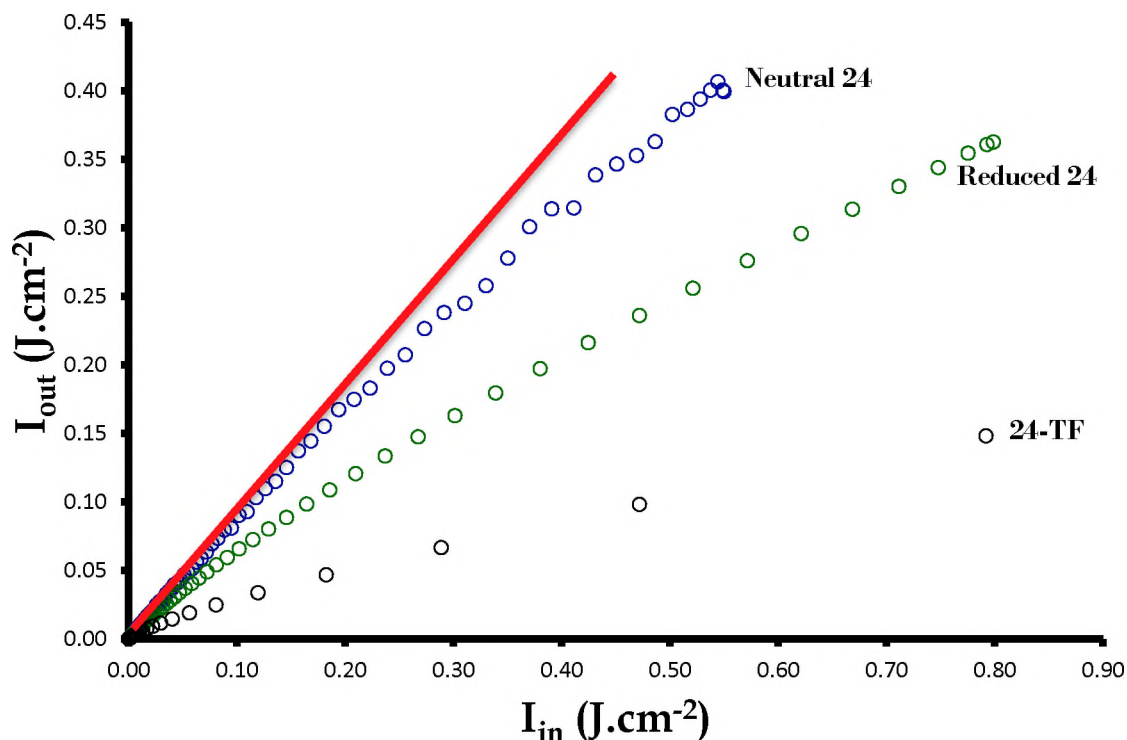


Fig. 5.13: Input intensity (I_{in}) against output intensity (I_{out}) for neutral 24 (in DMF), reduced 24 (in DMF in the presence of hydrazine) and 24-TF 532 nm.

Fig. 5.14, as an example for all molecules, further indicates a decrease in the transmittance for neutral 24, reduced 24 and 24-TF with increase in the input intensity. This behavior is in agreement with that observed in Fig. 5.12, with 24-TF showing more enhanced reduction in the transmittance. When exciting at different wavelengths, various processes co-exist [106,124] which could potentially compete

with RSA.

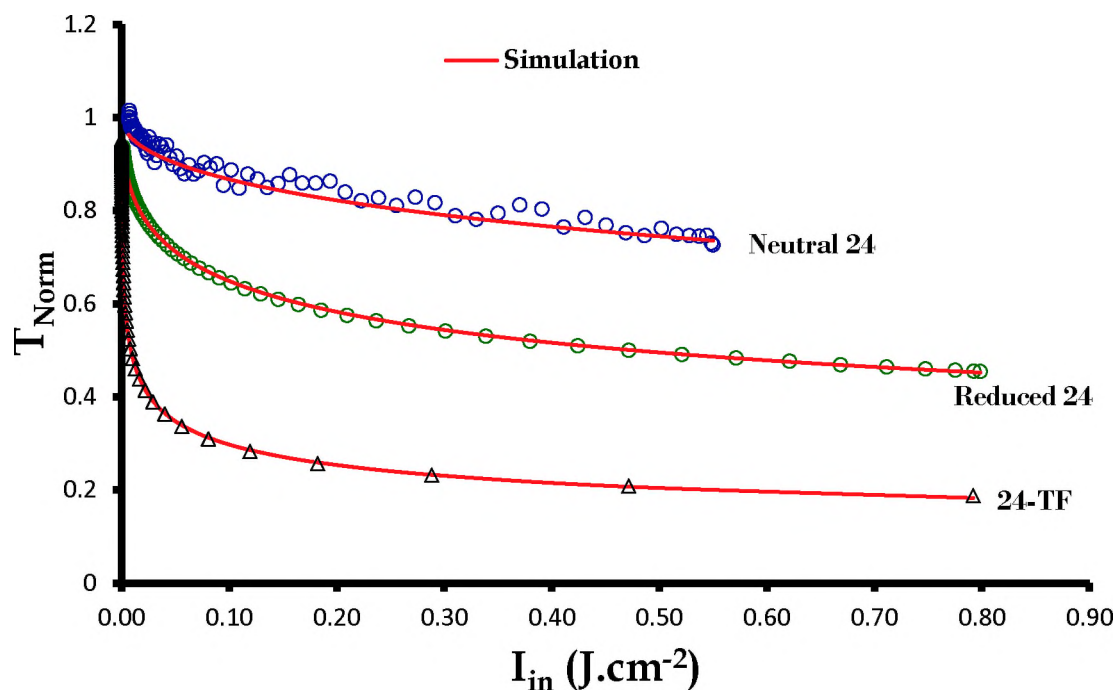


Fig. 5.14: Normalized transmittance (T_{Norm}) against I_{in} for neutral **24** (in DMF), reduced **24** (in DMF in the presence of hydrazine) and **24-TF** at 532 nm.

Processes that compete with RSA are initiated by absorption of a material. It is therefore important to verify the existence of RSA at 532 nm, particularly because LnPc_2 complexes have a BV band around this region which is likely to contribute to ground state absorption. The model for RSA of an optically active polyacene-based oligomer has been explained by Kojima et al [342], with the incident laser intensity (I_{in}) and the transmitted laser intensity (I_{out}) obeying Eq. 5.2:

$$\ln\left(\frac{I_{in}}{I_{out}}\right) = k(I_{in} - I_{out}) + A \quad 5.2$$

where k is a constant that depends on the absorption cross sections and lifetimes of the ground, excited singlet, and excited triplet states, while A is the absorbance of the ground state. To investigate the RSA existence, the previous reported procedure [343] was followed by plotting natural logarithm of I_{in}/I_{out} ratio against the $I_{in}-I_{out}$ difference as depicted by Eq. 5.2. If RSA is strongly affected by the other competing processes, the fitting is expected to deviate quite strongly from the linearity. As shown in Fig. 5.15, the fits are nearly linear (with the deviation at low $I_{in} - I_{out}$), suggesting the domination of RSA upon which the nonlinear optical behavior of neutral **24**, reduced **24** and **24-TF** materials is based. This applies to all complexes studied in this work.

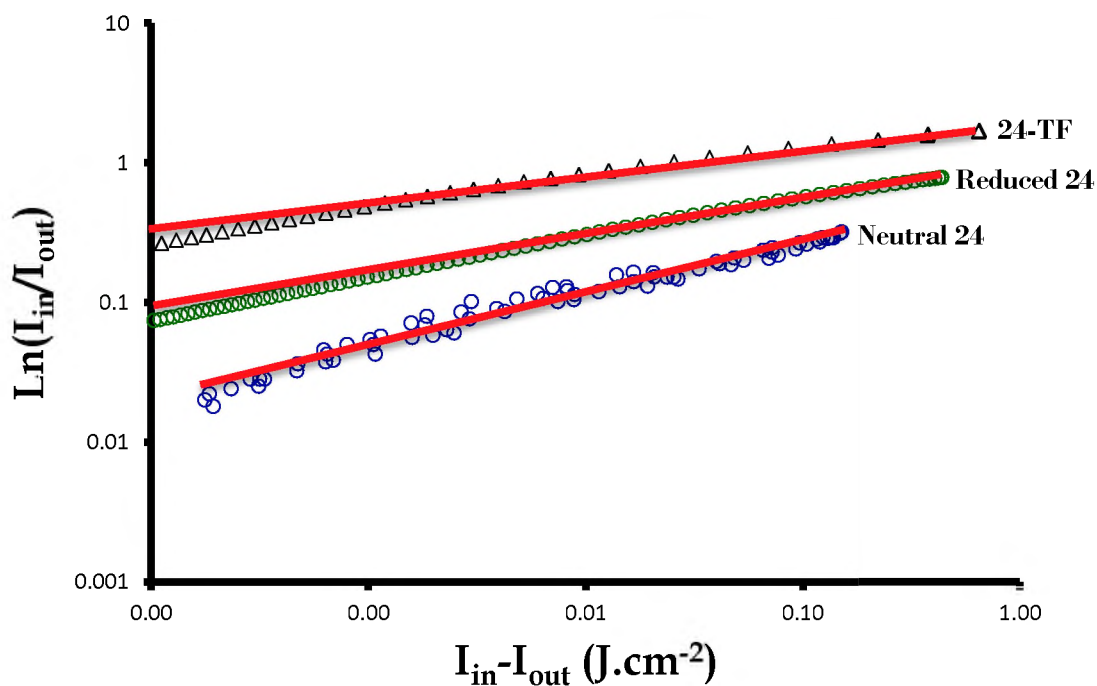


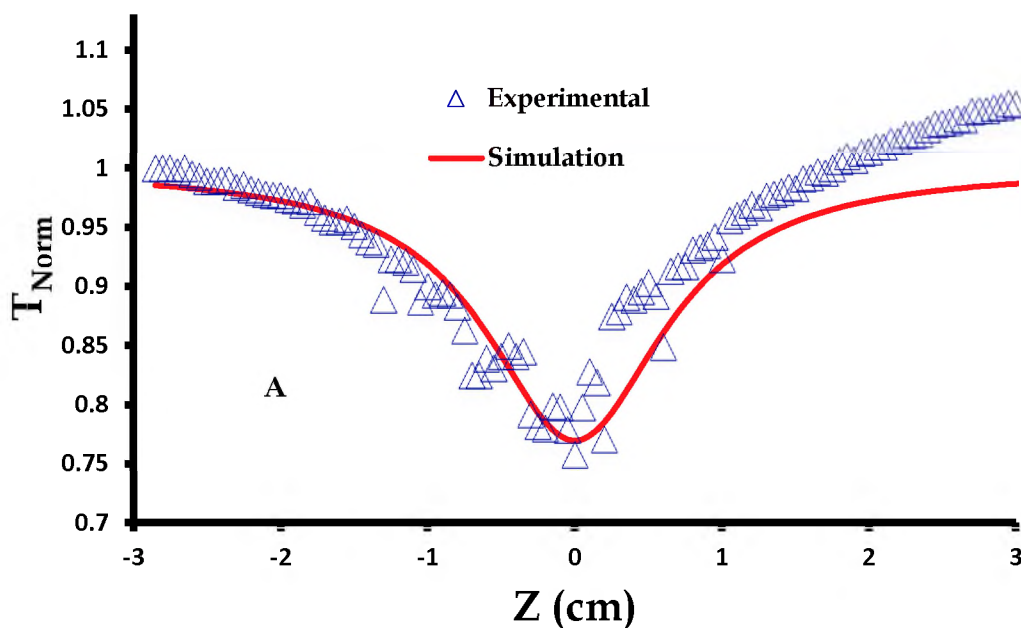
Fig. 5.15: Natural logarithm of I_{in}/I_{out} fraction against a change between I_{in} and I_{out} for neutral **24** (in DMF), reduced **24** (in DMF in the presence of hydrazine) and **24-TF** at 532 nm for investigation of RSA existence.

$\text{Im}[\chi^{(3)}]$ and I_{lim} values are much improved for reduced **24**, indicating that reduced LnPc_2 complex is more effective than the neutral counterpart. In thin films, **23-TF** is superior to **24-TF**, judging by $m[\chi^{(3)}]$, γ and I_{lim} values, **Table 5.1**.

Sub-summary: The $\text{Im}[\chi^{(3)}]$ and γ values of **22** in solution were larger than those of **23**. In comparison to reduced **24**, neutral **24** gave lower $\text{Im}[\chi^{(3)}]$ and γ values but larger I_{lim} values, showing the superiority of reduced forms of LnPc_2 complexes over the neutral ones in solution.

5.1.4 Nonlinear optical behavior of complexes 30

RSA was observed for complex **30**, Fig. 5.16A. Fig. 5.16B shows an open aperture Z-scan curve for **30**. The signals demonstrate a decrease in the transmitted beam due to the RSA effect of complex **30** and depend on concentration as is the case for all complexes in this work. Comparison of NLO data with other work from literature is subjective, because of the differences in the experimental conditions and procedures. For the hetero phthalocyanine-porphyrin tris derivative ($\text{Sm}_2(\text{Pc})(\text{TPP})_2$, TPP = tetraphenyl porphyrin) $\text{Im}[\chi^{(3)}] = 2.1 \times 10^{-13}$ esu and $\gamma = 2.2 \times 10^{-30}$ esu [131] and for $\text{Sm}_2(\text{TPP})(\text{Pc})_2$, $\gamma = 2.6 \times 10^{-30}$ esu [131]. These values are much lower than reported in this work for complex **30**.



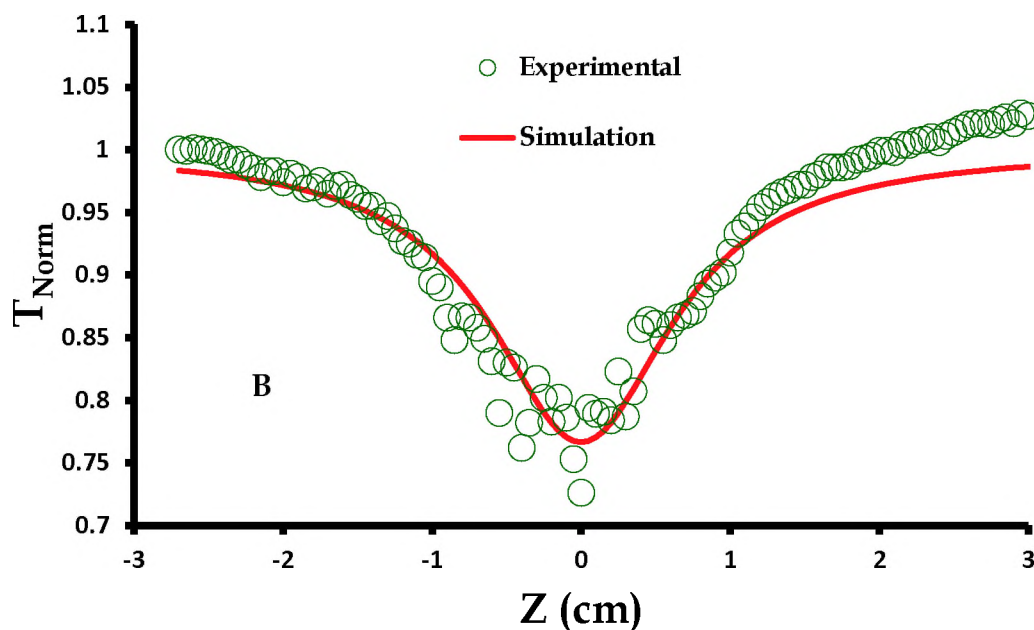


Fig. 5.16: Open aperture Z-scan curves obtained on simulation using (A) two photon absorption mechanism at 2.7×10^{-4} M. (B) was obtained on a two photon absorption simulation at 3.4×10^{-4} M. All two curves represent the behavior of complex **30** in DMF on exposure to highly intense light monitored by Z-scan technique.

5.2 Phthalocyanines with nanomaterials as conjugates

5.2.1 Complexes 18 and 19 with ZnO NPs

The advantage of linking Pcs to NPs which exhibit the NLO mechanisms is interesting and less complicated in terms of the NLO data analysis. Given that complexes **18** and **19** exhibit 2PA as discussed above and can be linked to ZnO NPs which also exhibit 2PA [248-249], linking was performed to observe any NLO changes in new systems compared to **18** and **19** alone. On linking to ZnO NPs, the RSA was enhanced as shown in Fig.

5.17 (**19** and **19-ZnO NPs_A** shown as examples). There was a larger reduction in transmittance for **19-ZnO NPs_A** (linked to the ZnO NPs through the phenoxy carboxy bridge) than for **19-ZnO NPs_B** linked through axial ligand (figure not shown for **19-ZnO NPs_B**). The former showed lower triplet quantum yield than the latter, **Table 5.2**. NLO behavior through RSA is expected to improve with triplet quantum yields. The larger reduction in transmittance for **19-ZnO NPs_A** could be related to more reduction in symmetry when the Pcs are linked via the bridging ligand than via the axial ligation for **19-ZnO NPs_B**.

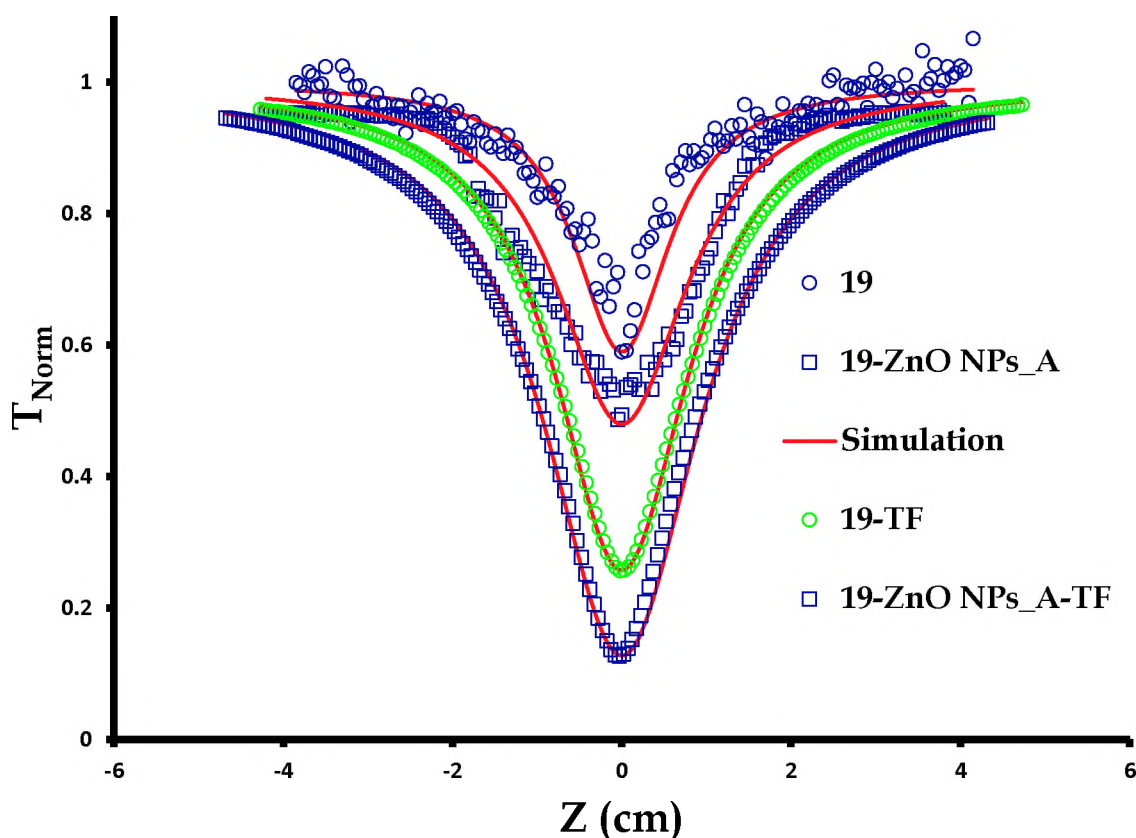


Fig. 5.17: Open aperture Z-scan curves for complexes **19**, **19-ZnO NPs_A** (in DMSO), **19-TF** and **19-ZnO NPs_A-TF** registered at 532 nm using a 10 ns pulse length-based laser at $\sim 35 \mu\text{J}$.

Complex **18-ZnO** NPs showed no RSA at all (figure not shown), irrespective of high triplet quantum yield in **Table 4.1**. The weak (or non-existent) NLO behavior for **18** (or **18-ZnO** NPs) could be related to their monomeric behavior (hence less π bonds) and to their symmetrical nature compared to complex **19** and its conjugates. As observed, the molecules with a large number of π -electrons (**19**, **19-ZnO NPs_A** and **19-ZnO NPs_B**) exhibit good RSA when compared to monomeric **18** and **18-ZnO** NPs. The same trend of RSA was observed in thin films where **19-TF**, **19-ZnO NPS_A-TF** and **19-ZnO NPS_B-TF** enhanced reduction in transmittance compared to **18-TF**. All the thin films showed larger reduction in transmittance than for solution as discussed above.

Both $\text{Im}[\chi^{(3)}]$ and γ values are larger for **19-ZnO NPs_A** and **19-ZnO NPs_B** where Pcs are linked to **ZnO** NPs compared to **19**. The values are also larger in thin films than in solution. In solution, **19-ZnO NPs_B** has larger $\text{Im}[\chi^{(3)}]$ and γ than **19-ZnO NPs_A**, but in thin films the values are larger for **19-ZnO NPs_A-TF** than for **19-ZnO NPs_B-TF**. The differences could be related to difference in symmetry in the different media. **Fig. 5.18** shows the input against output intensity plot for **19** and **19-ZnO NPs_A** (in DMSO) as well as **19-TF** and **19-ZnO NPs_A-TF**. While $\text{Im}[\chi^{(3)}]$ and γ values increase as an indication of better reduction of incident intensities by an optical limiter, I_{lim} should decrease to show fast response of an optical limiter in terms of transmittance as a result of the RSA effect. The I_{lim} values are listed in **Table 5.2** and followed the order: **19-ZnO NPs_A** < **19-ZnO NPs_B** < **19** < **18**; **19-ZnO NPs_A-TF** <

19-ZnO NPs_B-TF < **19-TF** < **18-TF**. In general, the I_{lim} values are lower for thin films. The I_{lim} ($J\ cm^{-2}$) values shown in literature are usually greater than $1\ J\ cm^{-2}$ [64,195,344]. The I_{lim} values for complexes are lower than $1\ J.cm^{-2}$, suggesting that all complexes studied in this work possess good NLO behavior in terms of I_{lim} ($J.cm^{-2}$).

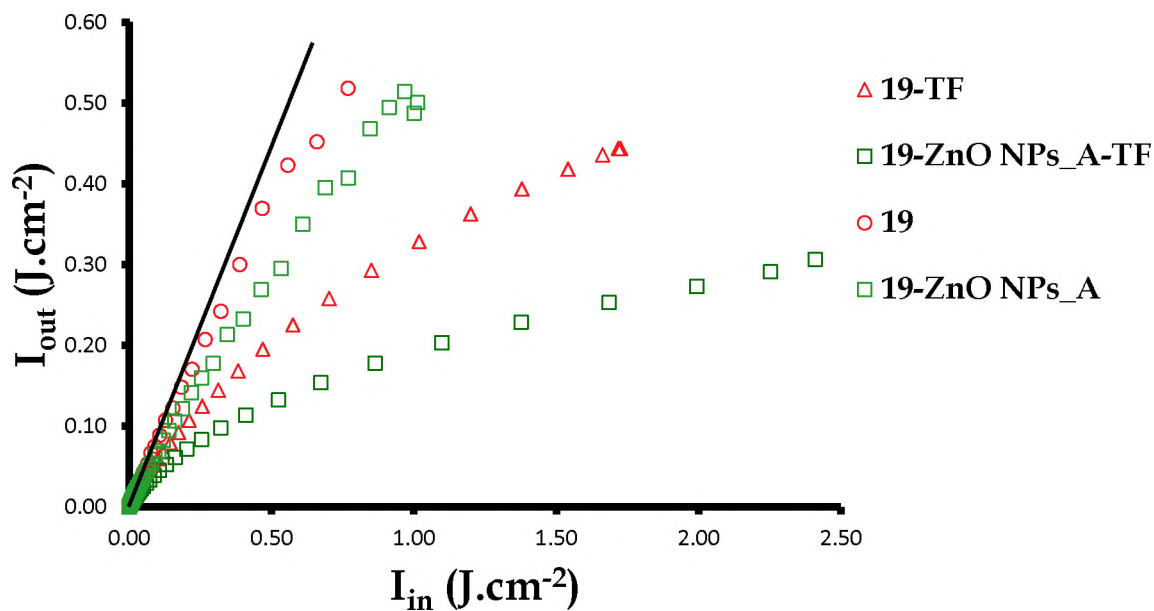


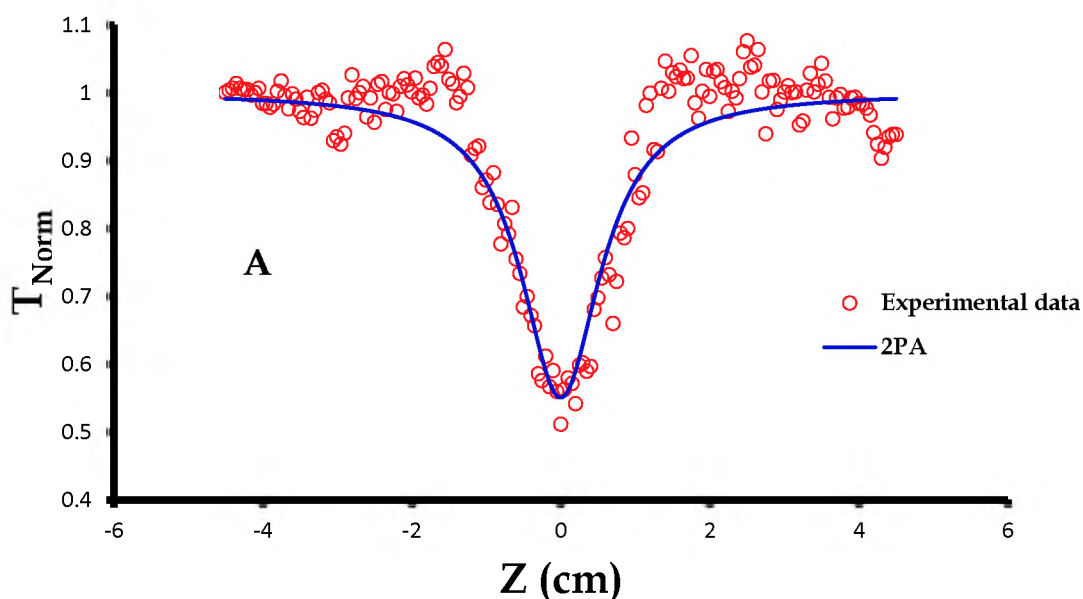
Fig. 5.18: Input against output intensity plot for complexes 19, 19-ZnO NPs_A (in DMSO), 19-TF and 19-ZnO NPs_A-TF obtained at 532 nm using a 10 ns laser pulses when employing 35 μJ of energy.

Table 5.2: Nonlinear optical parameters of complexes mono and binuclear phthalocyanines with ZnO NPs, NH-MWCNTs, NH-GONS and NH-rGONS as conjugates in DMSO and when embedded in poly (acrylic acid) obtained at 532 nm using a 10 ns laser pulses.

Complex	Solvent	$\text{Im}[\chi^{(3)}]$ (esu)	γ (esu)	I_{lim} ($\text{J}\cdot\text{cm}^{-2}$)
18	DMSO	1.10×10^{-10}	0.28×10^{-27}	0.99
19	DMSO	1.43×10^{-9}	3.69×10^{-27}	0.42
18-TF		3.35×10^{-9}	14.4×10^{-27}	0.36
19-TF		6.29×10^{-9}	27.0×10^{-27}	0.22
19-ZnO NPs_A	DMSO	2.38×10^{-9}	6.14×10^{-27}	0.25
19-ZnO NPs_B	DMSO	2.71×10^{-9}	6.99×10^{-27}	0.29
19-ZnO NPs_A-TF		58.9×10^{-9}	253×10^{-27}	0.12
19-ZnO NPs_B-TF		34.4×10^{-9}	148×10^{-27}	0.21
19-NH-MWCNTs	DMSO	2.65×10^{-10}	6.85×10^{-28}	0.055
19-NH-MWCNTs-TF		2.20×10^{-10}	5.67×10^{-28}	0.06
NH-GONS	DMSO	1.40×10^{-10}	3.61×10^{-27}	0.1
NH-rGONS	DMSO	4.43×10^{-10}	1.17×10^{-27}	0.03
19-NH-rGONS	DMSO	1.55×10^{-9}	4.00×10^{-27}	0.04
19-NH-GONS	DMSO	1.44×10^{-9}	3.71×10^{-27}	0.05
NH-GONS-TF		3.06×10^{-9}	7.90×10^{-27}	0.05
NH-rGONS-TF		3.51×10^{-9}	9.07×10^{-27}	0.07
19-NH-rGONS-TF		4.53×10^{-9}	1.17×10^{-26}	0.05
19-NH-GONS-TF		3.70×10^{-9}	9.55×10^{-27}	0.08

5.2.2 Complexes 18 and 19 with MWCNTs.

Fig. 5.19A and B shows the open aperture Z-scan signals indicative of reverse saturable absorption (RSA) profile for 19-NH-MWCNTs [175,183,185-187], taken at $0.19 \text{ GW}\cdot\text{cm}^{-2}$ and $0.48 \text{ GW}\cdot\text{cm}^{-2}$, respectively. It is evident from Fig. 5.19B that nonlinear response is dependent on I_0 and can lead to RSA signals going below 50% at $z = 0$. The $\text{Im}[\chi^{(3)}]$ and γ values for 19-NH-MWCNTs are less than for 19 alone under the same conditions in solution and thin films, showing quenching of NLO behavior of complex 19 in the presence of NH-MWCNTs.



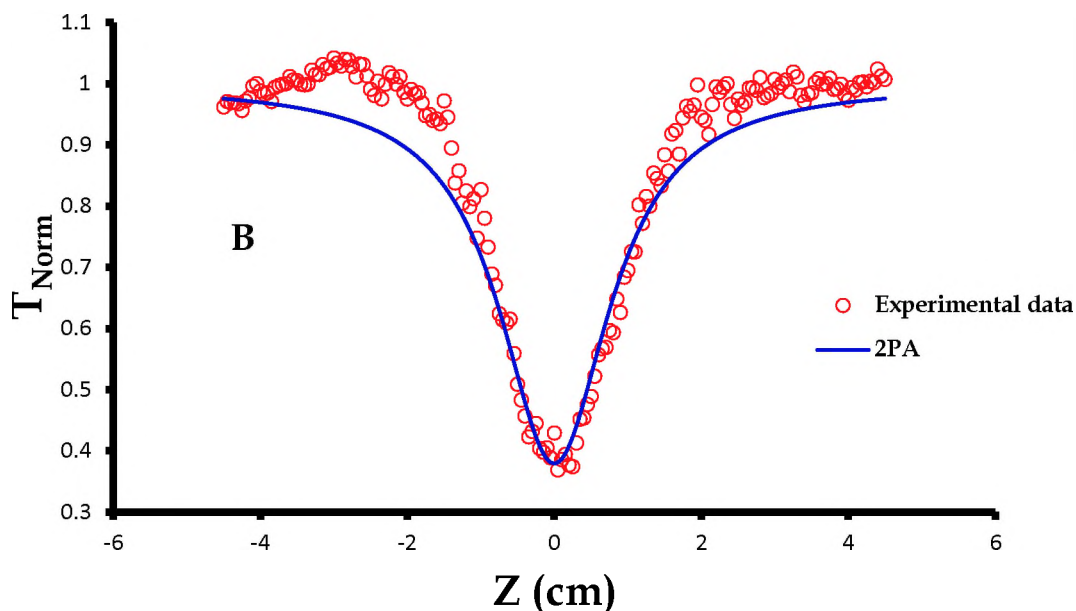


Fig. 5.19: Open-aperture Z-scan curves for 19-NH-MWCNTs at (A) $0.19 \text{ GW}\cdot\text{cm}^{-2}$ and (B) $0.48 \text{ GW}\cdot\text{cm}^{-2}$, all in DMSO.

Excited state absorption (ESA) and nonlinear scattering (NLS) are the two mechanisms that were employed in the interpretation of optical limiting effects for C60 and carbon black suspension [224,345,346]. For carbon nanotubes, NLS is a generally accepted dominant mechanism [347]. Fig. 5.20 shows a plot of input intensity against output intensity for 19-NH-MWCNTs in DMSO at $0.19 \text{ GW}\cdot\text{cm}^{-2}$. It can be seen that I_{out} increases slowly with fast increase in I_{in} , resulting in a nonlinear relationship and strong incident laser transmission reduction. The I_{lim} is much lower for 19-NH-MWCNTs compared to 19 alone. Even though in thin films (19-NH-MWCNTs-TF) the $\text{Im}[\chi^{(3)}]$ and γ values

decreased, Table 5.2, a decrease in I_{lim} shows the advantage of the combination of Pcs with NH-NH-MWCNTs.

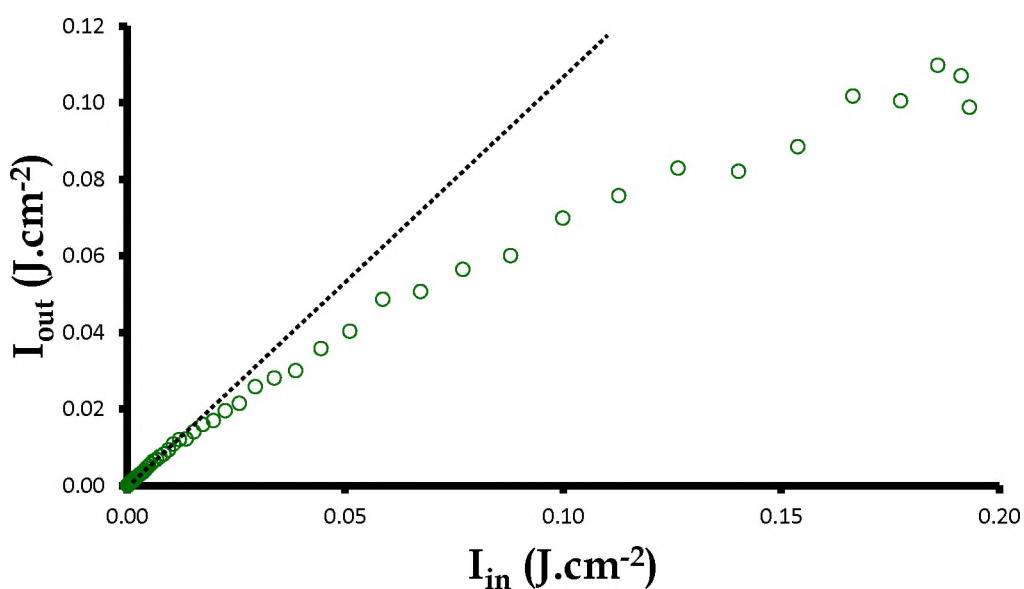


Fig. 5.20: Input intensity against output intensity for 19-NH-MWCNTs at 0.19 GW.cm⁻².

5.2.3 Complexes 19 with NH-GONS and NH-rGONS.

Fig. 5.21A shows the open aperture Z-scan curves obtained for 19-NH-rGONS (as an example of conjugates of 19 with GONS) at 0.23 GW.cm⁻². Fig. 5.21B shows the open aperture Z-scan curves for 19-NH-rGONS_TF. Thin films were studied at higher on-focus intensities (1.1 – 2.5 GW.cm⁻²), where more reliable data was obtained.

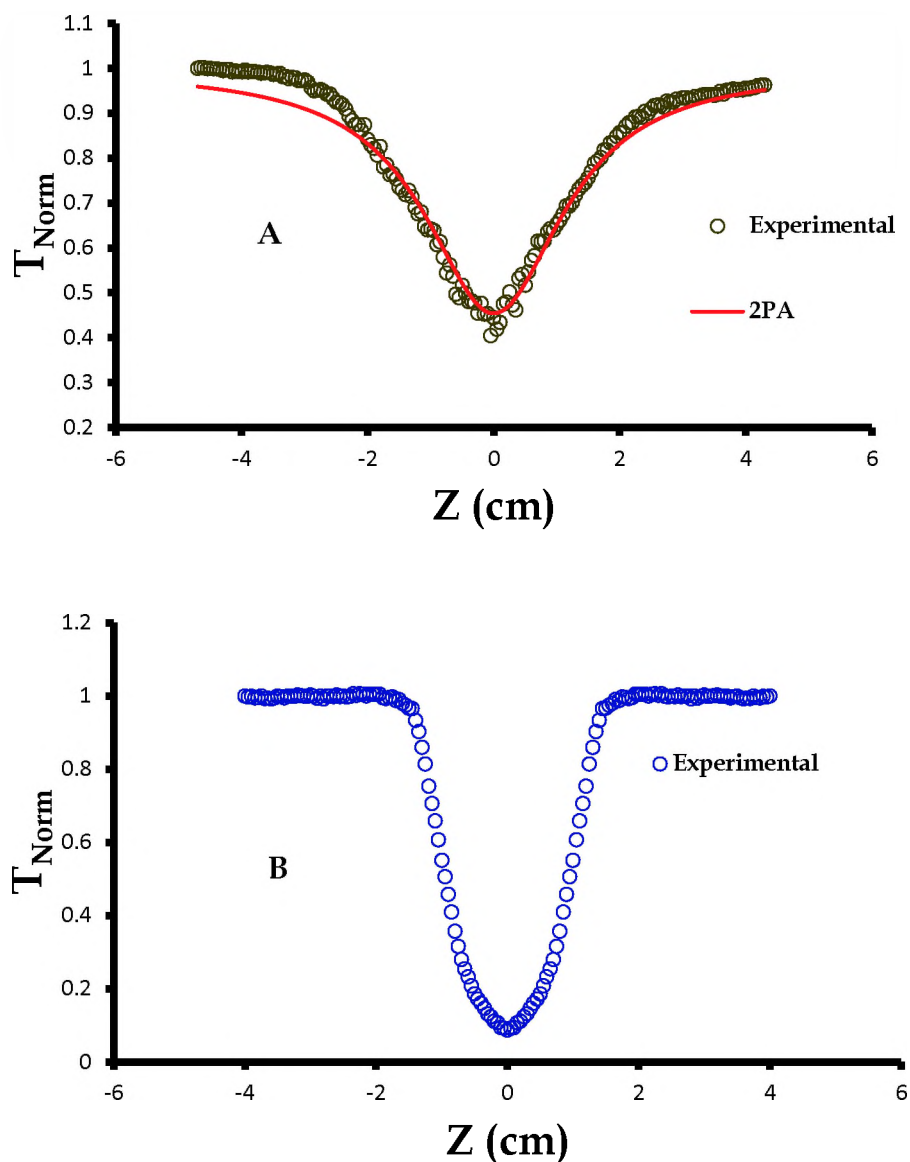


Fig. 5.21: Open-aperture Z-scan curves for (A) **19-NH-rGONS** at $0.23 \text{ GW}\cdot\text{cm}^{-2}$ in DMSO and (B) **19-NH-rGONS-TF** at $1.11 \text{ GW}\cdot\text{cm}^{-2}$.

It can be seen that there is stronger RSA in thin films than in solution. In comparison to complex **19** in solution, $\text{Im}[\chi^{(3)}]$ and γ values for NH-GONS and NH-rGONS are much lower. On linking **19** to NH-GONS and NH-rGONS, it was observed that the $\text{Im}[\chi^{(3)}]$

and γ values improved and were slightly larger than for **19** alone and much larger than for NH-GONS and NH-rGONS. The $\text{Im}[\chi^{(3)}]$ and γ values for NH-GONS-TF and NH-rGONS-TF were also lower than for **19**-TF, Table 5.2. I_{lim} values for NH-GONS and NH-rGONS in solution and NH-GONS-TF and NH-rGONS-TF were much lower than for **19** alone or **19**-TF, showing the advantage of NH-GONS and NH-rGONS over **19** alone or **19**-TF. For NH-GONS, the I_{lim} value is larger compared to NH-GONS-TF, but lower for NH-rGONS in solution than for NH-rGONS-TF. Interestingly, the I_{lim} value of **19**-NH-GONS is less than that of NH-GONS alone. For NH-rGONS and **19**-NH-rGONS, the I_{lim} value did not change much. $\text{Im}[\chi^{(3)}]$, γ and I_{lim} values for NH-GONS, NH-rGONS, **19**-NH-rGONS, **19**-NH-GONS, NH-GONS-TF, NH-rGONS-TF, **19** and **19**-TF are given in Table 5.2.

Chapter 6

Conclusions and future prospects

Conclusions

The synthesis of lanthanide phthalocyanines was achieved successfully. Covalent linkage of mono- and binuclear phthalocyanine to ZnO NPs, MWCNTs and GONS was also confirmed as an amide bond using FTIR. Ytterbium bis(phthalocyanine) (**23**) was found structurally distorted while Lanthanide bis(phthalocyanine) (**26**) was found aggregated. The optical limiting properties of lanthanide phthalocyanines and their conjugates were determined in solution and when embedded in poly (methyl methacrylate), poly (bisphenol A carbonate) and poly (acrylic acid). High third order susceptibilities and hyperpolarizabilities, and low limiting threshold values were found for the blue forms in the case of lanthanide bis(phthalocyanines) (**24b** and **28b**).

The low symmetry lanthanide phthalocyanines (**19**, **20** and **21**) also exhibited high third order susceptibilities and hyperpolarizabilities, and low limiting threshold values in solution and thin films. The peripherally substituted lanthanide phthalocyanines also possess higher third order susceptibilities and hyperpolarizabilities, and lower limiting threshold values compared to non-peripherally substituted lanthanide phthalocyanines. When linked to GONS, third order susceptibilities and hyperpolarizabilities were enhanced, while limiting threshold values were reduced.

When embedded in polymers (PMMA, PAA and PBC), the third order susceptibilities and hyperpolarizabilities increased, and limiting threshold values were further reduced.

In general, lanthanide phthalocyanines, alone or when linked to ZnO NPs, MWCNTs and GONS, showed good optical limiting properties in solution and thin films, except for

complex **18** and its conjugate with ZnO NPs. The extension of π -electron system improved $\text{Im}[\chi^{(3)}]$, γ and I_{lim} values. Bis(phthalocyanines) and trinuclear phthalocyanines with lanthanide ions of half-filled f-orbitals showed $\text{Im}[\chi^{(3)}]$ and γ values and lower I_{lim} values than those with either fully filled or empty f-orbitals.

Future prospects

The elongated π -electron systems in dilanthanide tris(phthalocyanines), the low symmetry binuclear phthalocyanines as well as the reduced forms of lanthanide bis(phthalocyanines) showed a huge potential in NLO application. However, the reduced forms of lanthanide bis(phthalocyanines) proved to be a challenge in terms of thin film preparation, hence no data is presented in this thesis. This, therefore, draws attention for future innovations on the thin film preparation with the reduced forms of lanthanide bis(phthalocyanines).

References

1. M. Hanack, H. Heckmann, R. Polley, *Meth. Org. Chem.(houben-Weyl), Phthalocyanines and Related Compounds*, 1998; Vol. E9d, p. 717.
2. P. Gregory, *J. Porphyrins Phthalocyanines* 3 (1999) 468.
3. N. B. McKeown, *Chem. Ind.* (1999) 92.
4. A. G. Dandridge, H.A.E. Drescher, J. Thomas, *Dyes British Patent*, 322 (1929) 169.
5. R. P. J. Linstead, *Chem. Soc.* (1934) 1016.
6. G. T. Byrne, R. P. Linstead, A. R. Lowe, *J. Chem. Soc.* (1934) 1017.
7. R. P. Linstead, A. R. Lowe, *J. Chem. Soc.* (1934) 1022.
8. C. E. Dent, R. P. Linstead, *J. Chem. Soc.* (1934) 1027.
9. C. E. Dent, R. P. Linstead, A. R. Lowe, *J. Chem. Soc.* (1934) 1033.
10. J. A. Elvidge, R. P. Linstead, *J. Chem. Soc.* (1955) 3526.
11. J. M. Robertson, *J. Chem. Soc.* (1934) 615.
12. J. M. Robertson, R. P. Linstead, C. E. Dent, *Nature* 135 (1935) 506.
13. J. M. Robertson, *J. Chem. Soc.* (1936) 1195.
14. J. M. Robertson, I. Woodward, *J. Chem. Soc.* (1937) 219.
15. J. M. Robertson, I. Woodward, *J. Chem. Soc.* (1937) 3536.
16. J. R. Darwent, P. Douglas, A. Harriman, G. Porter, M. C. Richoux, *Coord. Chem. Rev.* 44 (1982) 83.
17. A. B. P. Lever, M. R. Hempstead, C. C. Leznoff, W. Liu, M. Melnik, W. A. Nevin, P. Seymour, *Pure Appl. Chem.* 58 (1986) 1467.
18. J. H. Zagal, *Coord. Chem. Rev.* 119 (1992) 89.

19. O. L. Kaliya, E. A. Lukyanets, G. N. Vorozhtsov, *J. Porphyrins Phthalocyanines* 3 (1999) 592.
20. A. Sorokin, *Chem. Rev.* 113 (2013) 8152.
21. A. Sorokin, *In Photosensitizers in medicine, environment and security*; T. Nyokong, V. Ahsen, Eds., Springer: Dordrecht, 2012; p. 433.
22. J. D. Spikes, *Photochem. Photobiol.* 43 (1986) 691.
23. I. Rosenthal, *Photochem. Photobiol.* 53 (1991) 859.
24. R. Bonnett, *Chem. Soc. Rev.* 24 (1995) 19.
25. E. A. Lukyanets, *J. Porphyrins Phthalocyanines* 3 (1999) 424.
26. I. Rosenthal, *In Phthalocyanines: properties and applications*; C. C. Leznoff, A. B. P. Lever, Eds., VCH Publ. Inc.: New York, 1996; Vol. 4, p. 481.
27. R. Bonnett, *In Chemical aspects of photodynamic therapy*; Gordon and Breach, Amsterdam, 2000; p 199.
28. M. Wainwright, *In Photosensitisers in Biomedicine*; John Wiley & Sons: Oxford, 2009; p. 147.
29. H. Ali, J. E. van Lier, *In Handbook of Porphyrin Science*; K. M. Kadish, K. M. Smith, R. Guilard, Eds., World Scientific Publ.: Singapore, 2010; Vol. 4, p. 1.
30. S. M. B. Costa, S. M. Andrade, D. M. Togashi, P. M. R. Paulo, C. A. T. Laia, M. Isabel Viseu, A. M. Goncalves da Silva, *J. Porphyrins Phthalocyanines* 13 (2009) 509.
31. N. Sekkat, H. van den Bergh, T. Nyokong, N. Lange, *Molecules* 17 (2012) 98.
32. G. Jori, *J. Environ. Pathol. Tox.* 25 (2006) 505.

33. T. Maisch, *Anti-Infect. Agents Med. Chem.* 6 (2007) 145.
34. R. F. Donnelly, P. A. McCarron, M. M. Tunney, *Microbiol. Res.* 163 (2008) 1.
35. T. Maisch, *Mini-Rev. Med. Chem.* 9 (2009) 974.
36. P. Gregory, *J. Porphyrins Phthalocyanines* 4 (2000) 432.
37. R. Zhou, F. Josse, W. Göpel, Z. Z. Öztürk, O. Bekaroğlu, *Appl. Organometal. Chem.* 10 (1996) 557.
38. L. Valli, *Adv. Colloid Interface Sci.* 116 (2005) 13.
39. M. Bouvet, *Anal. Bioanal. Chem.* 384 (2006) 366.
40. Z. Z. Öztürk, N. Kılınc, D. Atilla, A. G. Gürek, V. Ahsen, *J. Porphyrins Phthalocyanines* 13 (2009) 1179.
41. L. Li, Q. Tang, H. Li, W. Hu, X. Yang, Z. Shuai, Y. Liu, D. Zhu, *Pure Appl. Chem.* 80 (2008) 2231.
42. G. de la Torre, M. Nicolau, T. Torres, *In Supramolecular Photosensitive and Electroactive materials*; H. S. Nalwa, Ed., Academic Press: San Diego, 2001; p. 1.
43. K. Ohta, K. Hatsusaka, M. Sugibayashi, M. Ariyoshi, K. Ban, F. Maeda, R. Naito, K. Nishizawa, A. M. van de Craats, J. M. Warman, *Mol. Cryst. Liquid Cryst.* 397 (2003) 325.
44. K. Hanabusa, H. Shirai, *In Phthalocyanines: Properties and Applications*; C. C. Leznoff, A. B. P. Lever, Eds., VCH Publ. Inc.: New York, 1993; Vol. 2, p. 197.
45. J. Simon, P. Bassoul, *In Phthalocyanines: Properties and Applications*; C. C. Leznoff, A. B. P. Lever, Eds., VCH Publ. Inc.: New York, 1993; Vol. 2, p. 223.

46. A. N. Cammidge, R. J. Bushby, *In Handbook of Liquid Crystals*; D. Demus, Ed., Wiley-VCH Verlag GmbH.: Weinheim, 1998; Vol. 2B, p. 693.
47. D. Wöhrle, G. Schnurpfeil, S. G. Makarov, A. Kazarin, O. N. Suvorova, *Makroheterocycles* 5 (2012) 191.
48. C. G. Claessens, U. Hahn, T. Torres, *Chem. Record* 8 (2008) 75.
49. V. M. Martinez-Diaz, D. Diaz Diaz, *J. Porphyrins Phthalocyanines* 13 (2009) 397.
50. M. G. Walter, A. B. Rudine, C. C. Wamser, *J. Porphyrins Phthalocyanines* 14 (2010) 759.
51. D. Wöhrle, L. Kreienhoop, D. Schlettwein, *In Phthalocyanines: Properties and Applications*; C. C. Leznoff, A. B. P. Lever, Eds., VCH Publ. Inc.: New York, 1996; Vol. 4, p. 219.
52. V. M. Martinez-Diaz, T. Torres, *In Handbook of Porphyrin Science*; K. M. Kadish, K. M. Smith, R. Guilard, Eds., World Scientific Publ.: Singapore, 2010; Vol. 10, p. 141.
53. H. Imahori, K. Kurotobi, M. G. Walter, A. B. Rudine, C. C. Wamser, *In Handbook of Porphyrin Science*; K. M. Kadish, K. M. Smith, R. Guilard, Eds., World Scientific Publ.: Singapore, 2012; Vol. 18, p. 57.
54. D. Schlettwein, T. Nyokong, *In Handbook of Porphyrin Science*; K. M. Kadish, K. M. Smith, R. Guilard, Eds., World Scientific Publ.: Singapore, 2012; Vol. 24, p. 389.
55. J. A. A. W. Elemans, R. van Hameren, R. J. M. Nolte, A. E. Rowan, *Adv. Mater.* 18 (2006) 1251.
56. G. de la Torre, C. G. Claessens, T. Torres, *Chem. Commun.* (2007) 2000.
57. L. Zhang, L. Wang, *J. Material. Sci.* 43 (2008) 5692.

58. G. Bottari, G. de la Torre, D. M. Guldi, T. Torres, *Chem. Rev.* 110 (2010) 6768.
59. F. D'Souza, O. Ito, *Chem. Soc. Rev.* 41 (2012) 86.
60. H. Schultz, H. Lehmann, M. Rein, M. Hanack, *Struct. Bond.* 74 (1991) 41.
61. M. M. Ayhan, A. Singh, C. Hirel, A. G. Gürek, V. Ahsen, E. Jeanneau, I. Ledoux-Rak, J. Zyss, C. Andraud, Y. Bretonnière, *J. Am. Chem Soc.* 134 (2012) 3655.
62. M. Hanack, T. Schneider, M. Barthel, J. S. Shirk, S. R. Flom, R. G. S. Pong, *Coord. Chem. Rev.* 235 (2001) 219.
63. M. Hanack, D. Dini, M. Barthel, S. Vagin, *Chem. Record* 2 (2002) 129.
64. G. de la Torre, P. Vazquez, F. Agullo-Lopez, T. Torres, *Chem. Rev.* 104 (2004) 3723.
65. Y. Chen, M. Hanack, W. J. Blau, D. Dini, Y. Liu, Y. Lin, J. Bai, *J. Mat. Sci.* 41 (2006) 2169.
66. H. S. Nalwa, J. A. Shirk, *In Phthalocyanines: Properties and Applications*; C. C. Leznoff, A. B. P. Lever, Eds., VCH Publ. Inc.: New York, 1996; Vol. 4, p 79.
67. S. R. Flom, *In Porphyrin Handbook*; K. M. Kadish, K. M. Smith, R. Guilard, Eds., Academic Press: San Diego, 2003; Vol. 19, p. 179.
68. N. Rapulenyane, E. Antunes, N. Masilela, T. Nyokong, *J. Photochem. Photobiol. A: Chem* 250 (2012) 18.
69. N. Masilela, T. Nyokong, *Synth. Met.* 162 (2012) 1839.
70. V. N. Nemykin, E. A. Lukyanets, *ARKIVOC* (2010) (i) 136.
71. C. Bozoglu, M. Arıcı, A. L. Uğur, A. Erdoğan, A. Koca, *Synth. Met.* 190 (2014) 56.
72. S. Bo, D. Tang, X. Liu, Z. Zhen, *Dyes Pigm.* 76 (2008) 35.

-
73. V. N. Nemykin, V. Y. Chernii, S. V. Volkov, *J. Chem. Soc., Dalton Trans.* (1998) 2995.
74. M. G. Vivas, L. de Boni, L. Gaffo, C. R. Mendonca, *Dyes Pigm.* 101 (2014) 338.
75. R. Zugle, T. Nyokong, *J. Mol. Catal. A: Chem.* 358 (2012) 49.
76. R. Zugle, C. Litwinski, T. Nyokong, *Polyhedron* 30 (2011) 1612.
77. Hideyuki Yoshiyama, Norio Shibata, Takefumi Sato, Shuichi Nakamura, Ta keshi Toru, *Org. Biomol. Chem.* 6 (2008) 4498.
78. S. Vigh, H. Lam, P. Janda, A. B. P. Lever, C. C. Leznoff, R. L. Cerny, *Can. J. Chem.* 69 (1991) 1457.
79. H. Lam, S. M. Marcuccio, P. I. Svirskaya, S. Greenberg, A. B. P. Lever, C. C. Leznoff, R. L. Cerny, *Can. J. Chem.* 67 (1989) 1087.
80. A. Gonzalez, P. Varquez, T. Torres, *Tetrahedron Lett.* 40 (1999) 3263.
81. A. Yu. Tolbin, V. E. Pushkarev, E. V. Shulishov, A. V. Ivanov, L. G. Tomilova, N. S. Zefirov, *Mendeleev Commun.* (2005) 24.
82. V. N. Nemykin, A. Y. Koposov, R. I. Subbotin, S. Sharma, *Tetrahedron Lett.* 48 (2007) 5425.
83. Y. Asano, A. Muranaka, A. Fukasawa, T. Hatano, M. Uchiyama, N. Kobayashi, *J. Am. Chem. Soc.* 129 (2007) 4516.
84. S. G. Makarov, O. N. Suvorova, C. Litwinski, E. A. Ermilov, B. Roeder, O. Tsaryova, T. Dülcks, D. Woehrle, *Eur. J. Inorg. Chem.* (2007) 546.
85. D. Lelievre, L. Bosio, J. Simon, J. J. Andre, F. Bensebaa, *J. Am. Chem. Soc.* 114 (1992) 4475.

86. D. Lelievre, O. Damette, J. Simon, *J. Chem. Soc. Chem. Commun.* (1993) 939.
87. K. Ishii, N. Kobayashi, Y. Higashi, T. Osa, D. Lelievre, J. Simon, S. Yamauchi, *Chem. Commun.* (1999) 969.
88. N. Kobayashi, Y. Higashi, T. Osa, *J. Chem. Soc. Chem. Commun.* (1994) 1785.
89. N. Kobayashi, T. Fukuda, D. Lelievre, *Inorg. Chem.* 39 (2000) 3632.
90. N. Kobayashi, H. Ogata, *Eur. J. Inorg. Chem.* (2004) 906.
91. Y. Asano, J. Sato, T. Furuyama, N. Kobayashi, *Chem. Commun.* 48 (2012) 4365.
92. A. Yu. Maksimov, A. V. Ivanov, Y. N. Blikova, L. G. Tomilova, N. S. Zefirov, *Mendeleev Commun.* (2003) 70.
93. A. Yu. Tolbin, V. E. Pushkarev, L. G. Tomilova, N. S. Zefirov, *Russ. Chem. Bull.* 55 (2006) 1155.
94. A. Yu. Tolbin, V. E. Pushkarev, L. G. Tomilova, N. S. Zefirov, *J. Porphyrins Phthalocyanines* 12 (2008) 1187.
95. T. V. Dubinina, A. V. Ivanov, N. E. Borisova, S. A. Trashin, S. I. Gurskiy, L. G. Tomilova, N. S. Zefirov, *Inorg. Chim. Acta* 363 (2010) 1869.
96. A. Yu. Tolbin, V. E. Pushkarev, L. G. Tomilova, N. S. Zefirov, *Macroheterocycles* 3 (2010) 30.
97. T. V. Dubinina, N. E. Borisova, K. V. Paramonova, L. G. Tomilova, *Mendeleev Commun.* 21 (2011) 165.
98. S. A. Trashin, T. V. Dubinina, A. V. Fionov, L. G. Tomilova, *J. Porphyrins Phthalocyanines* 15 (2011) 1195.
99. A. Yu. Tolbin, V. E. Pushkarev, L. G. Tomilova, *Mendeleev Commun.* 18 (2008) 94.

100. V. N. Nemykin, S. V. Dudkin, F. Dumoulin, C. Hirel, A. G. Gütrek, V. Ahsen, ARKIVOC (2014) (i) 142.
101. B. Zhu, X. Zhang, M. Han, P. Deng, Q. Li, J. Mol. Struct. 1079 (2015) 61.
102. T. Ceyhan, M. Korkmaz, M. K. Erbil, Ö. Bekaroğlu, J. Porphyrins Phthalocyanines 9 (2005) 423.
103. P. Şen, F. Dumludağ, B. Salih, A. R. Özkaya, Ö. Bekaroğlud, Synth. Met. 161 (2011) 1245.
104. M. J. F. Calvete, D. Dini, S. R. Flom, M. Hanack, R. G. S. Pong, J. S. Shirk, Eur. J. Org. Chem. (2005) 3499.
105. M. J. F. Calvete, D. Dini, M. Hanack, J. C. S ancho-García, W. Chen, W. Ji, J. Mol. Model 12 (2006) 543.
106. L. De Boni, L. Gaffo, L. Misoguti, C.R. Mendonça, Chem. Phys. Lett. 419 (2006) 417.
107. L. Chen, R. Hua, J. Xu, S. Wang, X. Li, S. Li, G. Yang, Spectrochim. Acta, Part A 105 (2013) 577.
108. R. Rousseau, R. Aroca, M. L. Rodríguez-Méndez, J. Mol. Struct. 356 (1995) 49.
109. R. W. Boyd, *Nonlinear Optics*; Academic Press: San Diego, CA, 1992.
110. C. Huang, K. Wang, J. Sun, J. Jiang, Eur. J. Inorg. Chem. (2014) 1546.
111. R. O. Ogbodu, E. Antunes, T. Nyokong, Dalton Trans. 42 (2013) 10769.
112. E. M. Maya, C. García, E.M. García-Frutos, P. Vázquez, T. Torres, J. Org. Chem. 65 (2000) 2733.
113. T. Ceyhan, M. Korkmaz, T. Kutluay, Ö. Bekaroğlu, J. Porphyrins Phthalocyanines 8 (2004) 1383.

114. N. Ozan, Ö. Bekaroğlu, *Polyhedron* 22 (2003) 819.
115. M. Quintiliani, E.M. García-Frutos, A. Gouloumis, P. Vázquez, I. Ledoux-Rak, J. Zyss, C.G. Claessens, T. Torres, *Eur. J. Org. Chem.* 2005 (2005) 3911.
116. M. Yüksek, T. Ceyhan, H. G. Yağlıoğlu, A. Elmali, Ö. Bekaroğlu, *Opt. Commun.* 281 (2008) 2970.
117. J. J. Doyle, J. Wang, S. M. O'Flaherty, Y. Chen, A. Slodek, T. Hegarty, L.E. Carpenter II, D. Wöhrle, M. Hanack, W.J. Blau, *J. Opt. A Pure Appl. Opt.* 10 (2008) 75101.
118. S. Tekin, U. Kurum, M. Durmuş, H. Yaglioglu, T. Nyokong, A. Elmali, *Opt. Commun.* 283 (2010) 4749.
119. K. Sanusi, T. Nyokong, *J. Photochem. Photobiol. A*: 303-304 (2015) 44.
120. W. Liu, J. Jiang, D. Du, D. P. Arnold, *Aust. J. Chem.* 53 (2000) 131.
121. A. G. Martynov, Y. G. Gorbunova, *Inorg. Chim. Acta* 360 (2007) 122.
122. C. R. Mendonça, L. Gaffo, L. Misoguti, W. C. Moreira, O. N. Oliveira Jr., S. C. Zilio, *Chem. Phys. Lett.* 323 (2000) 300.
123. H. G. Yağlıoğlu, M. Arslan, Ş. Abdurrahmanoğlu, H. Ünver, *J. Phys. Chem. Solids* 69 (2008) 161.
124. M.G. Vivas, E.G.R. Fernandes, M.L. Rodríguez-Méndez, C.R. Mendonca, *Chem. Phys. Lett.* 531 (2012) 173.
125. T. Ceyhan, G. Yağlıoğlu, H. Ünver, B. Salih, M. K. Erbil, A. Elmali, Ö. Bekaroğlu, *Macroheterocycles* 1 (2008) 44.

126. A. B. Karpo, V. E. Pushkarev, V. I. Krasovskii, L. G. Tomilova, *Chem. Phys. Lett.* 554 (2012) 155.
127. J. S. Shirk, J. R. Lindle, F. J. Bartoli, M. E. Boyle, *J. Phys. Chem.* 96 (1992) 5847.
128. C. Huang, Y. Zhang, J. Sun, Y. Bian, D. P. Arnold, *J. Porphyrins Phthalocyanines* 17 (2013) 673.
129. P. Zhu, N. Pan, R. Li, J. Dou, Y. Zhang, D. Y. Y. Cheng, D. Wang, D. K. P. Ng, J. Jiang, *Chem.-Eur. J.* 11 (2005) 1425.
130. Y. Bian, L. Li, D. Wang, C.-F. Choi, D. Y. Y. Cheng, P. Zhu, R. Li, J. Dou, R. Wang, N. Pan, D. K. P. Ng, N. Kobayashi, J. Jiang, *Eur. J. Inorg. Chem.* (2005) 2612.
131. W. Huang, H. Xiang, Q. Gong, Y. Huang, C. Huang, J. Jiang, *Chem. Phys. Lett.* 374 (2003) 693.
132. V.E. Pushkarev, E.V. Shulishov, Y.V. Tomilov, L.G. Tomilova, *Tetrahedron Lett.* 48 (2007) 5269.
133. C. Cadiou, A. Pondaven, M. L'Her, P. Jéhan, P. Guenot, *J. Org. Chem.* 64 (1999) 9046.
134. I.P. Kalashnikova, V.V. Kalashnikov, L.G. Tomilova, *Russ. Chem. Bull.* 58 (2009) 1413.
135. J. Jiang, D. K. P. Ng, *Acc. Chem. Res.* 42 (2009) 79.
136. P. Zhu, Y. Wang, M. Ren, X. Zhao, X. Zhang, *Inorg. Chim. Acta* 392 (2012) 10.
137. T. Kololuoma, J. A. I. Oksanen, P. Raerinne, J. T. Rantala, *J. Mater. Res.* 16 (2011) 2186.
138. A. Nas, N. Kahrman, H. Kantekin, N. Yaylı, M. Durmuş, *Dyes Pigm.* 99 (2013) 90.

139. W. Chidawanyika, C. Litwinski, E. Antunes, T. Nyokong, J. Photochem. Photobiol. A: 212 (2010) 27.
140. E. Orti, J.-L. Brédas, J. Chem. Phys. 89 (1988) 1009.
141. E. Orti, J.-L. Brédas, C. Clarisse, J. Chem. Phys. 92 (1990) 1228.
142. E. Orti, J.-L. Brédas, J. Am. Chem. Soc. 114 (1992) 8669.
143. V. Lemaure, M. Steel, D. Beljonne, D. J.-L. Brédas, J. Cornil, J. Am. Chem. Soc. 127 (2005) 6077.
144. J. Mack, M. J. Stillman, Inorg. Chem. 36 (1997) 413.
145. J. Mack, M. J. Stillman, J. Porphyrins Phthalocyanines 5 (2001) 67.
146. J. Mack, M. J. Stillman, Coord. Chem. Rev. 219–221 (2001) 993.
147. S. P. Keizer, J. Mack, B. A. Bench, S. M. Gorun, M. J. Stillman, J. Am. Chem. Soc. 125 (2003) 7067.
148. T. C. VanCott, Z. Gasyna, P. N. Schatz, M. E. Boyle, J. Phys. Chem. 99 (1995) 4820.
149. Z. Gasyna, P. N. Schatz, M. E. Boyle, J. Phys. Chem. 99 (1995) 10159.
150. S. Kahlal, A. Mentec, A. Pondaven, M. L'Her, J.-Y. Saillard, New J. Chem. 33 (2009) 574.
151. C. Dunfold, B. Williamson, E. Krausz, J. Phys. Chem. A 104 (2000) 3537.
152. N. Ishikawa, Y. Kaizu, Chem. Phys. Lett. 339 (2001) 125.
153. N. Ishikawa, O. Ohno, Y. Kaizu, H. Kobayashi, J. Phys. Chem. 96 (1992) 8832.
154. N. Ishikawa, O. Ohno, Y. Kaizu, J. Phys. Chem. 97 (1993) 1004.
155. R. Wang, R. Li, Y. Li, X. Zhang, P. Zhu, P.-C. Lo, D. K. P. Ng, N. Pan, C. Ma, N. Kobayashi, J. Jiang, Chem.-Eur. J. 12 (2006) 1475.

-
156. R. Weiss, J. Fischer, *Lanthanide phthalocyanine complexes*. In *The Porphyrin Handbook*, 1st ed., K. Kadish, K. M. Smith, R. Guilard, Eds., Academic Press Inc.: New York, NY, USA, 2006; Vol. 16, p. 171.
157. *Phthalocyanines Properties and Applications*, 1st ed.; Leznoff, C.C., Lever, A.B.P., Eds., VCH Publishers: New York, NY, USA, 1989; Vol. 1.
158. P. A. Franken, A. E. Hill, C. W. Peters, G. Weinreich, *Phys. Rev. Lett.* 7 (1961) 118.
159. J. A. Armstrong, N. Bloembergen, J. Ducuing, P. S. Pershan, *Phys. Rev.* 127 (1962) 1918.
160. J. Kerr, *Phil. Mag.* S. 50 (1875) 337.
161. J. Kerr, *Phil. Mag.* 8 (1875) 229.
162. J. Kerr, *J. Phys. Theor. Appl.* 8 (1879) 414.
163. Y. Chen, M. Hanack, Y. Araki, O. Ito, *Chem. Soc. Rev.* 34 (2005) 517.
164. R. S. S. Kumar, S. V. Rao, L. Giribabu, D. N. Rao, *Proc. of SPIE* 6875 (2008) 68751D.
165. M. Hanack, M. Lang, *Adv. Mater.* 6 (1994) 819.
166. N. B. Mckeown, *Phthalocyanine Materials: Synthesis, Structure and Function*, B. Dunn, J. W. Goodby, A. R. West, Eds., Cambridge University Press, 1998.
167. G. De La Torre, P. Vazquez, F. Agullo-Lopez, T. Torres, *J. Mater. Chem.* 8 (1998) 1671.
168. M. Feng, H. B. Zhan, Y. Chen, *Appl. Phys. Lett.* 96 (2010) 033107.
169. L. Polavarapu, N. Venkatram, W. Ji, Q. H. Xu, *ACS Appl. Mater. Interfaces* 1 (2009) 2298.
170. M. Calvete, G. Y. Yang, M. Hanack, *Synth. Met.* 141 (2004) 231.

171. C. W. Spangler, *J. Mater. Chem.* 9 (1999) 2013.
172. S. V. Rao, *Proc. SPIE* 7197 (2009) 719715.
173. F. Li, Z. He, M. Li, P. Lu, *Mater. Lett.* 111 (2013) 8.
174. L. Ma, Y. Zhang, and P. Yuan, *Opt. Express* 18 (2010) 17666.
175. R. S. S. Kumar, S. V. Rao, L. Giribabu, D. N. Rao, *Chem. Phys. Letters* 447 (2007) 274.
176. M. Hercher, *Appl. Opt.* 6 (1967) 94.
177. M. Sanghadasa, I. S. Shin, R. D. Clark, H. Guo, B. G. Penn, *J. Appl. Phys.*, 90 (2001) 31.
178. W. Su, T. M. Cooper, *Chem. Mater.* 10 (1998) 1212.
179. T. Xia, A. Dogatiu, K. Mansour, D. J. Hagan, A. A. Said, *J. Opt. Soc. Am. B* 15 (1998) 1497.
180. L. Smilowitz, D. McBranch, V. Klimov, J. M. Robinson, A. Koskelo, M. Grigorova, B. R. Mattes, R. C. H. Wang, F. Wudl, *Opt. Lett.* 21 (1996) 922.
181. A. Krivokapic, H. L. Anderson, G. Bourhill, R. Ives, S. Clark, L. J. McEwan, *Adv. Mater.* 13 (2001) 652.
182. G. Brusatin, R. Signorini, *J. Mater. Chem.* 12 (2002) 1964.
183. Y. Chen, L. Gao, M. Feng, L. Gu, N. He, J. Wang, Y. Araki, W.J. Blau, O. Ito, *Mini Rev. Org. Chem.* 6 (2009) 55.
184. P. Chen, I. V. Tomov, A. S. Dvornikov, M. Nakashima, J. F. Roach, D. M. Alabran, P. M. Rentzepis, *J. Phys. Chem.* 100 (1996) 17507.

185. M. Sheik-Bahae, A. A. Said, T. -H. Wei, D. J. Hagan, E. W. Van Stryland, *IEEE J. Quantum Electron.* 26 (1990) 760.
186. M. Sheik-Bahae, A. A. Said, E. W. Van Stryland, *Opt. Lett.* 14 (1989) 955.
187. E. W. Van Stryland, M. Sheik-Bahae, *In Characterization Techniques and Tabulations for Organic Nonlinear Materials*; M. G. Kuzyk, C. W. Dirk, Eds., Marcel Dekker, Inc.: New York, 1998; pp 655.
188. R. L. Sutherland, *Handbook of Nonlinear Optics*, Second Edition, Revised and expanded (New York, NY: Marcel Dekker, 2003).
189. E. M. García, S. M. O'Flaherty, E. M. Maya, G. de la Torre, W. Blau, P. Vázquez, T. Torres, *J. Mater. Chem.* 13 (2003) 749.
190. J. Simon, C. Sirlin, *Pure Appl. Chem.* 61 (1989) 1625.
191. D. Dini, M. Hanack, *In The Porphyrin Handbook: Physical Properties of Phthalocyanine-based Materials*, K.M. Kadish, K.M. Smith, R. Guilard, Eds., Academic Press, USA, 2003; Vol. 17, p. 22.
192. K. P. Unnikrishnan, J. Thomas, V. P. N. Nampoori, C. P. G. Vallabhan, *Chem. Phys.* 279 (2002) 209.
193. K. P. Unnikrishnan, J. Thomas, V. P. N. Nampoori, C. P. G. Vallabhan, *Synth. Met.* 139 (2003) 371.
194. T. Ceyhan, M. A. Özdağ, B. Salih, M. K. Erbil, A. Elmalı, A. R. Özkaya, Ö. Bekaroğlu, *Eur. J. Inorg. Chem.* (2008) 4943.
195. X. Wang, C.-L. Liu, Q.-H. Gong, Y.-Y. Huang, C.-H. Huang, J.-Z. Jiang, *Appl. Phys.* A 75 (2002) 497.

196. S. Saydam, E. Yılmaz, F. Bağcı, H. G. Yağlıoğlu, A. Elmalı, B. Salih, Ö. Bekaroğlu, *Eur. J. Inorg. Chem.* (2009) 2096.
197. M. Terrones, *Annu. Rev. Mater. Res.* 33 (2003) 419.
198. A. Oberlin, M. Endo, T. Koyama, *J. Cryst. Growth* 32 (1976) 335.
199. S. Iijima, *Nature* 354 (1991) 56.
200. T. Kuzumaki, O. Ujii, H. Ichinose, K. Ito, *Adv. Eng. Mater.* 2 (2000) 416.
201. T. Kuzumaki, K. Miyazawa, H. Ichinose, K. Ito, *J. Mater. Res.* 13 (1998) 2445.
202. I. Musa, M. Baxendale, G. A. J. Amaratunga, W. Eccleston, *Synt. Met.* 102 (1999) 1250.
203. I. Capek, *Adv. Colloid Interface Sci.* 63 (2009) 150.
204. I. Hadjipaschalis, A. Poullikkas, V. Efthimiou, *Renew. Sustainable Energy Rev.* 13 (2009) 1513.
205. S. L. Chou, J. Z. Wang, S. Y. Chew, H. K. Liu, S. X. Dou, *Electrochem. Commun.* 10 (2008) 1724.
206. P. Simon, Y. Gogotsi, *Nat. Mater.* 7 (2008) 845.
207. X. Liu, T. A. Huber, M. C. Kopac, P. G. Pickup, *Electrochim. Acta* 54 (2009) 7141.
208. H. J. Dai, *Surf. Sci.* 500 (2002) 218.
209. L. W. Ji, Z. Lin, M. Alcoutlabi, X. W. Zhang, *Energy Environ. Sci.* 4 (2011) 2682.
210. B. J. Landi, M. J. Ganter, C. D. Cress, R. A. DiLeo, R. P. Raffaele, *Energy Environ. Sci.* 2 (2009) 638.
211. C. de las Casas, W. Li, *J. Power Sources* 208 (2012) 74.
212. N. A. Kaskhedikar, J. Maier, *Adv. Mater.* 21 (2009) 2664.

-
213. E. Frackowiak, S. Gautier, H. Gaucher, S. Bonnamy, F. Beguin, *Carbon* 37 (1999) 61.
214. J. Kong, N. R. Franklin, C. W. Zhou, M. G. Chapline, S. Peng, K. Cho, H. Dai, *Science* 287 (2000) 622.
215. P. G. Collins, K. Bradley, M. Ishigami, A. Zettl, *Science* 287 (2000) 1801.
216. L. Liu, S. Zhang, T. Hu, Z.-X. Guo, C. Ye, L. Dai, D. Zhu, *Chem. Phys. Lett.* 359 (2002) 191.
217. Y. Zhang, Y. Song, Y. Gan, M. Feng, H. Zhan, *J. Mater. Chem. C* 3 (2015) 9948.
218. C. Li, C. Liu, F. Li, Q. Gong, *Chem. Phys. Lett.* 380 (2003) 201.
219. N. He, Y. Chen, J. Bai, J. Wang, W.J. Blau, J. Zhu, *J. Phys. Chem. C* 113 (2009) 13029.
220. J. Wang, W.J. Blau, *Chem. Phys. Lett.* 465 (2008) 265.
221. M. Yöksek, A. Elmali, M. Durmuş, H. G. Yaglioglu, H. Ünver, T. Nyokong, *J. Opt.* 12 (2010) 1.
222. M.C. Larciprete, R. Ostuni, A. Belardini, M. Alonzo, G. Leahu, E. Fazio, C. Sibilìa, M. Bertolotti, *Photon. Nanostr. Fundamen. Appl.* 5 (2007) 73.
223. C. Nitschke, S. M. O'Flaherty, M. Kroll, W. Blau, *J. Phys. Chem. B* 108 (2004) 1287.
224. J. Britton, M. Durmuş, Samson Khene, V. Chauke, T. Nyokong, *J. Porphyrins Phthalocyanines* 17 (2013) 691.
225. A. K. Geim, K. S. Novoselov, *Nat. Mater.* 6 (2007) 183.
226. J. Li, X. Zeng, T. Ren, E. van der Heide, *Lubricants* 2 (2014) 137.
227. T. Szabó, A. Szeri, I. Dékány, *Carbon* 43 (2005) 87.
228. H. He, J. Klinowski, M. Forster, A. Lerf, *Chem. Phys. Lett.* 287 (1998) 53.

-
229. A. Lerf, H. He, M. Forster, J. Klinowski, *Phys. Chem. B* 102 (1998) 4477.
230. S. Stankovich, D. A. Dikin, R. D. Piner, K. A. Kohlhaas, A. Kleinhammes, Y. Jia, Y. Wu, S. T. Nguyen, R. S. Ruoff, *Carbon* 45 (2007) 1558.
231. S. Stankovich, D. A. Dikin, G. H. B. Dommett, K. M. Kohlhaas, E. J. Zimney, E. A. Stach, R. D. Piner, S. T. Nguyen, R. S. Ruoff, *Nature* 442 (2006) 282.
232. L. Wang, Y. Ye, X. Lu, Y. Wu, L. Sun, H. Tan, F. Xu, Y. Song, *Electrochim. Acta* 114 (2013) 223.
233. W. Gao, L. B. Alemany, L. Ci, P. M. Ajayan, *Nat. Chem.* 1 (2009) 403.
234. G. Wang, J. Yang, J. Park, X. Gou, B. Wang, H. Liu, J. Yao, *J. Phys. Chem. C* 112 (2008) 8192.
235. Y. Si, E. T. Samulski, *Nano Lett.* 8 (2008) 1679.
236. A. K. Geim, *Science* 324 (2009) 1530.
237. P. Avouris, *Nano Lett* 10 (2010) 4285.
238. F. Schwierz, *Nat. Nanotechnol.* 5 (2010) 487.
239. N. Liaros, P. Aloukos, A. Kolokithas-Ntoukas, A. Bakandritsos, T. Szabo, R. Zboril, S. Couris, *J. Phys. Chem. C* 117 (2013) 6842.
240. X.-F. Jiang, L. Polavarapu, S. T. Neo, T. Venkatesan, Q.-H. Xu, *J. Phys. Chem. Lett.* 3 (2012) 785.
241. G.-K. Lim, Z.-L. Chen, J. Clark, R. G. S. Goh, W.-H. Ng, H.-W. Tan, R. H. Friend, P. K. H. Ho, L.-L. Chua, *Nat. Photonics* 5 (2011) 554.
242. A. M. Pinto, I. C. Gonçalves, F. D. Magalhães, *Colloids Surf. B: Biointerfaces* 111 (2013) 188.

-
243. W. Song, C. He, W. Zhang, Y. Gao, Y. Yang, Y. Wu, Z. Chen, X Li, Y. dong, Carbon 77 (2014) 1020.
244. A. P. Nikam, M. P. Ratnaparkhiand, S. P. Chaudhari, Int. J. Res. Dev. Pharm. L. Sci. 3 (2014) 1121.
245. H. Aleali, N. Mansour, J. Sci. I. R. Iran 21 (2010) 273.
246. D. Compton, L. Cornish, E. van der Lingen, Gold Bull. 36 (2003) 10.
247. S. Schwung, A. Rogov, G. Clarke, C. Joulaud, T. Magouroux, D. Staedler, S.Passemaid, T. Jüstel, L. Badie, C. Galez, J. P. Wolf, Y. Volkov, A. Prina-Mello, S. Gerber-Lemaire, D. Rytz, Y. Mugnier, L. Bonacina, R. Le Dantec, J. Appl. Phys. 116 (2014) 114306.
248. L. Irimpan, V. P. N. Nampoore, P. Radhakrishnan, Sci. Adv. Mater. 2 (2010) 578.
249. R. Sreeja, Jobina John, P.M. Aneesh, M.K. Jayaraj, Optics Communications 283 (2010) 2908.
250. J. R. Lakowicz, *Principles of Fluorescence Spectroscopy*, 3rd ed., Springer Science+Business Media, LCC, New York, 2006.
251. U. Resch-Genger, M. Grabolle, S. Cavaliere-Jaricot, R. Nitschke, T. Nann, Nat. Methods 5 (2008) 763.
252. M. D. Leistikow, J. Johansen, A. J. Kettelarij, P. Lodahl, W. L. Vos, Phys. Rev. B 79 (2009) 1.
253. S. Fery-Forgues, D. Lavabre, J. Chem. Educ. 76 (1999) 1260.
254. A. Gilbert, J. Baggott, *Essentials of molecular photochemistry*, library of congress, USA, (1995).

-
255. T. H. Tran-Thi, C. Desforge, C. Thiec, *J. Phys. Chem.* 93 (1989) 1226.
256. W. Spiller, H. Kliesch, D. Wöhrle, S. Hackbarth, B. Röder, G. Schnurpfeil, *J. Porphyrins Phthalocyanines* 2 (1998) 145.
257. K. Langa, J. Mosinger, D.M. Wagnerová, *Coord. Chem. Rev.* 248 (2004) 321.
258. I. Seotsanyana-Mokhosi, T. Nyokong, *J. Porphyrins Phthalocyanines* 8 (2004) 1214.
259. A. O. Ogunsipe, T. Nyokong, *J. Porphyrins Phthalocyanines* 9 (2005) 121.
260. M. S. Patterson, S. J. Madsen, R. Wilson, *J. Photochem. Photobiol. B: Biol.* 5 (1990) 69.
261. A. V. Ziminov, T. A. Yurre, S. M. Ramsh, M. M. Mezdrogha, *Phys. Solid state* 52 (2010) 1915.
262. M. Durmuş, S. Yeşilot, B. Coşut, A. G. Gürek, A. Kilic, V. Ahsen, *Syn. Met.* 160 (2010) 436.
263. J. G. Young, W. Onnebuagu, *J. Org. Chem.* 55 (1990) 2155.
264. R. D. George, A. W. Snow, *J. Heterocyclic Chem.* 32 (1995) 495.
265. D. Wöhrle, M. Eskes, K. Shigehara, A. Yamada, *Synthesis* (1993) 194.
266. W. Chidawanyika, T. Nyokong, *J. Photochem. Photobiol. A: Chem.* 202 (2009) 99.
267. P. Tau, T. Nyokong, *Electrochim. Acta* 52 (2007) 3641.
268. S. Gaspard, T.H. Tran-Thi, *J. Chem. Soc., Perkin Trans. 2* (1989) 383.
269. M. Durmuş, T. Nyokong, *Polyhedron* 26 (2007) 3323.
270. W. Chidawanyika, A. Ogunsipe, T. Nyokong, *New J. Chem.* 31 (2007) 377.
271. W. Chidawanyika, E. Antunes, T. Nyokong, *J. Photochem. Photobiol. A: Chem.* 195 (2008) 183.

-
272. N. Masilela, T. Nyokong, *Dyes Pigm.* 84 (2010) 242.
273. I. Scalise, E.N. Durantini, *Bioorg. Med. Chem.* 13 (2005) 3037.
274. X.-F. Zhang, X. Shao, H. Tian, X. Sun, K. Han, *Dyes Pigm.* 99 (2013) 480.
275. J. P. Fox, D. P. Goldberg, *Inorg. Chem.* 42 (2003) 8181.
276. F. Bertani, N. Cristiani, M. Mannini, R. Pinalli, R. Sessoli, E. Dalcanale, *Eur. J. Org. Chem.* (2015) 7036.
277. A. Joseph, G. L. Praveen, K. Abha, G. M. Lekha, S. George, *J. Lumin.* 132 (2012) 1999.
278. J. R. Lakowicz, *Principles of Fluorescence Spectroscopy*, 3rd ed., Springer Science+Business Media, LCC, New York, 2006.
279. K. Sanusi, E. K. Amuhaya, T. Nyokong, *J. Phys. Chem. C* 118 (2014) 7057.
280. A. Ogunsipe, J-Y. Chen, T. Nyokong, *New J. Chem.* 28 (2004) 822.
281. J. Kossanyi, D. Chachraroui, *Int. J. Photoenergy* 2 (2000) 9.
282. N. Kuznetsova, E. Makarova, S. Dashkevich, N. Gretsova, E. Kalmykova, V. Negrimovsky, O. Kaliya, E. Luk'yanets, *Obshch. Khim.* 70 (2000) 140.
283. A. G. Martynov, Y. G. Gorbunova, *Polyhedron* 29 (2010) 391.
284. J. Rusanova, M. Pilkington, S. Decurtins, *Chem. Commun.* (2002) 2236.
285. Ş. Merey, Ö. Bekaroğlu, *J. Chem. Soc., Dalton Trans.* (1999) 4503.
286. J. Jiang, M. Bao, L. Rintoul, D. P. Arnold, *Coord. Chem. Rev.* 250 (2006) 424.
287. M. Bao, N. Pan, C. Ma, D. P. Arnold, J. Jiang, *Vib. Spectrosc.* 32 (2003) 175.
288. P. Zhao, S. Xu, Z. Y. Li, F. S. Zhang, *Chin. Phys. Lett.* 25 (2008) 2058.

-
289. D. Sajan, N. Vijayan, K. Safakath, R. Philip, M. Karabakak, *Spectrochim. Acta Part A: Mol. Biomol. Spectrosc.* 108 (2013) 197.
290. A. Y. Tolbin, V. E. Pushkarev, G. F. Nikitin, L. G. Tomilova, *Tetrahedron Lett.* 69 (2009) 4848.
291. A. G. MacKay, J. F. Boas, G. J. Troup, *Aust. J. Chem.* 27 (1974) 955.
292. M. Moussavi, A. De Cian, J. Fischer, R. Weiss, *Inorg. Chem.* 27 (1988) 1287.
293. E. Yabaş, M. Sülü, F. Duamludağ, A. R. Özkaya, B. Salih, Ö. Bekaroğlu, *polyhedron* 42 (2012) 196.
294. G. Gümrükçü, M. Ü. Özgür, A. Altındal, A. R. A. R. Özkaya, B. Salih, Ö. Bekaroğlu, *Syn. Met.* 161 (2011) 112.
295. H. Konami, M. Hatano, A. Tajiri, *Chem. Phys. Lett.* 160 (1989) 163.
296. J.-L. Paillaud, *Doctoral Dissertation. Université Louis Pasteur: Strasbourg (France), 1991.*
297. A. Pondaven, Y. Cosien, M. L'Her, *New J. Chem.* 15 (1991) 515.
298. J. Jiang, W. Liu, W.-F. Law, J. Lin, D. K. P. Ng, *Inorg. Chim. Acta* 268 (1998) 141.
299. F. Lu, M. Bao, C. Ma, X. Zhang, D. P. Arnold, J. Jiang, *Spectrochim. Acta, Part A*, 59 (2003) 3273.
300. M. Kandaz, A.T. Bilgiçli, A. Altındal, *Synth. Met.* 160 (2010) 52.
301. N. Ishikawa, Y. Kaizu, *Coord. Chem. Rev.* 226 (2002) 93.
302. M. Bouvet, in *The Porphyrin Handbook: Applications of phthalocyanines* (Eds. K. M. Kadish, K. M. Smith, R. Guilard) Volume 19, Chp. 118, pp 43.

-
303. A. Yu. Tsivadze, G. Martynov, M. A. Polovkova, Yu. G. Gorbunova, *Russian Chem. Bull. Int. Ed.* 60 (2011) 2258.
304. Y. Zorlu, U. Kumru, Ü. İşci, B. Divrik, E. Jeanneau, F. Albrieux, Y. Dede, V. Ahsenand, F. Dumoulin, *Chem. Commun.* 51 (2015) 6580.
305. F.-L. Lu, *Polyhedron* 26 (2007) 3939.
306. R. Słota, G. Dyrda, M. Hofer, G. Mele, E. Bloise, R. del Sole, *Molecules* 17 (2012) 10738.
307. K. Katoh, Y. Yoshida, M. Yamashita, H. Miyasaka, B. K. Breedlove, T. Kajiwara, S. Takaishi, N. Ishikawa, H. Isshiki, Y. F. Zhang, T. Komeda, M. Yamagishi, J. Takeya, *J. Am. Chem. Soc.* 131 (2009) 9967.
308. N. E. Galanin, G. P. Shaposhnikov, *Russ. J. Org. Chem.* 48 (2012) 851.
309. Y. C. Yang, J. R. Ward, R. P. Seiders, *Inorg. Chem.* 24 (1985) 1765.
310. W. J. Schutte, M. S. Rehbach, J. H. Sluyters, *J. Phys. Chem.* 97 (1993) 6069.
311. E. J. Osburn, L. K. Chau, S. Y. Chen, N. Collins, D. F. O'Brien, N. R. Armstrong, *Langmuir* 12 (1996) 4784.
312. H. Enkelkamp, R. J. M. Nolte, *J. Porphyrins Phthalocyanines* 4 (2000) 454.
313. M. J. Stillman, T. Nyokong, in *Phthalocyanines – Properties and Applications*; A.B.P. Lever, C.C. Leznoff, Eds., vol. 1, VCH, New York, 1989. Chapter 3.
314. T. Nyokong, in: J. Jiang (Volume Ed.), D.M.P. Mingos (Series Ed.), *Structure and Bonding: Functional Phthalocyanine Molecular Materials*, vol. 135, Springer, 2010, pp. 45.
315. M. L. Rodriguez-Mendez, R. Aroca, J. A. De Saja, *Chem. Mater.* 4 (1992) 1017.

316. D. Battisti, L. Tomilova, R. Aroca, *Chem. Mater.* 4 (1992) 1323.
317. T. Nyokong, H. Isago, *J. Porphyrins Phthalocyanines* 8 (2004) 1083.
318. T. Fukuda, S. Homma, N. Kobayashi, *Chem. Eur. J.* 11 (2005) 5205.
319. A. Y. Lebedev, M. A. Filatov, A. V. Cheprakov, S. A. Vinogradov, *J. Phys. Chem. A* 112 (2008) 7723.
320. T. Yonekura, T. Ohsaka, F. Kitamura, K. Tokuda, *J. Porphyrins Phthalocyanines* 9 (2005) 54.
321. A. J. Martynov, E. A. Safonova, Yu. G. Gorbunova, A. Yu. Tsivadze, *Russ. J. Inorg. Chem.* 55 (2010) 347.
322. N. Ishikawa, Y. Kaizu, *Chem. Phys. Lett.* 228 (1994) 625.
323. L. Li, J.-F. Zhao, N. Won, H. Jin, S. Kim, J.-Y. Chen, *Nanoscale Res. Lett.* 7 (2012) 386 (8 pages).
324. J. L. Bahr, J. Yang, D. V. Kosynkin, M. J. Bronikowski, R. E. Smalley, J. M. Tour, *J. Am. Chem. Soc.* 123 (2001) 6536.
325. C. D. Geddes, J. R. Lakowicz, *J. Fluoresc.* 12 (2002) 121.
326. M. N. Yarasir, M. Kandaz, O. Güney, B. Salih, *Spectrochim. Acta A Mol. Biomol. Spectrosc.* 93 (2012) 379.
327. L. Tomachynski, I. Tretyakova, J. Hanuza, J. Legendziewicz, *J. Photochem. Photobiol. A: Chem.* 214 (2010) 128.
328. N. C. Maiti, M. Ravikanth, *J. Chem. Soc. Faraday Trans.* 91 (1995) 4369.
329. J.A. Lacey, D. Phillips, *Photochem. Photobiol. Sci.* 1 (2002) 378.

-
330. K. Ishii, N. Kobayashi, in: K.M. Kadish, K.M. Smith, R. Guilard (Eds.), *The Porphyrin Handbook*, vol. 16, Elsevier, 2003 (Chapter 1).
331. K. Nonomura, T. Loewenstein, E. Michaelis, D. Wöhrle, T. Yoshida, H. Minoura, D. Schlettwein, *Phys. Chem. Chem. Phys.* 8 (2006) 3867.
332. L. Dai, *Intelligent Macromolecules for Smart Devices: From Material Synthesis to Device Applications*, Springer-Verlag, Berlin, 2004.
333. G. L. Wood, M. J. Miller, A. G. Mott, *Opt. Lett.* 20 (1995) 973.
334. S. Fu, X. Zhu, G. Zhou, W.-Y. Wong, C. Ye, W.-K. Wong, Z. Li, *Eur. J. Inorg. Chem.* (2007) 2004.
335. C. Zhan, W. Xu, D. Zhang, D. Li, Z. Lu, Y. Nie, and D. Zhu, *J. Mater. Chem.* 12 (2002) 2945.
336. B. Gu, W. Ji, P. S. Patil, and S. M. Dharmaparakash, *J. Appl. Phys.* 103 (2008) 103511.
337. B. Gu, W. Ji, P. S. Patil, S. M. Dharmaparakash, H.-T. Wang, *Appl. Phys. Lett.* 92 (2008) 091118.
338. J. Britton, C. Litwinski, T. Nyokong, *J. Porphyrins Phthalocyanines* 15 (2011) 1239.
339. C. Piechocki, J. Simon, J.J. Andre, D. Guillon, P. Petit, A. Skoulios, P. Weber, *Chem. Phys. Lett.* 122 (1985) 124.
340. Q. Zheng, G.S. He, P.N. Prasad, *Chem. Phys. Lett.* 475 (2009) 250.
341. N. Pan, L. Rintoul, D. P. Arnold, J. Jiang, *Polyhedron* 21 (2002) 1905.
342. Y. Kojima, T. Matsuoka, N. Sato, H. Takahashi, *Macromolecules* 28 (1995) 2893.
343. B. Aneeshkwnar, P. Gopinath, C. P. G. Vallabhan, V. P. N. Nampoori, P. Radhakrishnan, *J. Opt. Soc. Am. B* 20 (2003) 1486.

344. S. M. O'Flaherty, S. V. Hold, M. J. Cook, T. Torres, Y. Chen, M. Hanack, W. J. Blau, *Adv. Mater.* 15 (2003) 19.
345. R. Crane, K. Lewis, E. W. Van Stryland, and M. Khoshnevisa, eds., *Materials for Optical Limiting I* (Materials Research Society, Warrendale, Pa., 1994).
346. P. Hood, R. Pachter, K. Lewis, J. W. Perry, D. Hagan, and R. Sutherland, eds., *Materials for Optical Limiting II* (Materials Research Society, Warrendale, Pa., 1997), Vol. 374.
347. X. Sun, Y. Xiong, P. Chen, J. Lin, W. Ji, J. H. Lim, S. S. Yang, D. J. Hagan, E. W. Van Stryland, *Appl. Opt.* 39 (2000) 1998.